UNIVERSITÀ DEGLI STUDI DI MILANO

FACOLTÀ DI SCIENZE E TECNOLOGIE

Ph.D. Course in Industrial Chemistry - XXXVIII Cycle

Dipartimento di Chimica

Towards Sustainable Materials for CO_2 Remediation: From Functional Carbon-Hydroxyapatite Composites to Waste-Derived Resources

Ph.D Thesis of:

Michele Bigica

Supervisor:

Prof. Antonella Gervasini

Co-supervisor:

Dr. Sebastiano Campisi

Dr. Pierangela Cristiani

Ph.D. course coordinator:

Prof. Laura Prati

a.y. 2024/2025

UNIVERSITÀ DEGLI STUDI DI MILANO

Corso di dottorato in INDUSTRIAL CHEMISTRY
ciclo XXXVIII

DIPARTIMENTO DI CHIMICA

"SVILUPPO DI MATERIALI CATALITICI CONDUTTIVI A BASE DI CARBONE E IDROSSIAPATITE PER PROCESSI DI ELETTROMETANOGENESI"

Towards Sustainable Materials for CO_2 Remediation: From Functional Carbon-Hydroxyapatite Composites to Waste-Derived Resources

Settore CHEM-02/A - Chimica fisica

Tesi redatta con il contributo finanziario dell'Unione europea -
Next Generation EU e RSE S.p.A. - Ricerca sul Sistema Energetico

CUP n. G43C22002300004

Ph.D. Student MICHELE BIGICA
Matr. R13938
ORCID n. 0009-0007-7838-711X

TUTOR: Prof.ssa ANTONELLA GERVASINI

CO-TUTOR: Dr. SEBASTIANO CAMPISI, Dr.ssa Pierangela Cristiani

COORDINATORE DEL DOTTORATO: Prof.ssa LAURA PRATI

A.A. 2024-2025

Abstract

Sustainable development represents one of the most urgent challenges nowadays, involving a complex and multidimensional interplay of environmental, economic, and social factors. The transition to a circular economy is increasingly regarded as a key pathway to enhance environmental sustainability by replacing the linear “take-make-dispose” model with approaches focused on recycling, reusing, and reducing waste. The Ph.D. project, in collaboration with a national research center, Ricerca sul Sistema Energetico (RSE S.p.A.), explores sustainable chemistry applied to both materials and processes for energy and environmental applications. Two complementary research directions were investigated: CO_2 conversion through bio-electrochemical and electrochemical routes, and development of sustainable functional materials from biomass and wastes. These research directions converge on a common theme, namely the investigation of carbon-based materials and hydroxyapatite, including their combination into innovative composite materials for environmental applications.

The focus of the research was firstly directed toward the study of CO_2 bioelectromethanogenesis (BEM), a process in which microbial metabolism works in synergy with electrochemical systems to reduce carbon dioxide into methane (CH_4). Ternary composite cathodes based on biomass-derived carbon, copper nanoparticles, and hydroxyapatite were designed and characterized. After morphological and structural characterization, HAP-containing biocathodes were proven to promote a more CH_4 productive BEM process than HAP-free materials, owing to their ability to increase surface area, adsorb bicarbonate species, buffer the local pH, and promote microbial adhesion. Despite the remarkable CH_4 production, this composite suffers from low stability due to the lack of homogeneous distribution of hydroxyapatite on the carbon scaffold. To overcome this issue, during the period abroad in Lille (France), granted by Erasmus+ Traineeship in collaboration with Dr. Vitaly Ordomsky from CNRS-Université de Lille, a one-pot strategy was employed to synthesize a carbon nitride (CN) as a conductive scaffold, combined with HAP and copper nanostructures (HAP_Cu@CN). Advanced characterization techniques, including X-ray diffraction, TEM, and XPS, confirmed the presence of CN material and the successful integration of the components, particularly

HAP, completely embedded with carbon nitride scaffolds. HAP_Cu@CN, tested in CO_2 electroreduction test (CO_2ER), showed selectivity, expressed as Faradic Efficiency (FE), of 60% at -1.0 V *vs* RHE in the formation of formate, $HCOO^-$, with H_2 from hydrogen evolution reaction (HER) identified as the other detected product, demonstrating that HAP addresses the reaction pathway, by modifying the local reaction environment and stabilizing intermediates through non-covalent interactions, without significantly hindering charge transfer.

Building on the sustainable processes investigated for CO_2 emission mitigation in the first part, the second part of the thesis addresses material sustainability by optimizing individual components of the composite materials (specifically carbon scaffold and hydroxyapatite) with waste- and biomass-derived alternatives and greener production pathways. Biochar was produced from sugarcane biomass through two pyrolysis temperatures, while hydroxyapatite was extracted from waste-to-energy plant ashes. From a morphological point of view, by XRPD and Raman spectroscopies, the sugarcane-derived biochar exhibited high surface area and graphitic features, thanks to the high content of lignocellulosic component. The surface area obtained, after pyrolytic treatment, increased by 10-times of order of magnitude in respect to the biochar used for bioelectromethanogenesis, reaching 200 and 100 $m^2\ g^{-1}$, for the two chosen pyrolysis temperatures. As for graphitic properties, both materials demonstrated enhanced order and disordered bands, which are indicative of the presence of graphitization of the materials and consequently their conductive properties. With these preliminary results, sugarcane-derived biochar emerges as a promising component for efficient electrocatalysts, combining high specific surface area with improved electrical conductivity. The simultaneous enhancement of porosity and graphitic character suggests its suitability for electrochemical applications where both active surface availability and charge transport are critical factors.

On the other hand, ash-derived HAP samples showed tuneable crystallinity, Ca/P ratios, and surface acid-base properties depending on extraction conditions. Particularly, four HAPs were extracted, changing mixing techniques, temperature, and maturation time. Since the sources were inorganic ashes, which could contain many impurities, the composition of HAP samples included many *hetero atoms*, with a marked difference in Ca/P ratio for two of the HAP samples (HAP_3 and HAP_4).

However, all four samples demonstrated typical features of synthetic HAP in terms of specific surface area, structure, and surface moieties, analysed through N_2 adsorption-desorption isotherms, XRPD, FT-IR, and Raman spectroscopies, respectively. Furthermore, a deep surface studies were carried out through isothermal liquid-solid titration and volumetric microcalorimetry, analysing the number of acid and basic sites (and relative ratio A/B, amphoteric index) and their relative strength, respectively. Further going into details, two samples (HAP_1 and HAP_2) showed higher crystallinity, lower specific surface area and a more amphoteric nature (even though it is always shifted towards basicity) with an A/B ratio higher than 0.30. On the other hand, more amorphous HAPs (HAP_3 and HAP_4) displayed higher densities of amphoteric, predominantly basic sites (A/B < 0,30), which are relevant for catalytic applications. These results demonstrate that waste ashes can be effectively valorised into functional inorganic materials with specific properties by tailoring extraction parameters.

Overall, this work shows how sustainable chemistry can be addressed through complementary approaches, including the use of green materials, rational structural design, and the optimization of catalytic processes.

List of Figures

List of Tables

List of symbols and abbreviations

A/B: Acido-Basicity ratio

ACP: Amorphous Calcium Phosphate

BA: Benzoic Acid

BA: Bottom ashes

BEM: Bioelectromethanogenesis

BES: Bio Electrochemical System

BET: Brunauer-Emmet-Teller model

BJH: Barrett-Joyner-Halenda model

BP2G: Bio-Power-to-Gas

CaP: Calcium Phosphate

CCS: Carbon Capture and Storage

CCUS: Carbon Capture, Utilization and Storage

C_{dl}: Double Layer Capacitance

CO_2ER: CO_2 Electroreduction

COF: Covalent Organic Framework

C_s: Specific Capacitance

CV: Cyclic Voltammetry

DET: Direct Electron Transfer

ECSA: Electrochemical Surface Area

EDX: Energy Dispersive X-Ray

FA: Fly ashes

FE: Faradic Efficiency

FT-IR: Fourier Transformed Infrared Spectroscopy

GI: Glucose Isomerase

HAP: Hydroxyapatite

HER: Hydrogen Evolution Reaction

HPLC: High Performance Liquid Chromatography

HT: Hydrotalcite

I.A/ I.B: Intrinsic Acidity/Basicity

ICP: Inductevly Coupled Plasma

IET: Indirect Electron Transfer

IPA: Isopropyl alcohol

LCA: Life Cycle Assessment

LSV: Linear Sweep Voltammetry

MS: Maize Stalk

NMR: Nuclear Magnetic Resonance

NP: Nanoparticles

OCP: Octacalcium Phosphate.

OCP: Open Circuit Potential

OER: Oxygen Evolution Reaction

P2G: Power-to-Gas

P2M: Power-to-Methane

PEA: Phenylethyl amine

PZC: Point of Zero Charge

SDG: Sustainable Development Goals

SEM: Scanning Electron Microscopy

TCD: Thermal Conductivity Detector

TEM: Transmission Electron Microscopy

TGA: Thermogravimetric Analysis

VFA: Volatile Fattu Acids

WtE: Wasto to Energy

XPS: X-Ray Photoelectron Spectroscopy

XRF: X-Ray Fluorescence

XRPD: X-Ray Powder Diffraction

Preface

After intensive industrialization and high exploitation of energy and material resources, a sustainable approach to the production of energy, production of materials, and innovative processes is needed to ensure well-being for the planet and, consequently, the people and the overall ecosystems.
Among all the environmental problems nowadays, CO_2 remediation has gained a lot of attention due to the continuous increase in carbon dioxide concentration in the atmosphere.

These aspects are briefly discussed in the INTRODUCTION of the thesis, which provides an overview of sustainability principles, the CO_2 issue, and remediation technologies, highlighting the role and advantages of sustainable materials.

Following this introductory overview, the thesis work focuses on CO_2 electrochemical remediation techniques, including an innovative bio-electrochemical approach and the more traditional electrochemical reduction. These processes have been investigated through the design and application of a composite electrocatalyst consisting of a carbon scaffold support, copper nanoparticles as active sites, and hydroxyapatite (HAP) as a functional modifier. On the other hand, sustainability principles have been aligned with the circular economy concepts, with particular emphasis on the valorisation of waste for materials synthesis. Knowing that carbon scaffold and HAP are important components of the electrocatalyst for CO_2 remediation strategies, new sources for both materials have been investigated
The EXPERIMENTAL SECTION details the experimental procedures and analytical techniques used throughout the research.
The RESULTS chapter is divided into two main parts: the first (Results 3) focuses on the bio-electrochemical reduction of CO_2 and on the application of a novel composite electrocatalyst in the electrochemical reduction; the second part (Results 4) presents the principal physico-chemical characteristics of carbon materials and hydroxyapatite obtained from waste-derived sources. Overall, this work highlights how sustainability applied to chemistry can integrate rational design,

applying it to catalytic processes and material sourcing. By coupling CO_2 remediation with materials engineering, it contributes to environmental challenges while laying the groundwork for future development of efficient, sustainable organic–inorganic catalysts for remediation technologies.

Introduction

1. Towards a sustainable world

1.1. Environment and sustainable production

After industrialization, the relationship between human development and the natural environment has become a crucial global concern. For the (apparent) improvement of the life-quality, industrial growth, intensive resource use, and rising levels of pollution have pushed the ecosystem close to its limits. In this context, sustainable production represents a strategic approach to ensure economic progress while preserving environmental quality. Through sustainable production, environmental challenges such as resource depletion, climate change, and biodiversity loss can be addressed and resolved. The main purpose of sustainable production is minimizing resource consumption while reducing waste and emissions, maintaining high economic profit. For doing so, it requires a shift from the traditional linear model of take-make-dispose to a more responsible and circular model, where materials are used, recycled, and responsibly managed. To truly implement sustainable production, industries must adopt a set of connected principles that guide both technological choices, source management, and eco-friendly strategies. Firstly, eco-efficiency focuses on maximizing value while minimizing the use of energy, raw materials (e.g., water), thereby reducing emissions and waste without compromising performance or quality. Life Cycle Assessment (LCA) extends this approach by assessing environmental impacts (positive or negative) across all stages of a product's life (from resource extraction to final disposal). Furthermore, cleaner production emphasizes preventive strategies to reduce pollution, to select safer (or greener) materials for decreasing cost for the search/production and materials in end-of-pipe treatments, which are commonly used in linear economy production. Last but not least, the integration of renewable sources supports the decarbonization and promotes fewer environmental impacts (from the source). Together, these principles provide a framework for aligning industrial production with long-term environmental protection and social benefits.

These principles, if applied, could offer multiple benefits. From the environmental perspective, a more responsible production reduces greenhouse gas emissions, preserves natural resources, and safeguards ecosystems. Economically, it lowers energy and material costs while stimulating innovation and competitiveness, even in the sustainability market. Socially, it promotes safer working environments and enhances the well-being of communities affected by industrial activities. Even though the benefits are numerous and appealing, the transition to a sustainable production is not free from challenges. High investment costs, the need for specialized technical expertise, and resistance to organizational change can significantly slow the transition toward sustainable processes. These barriers often discourage industries from adopting innovative but *unknown* technologies, even when long-term benefits are clear. Targeted incentives, supportive regulatory frameworks, and increased public awareness can help reduce financial and perceptual risks. In parallel, investing in education, training, and highly specialized skills is crucial to enable effective implementation and long-term integration of sustainable solutions.

In conclusion, sustainable production is fundamental for aligning industrial activities with environmental preservation, while balancing economic and social growth with ecological responsibility, ensuring that today's development does not compromise the future of the Earth.

A central goal of sustainability strategies is the control of emissions and the progressive decarbonization of industrial, societal, and energetic systems. Emission control within a sustainable development idea focus on both toxic gases and greenhouse gases. Many harmful compounds have not greenhouse power, but the latter poses anyways risks to human health and ecosystem. Nevertheless, this thesis specifically focuses on CO_2 remediation, as carbon dioxide is one of the most abundant ad impactful greenhouse gases driving climate change and global warming. Greenhouse gases are compounds present in the atmosphere, responsible for the so-called greenhouse effect: a phenomenon occurring in the Earth's atmosphere under the influence of solar radiation, particularly the infrared radiation of the light. The energy from the sun is absorbed by land, water, and vegetation, and re-emitted as heat in the form of longer-wave infrared radiation. Normally, this radiation would escape into space but greenhouse gases, primarily as carbon dioxide (CO_2), methane (CH_4), nitrous oxide (N_2O), can absorb a portion of the infrared radiation emitted by the

Earth, trapping the heat. Going further, the interaction of infrared radiation with greenhouse gas molecules, primarily CO_2, CH_4, and N_2O, induces vibrational or rotational motions in these molecules. This internal motion imparts energy to the molecules that is radiated back into the atmosphere. This process generates additional thermal radiation, increasing the temperature of the surrounding air and the Earth's surface.

Reducing greenhouse gas emissions is essential not only to meet climate targets but also to mitigate long-term environmental risks associated with unsustainable development models, that are the widely used nowadays. In this context, understanding the role and impact of specific emitted species becomes crucial, as it guides both technological innovation and policy actions aimed at climate mitigation. Among these species, a particular case is carbon dioxide (CO_2). CO_2 present in the atmosphere arises from the combination of natural carbon cycle processes, such as respiration, volcanic activity, and organic matter decomposition, and anthropogenic activities, including fossil fuel combustion, industrial production, and deforestation. Under natural conditions, these fluxes are balanced by carbon sinks like soils and vegetation, maintaining a relatively stable atmospheric concentration. However, human activities have significantly accelerated CO_2 emissions, disrupting this equilibrium and exceeding the Earth's capacity for natural reabsorption. As a result, atmospheric CO_2 has accumulated to unprecedented levels, making it a central driver of climate change and amplifying risks for ecosystems, human health, and socio-economic stability. Although CO_2 is not toxic at ambient concentrations, it has indirect harmful effects due to its impact on the environment because it has intrinsic greenhouse power. For a chemical point of view, CO_2 has a linear arrangement between a single carbon and two oxygen atoms. This dipole structure facilitates an interaction with infrared radiation. Furthermore, the lifespan of CO_2 in the atmosphere is around 150-200 years, before reabsorption. Considering the heat-trapping characteristics measured in terms of global warming potential, CH_4 is 23 times more effective, and N_2O is 296 times more effective than CO_2.[1] However, the amount of CO_2 in the Earth's atmosphere significantly exceeds the amounts of CH_4 or N_2O making it of much greater concern. The continued accumulation of CO_2 in the atmosphere makes it the most troubling of the three major greenhouse gases. The problem will exacerbate with continued emissions. Considering the long lifespan of CO_2 as a gas, the achieved

temperature level will persist for several decades even if emissions were reduced to zero.

For these reasons, elevated atmospheric CO_2 levels intensify the greenhouse effect, leading to global warming, climate change, and a cascade of environmental alterations, such as unexpected weather events, bothering of sea levels, and changes in ecosystems, which can affect human health and the overall well-being. The sustainability of carbon-related processes has therefore become a central challenge in mitigating the impacts of CO_2 emissions. Achieving sustainable carbon management requires an integrated approach that limits the emissions from the source, during the process, and at the end of the process itself. To reach these connected goals, a transition towards renewable energy sources and materials is needed. Furthermore, residual and unavoidable CO_2 emissions call for complementary strategies based on carbon capture, utilization, and storage (CCUS). Carbon capture enable the separation of CO_2 from the point where it is produced; utilization pathways transform carbon dioxide into fuels, energy carriers, or platform chemicals, contributing to reach equilibria for the CO_2 cycle; carbon storage provides a tool to sequester CO_2 temporarily, and extract it when it becomes a source for energy or material production.

Together, these strategies support a shift from a linear, fossil-based carbon economy to a more resilient and sustainable carbon cycle aligned with long-term climate and environmental goals. CO_2 management represents a good example of the application of sustainability principles in technological development.

1.2. The role of chemistry for sustainability

To fully comprehend the importance of sustainability, it is important to start from its definition and what it concerns from different points of view. Sustainability is the ability to maintain or support economic, environmental, or social processes over time continuously without depleting natural resources, so that they will remain available for future generations. Generally, sustainability refers to three main pillars and dimensions: environmental protection, economic growth, and social impact.[2] The three pillars seem to be distinct in a first attempt: “environmental sustainability” emphasize the maintenance of natural resources (water, air and soil) and natural equilibrium; economic growth refers not simply to an increase in production or consumption, but to the creation of long-term

prosperity; finally, “social effect” means eradicate poverty and hunger, as well as to combat inequality. In 1983, the United Nations (U.N.) created the World Commission on Environment and Development to study the connection between ecological health, economic development, and social equity, that has become the standard in defining sustainable development: a development emerges only when these three pillars work together. Economic growth does not come at the expense of the environment and does not look only for profit, but it preserves natural resources, and it guarantees social equity. Fundamentally, sustainability is not merely an environmental goal, but a complex framework that integrates ecological integrity, economic viability, and social justice into the decision-making process.[3]

The increasing evidence of climate change, pollution, depletion of resources forced the worldwide communities to change the model of production to a sustainable idea. For this reason, over the past decades, the sustainability concept has evolved from theory to a concrete priority guiding policies, industrial choices, and scientific research. Notably, U.N. thought of a global plan called 2030 Agenda for Sustainable Development, which defines 17 Sustainable Development Goals (SDGs) to reach the three pillars in the most equitable way, as depicted in **Figure** 1-1.

Figure 1-1 Sustainable Development Goals (SDGs) of U.N. 2030 Agenda divide by each pillar of sustainability concept.[4]

Chemistry and chemical processes play an essential role in helping society achieve the SDGs. Among the 17 goals, chemistry can have an active role for achieving some of them. The scientific communities identified seven SDGs: zero hunger, good health, clean water, clean energy, industry innovation, responsible consumption, and climate action where chemistry can be fully applied and be a useful tool for achieving them. Food chemistry supports the development of safer and more resilient agricultural practices by improving nutrient preservation from infestations and enhancing food quality. At the same time, medicinal chemistry drives progress in medical diagnostics and drug discovery. For Clean Water SDG, new methods of water purification and lower-cost desalination processes will contribute to achieving universal access to safe and affordable drinking water. Water quality will be improved through the deployment of greener technologies and pollution prevention strategies. In a broad sense, chemistry plays a fundamental role in achieving SDG 7 (Affordable and Clean Energy) through the development of innovative materials for renewable energy technologies, the improvement of energy efficiency in chemical processing industries, and the advancement of cleaner and more sustainable fuel alternatives. These innovations not only contribute to decreasing the carbon footprint of the energy sector but also foster industrial innovation and sustainable infrastructure, in line with SDG 9. Furthermore, by integrating clean energy solutions and renewable resources into industrial production, chemistry enables more responsible consumption and production patterns (SDG 12) and supports global efforts to mitigate climate change **(**SDG 13**).** In this interconnected framework, the chemical sciences emerge as a key driver in promoting technological progress that safeguards both the environment and the well-being of the planet.

The role of chemistry for the above-described sustainable goals is important to face environmental crises and increased societal demand. Firstly, the chemical industry needs to change its profound principles. Traditionally, this industry has operated on a linear model characterized by converting resources into products that are wasted at the end of their life, as shown in **Figure** 1-2. At the heart of the linear model is the reliance on fossil fuel feedstocks, which contribute to greenhouse gas emissions. This linear model is eventually more profitable but in contrast with the environment stability, human health, and equity society. Generally, the processes prioritize yield over environmental impact. Many conventional chemical syntheses involve hazardous reagents and toxic

solvents and tons of water. These substances are firstly highly toxic, posing risks to human health leading to environmental contamination. After the use of the product, the linear approach results in significant waste, including non-degradable and harmful byproducts that persist in the environment, contributing to pollution and harming ecosystems and human health.

Figure 1-2 Representation of "linear model" of processes and products.[5]

These challenges combined with the sustainable goals of U.N illustrate the issues within the linear chemical industry, highlighting the need for a paradigm shift: green chemistry and circular chemistry. Green chemistry is an innovative approach that looks for the design of chemical products and processes in a way that minimizes or eliminates the use and generation of hazardous substances, taking into account also renewable resources and care for human health and the environment. At the heart of green chemistry are its 12 foundational principles, which provide the tools for reducing environmental impact and enhancing efficiency within the chemical industry. The benefits of green chemistry are extensive, and they show once more the connection between environment-society-economics: by reducing chemical hazards and waste, green chemistry decreases the environmental footprint, leading to cleaner air and water, positively impacting also on human health. Economically, green chemistry encourages to the use of cheaper raw material by utilizing renewable feedstocks, enhancing more markets to be involved due to the lower costs, which translates into enhanced market competition.

Circular chemistry represents a shift in chemical processes, moving away from the traditional linear model of ‘‘take-make-dispose’’ to a more sustainable, circular approach (**Figure** 1-3). This strategy aims to maintain resources within the economy indefinitely, minimizing wastes and promoting the reuse and recycling of materials. Circular chemistry views waste as a valuable input rather than an output, highlights the importance of efficiency over quantity, emphasizes recycling and reuse and identifies and quantifies environmental impacts and inefficiencies at every stage of a product’s life. [6]

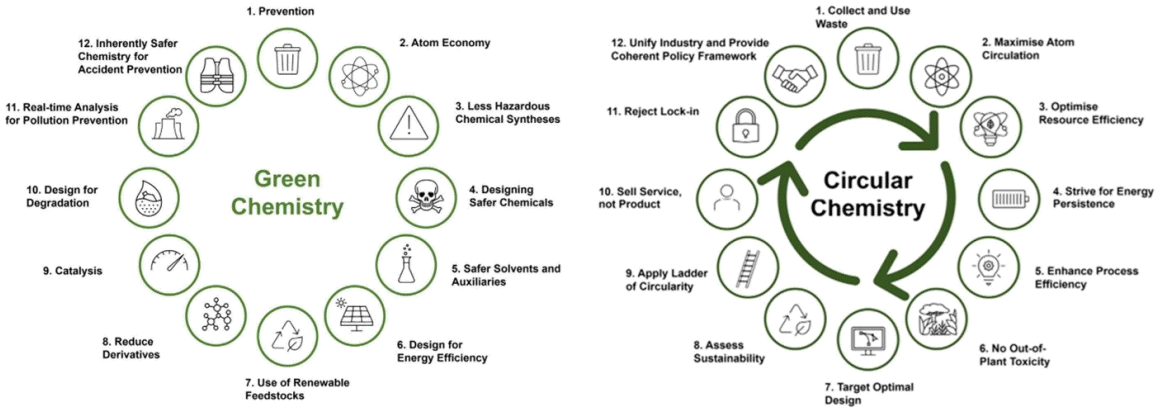

Figure 1-3 Representation of Green Chemistry principles and Circular Economy strategies.[6] (Reproduced with permission from Ref. 6).

Integrating principles of green chemistry, circular chemistry and Sustainable Development Goals creates a comprehensive net that goes beyond traditional chemical practices. These “new” industrial processes minimize their environmental footprint and contribute positively to human health and society in each stage of a product life. By embracing this framework, one of the most important challenges in the chemical communities is the CO_2 management through carbon capture and utilization technologies (CCUs), which represent a real application of all the principles. Furthermore, the development of sustainable materials and catalysts capable of converting CO_2 into valuable products embodies the essence of green and circular chemistry: turning a major environmental issue into an opportunity for innovation and contributing directly to climate action and resource circularity.

In this context, the Phd project focuses both on CO_2 reduction techniques and on the development of sustainable materials, that can be implemented in the catalytic conversion of CO_2.

1.3. Addressing CO_2 Emissions: strategies for Capture, Storage, and Utilization

Global greenhouse gas emissions have been rising since the start of the industrial revolution, and the greenhouse effect has become more severe decade by decade. The main effect of increased concentration of greenhouse gases is climate change, which is now a major challenge we must address. Statistics show that CO_2 is the primary cause of the greenhouse effect, making up more than 70% of global greenhouse gases, with the rest being water, methane, nitrous oxide, and various fluorinated gases.[7,8] Since 1970, CO_2 emissions have surged by about 90%, from 16 Gton ($16 \cdot 10^9$ t) in 1970 to 37.8 Gton ($37.5 \cdot 10^9$ t) in 2024.[9] This increase in CO_2 emissions intensifies the greenhouse effect, leading to sea-level rise, glacier melting, and ocean acidification, raising concerns about changes in our ecological environment.[10]

The main challenge is to limit global temperature rise to well below 2 °C above pre-industrial levels, as outlined in international climate agreements.[11] However, the continuous reliance on fossil fuels makes achieving this goal daunting. Current mitigation strategies need to address the substantial volumes of CO_2 released into the atmosphere, particularly from heavy industries and power generation. In this context, finding effective solutions to CO_2 emissions has become a popular research topic: the situation necessitates immediate and scalable solutions to prevent further environmental damage and ensure a transition towards a sustainable future.

Carbon Capture, Utilization, and Storage (CCUSs) technologies have emerged as critical components in the effort to reduce CO_2 emissions.[12] These technologies are designed to capture CO_2 directly from emission sources, such as power plants and industrial facilities, preventing its release into the atmosphere.[13] Captured CO_2 can either be stored in deep geological formations (carbon capture and storage, CCS) or utilized in various applications such as chemical production or enhanced oil recovery (carbon capture and utilization, CCU). Recent advancements in CCUS

technologies, particularly in the areas of advanced sorbents, high-performance membranes, and electrochemical techniques, have significantly improved capture efficiency and cost-effectiveness.[14,15] Furthermore, the utilization of captured CO_2 to produce valuable products, as shown in **Figure** 1-4, such as fuels and chemicals, offers an additional incentive for industries to adopt CCUS.[16] Despite these advancements, significant challenges remain, especially concerning the long-term stability of CO_2 storage and the high costs associated with these technologies.

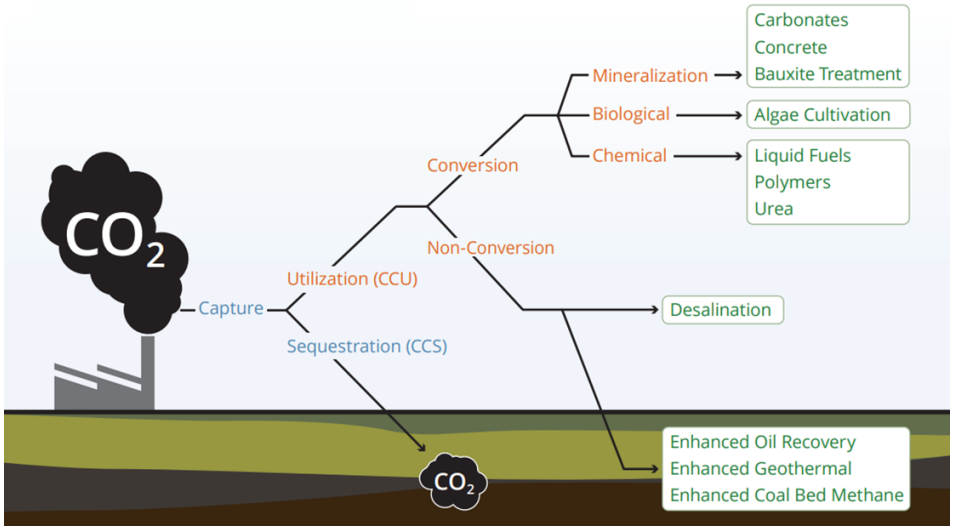

Figure 1-4 Schematic representation of the main Carbon Utilization and Storage technologies.[17]

Carbon capture (CC) technologies can be a useful tool for mitigating emissions with three methodologies: pre-combustion, post-combustion, and oxyfuel combustion methods. In pre-combustion capture, CO_2 is removed from the fuel (natural gas or coal) before it is burned by converting the fuel into syngas, a mixture of hydrogen and carbon monoxide. The carbon monoxide is reacted with steam in a catalytic reactor, called a shift converter, to produce CO_2 and additional hydrogen. The CO_2 can then be separated, usually by a physical or chemical absorption process, while the hydrogen serves as a green energy carrier. Post-combustion capture, on the other hand, focuses on treating the waste gases after combustion, where chemical solvents or filters (based on amines) selectively absorb CO_2. Finally, oxy-fuel combustion uses pure oxygen, generating a gas rich in CO and water, which simplifies the separation techniques, reducing the cost.

Carbon storage technologies (CCS) involve capturing CO_2 from industrial emissions, transporting it in compressed form, and injecting it into deep geological formations such as depleted oil and gas fields, where it can be stored for long periods. CCS and CC represent key technological routes for limiting CO_2 emissions from industrial and energy sectors.

Alongside storage and capture, CO_2 can be used as a carbon source in Carbon Utilization techniques (CCU) to reach a net-zero carbon process. Different utilization technologies have been developed such as mineralization, biological, and chemical ones. CO_2 can be converted into various chemical products and synthetic fuels that can replace current chemical feedstock in the chemical, pharmaceutical, and polymer industries. Since CO_2 is a stable molecule, with the Gibbs free energy of formation for the C-O bond being −394 kJ per mol, converting it requires a lot of energy to break its chemical bonds and innovative catalysts to increase reaction rates. There are many ways to convert CO_2 into chemicals or fuels, including electrochemical, catalytic, photochemical, biochemical, and hybrid methods.

1.4. Electrochemical conversion of CO_2 as a sustainable process

One of the most studied technologies due to its intrinsic challenges is the CO_2 electroreduction (CO_2ER). The electrochemical conversion of CO_2 offers a promising strategy to both stabilize and valorise carbon dioxide by transforming it into useful chemicals and fuels. Advances in electrocatalysts are improving the efficiency, selectivity, and durability of these processes, enabling controlled CO_2 reduction while contributing to carbon recycling and a circular economy. However, this electrocatalytic process poses two major challenges: activating the chemically inert CO_2 molecule and directing selectivity and electron transfer toward the desired products.

In this context, this thesis will focus on electrocatalyst design for CO_2ER process and also for an innovative approach, that is bioelectromethanogenesis, explored in collaboration with RSE S.p.A.

1.4.1. An innovative approach: bioelectromethanogenesis

Building on the recent advances in CO_2 electrochemistry, bioelectromethanogenesis emerges as an innovative and highly promising approach for carbon management and renewable energy storage. Hydrogenotrophic methanogens (microorganisms and bacteria) are combined with electrochemical setups to directly convert CO_2 into methane, effectively stabilizing carbon in a usable form while producing a renewable energy carrier.[18] Unlike traditional electrochemical CO_2 reduction, bioelectromethanogenesis adds the natural metabolic pathways of microorganisms, which interact synergistically with electrode materials to enhance selectivity, efficiency, and long-term stability.

It is not possible to discuss about bioelectromethanogenesis without talking about power-to-gas (P2G) technologies. P2G represents an innovative approach to store renewable electricity by converting it into gaseous fuels, such as hydrogen or methane, which can be used immediately in the infrastructure. In a typical P2G system, surplus electricity from renewable sources drives the electrolysis of water to produce hydrogen, which can either be stored directly or further combined with carbon dioxide to generate methane through chemical or electrochemical pathways. Power-to-gas serves as a key component in the chemical processes for sustainability, applying circular economy principles in an energetic perspective, linking carbon mitigation and energy production. [19]Bioelectromethanogenesis (BP2G) has been viewed as a particular P2G technologies, called power-to-methane system: the CH_4 produced can be used directly as fuel or valorised into other valuable product (**Scheme** 1-1), without the use of external hydrogen produced by water electrolysis due to the presence of methanogens.

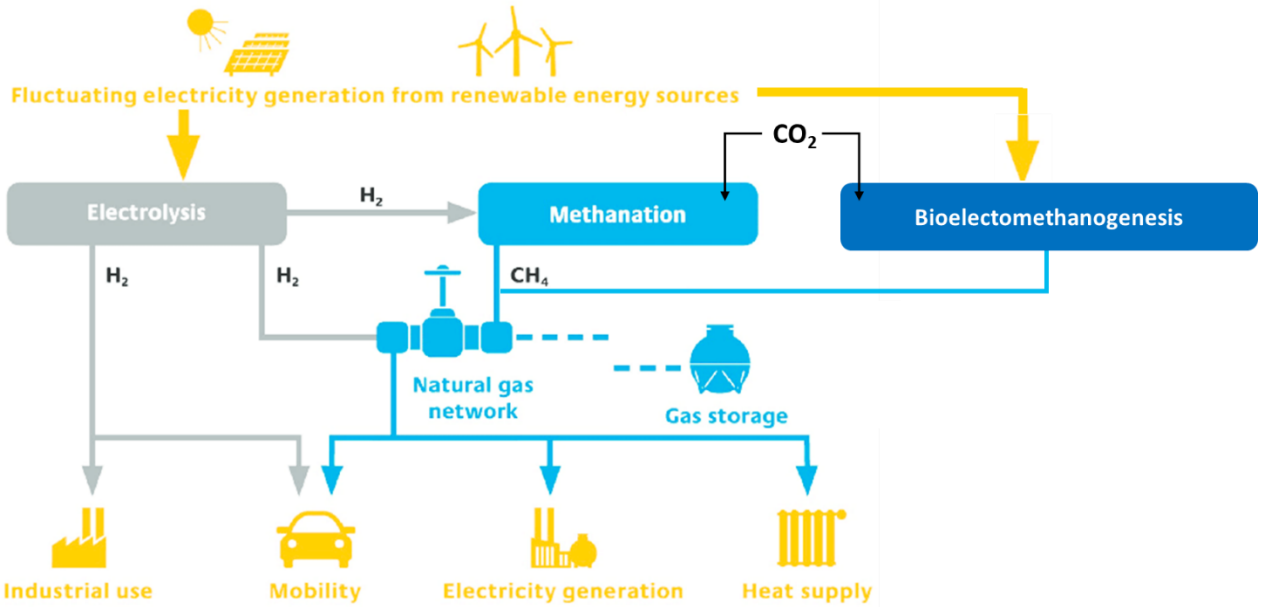

Scheme 1-1 Representation of Power-to-Gas technology combined with CO_2 utilisation.

In a B2PG (**Scheme** 1-2), electromethanogenesis and methanation are catalysed by seven orders of methanogenic microorganisms that belong to the *Archaea* domain. The applications of these microorganisms in new biotechnologies for biogas upgrading refer to the more recent period of the last ten years. In conventional methanogenesis, CH_4 is produced and released by *Archaea* metabolism, using H_2 as the electron donor. Differently, in the bioelectrochemical production of methane electrons are supplied by a cathode: the electrons come from the cathode and an external voltage is applied to drive the electrons themselves. The electrons are transferred from the electrode to microorganisms living in the biofilm growing on the cathode surface by three different ways, schematically: directly, indirectly or thanks to syntrophic relations. Direct electron transfer (DET) consists in the direct uptake of electrons from the cathodic surface by components of electroactive microorganisms; in Indirect Electron Transfer (IET) single microorganisms and mixed pools can produce electroactive mediators (e.g. H_2, methanol, acetate) that act as electron shuttles. Finally, syntropic relation means a co-adiuvation of different pool microorganism in which some microorganisms can collect electrons from the cathode and transfer them to other microorganisms

thanks to peculiar structures such as conductive *pili*. In all the three mentioned mechanism, the overall metabolism reaction is identical to the CO_2 reduction shown in Eq. 1-1.

$$CO_2 + 8H^+ + 8e^- \rightarrow CH_4 + 2H_2O \ (\Delta G^0 = -130.7\ KJ\ mol^{-1}, T = 25°C, E^0 = -0.244\ V\ vs\ SHE)$$

Eq. 1-1

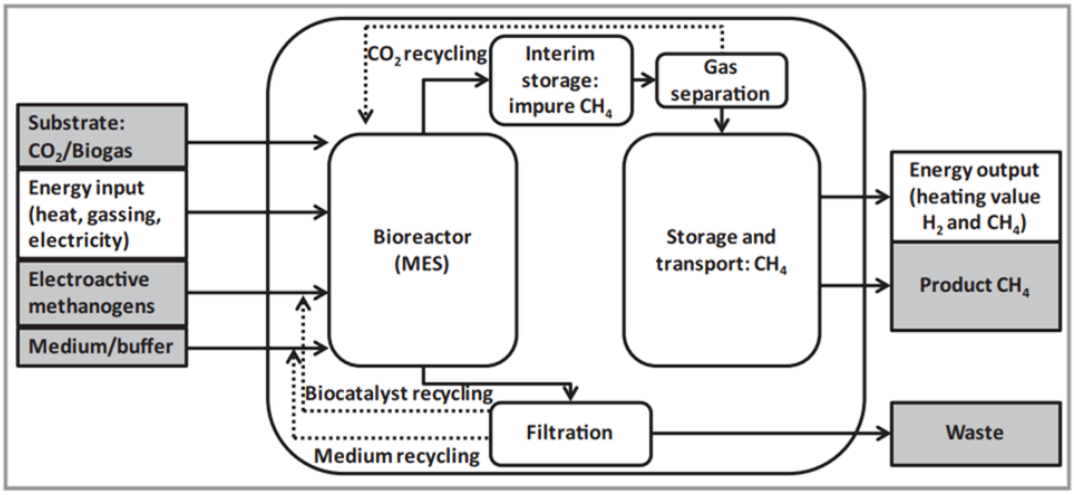

Scheme 1-2 Schematic view of Bioelectrochemical System in a Power-to-Gas technology.[19] (Reproduced with permission from Ref. 19).

Bioelectrochemical systems (BES) combine electrochemistry with the biocatalysis of microorganisms. The fundamental components of BESs are electrodes, i.e., anode and cathode, connected in an electric circuit. The system becomes a BES when microorganisms act as active components on the anode, cathode, or both, as showed in **Figure** 1-5.

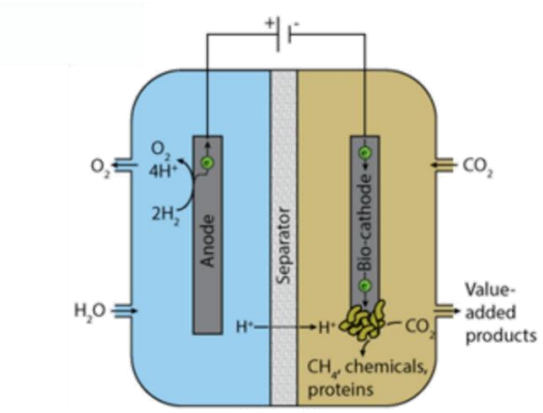

Figure 1-5 Schematic representation of a microbial electrolysis cell as a bioelectrochemical system: in the anodic chamber, water splitting is the main reaction occurring, while in the cathodic chamber, CO_2ER was carried out on a bio-electrode with microorganisms attached to it.[20]

For the purpose of the PhD, the anodic compartment is abiotic and the main reaction occurring on it is water electrolysis, producing oxygen (O_2) and protons (H^+). Conversely, the cathode is biotic due to the presence of microorganisms. Cathode electrodes for BES application can be made of metals (noble metals, nickel, copper, and titanium), metal alloys (stainless steel), or carbonaceous materials. Metal electrodes possess high mechanical strength, but low biocompatibility, and high corrosiveness, while carbonaceous materials are particularly suited as electrode material due to high surface area, conductivity, and biocompatibility. To further enhance the selective bioelectromethanogenesis, carbon scaffold, which is not electrochemically selective for CO_2 reduction, could be doped or coated with nanoparticles or inorganic modifier to form a composite material. In this way, the composite materials obtained could act in two ways, producing electrochemically added value reduced products and ensuring stability of the metabolism of the methanogens.

In addition to the proper design of the biocathode, other key factors are essential to a functional BES: applied potential, current density, and reactor configuration. Besides microorganism conditions, electrochemical conditions, and cathode design, the choice of solution (catholyte) is rather important: solution chemistry, including pH, ionic strength, and the presence of buffering species or electron donors, can impact both microbial metabolism and electrochemical reactions. Optimizing all these parameters in an optimal way is essential to maximize methane yield, coulombic efficiency, and long-term stability of bioelectrochemical systems.

1.4.2. Electrochemical reduction of CO_2

Alongside innovative technologies such as bioelectromethanogenesis, CO_2ER has been continuously investigated as a CCU technology. Since the pioneering work of Hori and Ikeda[21], who demonstrated the feasibility of CO_2 electrocatalytic reduction on metal electrodes, different catalysts have been tested in CO_2ER, from metal catalysts to composite materials.[22]

Electrocatalysts are the central active component in electrolysis systems and have attracted substantial attention from researchers in recent years. In the CO_2ER field, numerous catalysts have been developed by varying the type of electrode material, morphology, and surface area, among others. These catalysts have been examined under a subset of operating conditions in a variety of cell architectures but with the same goal: activation of CO_2 molecules and direction of selectivity of the process. Upon activation, local CO_2 concentration may be an issue as it has low solubility in water (ca.1.45 g L^{-1} at ambient temperature and pressure), posing the major issue of diffusive limitation to CO_2 reduction processes in aqueous electrolyte: adsorbent material design is an important tool for overcoming this initial problem.

Then, the activation of a linear aqueous CO_2 molecule is the initial step of CO_2ER. Without electrocatalysts, the activation of CO_2 reduction is considered to be difficult, due to the stability of CO_2 molecule and the very negative redox potential for the first electron transfer to form the $CO_2^{\bullet-}$ radical intermediate (-1.2 V *vs* RHE). Owing to the feasible stabilization of $CO_2^{\bullet-}$ or other intermediates on the surface of electrocatalysts, a much less negative required potential can be achieved.[23] As seen in **Figure** 1-6, due to the multiple electrons and protons required for CO_2ER

products, a series of transfer steps are needed to obtain a certain product. It is then challenging to directly regulate product selectivity for species formed at similar thermodynamic potentials. Many approaches in research have attempted to overcome these challenges through the rational design of electrocatalysts, where the CO_2ER activity of different reactions can be promoted through feasible reaction pathways towards desired products.

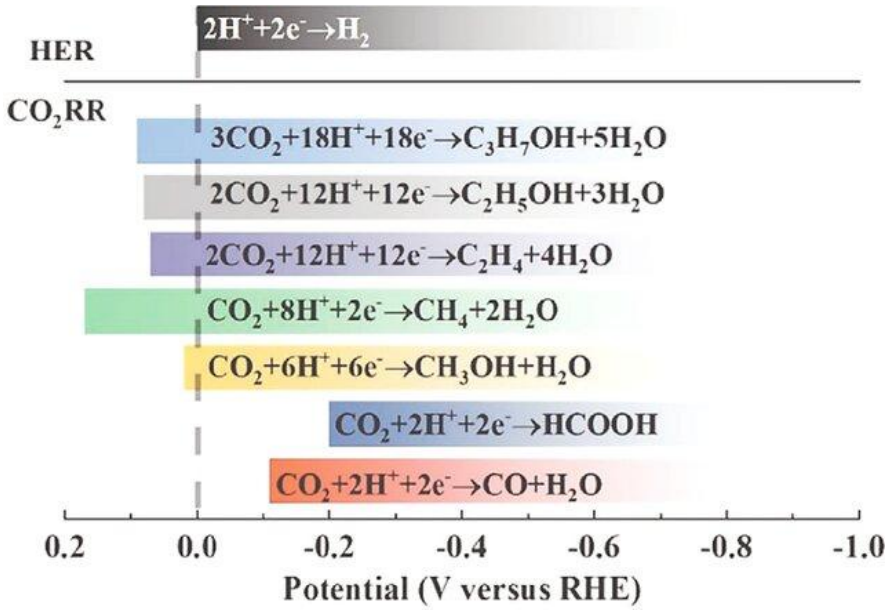

Figure 1-6 The thermodynamic potentials for CO_2 reduction reaction and hydrogen evolution reaction (HER) in the aqueous electrolyte under standard conditions (T= 25 °C, p = 760 Torr, $[H^+]$ = 1 mol L^{-1}).

To develop electrocatalysts with improved activity (or reaction rate) for CO_2ER, there are then two general approaches, which can be used: i) increasing the number of active sites in a defined electrolysis area, ii) increasing the intrinsic activity of each active site. For the first strategy, the number of active sites can be increased through the rational design of larger electrode nanostructures or through the precise control of particle size or higher surface area. This strategy could be hindered by stability over time due to sintering or agglomeration into metal clusters under operating conditions.

The second strategy involves the choice of catalysts with low affinity for hydrogen evolution reaction (HER). For this approach, one of the most studied metals is copper: more than 16 reaction products

have been reported for CO_2ER on Cu-based electrocatalysts[24,25]. Among high-added-value products, methane, ethylene, and ethanol are those generally detected in relevant quantities.

In the search for an optimal electrocatalyst, various types of materials have been typically screened for their redox potentials, electron transfer rates, chemical kinetics, and current efficiencies. Among the electroactive materials, copper (Cu) is one of the most extensively investigated metal electrocatalysts, as it is the only metal active phase able to catalytically produce both various oxygenates and hydrocarbon species.[24] The Cu-nanostructures are usually dispersed onto carbon support to enhance metal dispersion, increase the overall conductivity of the material, and avoid agglomeration and passivation.

However, copper nanoaggregates and carbon scaffold could not be the only constituents for a highly active and selective electrocatalyst; recent studies explored the use of modifiers as a third electrocatalyst component for directing and steering the selectivity of CO_2 electrochemical reduction.[26] By leveraging the unique characteristics of each component, composite materials enable improved electron transfer, optimized adsorption of CO_2 and intermediates, and controlled product selectivity, limiting hydrogen evolution reaction (HER) and decreasing overpotential. In this thesis, it is reported a novel composite based on a carbon nitride electrocatalyst co-functionalized with copper as the active phase and hydroxyapatite as an inorganic modifier.

1.4.3. Two routes for CO_2 reduction

Before going into details of each process results, a comparative view is needed. As it has been discussed in the previous paragraphs, the electrochemical conversion of carbon dioxide represents a key technological pathway toward carbon neutrality and circular carbon utilization. Among the available approaches, traditional CO_2 electroreduction (CO_2ER) and bioelectromethanogenesis (BEM) have emerged as two fundamentally different yet conceptually related strategies. While both rely on electron-driven CO_2 reduction at a cathode, they differ substantially in, operating conditions, selectivity control, and technological maturity.

Traditional CO_2 electroreduction is an abiotic process in which CO_2 is reduced at the surface of heterogeneous electrocatalysts, typically metals. The reaction proceeds through adsorption of CO_2 and formation of surface-bound intermediates (e.g., $CO_2^{\bullet -}$, *COOH, *CO, *HCOO), followed by proton-electron transfer steps. Product selectivity is governed by the catalyst surface structure. However, challenges remain in terms of long-term stability, catalyst degradation, competing hydrogen evolution reaction (HER), mass transport limitations, and overall energy efficiency.

In contrast, bioelectromethanogenesis is a hybrid bioelectrochemical process in which electroactive microorganisms catalyze the reduction of CO_2 to methane using electrons supplied by a cathode. Microorganisms utilize electrons and complexed electrolyte (rich in nutrients for the biotic part of the cell) to generate CO_2 reduced products. BEM typically operates under mild conditions (ambient temperature, neutral pH) and exhibits high product specificity, as methane is the predominant metabolic product. This intrinsic selectivity represents a major advantage compared to abiotic CO_2ER, where product distribution often requires precise catalyst engineering. As a result, BEM avoids the formation of complex product mixtures, but it is constrained to methane production, limiting product flexibility compared to CO_2ER platforms capable of generating CO, formate, methanol, ethylene, ethanol, and other value-added chemicals.

From a kinetic point of view, traditional CO_2ER and BEM systems are limited by low mass transfer within the electrode surface and electron uptake efficiency. Another similarity regards the presence of high overpotentials, which can reduce overall energy efficiency depending on cell design and

membrane configuration.

From a sustainability perspective, BEM offers advantages in terms of operating conditions and catalyst renewability, as the active component is a living system capable of adaptatio. However, it is restricted to methane production, which, although compatible with existing natural gas infrastructure, may not fully exploit the chemical diversity accessible through CO_2ER. Traditional electroreduction, on the other hand, provides broader chemical versatility relies on selectivity issue inorganic catalysts that may involve critical raw materials and exhibit stability issues.

In summary, traditional CO_2 electroreduction and bioelectromethanogenesis represent complementary strategies for carbon dioxide valorization. CO_2ER offers high flexibility, faster kinetics, and access to a wide spectrum of chemicals, whereas BEM provides exceptional selectivity toward methane under biologically driven conditions. In the following table (**Table** 1-1), the main similarities, advantage and disadvantages are present for both processes.

Table 1-1 Comparative view between CO_2ER and bioelectromethanogenesis processes

	Traditional CO_2 Electroreduction (CO_2ER)	**Bioelectromethanogenesis (BEM)**
Catalyst	Metal active center	Biocompatiblae cathode (metal center and microorganisms)
Main products	CO, formate, CH_4, methanol, and C_{2+}, hydrocarbons	Mainly CH_4
Operating conditions	alkaline electrolytes	Neutral pH, ambient temperature, anaerobic environment
Catalyst stability	Possible degradation, poisoning, or restructuring	Poisoning of biofilm
Advantages	High reaction rates; high current densities; wide range of products; compatibility with industrial electrochemical reactors	Very high selectivity to methane; operates under mild conditions; Power-to-gas technology
Disadvantages	Competing hydrogen evolution reaction; catalyst stability issues; complex product separation	Slow kinetics; low current density, microbial stability

1.5. Beyond the process: towards sustainable materials

1.5.1. Biochar from vegetable biomass

Alongside sustainable processes, the transition toward a more sustainable and circular economy increasingly depends on the development of sustainable materials that minimize environmental impact while maintaining high performance and functionality. Sustainable materials are designed with a life-cycle perspective, aiming to reduce the consumption of non-renewable resources, lower carbon emissions, and enable recyclability or biodegradability at the end of their use.[27,28]

In the context of sustainable materials development, carbon is the most abundant element in the biosphere after oxygen.[29] Nature utilizes these elements coupled with hydrogen to provide the basis for renewable energy storage (e.g., carbohydrates). Analogously, carbon-based systems are increasingly performing a major role in emerging technologies. Biochar and carbon materials are produced from biomass, naturally present in nature and is a sustainable source of carbon. Biochar is a black, carbon-rich and porous solid material (similar to charcoal) that can be produced through thermochemical conversion of biomass in the presence of little or no oxygen. Furthermore, converting biomass to carbon materials is even a process of negative carbon emission, which can help alleviate the pressure of global warming.[30] Notably, the development of more flexible routes to new carbon materials derived from renewable resources has only recently become a topic of significant interest because the biochar shows versatile physicochemical properties and can have a wide applicability in diverse fields. These applications are widely spread, comprising electrodes in energy storage devices, electrocatalysis, photocatalysis, heterogeneous catalysis, biofuels, and so on.[29] Different studies have been conducted to explore different approaches for biochar production and identify the relationship between preparation techniques and the resulting physico-chemical characteristics. The most common technique is the pyrolysis (with slow or fast heating), often used alongside gasification. Different methods have been also studied, tested, and developed to alter and tune the properties of biochar to maximize its performance in specific applications. Examples of such treatments include acid or alkaline modifications and exposure to gaseous agents (usually, steam,

CO_2, air, and ammonia).[31]

As pyrolysis is one of the most used techniques, a brief introduction on this method is provided. Pyrolysis involves heating vegetable biomass in an inert atmosphere, preventing combustion and allowing the material to reach temperatures beyond its thermal stability limit. This process strips out small molecules, thus leaving a more stable carbon-rich biochar. During pyrolysis, cellulose or hemicellulose, the primary polymeric components of vegetable biomass, first depolymerize into oligosaccharides, and their glycosidic bonds can subsequently undergo dehydration, decarboxylation, aromatization, and intramolecular condensation to form solid carbon (**Figure** 1-7).[32] Several parameters during the synthesis influence the properties of the resulting carbon materials, including temperature, pressure, feedstock type, heating rate, and reaction time.[33] Pyrolysis can be classified as slow or fast depending on the heating rate: for slow pyrolysis the rate is between 0.5 and 20 °C min^{-1}, while for fast pyrolysis the ramp is from 10 to 200 °C s^{-1}. In slow pyrolysis, increasing the pyrolysis temperature decreases the volatile matter content (and consequently the H and O content), enriching the fixed carbon fraction and producing materials with higher basicity in water and larger specific surface areas.[31,34] In contrast, fast pyrolysis promotes the depolymerization of biomass into volatile components, which reduces the biochar yield and modifies the morphology and surface properties, resulting in lower pH values in solution and generally smaller surface area.

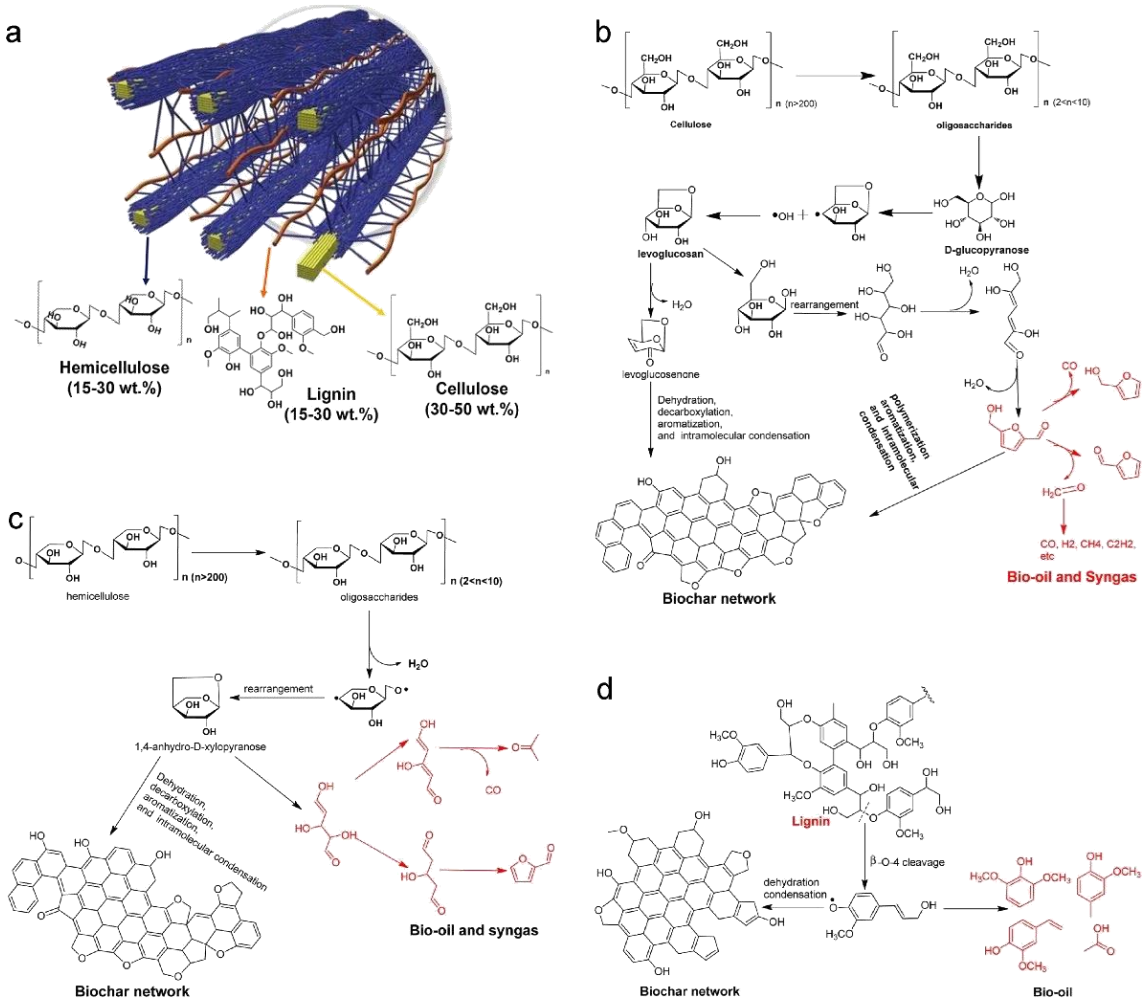

Figure 1-7 Mechanism of the model components in lignocellulosic biomass during the pyrolysis. (a) Structures of hemicellulose, cellulose, and lignin in lignocellulosic biomass; (b) mechanism of carbonization of cellulose; (c) mechanism of carbonization of hemicellulose; (d) mechanism of carbonization of lignin.[33] (Reproduced with permission from Ref. 33).

Generally, for biochar utilized in catalytic applications, high SSA and high adsorption capacity can be promising features for an optimal choice of pyrolytic treatment and biomass source selection. Going into details, for electrochemical applications, high specific surface areas, pore distribution, high conductivity, high carbon content, low ash content, and high N content are the desired properties. Some properties are affected by temperature in opposite ways, such as SSA and low ash content, while some are not, such as pore distribution. Therefore, slow pyrolysis is more suitable compared to fast pyrolysis or gasification.[35]

Another important parameter that can lead to different biochars is the feedstock used as the carbon source. The main categories are woody biomasses and herbaceous biomasses, which typically differ in the lignin and hemicellulose content. It is shown that higher lignin content results in a better yield of biochar production and provides overall better physicochemical properties such as high porosity and high aromatic carbon content. Over the past few decades, there has been a notable rise in sugarcane production, driven by the increasing demand for sugar, ethanol and food industry. Consequently, the sugar industry generates a significant amount of agricultural waste. Extensive research has revealed a promising pathway for enhancing energy recovery and functional materials through the conversion of agricultural residues into biochar.[36] Starting from sugarcane biomass, biochar has demonstrated important physicochemical properties like higher surface area and porosity, low bulk density, higher cation exchange capacity, neutral to high pH, and higher carbon content.

For these reasons, in this thesis, pyrolysis treatment of sugarcane and application of biochar as catalyst support in CO_2 remediation techniques has been further developed and discussed.

1.5.2. From ashes to valuable calcium phosphate materials.

In addition to biomass-derived materials such as biochar, sustainable materials can also originate from inorganic components of waste sources. Industrial residues and solid wastes, for instance, represent a valuable and often underutilized resource for material recovery.

Waste-to-energy (WtE) is an important waste management technology that not only degrades organic pollutants and reduces the volume and mass of residues but also generates district heating and electricity. WtE is an innovative energy production technology, which is still spreading within the world, but it has an intrinsic disadvantage: the production of ashes (also called *bottom ashes, BA*). Ashes from waste-to-energy plants have attracted growing attention due to their rich content of metallic species, silicate, and calcium phosphate phases. BA accounts for 80 wt % of the total incineration. residues, with a mass ratio of bottom ash to fly ash (FA) from 4:1 to 5:1. Bottom ashes (which part of the composition is reported in **Table** 1-2) typically contain CaO, SiO_2, compounds of Al, Fe, Mg, Na, K, and Cl, as well as potentially toxic elements like Cr, Ni, Cu, Zn, Cd, Hg, and Pb.[37,38] As the most significant portion of solid residue in WtE, BA has the potential to be repurposed as a functional material. However, the presence of various heavy metals makes the utilization of these residues challenging. Specifically, pure metal pieces are recycled from the BA and reused in society, while chemically bound metals and other non-precious components are not recovered.

Table 1-2 Average content of major elements (as oxides) for nordic BA samples as exemplificative samples.

Oxides[a]	wt %
SiO_2	38.7
Al_2O_3	9.8
CaO	15.0
Fe_2O_3	14.4
K_2O, MgO, MnO, Na_2O, P_2O_5, TiO_2	< 3.0

a. The other elements (metallic traces) are reported in Ref. [38]

Only in very few cases, the mineral fraction of incinerator bottom ash, i.e., BA after metal sorting, has been reused for construction purposes outside landfills.[39] However, most of the ashes are even

considered hazardous wastes and are directly scattered. If not managed effectively, improper ash disposal, whether through landfilling, co-disposal, or ocean dumping, can lead to environmental contamination. The challenge lies in ash's full integration into circular economy practices, including metal recovery, material valorisation, and reducing reliance on landfilling.[40] Addressing these challenges through proper treatment, regulation, and innovative utilization methods can unlock the potential benefits of ash from WtE plants. This approach is crucial for minimizing environmental impacts and maximizing its value in various applications, relying on sustainable principles. Metal extraction from bottom ashes has been highly encouraged due to the higher market cost of the metallic species themselves.[41] The techniques for extracting metals from bottom ashes typically begin with physical separation methods (e.g., magnetic, gravity, filtration, or electrodeposition). These are often followed by chemical methods which involve complexing agents or solvents. The goal is to efficiently recover ferrous, non-ferrous (Al, Cu, Zn), and precious metals, frequently by combining multiple techniques to maximize overall yield and resource efficiency. On the other hand, the non-precious inorganic part (metal oxides, silicate, phosphates) has been continuously underrated, leading to landfill without further valorisation. In this context, to apply sustainable and circular economy principles, the valorisation of these non-precious species is quite central. For example, these fractions can be recovered and repurposed as precursors for the synthesis of functional materials, such as mesoporous silica and silica-based composites[42] or calcium phosphate (CaP), with potential applications in catalysis, adsorption, and environmental remediation. This approach not only contributes to waste valorisation and resource efficiency but also aligns with the principles of circular chemistry by transforming residues from energy recovery processes into valuable secondary raw materials. Generally, with the term CaP, a variety of different compounds composed of calcium, phosphorus, and oxygen (in different stoichiometric ratios) are comprised. Among this variety of materials, calcium hydroxyapatite (HAP) has been the focus of the PhD thesis. Calcium hydroxyapatite has been deeply studied due to its unique morphological, structural, compositional, and biological properties, which have enabled its application across a wide range of fields, including bioengineering, medical applications, adsorption, and heterogeneous catalysis. It is

important to define some important physico-chemical characteristics of HAP that highlight the reason why HAP can be used in many fields.

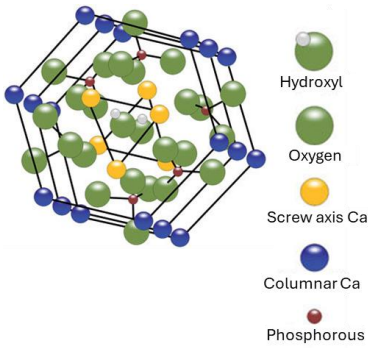

Figure 1-8 representation of unit cell of HAP crystalline structure with highlighting of the atomic composition (Ca, P, OH^-).[43]

HAP crystallizes in two different crystal structures: monoclinic and hexagonal. The monoclinic phase (space group P21/b) is more energetically stable but the hexagonal phase (with lattice parameters of a = b = 9.37 Å and c = 6.88 Å) predominates in both natural and synthetic HAP due to the presence of defects and impurities, which make it easier to form. The crystal structure of HAP consists of a compact arrangement of PO_4 tetrahedra, with Ca^{2+} ions distributed among them, intercalating also OH^- ions (on the c-axis), as depicted in Figure 1-8. Specifically, a packed arrangement of PO_4 tetrahedra defines two distinct channels: one delimited by the *columnar* Ca^{2+} ions (with a channel diameter of 2.5 Å), and the other bordered by *triangular* Ca^{2+} ions (with a channel diameter of 3.5 Å), which hosts the OH^- anions. These channels make the hydroxyapatite structure highly flexible, allowing ionic substitutions within the lattice. The flexibility of the HAP structure allows hydroxyapatite to incorporate a wide range of ions into its lattice with a small distortion of the original structure. These substitutions can occur at various sites within the apatitic structure: cationic and anionic substitution. Finally, the presence of different sites (or different ions due to substitution) declines differently the overall surface reactivity of HAP. For the *bare* HAP, the reactivity is a complex interplay between distinct chemical sites, namely, calcium, phosphate, and hydroxide sites. Its surface reactivity depends on the balance between Lewis acidic sites of Ca^{2+} sites and Brønsted acido-basicity of surface CO_3^{2-}, PO_4^{3-}, OH^- groups, which can undergo protonation-deprotonation (Figure 1-9).[44]

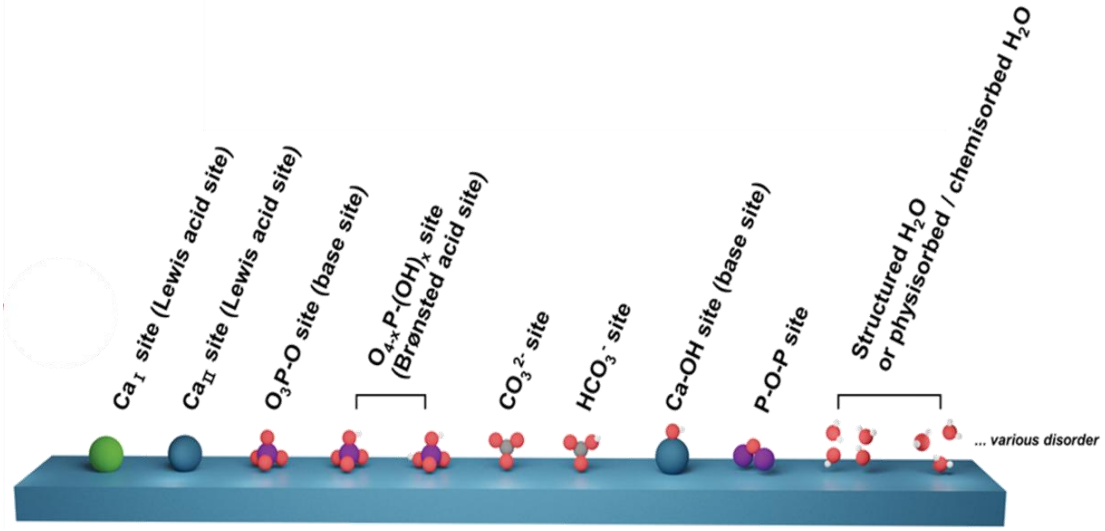

Figure 1-9 Representation of main acid and base sites on the surface of HAP. [45] (Reproduced with permission from Ref. 45)

Thanks to its high lattice flexibility and structural stability, hydroxyapatite is a highly versatile material, and its use in environmental protection has grown in recent years. Its peculiar structure allows surface modifications that create a more reactive surface, tailored to specific applications of HAP-based materials. HAP can be obtained synthetically or naturally from chemical, biological sources, or wastes. Tailoring the synthetic parameters or the extraction process parameters, different surface properties can be obtained while maintaining the main morphological and structural features. Starting from wastes, the presence of external elements can induce defects, modify surface properties, which often enhancing adsorption capacity and catalytic performance. Furthermore, using ashes aligns more closely with circular economy and resource valorisation principles.[46]

Part of this thesis has explored the extraction of different hydroxyapatites from waste-to-energy plant ashes, their physicochemical characterization, and their application also in catalytic processes, with a comparison to synthetic HAP.

To elucidate the diverse physicochemical and surface features of ashes-derived HAP, the isomerisation of glucose into fructose has been chosen as model reaction. The reaction fully aligns with the sustainability principles discussed above. In the context of the transition from a fossil-based economy to renewable resources, the development of catalytic processes enabling biomass valorisation is essential to support a circular and environmentally responsible manufacturing sector. Furthermore, the setup and the product identification with low possibilities of side reactions, make

the glucose isomerisation reaction a powerful model reaction to evaluate physicochemical properties of catalysts. As a matter of fact, through this model reaction, it is possible to evaluate how extraction routes influence material properties and catalytic behaviour, while simultaneously enhancing overall sustainability through the valorisation of incineration ashes as secondary resources.

Experimental Section

2. Experimental approaches

2.1. Preparation of materials

2.1.1. Preparation of calcium phosphate materials

Generally, the term “calcium phosphates” refers to a family of inorganic compounds composed of calcium, phosphorus, and oxygen, and, in some cases, also hydrogen. In strict terms, phosphates are salts that contain anionic units formed either by a single PO_4 tetrahedron or by the condensation of multiple PO_4 groups sharing one, two, or three oxygen atoms. From this basic geometric concept, an essentially limitless variety of structures can be generated for condensed phosphate anions, resulting in a complex and multifaceted phase diagram. Each phase is formed under specific conditions of pH, temperature, and stoichiometry. In this thesis, the focus will be on the calcium orthophosphate family, particularly calcium hydroxyapatite ($Ca_{10}(PO_4)_6(OH)_2$, HAP), which is formed at basic pH (pH > 10) and high temperature (80°C) with a Ca/P molar ratio of 1.67. Even though HAP is not the kinetically favored form (which is amorphous calcium phosphate, ACP), it is the most thermodynamically stable one.

2.1.1.1. *Synthesis of stoichiometric hydroxyapatite*

Calcium hydroxyapatite was prepared by a precipitation method using $Ca(NO_3)_2$ (0.167 M) and $(NH_4)_2HPO_4$ (0.100 M) aqueous solutions as Ca and phosphate sources, following the reaction below:

$$10\ Ca(NO_3)_2 + 6\ (NH_4)_2HPO_4 + 8\ NH_4OH \rightarrow Ca_{10}(PO_4)_6(OH)_2\downarrow + 20NH_4NO_3 + 6H_2O$$

As reported in the literature[47], basic pH (8-10) and relatively high temperature (80 °C) conditions are needed to obtain a stoichiometric crystalline calcium hydroxyapatite. The $(NH_4)_2HPO_4$ solution was initially mixed with 50 mL of NH_4OH solution (30%) under N_2 atmosphere. The pH of the solution

was measured by pH electrode system to be 10.0 ± 0.2. The prepared mixture was heated at 80 °C in an oil bath and maintained under magnetic stirring. The flask was equipped with a reflux condenser, and connected to a peristaltic pump, through which $Ca(NO_3)_2$ solution was dropped at a flow rate of 1.7 mL·min^{-1}. To keep the pH above 8 throughout the synthesis, 10 mL of 30% NH_4OH solution was added periodically every 30 minutes (total added volume of 40 mL). The synthetic method is summarized in **Scheme** 2-1. Once all the $Ca(NO_3)_2$ solution had been added, the suspension was filtered under vacuum, and the precipitate was washed with water until the pH of wash waters was neutral, indicating the elimination of ammonia from the salt. Then, the obtained white solid (HAP) was dried in an oven at 50 °C under vacuum overnight and subsequently at 120 °C under atmospheric pressure for 8 hours.

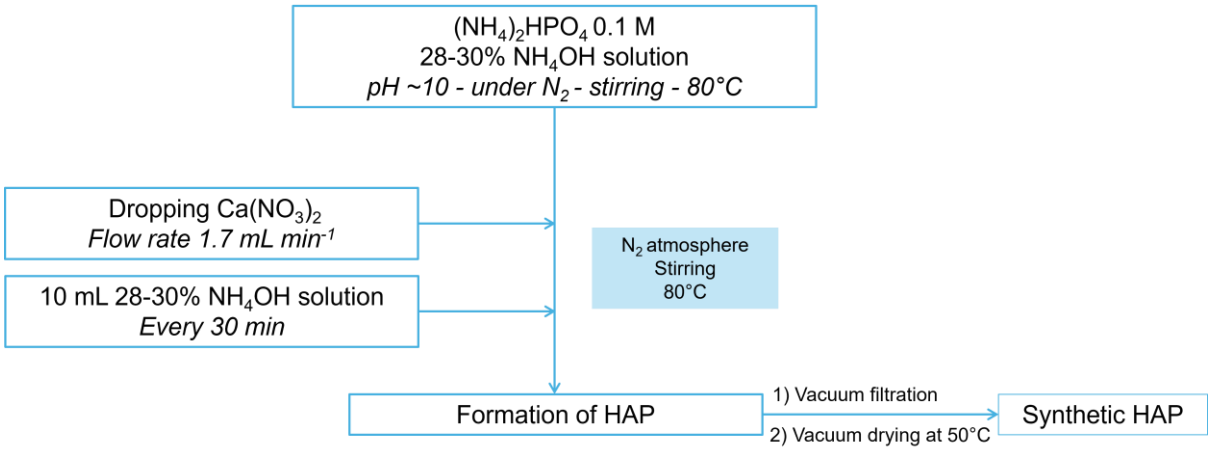

Scheme 2-1 Schematic representation of the co-precipitation method for the synthesis of stoichiometric HAP sample.

2.1.1.2. *Preparation of ashes-derived hydroxyapatite*

Four ashes-derived apatite samples (HAP_1, HAP_2, HAP_3, HAP_4) were kindly supplied by the CNR-ISSMC Istituto di Scienza, Tecnologia e Sostenibilitá per lo sviluppo dei Materiali Ceramici, National Research Council (CNR) of Faenza (Italy). The provided samples were prepared by a 2-step procedure: extraction and recrystallization processes. Initially, ashes derived from a waste-to-energy facility (Centrale Termoelettrica a Fonti Rinnovabili di Faenza - Enomondo Herambiente/Caviro Extra) were ground and sieved to a particle size below 150 µm to obtain a fine powder. The sieved ashes were then suspended in a 2 M HCl solution (1 g of powder per 100 mL of

solution), and stirred for 1 h at 25°C. The suspension was filtered, and the resulting acidic leachate, containing Ca^{2+} and PO_4^{3-} ions, was used as the starting solution for hydroxyapatite reprecipitation. The acidic solution was mixed with 1M NaOH solution under stirring (at a 1:2 leachate:base volume ratio), yielding a final pH of 11. Hydroxyapatite samples were then obtained following the same reprecipitation method, applying small variations in the experimental parameters to produce four distinct samples: a) for HAP_1, the acidic solution was added into the basic one with peristaltic pump at 0.7 mL min^{-1} at 40 °C and matured for 1 h; b) for HAP_2, the acidic solution was added into basic one with peristaltic pump at 0.3 mL min^{-1} at 40 °C and matured for 1 h; c) for HAP_3, the acidic solution was added at once into the basic one and stirred for 1 h at 25°C; for HAP_4, the acidic solution was added at once into the basic one and stirred for 5 min at 25°C. The obtained powders were separated by centrifugation, washed with distilled water, and dried overnight at 120 °C. In **Table** 2-1, a summary of all the conditions is reported.

Furthermore, to evaluate thermal stability of ashes-derived hydroxyapatite, the materials were stirred with MilliQ water (100 mg of sample per 100 mL of water) at 90°C for 8 hours. Then the suspension was filtered, and the powder was collected and dried overnight at 120 °C. The materials are labelled as *HAP_X_WT*, where X denotes the label of the sample.

Table 2-1 Parameters used for the extraction of hydroxyapatites from ashes of the energy-to-waste plant.

Samples	HAP_1	HAP_2	HAP_3	HAP_4
		Parameters[a,b]		
Dripping of acidic solution *mL min*^{1}	0.7	0.3	At once	At once
Temperature *°C*	40	40	25	25
Final pH	10.9	11.2	11.0	11.0
Maturation time *min*	60	60	60	5

a. Extraction process of Ca^{2+} and PO_4^{3-} from ashes through suspension with HCl 2 M for 1 h at 25°C.
b. Re-crystallization process of leachate solution into basic solution of NaOH 1 M ($V_{leachate}/V_{NaOH}$ = 1:2).

2.1.2. Preparation of biochar

Various biochars were produced starting from different raw materials through pyrolysis under N_2 in a temperature range between 600 °C and 900 °C. The sources of biochar used in this work belong to two different kinds of canes. Specifically maize stalk and sugarcane were used, resulting in a total of two distinct source material types.

Cane feedstocks underwent a pyrolysis procedure distinct from that applied to other biochar sources, particularly regarding the final treatment temperature, following insights from previous studies on lignocellulosic materials. [48] :

Pyrolysis of canes: to obtain an electrically conductive material, the canes were positioned in a quartz tube inside a horizontal furnace (Carbolite) and pyrolyzed at a controlled temperature. The pyrolysis procedure of the material was carried out according to the following protocol: two h at 25 °C, slow heating (5 °C·min^{1}) up to 900 ◦C, one h residence time at 900 °C and cooling down to 25 °C. During the treatment, N_2 flowed constantly at 1 NL·h^{-1}. The obtained materials were labelled as MS_900

(for maize stalk) and ECCO_900 (for sugarcane). For reference, a different temperature of pyrolysis was used for ECCO materials: 600°C for 1 h, resulting in ECCO_600 as labelled material.

2.1.3. Preparation of composite materials

Different composite materials were prepared by different methodologies and then applied for bioelectromethanogenesis or electroreduction of CO_2. These composite materials comprised carbon support, copper nanostructures and hydroxyapatite.

2.1.3.1. *Composite electrocatalysts for bioelectromethanogenesis*

For bioelectromethanogenesis, maize stalk-derived biochar (MS_900), commercial copper nanoparticles (Cu NPs, Sigma-Aldrich, CAS N° 744-05-08, ø = 25 nm) and synthetic hydroxyapatite were assembled to create a composite material with synergistic properties. The composite materials were prepared varying the weight content of each component; in particular, copper and hydroxyapatite content changed from 5 to 20 wt%. Furthermore, reference materials containing only copper or only hydroxyapatite were prepared. All resulting materials were labelled as xCu/yHAP-biochar, where *x* and *y* represent the weight percentages of copper nanoparticles and hydroxyapatite, respectively. The four biochar-based materials obtained included two ternary composites (5Cu/5HAP-biochar and 20Cu/10HAP-biochar) and two reference binary composites (10HAP-biochar and 20Cu-biochar).

The preparation followed a multi-step protocol for all biochar-based composites of different compositions, schematized in Scheme 2-2. Cu NPs and pulverized biochar (MS_900) were weighed to obtain 100 mg of the final composite, and both were dispersed in 40 mL of isopropyl alcohol (IPA). The pH of the suspensions was adjusted to 10 by adding a 0.1 M KOH aqueous solution. Both suspensions were sonicated for 30 minutes to achieve a fine dispersion. The Cu NPs suspension was then added in a single shot to the MS_900 suspension. The resulting mixture was stirred at room temperature for 24 h, then filtered on a 0.45 µm Nylon membrane and dried at 110 °C for 45 minutes. The final binary material (xCu-biochar) and HAP (properly weighed, for the ternary composites) were each dispersed in 90 mL of MilliQ water and sonicated for 45 minutes. Then, the

HAP suspension was added in one shot to the biochar suspension. The resulting mixture was stirred for 24 h at room temperature. Finally, the powder (xCu/yHAP-biochar) was vacuum filtered on a 0.45 µm Nylon membrane, washed with MilliQ water, and dried at 110 ◦C for three hours. The reference binary materials were prepared through the above-described procedure using only Cu NPs or only HAP, deposited on pulverized MS_900, to obtain 10HAP-MS900 and 20Cu-MS_900

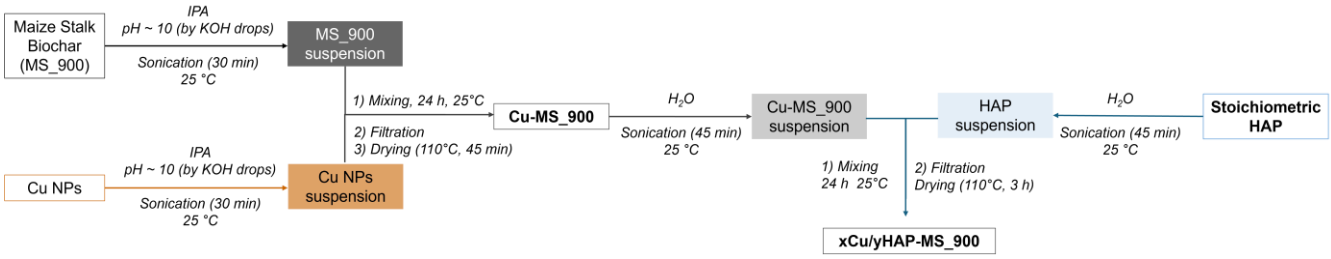

Scheme 2-2 Schematic representation of the multi-step protocol for the preparation of the ternary composite material for bioelectromethanogenesis.

2.1.3.2. *Composite electrocatalysts for CO_2 electroreduction*

For the electrochemical reduction of CO_2, a composite material was synthesized through one-pot synthesis of carbon nitride scaffold functionalized with synthetic hydroxyapatite and copper nanoaggregates.

One-pot synthesis of the composite material was carried out in the tubes of a Radleys Carousel (Radleys Accelerating Chemistry, France). In a typical synthesis, the tubes were charged with piperazinedicarbaldehyde (0.17 g), melamine (0.10 g), HAP powder (0.1 g), pre-obtained by synthesis, $Cu(NO_3)_2$ (0.17 g), and 2,5-diaminohydroquinone (0.18 g) as the ligand, together with DMSO (12 mL). The suspension was degassed under dry N_2 and refluxed at 180 °C for 72 h in an inert atmosphere. After cooling to room temperature, the precipitated product was isolated by filtration and washed with dry ethanol, acetone, tetrahydrofuran, and dichloromethane sequentially to remove the organic residues after the reaction. The formed composite, labelled as HAP_Cu@CIN_1, was dried overnight at 80°C. Finally, the ternary composite, labelled as HAP_Cu@CN, was obtained by calcination of the relative precursor HAP_Cu@CIN_1, under a N_2 atmosphere at 450 °C for 3 h.

For reference, a Cu-free binary sample (HAP@CIN-1), a HAP-free binary sample (Cu@CIN-1), and the bare CIN-1 were synthesized following the same procedure described above. The final samples: HAP@CN, Cu@CN, and CN were obtained after thermal annealing of CIN-precursors in the same conditions described above. Furthermore, by the same procedure described above, other three different samples with different amounts of HAP (5, 25, 50 wt.%) were prepared to obtain 5HAP_Cu@CIN-1, 25HAP_Cu@CIN-1 and 50HAP_Cu@CIN-1, respectively. The CIN-precursors after thermal annealing (N_2 atmosphere at 450 °C for 3 h) were converted in 5HAP_Cu@CN, 25HAP_Cu@CN and 50HAP_Cu@CN.

All the composites prepared for traditional CO_2ER and bioelectromethanogenesis are listed and classified in **Table** 2-2, in terms of carbon scaffold, components and relative weight percentages.

Table 2-2 Summary of composite materials used as catalyst for different CO_2ER techniques.

Composite	Carbon Scaffold	Other components	Preparation method	Utilization
5Cu/5HAP-MS_900	Pyrolyzed maize stalk[a]	Cu NPs (5 wt%) s-HAP (5 wt%)	Multi Step Protocol	Bioelectromethanogenesis
20Cu/10HAP-MS_900		Cu NPs (20 wt%) s-HAP (10 wt%)		
10HAP-MS_900		s-HAP (10 wt%)		
20Cu-MS_900		Cu NPs (20 wt%)		
HAP_Cu@CN	C=N framework[b]	Cu (10 wt%) s-HAP (10 wt%)	One Pot methodology	CO_2 electrochemical reduction
Cu@CN		Cu (10 wt%)		
HAP@CN		s-HAP (10 wt%)		
5HAP_Cu@CN		Cu (10 wt%) s-HAP (5 wt%)		
25HAP_Cu@CN		Cu (10 wt%) s-HAP (25 wt%)		
50HAP_Cu@CN		Cu (10 wt%) s-HAP (50 wt%)		

a. The pyrolysis occurred with slow heating (5 °C·min ^{1}) up to 900 ◦C for 1 h at 900 °C under N_2 (1 NL·h^{-1}) to obtain MS_900;

b. C=N framework obtained from COF synthesis obtained from condensation of melamine and piperazine dicarbaldehyde, followed by thermal annealing (450°C, 3 h, N_2 atmosphere).

2.2. Characterization techniques

All the synthesized materials were thoroughly characterized using a range of techniques, with particular emphasis on their composition, structure, morphology, and surface properties.

2.2.1. Compositional characterization

Quantification of elements (Ca, P, Mg, Na) in hydroxyapatite samples was performed using inductively coupled plasma optical emission spectroscopy (ICP-OES) with Agilent 5100 ICP-OES spectrometer from Agilent Technologies. Samples were prepared by dissolving 20 mg of sample powder in 100 mL of 2 wt% HNO_3 solution. A concentration/emission calibration curve was made in the concentration range 1–100 ppm using standard solutions of the analyzed elements (Ca, P, Mg, and Na), obtained by dilution of certified 1000 ppm standards (Sigma Aldrich).

The elemental composition of the composite samples (powder form) was determined with an M4 TORNADO energy-dispersive micro-X-ray fluorescence (XRF) spectrometer (Bruker). This instrument is equipped with two anodes: a rhodium X-ray tube (50 kV, 600 mA, 30 W) and a tungsten X-ray tube (50 kV, 700 mA, 35 W). For sample characterization, the rhodium X-ray tube with a polycapillary lens enabling excitation of an area of 200 µm was used. The silicon-drift-detector Si(Li) with a resolution of 145 eV at 100,000 cps (Mn Kα) with a Peltier cooling (−20 °C) was utilized. The measurements were carried out under vacuum. Quantitative analysis was done using fundamental parameter (FP) (standardless).

The compositions (CHNS) were determined using the Thermo Scientific FlashSmart automated analyzer. For CHNS determination, the samples were weighed in tin containers and introduced into the combustion reactor. The reactor was filled with copper oxide, followed by wire-reduced nickel, and maintained at 950°C, and operated with dynamic flash combustion of the sample. The N, C, H, and S were detected as N_2, CO_2, H_2O, and SO_2, respectively. The resulting gases were separated on a packed column heated at 65°C in an oven and detected by a TCD (thermal conductivity detector).

^{31}P solid-state NMR experiments were performed using a Bruker AVANCE III 500WB spectrometer equipped with a 4mm triple H/X/Y resonance MAS probe. The sample size was 200 mg. The resonance frequency of ^{31}P nucleus was 202.4 MHz. The HPDEC-MAS (High Power Decoupling - Magic Angle Spinning) technique was used for spectra acquisition with a 10 kHz spinning speed, accumulation of 64 scans, and 60 s repetition delay over a spectral width of 300 ppm. All spectra were registered at room temperature. The ^{31}P chemical shifts were referenced to an external standard 80 wt% H_3PO_4.

2.2.2. Structural and morphological characterization

N_2 adsorption/desorption isotherms were collected at liquid nitrogen temperature (-196 °C) using a 1990 version Sorptomatic instrument (Thermo Scientific) to evaluate the specific surface area and porosity. Before analysis, the dried sample (sieved between corresponding to 75-180 µm interval through certificate sieves, 80-200 mesh) was outgassed under vacuum conditions (10^{-2} torr) for 16 hours at 150 °C for apatite samples and 4 hours at 300°C for carbonaceous-based materials to remove any moisture and other species adsorbed on the surface and from the pores. Starting from Brunauer-Emmet-Teller (BET) equation (Eq. 2-1), applied in the adsorption branch at low-pressure region ($0.05 < p/p_0 < 0.3$), monolayer volume (V_{mon}) can be obtained:

$$\frac{{}^{p}/_{p_0}}{V_{ads}\left(1-{}^{p}/_{p_0}\right)} = \frac{1}{V_{mon}C} + \frac{C-1}{V_{mon}C}\left({}^{p}/_{p_0}\right) \qquad \text{Eq. 2-1}$$

where V_{ads} ($cm^3\ g^{-1}$ STP) is the amount of N_2 adsorbed at relative pressure p/p_0, and C is the BET constant related to the energy of monolayer adsorption. Once V_{mon} is known, the specific surface area (SSA in $m^2\ g^{-1}$) is calculated through Eq. 2-2

$$SSA = \frac{V_{mon} \cdot N_A \cdot \sigma_{N2}}{V_m \cdot m_{sample}} \qquad \text{Eq. 2-2}$$

where N_A is the Avogadro constant, m_{sample} (g) is the sample mass, and V_m and σ_{N2} are the molar volume and cross-sectional area of N_2, respectively.

Pore volume and pore size distribution were derived from the desorption branch ($0.3 < p/p_0 < 0.95$)

of the isotherms using the Barrett-Joyner-Halenda (BJH) model, which employs the modified Kelvin equation for cylindrical pores (Eq. 2-3):

$$\ln\left(^{p}/_{p_0}\right) = -\frac{2\gamma V_M}{RT\left(r_p - t_c\right)} \qquad \text{Eq. 2-3}$$

where r_p is the pore radius, t_c is the thickness of the adsorbed multilayer film formed before pore condensation, and γ and V_M are the surface tension and molar volume of liquid N_2, respectively. ADP (Advanced Data Processing) Software by Thermo Fisher and the MILES-200 program were used to process the experimental data for using the 3-parameter BET equation.

TEM-EDX analysis was performed using a FEI TECNAI F20 Field Emission Gun (FEG) transmission electron microscope. The instrument was equipped with a S-Twin lens that led to a resolution of 0.24 nm coupled with Energy dispersive X-Ray measurements (EDS) and selected area electron diffraction (SAED). The imaging system was composed of one TV rate 626 Gatan and one slow scan 794 Gatan CCD cameras (Gatan, Peasanton, CA, United States). The system operated with an accelerating voltage of 200 kV. Investigated samples were prepared by dispersing the powder (*ca.*4-5 mg) in 5 mL of isopropanol and ultrasonicated. The suspension (~ 5µl) was deposited on a carbon-coated Au grid (for copper-containing materials) or Cu grid (for copper-free materials) and dried under an infrared lamp for 5 minutes before proceeding with the analysis.

Routine powder X-ray diffraction patterns were recorded at room temperature (RT) using a Philips Powder (PW3020) X-ray diffractometer equipped with a PW 1830 generator, a monochromator in graphite, with Cu Kα (λ = 1.5418 Å) radiation. The X-ray tube operated at 40 kV × 40 mA. The diffraction patterns were collected in the 8°–60° 2θ range at 0.6° min^{-1} (in 2θ) with a step size of 0.05° (in 2θ). Match! Software from Crystal Impact GbR was used for phase identification from diffraction data. Cell parameter refinement was performed through the UnitCell software. For RSE S.p.A. facilities, XRPD analyses were carried out with Rigaku Miniflex 600 diffractometer equipped with a monochromator and a Cu Kα radiation (λ=0.15406 nm). A step scan of 0.02 θ. and a scan rate of 1 θ·min^{-1} were used.

Scanning Electron Microscope (SEM) and SEM with Secondary Electrons (SEM-SE) analyses were performed at RSE S.p.A. facilities with a Zeiss Gemini electron microscope.

Raman spectra were recorded on a XploRA Raman confocal microscope from Horiba Jobin Yvon. A 532 nm diode laser was used to excite the samples. The scattered light was guided through a 150 µm pinhole, dispersed and collected using a Peltier-cooled CCD. The laser power was reduced using density filters to avoid sample alteration.

Thermogravimetric analyses (TGA) were performed on a TA Instruments' HI-Res modulated TGA 2950 thermogravimetric analyzer. Approximately 10 mg of each sample was weighed in an aluminium pan and loaded inside the TGA chamber of the instrument. The analysis, performed under 10 mL min^{-1} of N_2, consisted in a heating ramp of 5 °C min^{-1}, followed by an isothermal step of 2 hours at 400 °C. The software used for data acquisition and treatment was TA Instrument's Universal V3.9A

2.2.3. Surface characterization

The X-ray photoelectron spectroscopy (XPS) was carried out using a Kratos Axis Ultra DLD spectrometer (Kratos Analytical), equipped with a monochromatic Al Kα X-ray source (1486.6 eV) operating at 225 W (15 kV, 15 mA). The instrument base pressure was 5×10^{-10} torr and a charge neutralizing system was used for all acquisitions. Analysis was performed at a pass energy of 40 eV and a step size of 0.1 eV. XPS is based on the photoelectric effect, where electrons are emitted from the surface when irradiated with X-rays. By knowing the energy of the X-ray photons (hν) and measuring the kinetic energy (E_{kin}) of the emitted electrons, the binding energy (EB) of each electron can be calculated using Eq. 2-4:

$$BE = h\nu - E_{kin} \qquad \text{Eq. 2-4}$$

Because each element has characteristic binding energies, XPS can be used to identify the elemental composition of a material's surface. Moreover, it offers insights into the chemical state of the elements since slight shifts in binding energy reveal changes in oxidation states or differences

in chemical environments. The adventitious carbon (C1s peak at 284.6 eV) was excluded from the quantitative analysis to ensure precise determination of surface species. XPS spectra are analysed by deconvoluting peaks corresponding to different elements and chemical states, offering insight into surface chemistry and oxidation state. For quantitative analyses, atomic percentages of each element present on the surface are calculated from the area of each peak.

Surface charge of samples was studied through the determination of the Point of Zero Charge (PZC), which is the pH at which their surface has a net charge of zero. PZC was determined through pH-drift method using the salt addition technique: approximately 0.05 g of sample powder was put in contact with a series of electrolyte solutions with a constant ionic strength (KCl solution 0.5 M) but different pH values (5-10), by adjusting drop by drop with HCl 0.04 M (for acidic pH) or NaOH 0.09 M (for basic pH). The initial pH of each suspension was measured, and all the suspensions were kept in a thermostated water bath at 25 °C under magnetic stirring for 20 hours. The final pH values were then measured, and the change in pH (ΔpH) was calculated and plotted against the initial pH. The PZC was identified as the point where ΔpH is zero, i.e., the intercept with the x-axis.

Quantification of surface acid and basic sites of samples was performed by liquid-solid phase titration, using 2-phenylethylamine (PEA) and benzoic acid (BA) as basic and acid probes, respectively. Titrations were carried out in cyclohexane for *fresh* samples (determination of intrinsic acidity and basicity, I.A. and I.B.), in cyclohexane for samples treated in *water,* and in water solution (determination of effective acidity and basicity, E.A. and E.B., respectively). A flow sheet and a scheme of the modified HPLC line employed for the titrations are reported in **Figure** 2-1.

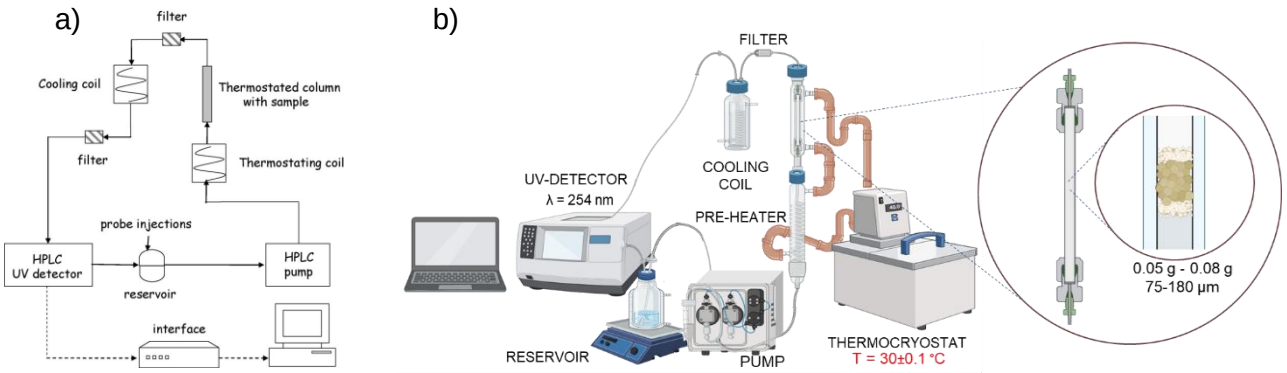

Figure 2-1. Scheme (a) and images (b) of the modified HPLC line for recirculation acid/base solid liquid titration.

Dried sample (ca. 80 mg for acidity measurements and ca. 40 mg for basicity analyses, (sieved between corresponding to 75-180 µm particles interval through certificate sieves, 80-200 mesh) was placed in a sample holder (stainless steel tube, Ø = 2 mm, h = 12 cm) between two sand pillows. The sample was pretreated by thermal treatment (350°C in 8 mL min^{-1} air flux for 4 h) and successively vacuum-wetted with the appropriate solvent (water or cyclohexane). The sample holder was then mounted on a recirculation modified chromatographic line (HPLC), equipped with a Waters 515 pump and a monochromatic UV detector (Waters, model 2487, working at fixed λ = 254 nm). During the analyses, the sample was thermostated at 30.0 ± 0.1°C by a thermocryostat (MGW LAUDA, K2R). By means of successive injections of known amounts of PEA (50 µL, ca. 0.10 M in both solvents) or BA (50 µL, ca. 0.05 M in both solvents) solutions, A characteristic 'step chromatogram' was obtained (**Figure** 2-2), where each step corresponds to the attainment of adsorption equilibrium. The detected signal rose from the difference between the amount of probe injected and the amount adsorbed by the sample. The non-adsorbed fraction represents the equilibrium probe concentration (C_e) and appears as a plateau in the chromatogram. This plateau resulted from the HPLC system operating in recirculation mode, ensuring that the probe concentration at equilibrium, and consequently the signal, remains constant. The height of the signal is directly related to the non-adsorbed amount of probe: at the beginning of the analysis, the height

of the signal is very low because all the injected probe is adsorbed on the sample. At each injection, the residual probe increased as the sample is gradually reaching saturation, which can be considered achieved when the heights of the step arethe same for 2-3 successive injections, meaning that all the residual probe is directly proportional to the injected ones and no adsorption is detected.

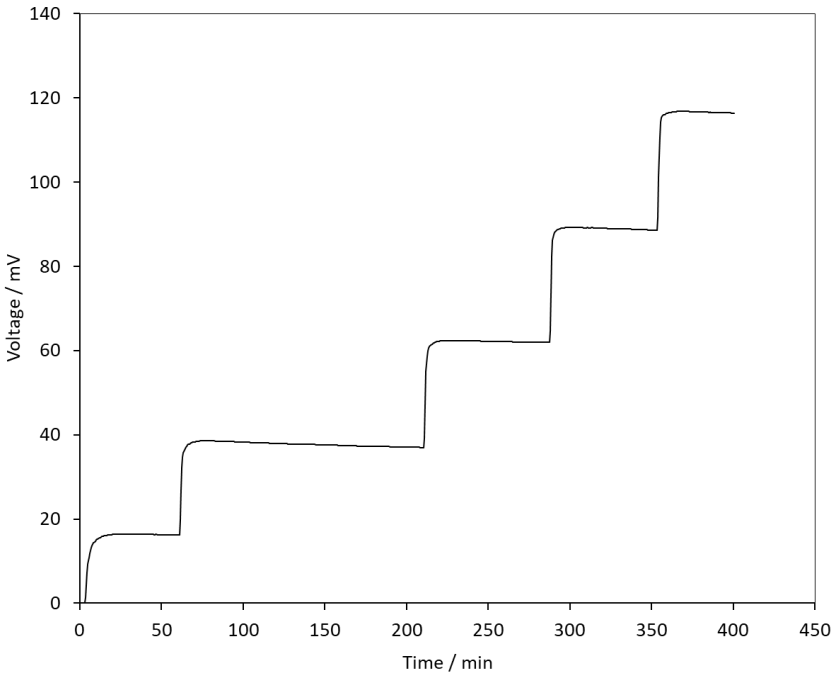

Figure 2-2 Example of step-chromatogram obtained from a solid-liquid titration.

After the collection of the first adsorption isotherm (I run), pure solvent was flowed (0.3 mL min^{-1}) through the saturated sample for ca. 16 h, thus permitting desorption of the probe molecules adsorbed on weakly interacting sites. Then, a second PEA or BA titration was performed on the same sample (II run), to discriminate strong and weak adsorption sites. Further details on the data analysis are provided in the Par. S.1 of the Appendix.

The strength of acid/basic adsorption sites was quantified by adsorption microcalorimetry of NH_3 and SO_2 (Air Liquide, purity >99.9%) probe molecules, respectively. In adsorption microcalorimetry, the sample is maintained at a constant temperature while a known amount of probe molecule adsorbs

onto its surface; the resulting heat is monitored by a heat-flow detector that produces a signal proportional to the heat evolved per unit time, recording in the meanwhile the pressure evolution. The heats of adsorption were measured in a heat-flow microcalorimeter of the Tian-Calvet type (C80 from Setaram) linked to a handmade glassy volumetric line equipped with a Barocel capacitance manometer (Datametrics) for pressure measurements.

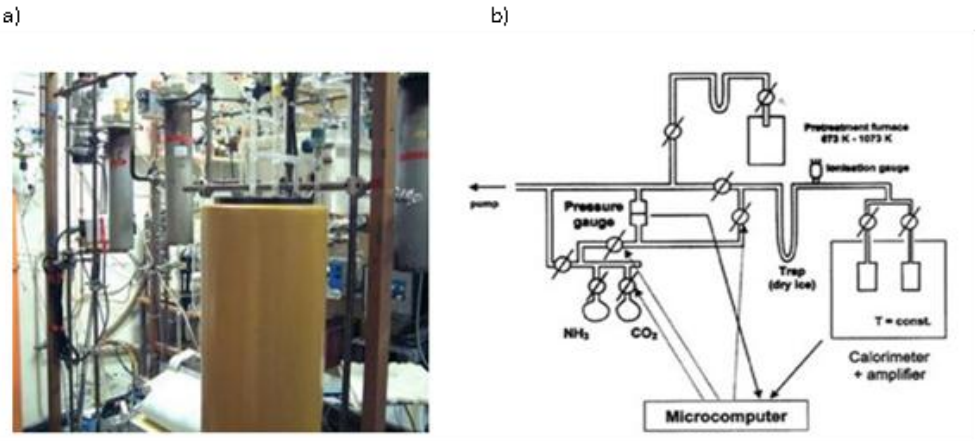

Figure 2-3 C80 Tian Calvet microcalorimeter from Setaram a), scheme of microcalorimetric volumetric line b).

The Tian-Calvet type microcalorimeter usually employs two identical cells, one containing the sample under investigation and the other serving as a reference element to compensate for all the thermal effects due to the equipment. The C80 microcalorimeter (**Figure** 2-3-a) allows for measuring the evolved heats, equal to the adsorption/desorption enthalpy of the process (since it is isobaric), at constant temperature in the 25 – 300 °C range, through thermocouples in the cell itself. The enthalpy of adsorption/desorption corresponds to a thermogram peak, which area is proportional to the evolved heat (Par. S.1. 2). The volumetric apparatus equipped with a Barocel pressure trasducer (**Figure** 2-3-b) measures the decrease of gas pressure from a reservoir in which the gas/vapor is stored towards the line and the calorimetric cell in which it is expanded.

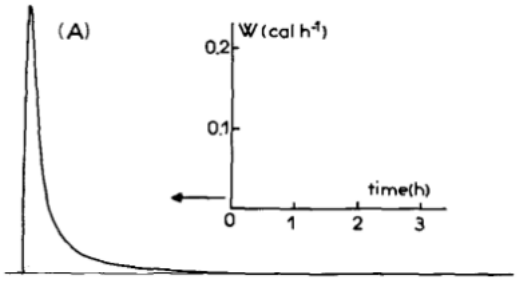

Figure 2-4 Example of a thermogram obtained from the injection of a dose of probe on the sample put in the calorimetric cell. The peak area ($\int \boldsymbol{W}\, \boldsymbol{dt}$) corresponds the evolved heat (μcal). The insights show the XY axis and relative units of measures.

In a typical experiment, about 0.100 g of sample was first pretreated directly in the quartz calorimetric cell overnight at 300 °C under vacuum ($7.5 \cdot 10^{-8}$ torr). Then, the cell was removed from the pretreatment oven and cooled down, placed inside the calorimeter at 80 °C, and connected to the volumetric line. The whole setup was then outgassed until a pressure of $7.5 \cdot 10^{-6}$ torr was reached. Upon reaching both the required level of vacuum and the thermal equilibrium of the system, small and known doses of probe molecule were introduced into the cell containing the sample, giving a thermogram signal as in **Figure** 2-4, until a final equilibrium pressure of about 0.5 torr was achieved. The volume of each dose was minimized to detect any change in adsorption heats evolved with increasing coverage of surface-active sites, thus studying the heterogeneity of the sample surface. The sample was then outgassed for 30 min at the same temperature, and a second adsorption run was performed at 80 °C until an equilibrium pressure of about 0.2 torr was reached.

2.2.4. Electrochemical characterization

For the materials employed in the CO_2 remediation reaction, in addition to the physicochemical characterization, electrochemical analysis was also important. Cyclic voltammetry (CV) and linear sweep voltammetry (LSV) were performed to evaluate key information on charge transfer properties, the density of electroactive sites, and the onset potential of the reaction.

The electrocatalytic characterization was performed using a BioLogic SP-300 electrochemical test station with a conventional three-electrode configuration consisting of an inked carbon paper electrode coated with composite material, Ag/AgCl, (in KCl saturated solution or 3 M KCl), and Pt coil as working, reference, and counter electrodes, respectively. Before starting the experiments, an aqueous electrolyte solution (0.1 M $KHCO_3$) was deaired by bubbling CO_2 or N_2 for at least 30 min.

Cyclic voltammetry curves were recorded in a non-Faradic region to evaluate the extent of double-layer capacitance (C_{dl}) and electrochemical surface area (ECSA). CV was performed in the range from 0.58 V to 0.68 V (vs RHE) with different scan rates (from 10 to 100 mV s^{-1}). By the slope of the scan rate *vs* the capacitive current (i_c) curve, the C_{dl} was obtained, and ECSA was calculated from the ratio C_{dl}/Cs, with C_s is the specific capacitance of the material. As carbon matrix is the main component of the composites, a plausible value of 7.5 µF cm^{-2} as C_s was selected, based on studies on other carbon-based materials.

Linear sweep voltammetry (LSV) measurements were carried out to evaluate the electrocatalytic performance of the materials, particularly in terms of onset potential and current density associated with the target reaction. LSV polarization curves were recorded at a scan rate of 20 mV s^{-1} after bubbling of N_2 or CO_2 for 30 minutes.

2.3. Bioelectromethanogenesis and CO_2ER tests on composite materials

2.3.1. Bioelectromethanogenesis test

The composite materials (**xCu/yHAP-biochar**, described in section 2.1.3.1) and the reference materials (10HAP-biochar and 20Cu-biochar) were tested in a bioelectromethanogenesis test for the conversion of CO_2 into CH_4, through the combination of microbial activity and electrochemical reduction. Firstly, the composites were deposited onto the electrode, and secondly, the microbial electrolysis was performed.

For the deposition, a dip coating procedure was carried out. It consisted of immersing the previously pyrolyzed biochar (MS_900, before grinding) in an aqueous suspension (100 mL of MilliQ water for 100 mg of powder) of the four composites (10HAP-biochar, 20Cu-biochar, 5Cu/5HAP-biochar, and 20Cu/10HAP-biochar) previously obtained. Suspensions were first sonicated for ten minutes to achieve good mixing, and the biochar was immersed in the suspension for ten minutes. The electrode thus obtained was dried at 110 °C for three hours.

For the CO_2 reduction test, two apparatus of six double-chamber bioelectrochemical systems (BESs) were operated in parallel. A schematic of the electrochemical cell is reported in **Figure** 2-5. Each cell was equipped with Ti-mesh, dip-coated MS_900, and 3 M Ag/AgCl as anode, cathode, and reference electrode, respectively, that were connected to a current generator (AMEL S.r.L.). Two difference electrolytic solution were used for anodic and cathodic chamber, divided by a proton exchange membrane (PEM NAFION 417): the anolyte was a 0.2 M solution of Na_2SO_4, while the catholyte solution consisted of the inoculum, containing *Archaea* and *Bacteria* type of microorganisms retrieved from a biogas plant, supplied with 2.54 g L^{-1} KH_2PO_4, 11.7 g L^{-1} $Na_2HPO_4 \cdot 12H_2O$, 0.53 g L^{-1} NH_4Cl, 0.1 g L^{-1} Na_2SO_4, 5.0 g L^{-1} $NaHCO_3$, and vitamins. The BESs were kept at 45±1 °C with a thermostatic bath, and CO_2 was fluxed for 40 min at a flux of 0.5 NL h^{-1}.

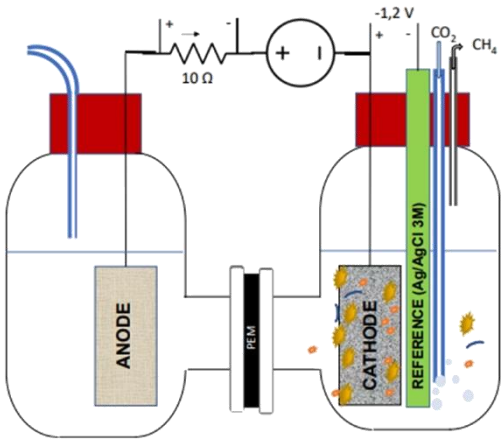

Figure 2-5 Schematic representation of BES double chamber electrolyser.

A polarization between the anode and cathode was imposed to achieve − 1.2 V between the cathode and reference (approximately − 1 V vs. SHE). The total duration of the experiments was 200 h (8 days) and was replicated twice. For each material, an abiotic (without microorganisms) condition was also tested. After the test, the gaseous products (CH_4, H_2, and CO_2) were analysed using a gas chromatograph (Agilent 3000A micro-GC) with the software “SOPRANE”. The sample for the GC was taken from the headspace of the cathode chamber with gas bags of 5 L connected to the gas outlet. The Volatile Fatty Acids (VFAs) present in the initial inoculum solution and produced at the end of the test were analysed by Ionic Chromatography (IC, Dionex 300), equipped with the S9-SC column and chemical suppressor AMMSIC. The sample intended for the analysis through IC (10 mL) was withdrawn and stored at 2 °C before the measurement. Finally, microbial communities grown on the surface of the electrodes were characterized through scanning electron microscopy equipped with X-Ray detector (SEM-EDS), coupled with sequencing of RNA genes of Bacteria and Archaea, using MiSeq Illumina sequencing, to obtain the taxonomic characterization.

2.3.2. CO_2 electrochemical reduction

For the electrochemical reduction of carbon dioxide, carbon nitride-based materials (presented in section 2.1.3.2), obtained from a one-pot synthesis, were employed (**CN-based** materials: Cu@CN and HAP_Cu@CN as binary and ternary principal materials).

Firstly, carbon paper was prepared as support: the catalyst (ca. 10 mg) was uniformly dispersed in 300 µL of ethanol/water (1:1) and 50 µL of 5 wt% Nafion, and subsequently ultrasonicated for 0.5 h to form a homogeneous catalyst slurry (*catalyst ink*). Defined amount of ink (150µL) was drop-casted onto the Toray carbon paper (1×1 cm^2) and allowed to dry at room temperature (RT) for 24 h. The electrocatalytic tests were performed using a BioLogic SP-300 electrochemical test station with a conventional three-electrode configuration consisting of the inked carbon paper electrode coated with composite material, Ag/AgCl (in a KCl saturated solution), and Pt coil as working, reference, and counter electrodes, respectively. During the chronoamperometric tests (CA), CO_2 was continuously bubbled inside the electrolytic solution of 0.1 M $KHCO_3$. Each potential, in the range from -1.3 V to -1.8 V (*vs* Ag/AgCl), corresponding to -0.5 V to -1-0 V (*vs* RHE), was maintained for 1 h continuous flow of CO_2 at 10 mL min^{-1} . After the test, the gaseous products were analyzed through gas chromatography (GC, Agilent 8860, combined with a flame ionization detector and a thermal conductivity detector) through external standard calibrations, while a Bruker 300 MHz ^1H liquid NMR spectrometer was utilized for quantification of species in the electrolyte samples in the presence of DMSO as an internal standard.

To evaluate the selectivity of the catalysts, faradic efficiency (FE) was calculated through Eq. 2-5:

$$\mathrm{FE}\ (\%) = \frac{(\text{mole percentage} \times \mathrm{n} \times 96500\ )}{\mathrm{Q}} \qquad \text{Eq. 2-5}$$

where mole percentages were calculated from GC or ^1H NMR analysis (for gaseous and liquid products, respectively), n (mol) is the number of electrons (transferred for each product), 96500 (C mol^{-1}) is the Faradic constant, and Q (C) is total charge passed during the CA experiment. Q is calculated by Eq. 2-6:

$$\mathrm{Charge}\ (\mathrm{Q}) = \mathrm{I} * \mathrm{t} = \mathrm{j} * \mathrm{A_{geo}} * \mathrm{t} \qquad \text{Eq. 2-6}$$

Where I (A) is the current intensity, j ($A \cdot cm^{-2}$) is the current density at each potential from the system, A_{geo} (cm^2) is the geometric area of the carbon paper electrode, and t (s) is the time of the chronoamperometric test.

2.4. Catalytic isomerization of glucose into fructose through sustainable hydroxyapatites

The catalytic reaction of isomerization of glucose was performed in an aqueous phase in an autoclave batch reactor. The catalyst powder (ca. 0.2 g), previously dried in an oven at 120°C for 12 hours, was introduced into a stainless-steel autoclave along with the aqueous glucose solution (50 mL of 2 wt% solution), keeping the catalyst/substrate ratio of 1/5. The autoclave was then sealed and heated to the target temperature (T = 120°C). The initial reaction time (t_0) was defined when the temperature of 120 °C was attained (after ca. 15 minutes of heating). Independent reaction tests were carried out for each different time points (10, 30, 60, 90, and 120 minutes). At the end of each run, the autoclave was rapidly cooled in an ice bath for thermal quenching, and the reaction mixture was filtered: the solid was dried, and the aqueous solution was collected for liquid chromatography analysis. The reaction mixtures were analyzed in a high-performance liquid chromatographic (HPLC), equipped with a Sugar-Pack I (300 × 6.5 mm, 10 µm particle size, Waters, Sesto San Giovanni, Italy) column operating at 90 °C and eluted with an aqueous solution of Ca–EDTA (10^{-4} mol L^{-1}), and refractive index (Waters 410) as detector was used. The concentrations of the chemical compounds in solution were quantified through external calibration using standard solutions of glucose and fructose (**Figure** S-6-20). From the quantification of the analytes conversion (x %), selectivity towards fructose ($Sel_{fructose}$ %) and carbon balance were calculated by the following equations (Eq. 2-7, Eq. 2-8, Eq. 2-9, respectively):

$$x\,\% = \frac{n_{0,Glu} - n_{t,Glu}}{n_{0,Glu}} * 100 \qquad \text{Eq. 2-7}$$

$$\mathrm{Sel_{fructose}}\% = \frac{n_{t,Fru}}{n_{0,Glu} - n_{t,Glu}} * 100 \qquad \text{Eq. 2-8}$$

$$\text{Carbon balance} = \frac{n_{t,Glu} + n_{t,Fru}}{n_{0,Glu}} \qquad \text{Eq. 2-9}$$

Where $n_{0,\,Glu}$ is the initial moles of glucose, $n_{t,Glu}$ is the moles of glucose at defined time t (10, 30, 60, 90 or 120 minutes) and $n_{t,Fru}$ is the moles of fructose produced at defined time t. The obtained

conversion values are then normalized based on the equilibrium conversion of the reaction at 120 °C, calculated using the proper equilibrium constant calculated and extrapolated from the free Gibbs Energy at 120 °C, according to the procedure of Tewari et Goldberg[49] (further details are reported in Appendix 6.3).

Results

3. Sustainable electrochemical processes: reduction of CO_2

3.1. Bioelectromethanogenesis

The growing demand for renewable energy storage solutions has led to the development of Power-to-Gas (P2G) technologies, which represent a sustainable strategy to convert energy to fuels. Particularly, P2G technologies exploit the surplus electrical energy from renewable sources, avoiding energetic loss. Among P2G technologies, Power-to-Methane (P2M) processes represent a highly sustainable system. P2M systems are particularly attractive as they can convert CO_2 to methane, which can be directly distributed and used in the existing infrastructure. The P2M systems exploit the CO_2 hydrogenation reaction using H_2 produced in an electrolyzer powered by electric energy from renewable sources. Many challenges are faced by P2G systems, which could theoretically be highly sustainable. One of the primary problems is the energy efficiency, since both CO_2 hydrogenation and water electrolysis are highly energy-intensive processes. Secondly, because of the sluggish kinetics of electrochemical reduction, P2M systems productivity and selectivity are still very poor when compared to traditional chemical methanation. Furthermore, reactor design and scale-up are still challenging from an engineering standpoint as ideal performance needs exact control over solid-gas-liquid mass transfer. However, energy demands, and environmental issues push for new systems that can overcome the above-mentioned problems.

In this chapter, a P2M technology is discussed: bioelectromethanogenesis.

Bioelectromethanogenesis is defined as a bioelectrochemical system (BES) that combines electrochemical and microbial processes[50], exploiting the metabolic activity of micro-organisms as

biocatalysts for redox reactions.[51] In this technique, the cathode serves as an electron source that drives electrochemical reduction, but it also serves as support for methanogenic microorganisms (Archaea), where microbial adhesion[52], electron transfer, and metabolic activity occur.[53] Therefore, the electrode material must simultaneously ensure efficient charge transport, chemical stability, and a suitable surface environment to support microbial colonization and activity. The following chapter focuses on the study of a novel composite material based on biochar, hydroxyapatite, and copper nanoparticles.[54,55] This composite was investigated to assess its physicochemical, electrochemical properties, and its catalytic capabilities. Furthermore, the specific role of HAP as a biologically favorable support for methanogens was deeply studied, enabling effective integration between the electrochemical and microbial processes.

3.1.1. Preparation and characterization of composites

The choice of materials was directed to combine good electrochemical properties and biological compatibility with microorganisms. For this reason, a carbon-based scaffold was selected as a conductive scaffold, copper nanoparticles as the active phase for electrochemical conversion, and further modification with the inorganic components to introduce bioactive functionalities. The composite was thought to integrate electrochemical and biological activities to enhance the production of C-reduced products. To explore suitable cathodic materials, five different materials were prepared, characterized, and tested in BES cells. The materials comprised the bare biochar (pyrolized maize stalk, MS900), two binary composites (10HAP-MS900 and 20Cu-MS900), and two ternary composites 5Cu/5HAP-MS900 and 20Cu/10HAP-MS900, following the multistep procedure described in 2.1.3.1. The multistep protocol involved, as the first step, the pyrolysis of biochar under an inert atmosphere; the second step comprised the functionalization of biochar with copper nanoparticles, hydroxyapatite, or both. It is important to clarify the rationale behind the selected composite composition, particularly the choice of the relative amounts of each component. The composition has been optimized based on previous works, where different compositions were explored to finally detect the optimal one for both enhanced methane production and hydrogen limitation. [20,56] Low amount of copper (< 10 wt%) limits the overall activity of the systems, on the other

hand increasing HAP as ternary components can hinder the conductivity of the system, limiting the BES to become a biological reactor without enhancing the methane production. To fully highlight, these main differences, alongside the 20Cu/10HAP-MS900 with 20 wt% of Cu nanoparticles and 10 wt% (NPs) of HAP, 5Cu/5HAP-MS900 was also prepared with lower amount of Cu NPs and HAP (5 wt% for each component).

Before analyzing the composites in their physico-chemical characterization, biochar obtained from pyrolysis was characterized to assess the principal morphological features after the thermal treatment. After pyrolysis, MS900 preserved its mechanical integrity while showing an enhanced surface porosity. this morphological change is accompanied by a weight loss of 75%, consistent with the thermal decomposition of the lignocellulosic structure. During pyrolysis, hemicellulose undergoes a series of different reactions such as depolymerization, fragmentation, and cross-linking that result in the formation of a porous carbon scaffold. [57,58] Furthermore, the development of porosity is associated with the removal of volatile organic compounds and water (even if maize stalk waste is not rich in moisture content). As from SEM analyses (**Figure** S-6-4-a), the obtained biochar is predominantly macroporous with average dimension for 50 ± 10 µm.

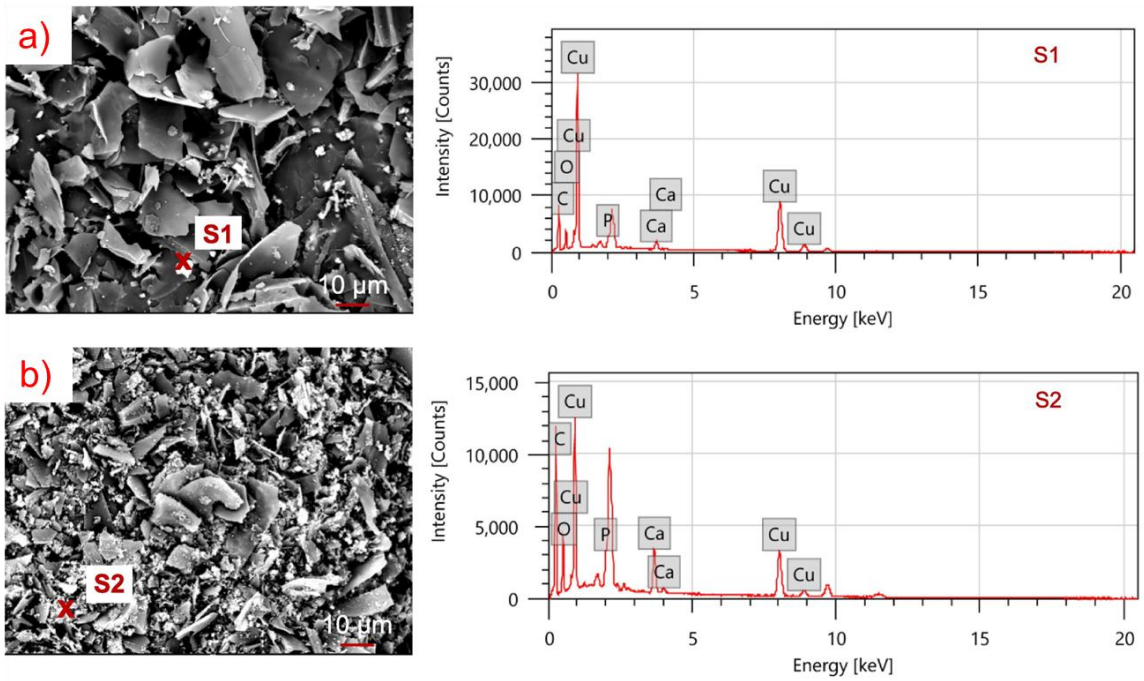

Figure 3-1 SEM-SE micrographs with respective EDS spectra (right) of a) 5Cu/5HAP-MS900; b) 20Cu/10HAP-MS900. Each spectrum was recorded in a single point of the sample marked by a red x.

Functionalized biochar powder samples (20Cu-MS900, 10HAP-MS900, 20Cu/10HAP-MS900, 5Cu/5HAP-MS900) were observed by SEM analyses (**Figure** 3-1). From a preliminary observation, micrometric structures can be clearly distinguished across the biochar surface, appearing as flake agglomeration of different shapes and sizes. These morphologies are attributed to HAP structures dispersed onto the carbon support. To confirm, EDX analyses, displayed in **Figure** 3-1 performed on selected regions revealed the presence of C, Cu, Ca, O and P, which are elements expected in the composite (with Cu and HAP). As for the distribution, for 20Cu/10HAP-MS900, a homogeneous distribution of the elements has been observed, while for 5Cu/5HAP-MS900 the elemental maps (**Figure** S-6-4-b,c) showed only partial spatial overlap among the Cu, Ca, P, and O signals, indicating a less uniform dispersion of the active components within the carbon matrix.[59]

Further structural characterization was performed by X-ray powder diffraction (XRPD) to evaluate the phase composition of the prepared composites. The diffraction patterns of 5Cu/5HAP-MS900 and 20Cu/10HAP-MS900 are displayed in **Figure** 3-2.

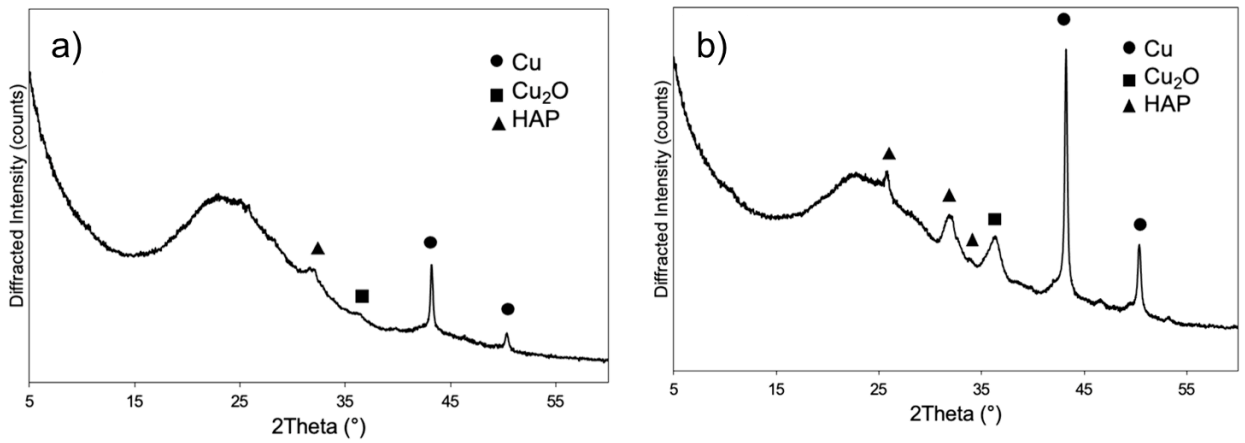

Figure 3-2 XRD patterns of a) 5Cu/5HAP-MS900 and b) 20Cu/10HAP--MS900 samples. The main reflection peaks of recognized phases are indicated with different shapes: metallic copper Cu (●), Cu_2O (■) and HAP (▲).

Both patterns are dominated by a broad background in the 2θ range of 20°-30°, which corresponds to the (002) reflection peak of aromatic carbon layers, and it indicates the presence of small graphitic domains within the biochar. In the two patterns, distinct reflection peaks attributed to metallic copper

(JCPDS 01-070-3038) were detected at 2θ of 43.2° and 50.0°, related to the (111) and (200) planes, respectively, confirming the presence of copper nanoparticles in Cu^0 oxidation state. A weaker reflection at 2θ = 36.5° was assigned to the (111) plane of Cu_2O (JCPDS 00-065-3288), suggesting partial oxidation of copper during preparation of the material due to the exposure to air. The incorporation of crystalline HAP (JCPDS 00-064-0738) was supported by the presence of weak but characteristic reflection peaks at 2θ of 26° and 32° corresponding to (002) and (211) planes. Particularly, the HAP reflection peaks are less intense in the 5Cu/5HAP-MS900 composite due to the low amount of inorganic phase incorporated. For both materials, the peaks are less visible because of the broad amorphous background generated by the carbonaceous phase, which partially masks the crystalline HAP signals. Overall, the relative intensities of the graphitic domain of carbon scaffold, copper NPs, and hydroxyapatite peaks across the different patterns corroborate the different proportions of these components in each composite, confirming the compositional tuning of the materials.

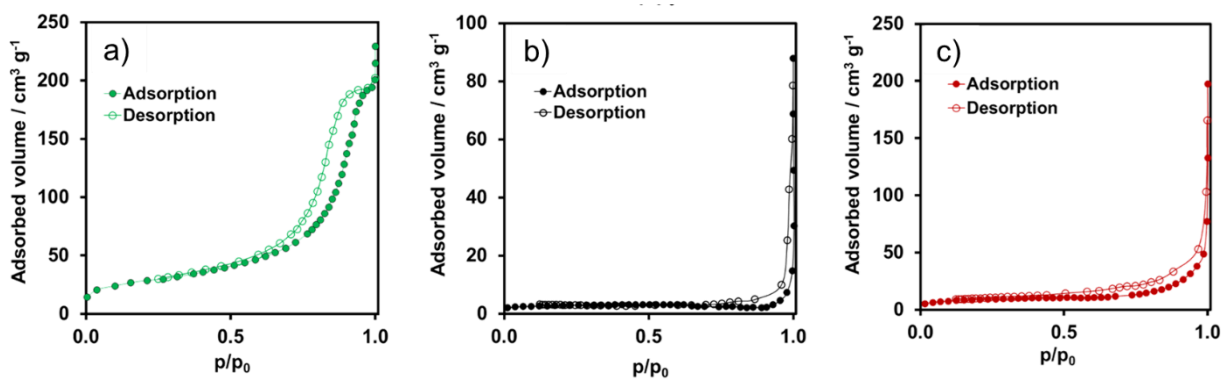

Figure 3-3 N_2 adsorption/desorption isotherms collected on a) HAP; b) biochar; c) 10HAP-20Cu/C composite (as representative of composite biocathode).

As bioelectromethanogenesis is an interfacial process in which surface area and porosity can influence the catalytic properties, the morphological features revealed by N_2 adsorption-desorption isotherms are particularly relevant (**Figure** 3-3). In **Figure** 3-3-c, the adsorption-desorption isotherms of bare HAP, biochar, and 10HAP-20Cu/C composite are reported to evaluate the main differences in pore structure among the studied materials. According to the IUPAC classification of physisorption isotherms, the HAP sample exhibits a Type IV isotherm with a pronounced hysteresis loop, indicative

of well-developed mesoporosity. The specific surface area (SSA) was 96 m^2 g^{-1} with a pore size distribution in the mesoporous range centered around 4-12 nm.[60] In contrast, adsorption-desorption isotherm of biochar shows a profile closer to Type II, characteristic of non-porous or macroporous material. The absence of mesoporosity is associated with low surface area, as reported in **Table** 3-1 (SSA was 9 m^2 g^{-1}), approximately one order of magnitude lower than that of HAP. Interestingly, the incorporation of 10wt% of HAP (and 20 wt% copper nanoparticles) for the 20Cu/10HAP-MS900 composite, onto the biochar matrix resulted in a significant enhancement of the surface area, reaching 31 m^2 g^{-1}. This increase demonstrates the crucial role of hydroxyapatite in improving the surface and textural properties of biochar-based composites, which can limit the overall performance of the catalyst. The presence of mesopores and macropores is particularly favourable for the bioelectromethanogenesis cathode, as they facilitate gas diffusion (CO_2 and H_2) and ensure good wettability by water, while also providing an accessible environment for microbial colonization.

Table 3-1 Morphological and electrochemical surface area of bare biochar, binary and ternary composites.

SSA	SSA[a] m^2 g^{-1}	C_{dl}[b] µF cm^{-2}	ECSA[c] cm^2
MS900	**9.0**±0.1	**$5.4 \cdot 10^{-1}$** ± $5.2 \cdot 10^{-2}$	**$7.2 \cdot 10^{-2}$** ± $6.5.10^{-3}$
10HAP-MS900	n.d.	**$6.1 \cdot 10^{-2}$** ± $5.5 \cdot 10^{-3}$	**$8.2 \cdot 10^{-3}$** ± $7.4 \cdot 10^{-4}$
20Cu-MS900	n.d.	**$6.6 \cdot 10^{-3}$** ± $9.9.10^{-4}$	**$8.8 \cdot 10^{-4}$** ± $1.2 \cdot 10^{-4}$
5Cu/5HAP-MS900	n.d.	**$1.2 \cdot 10^{-2}$** ± $1.0.10^{-3}$	**$1.6 \cdot 10^{-3}$** ± $1.3 \cdot 10^{-4}$
20Cu/10HAP-MS900	**31.1**±0.2	**$6.7 \cdot 10^{-3}$** ± $1.7 \cdot 10^{-3}$	**$8.9 \cdot 10^{-4}$** ± $2.2 \cdot 10^{-4}$

a. Evaluated by BET 2-parameter. The standard deviation was obtained from error propagation on Eq. 2-2. starting from the experimental value of V_m (and its relative standard deviation).
b. Evaluate from CV analyses. Each CV was reproduced three times.
c. ECSA was evaluated from linearization of C_{dl} and scan rate. Deviation standard was calculated from error propagation.

3.1.2. Electrochemical characterization

The evaluation of surface properties also involves electrochemical properties. One of the most important surface features is the electrochemically active surface area (ECSA). The ECSA of the composite electrodes was determined within a potential window of ± 25 mV *vs*. Open Circuit Potential (OCP), under the assumption that no faradaic processes occurred in this range. ECSA evaluation is correlated to the capacitive behavior of the electrode-electrolyte interface, and it is calculated as the ratio C_{dl}/C_s, where C_s is the specific capacitance of the material (7.5 $\mu F \cdot cm^{-2}$, typical of carbon material).[61] The same C_s value was applied to all electrodes, given the low content of dopants (<20 wt%). ECSA results (**Figure** S-6-5) are reported in **Table** 3-1 and indicate significant variations depending on the electrode composition. The pristine biochar exhibited the highest ECSA value ($7.2 \cdot 10^{-2}$ cm^2), while Cu-functionalized materials showed ECSA with two orders of magnitude lower ($8.8 \cdot 10^{-4}$ cm^2). Higher copper loading drastically reduced the active area. This change could be partially explained by i) the absence of a network of Cu nanoparticles on the surface that could better distribute the charge, demonstrating segregation of copper phase on the biochar. On the other hand, the addition of only HAP caused a moderate decrease in ECSA value due to the insulating properties of HAP. For the ternary composites, the effect of hydroxyapatite and Cu NPs on the electrochemically active surface appears less straightforward ($8.9 \cdot 10^{-4}$ cm^2), suggesting a possible synergistic interaction between the metallic and inorganic phases. Higher ECSA is a favourable factor for the bioelectromethanogenesis test because large ECSA value increases the available interfacial region where electrochemical and biochemical interactions can occur.

3.1.3. Bioelectromethanogenesis test

Bioelectromethanogenesis tests were performed in two sets of six double-chamber BESs in parallel, following the procedure described in 2.3.1. Each cathodic chamber was filled with catholyte solution rich in different salts and Archaea domain microorganisms from an industrial inoculum. After 8 days, the gases were collected and analysed, while the solution was characterized to detect the development of new microorganisms. For the catalytic perspective, CH_4 production was influenced

by the nature and functionalization of the cathode. **Figure** 3-4 shows the results of gas analyses after the test, reporting the moles of CH_4, H_2, and CO_2 found normalized for the ECSA value. Undoped biochar exhibits different CH_4 production (13 $\mu mol \cdot cm^{-2} \cdot L^{-1}$), than only carbon cloth (CC), which showed only 3 $\mu mol \cdot cm^{-2} \cdot L^{-1}$ due to the better microorganism's settlement.

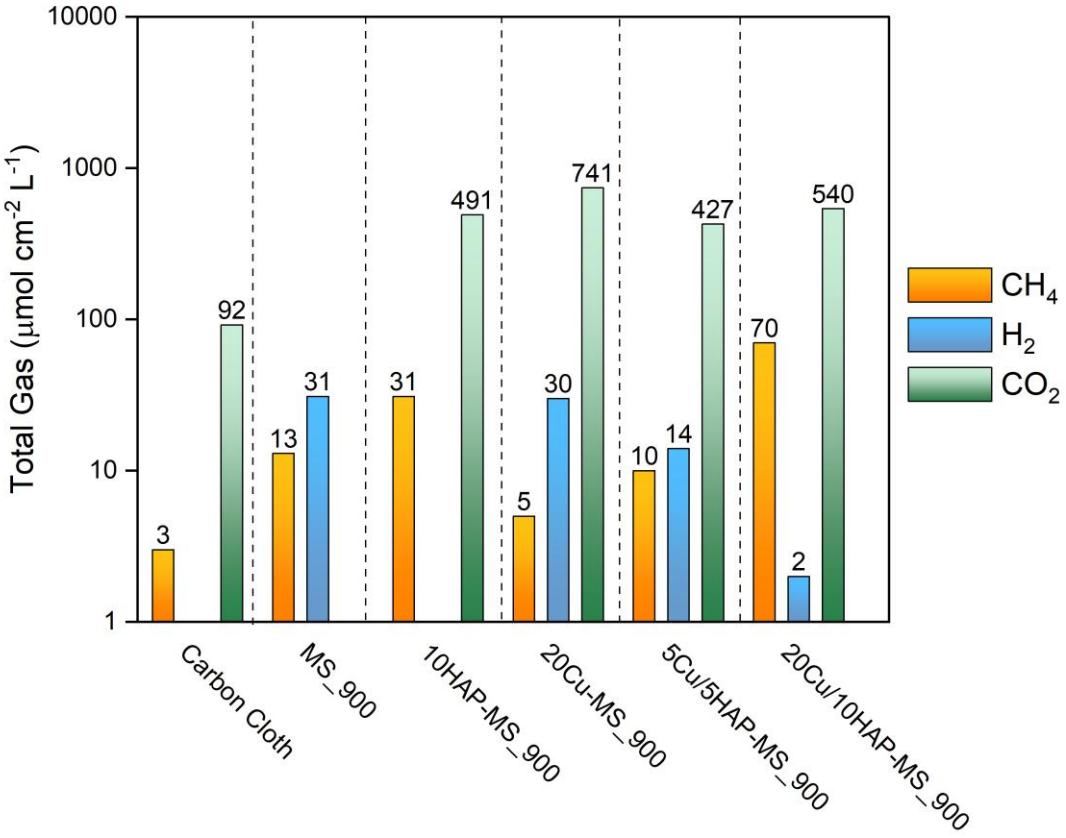

Figure 3-4 Histograms of CO_2, H_2, and CH_4 concentrations measured after 8 days of bioelectromethanogenesis. Experiments were conducted at 45 ± 1 °C, with CO_2 continuously supplied for 40 min at a flow rate of 0.5 NL h^{-1}, under an applied potential of -1.2 V vs SHE.

Residual CO_2 was included coupled with H_2 and CH_4 gaseous products, even though CO_2 is the reactant of bioelectromethanogenesis, because it provides information about the CO_2ER pathways. The residual CO_2 measured (starting from 15 mmol) in the gas phase is related to the extent of reactants consumptions and possible competing processes. Variation of CO_2 levels indicates whether the reagent is effectively reduced, lost due minor leaks, and converted in carbonate or bicarbonate species under alkaline conditions (pH >10). For instance, stable levels of CO_2 are visible when HAP is admixed in the composite due to the possible pH buffer as it will be discussed in the following paragraphs.

The binary reference materials (HAP-free and Cu-free) showed a limited production of methane and hydrogen (the latter deriving from the hydrogen evolution reaction pathway).[62,63] Specifically, 10HAP-MS900 produced only a low amount of CH_4 (31 μmol·cm^{-2}·L^{-1}), whereas 20Cu-MS900 showed a marked increase in H_2 production (30 μmol·cm^{-2}·L^{-1}) compared to bare MS900. The higher activity toward H_2 observed for 20Cu-MS900 is attributed to the enhanced reductive capability of copper sites. Notably, this activity is associated with HER rather than CO_2 reduction, confirming that this binary material does not promote biological methanogenesis and may even inhibit microbial activity. On the other hand, 10HAP-MS900 showed methane production even though no active sites are present in the composite: the production of CH_4 is directly related to biological activity.

Interestingly, the first ternary materials showed CH_4 formation, confirming the synergistic effect on the CO_2 reduction process. 5Cu/5HAP-MS900 showed both methane and hydrogen production in an equimolar ratio: 10 μmol·cm^{-2}·L^{-1} and 14 μmol·cm^{-2}·L^{-1} for CH_4 and H_2 respectively. Unfortunately, the methane production is like the bare biochar, not showing enhanced activity for methane production. The lack of CH_4 production is related to the poor content of both copper and HAP which make this ternary material (5Cu/5HAP-MS900) like the bare biochar (MS-900).

The combined effect of Cu NPs and HAP was observed in cathodes functionalized with the highest percentages (20Cu/10HAP-MS900), where methane production reached 70 μmol·cm^{-2}·L^{-1}.[64] The use of a ternary composite material in an optimized composition validates the composition studied in previous work and the CH_4 production is comparable to other BES systems (such as Gajaray et al[65] work with 30-days operating bioreactor) , achieving the same production in shorter times. The main result suggests a strong selectivity towards methane in the presence of a metal active phase, an inorganic modifier, and microorganisms. Before focusing on the main role of HAP in the ternary material, it is important to analyze two aspects: i) the pathways for CO_2 conversion on the reference material and binary composites, ii) the microbiological change of the inoculum after the reaction. Starting with the possible pathways of the reaction, alongside gas analyses after the test, the content of volatile fatty acids (VFAs) in solution was measured. VFAs (C_2 and C_3 compounds) can be produced by C-C coupling of the electrochemical test when high voltage (-1.0 V *vs* RHE) or current

is applied.[66] VFAs results are presented in **Figure** S-6-6. Bare biochar and 10HAP_MS900 produced approximately 6 mg L^{-1} of VFAs, while, as expected, the presence of Cu in the composite (20Cu-MS900) catalyzes the transformation of CO_2 into C_2 or C_3 hydrocarbons, visible from the high values of VFAs in the solution (ca. 49 mg L^{-1}). Ternary materials have also, in this case, different behaviour: 5Cu/5HAP-MS900 showed the same production of VFAs as the copper binary composite, while 20Cu/10HAP-MS900 produced comparable values to the pure biochar (12 mg L^{-1}). These results further indicate that HAP can positively affect the reaction in terms of selectivity, hindering possible parasitic reactions taking place.

Being BES, an electrochemical system that involves biological transformation, the genera of Archaea and Bacteria present after the reaction can also explain the enhanced results of ternary materials.[67–69] The starting inoculum was filled with *Methanobacterium* as the main genus, which is known to have methanogenesis properties. After the reaction, HAP-doped material showed the same genera of Archaea, which contributed to the methane formation, and for Bacteria genera, the most abundant was the protein-bacteria group, which is very active in biodegradation of alkanes into $-CH_3-$ building blocks that are easily protonated to form CH_4 molecules.

Since 20Cu/10HAP-MS900 is an innovative composite successfully tested in this work for the first time in the literature, it is important to evaluate the performance comparing to the literature as reported in **Table** 3-2. Most of the BES configuration exhibited a similar coulombic efficiency (CE) for methane around 60%. The average CE depends on the cathode material, with the lowest value observed for the CC electrode. When CC is replaced by biochar or structured carbon (graphitized carbon or carbon felt) in the cathodic chamber, the amount of methane produced approximately doubles.[70–72] In fact, to furtherly reduce the costs and the environmental impact, the use of bio-based and fully recyclable materials, such as biochar, will be crucial. Using a biochar cathode material that have a similar productivity, enhance the sustainability of the material and consequently of the process. Another important advantage of using a HAP-doped biochar is the time of methane production. The methane generation with this composite occurs considerably faster than in the other tested systems. Specifically, methane production comparable to the highest values reported in the literature was achieved in less than a quarter of the typical time required (8 days versus 30 days or

more) under a CO_2 sparging configuration.[73] The improved performances are also related to morphological modifications. These modifications increase surface area and conductivity leading to better performances as it has been observed in previous works.[74] Finally, the material and its relative process are completely part of BES systems. In other works, the overall efficiency of bioelectrochemical systems can often be improved when they are integrated with other complementary technologies. Coupling bioelectrochemical reactors with anaerobic digestion can significantly enhance methane production, improve carbon conversion, and increase the overall energy recovery of the system. In these hybrid configurations, higher methane yields and faster production rates are observed compared to conventional anaerobic digesters operating alone.[75] For example, experimental studies have reported methane production increases of more than 40% when a bioelectrochemical system is integrated with anaerobic digestion, highlighting the strong synergistic effect between the two processes. The composite designed for bioelectromethanogenesis performs similarly to traditional anaerobic digesters, according to a review of the literature, reaching 60% of CH_4 efficiency. Its primary benefit is that it offers a more physiologically appropriate environment for longer periods of time, which suggests improved system stability. There is still space for development, though, as the composite exhibits some variability and unevenly distributed active sites, which might reduce its overall effectiveness. The durability is due to the presence of hydroxyapatite which is a novelty for electrochemical processes.

Since 20Cu/10HAP-MS900 showed remarkable properties in CH_4 formation, the presence of copper active sites and overall a hydroxyapatite modifier have been discussed.[76,77] As the main change in composition is due to the higher presence of HAP, in the next paragraph the role of HAP was deeply studied for bioelectromethanogenesis system.

Table 3-2 Comparative view of recent bioelectrochemical systems for bioelectromethanogenesis process

Inoculum	Cathode Material	Separator double chamber	T *(°C)*	Cathode Polarization *(V)*	Current	Yield or productivity *%*	CCE-CH_4	Ref.
Anaerobic granular sludge	Fe gauze-packed carbon felt	CEM	30	−1 (vs Ag/AgCl)	8 A m^{-2}	22 L m^{-2} d^{-1}	>90 %	[74]
WWTP[d] Anaerobic sludge	Electroless copper	Nafion 117	30	−0.9 (vs Ag/AgCl)		155 nmol cm^{-3} d^{-1}	22 %	[72]
WWTP[d] Anaerobic sludge	Carbon felt	Nafion 117	Room	−1.1 (vs Ag/AgCl)	5.6 A m^{-2}	9 L m^{-2} d^{-1}	65 %	[71]
MEC	Graphitized granular carbon	CMI-7000S	35	/	45 A m^{-2}	23.36 ± 3.63 m^3 m^{-3} d^{-1}	64 %	[70]
Activated sludge	Carbon felt	CEM	30	-0.9 (vs Ag/AgCl)	16.5 A m^{-2}	36.6 mL m^{-2} d^{-1}	89	[73]
				-1.0 (vs Ag/AgCl)	45.5 A m^{-2}	54.2 mL m^{-2} d^{-1}	92	
Biogas plant wastewater	Cu/HAP[c] Biochar	Nafion 417	45	−1 (vs SHE)	1.2 mA cm^{-2}	866 mmol m^{-2} d^{-1}	64 %	This work

3.1.4. Role of HAP properties in bioelectromethanogenesis

Although HAP has gained attention as a catalytic or photocatalytic support, due to its highly functionalized surface, its role in bioelectrocatalysis remains unexplored. Therefore, once assessed that its presence could enhance bioelectromethanogenesis results, HAP is explored as a key component with emphasis on its surface characteristics in microbial adhesion, reaction kinetics, and electron transfer process. Different characterizations were carried out to propose an effective role in ternary composites. In the previous section, morphological and structural analyses (XRPD and N_2 adsorption/desorption isotherms) confirmed: i) the integration of HAP phase in the composite; ii) the presence of mesoporosity given by HAP to the macroporous biochar; iii) the dispersion of HAP nanorods in the external area of the composite. SEM analyses and respective EDX spectrum (**Figure** 3-5-a, b) of the composite in contact with the inoculum showed that the absence of HAP in the internal section of biochar macropores was also associated with a lack of colonization by microorganisms. The spectrum collected in the colonized area displayed the peaks corresponding to Ca, P, and Cu, indicating that surface colonization occurred in the HAP region.[78] The strong microbial affinity toward hydroxyapatite surfaces may originate from the unique bio-interface environment formed by the amphoteric nature of hydroxyapatite in aqueous media.[79,80] The amphoteric behavior of the HAP surface derives from the simultaneous presence of Ca^{2+} and PO-H acidic sites (Lewis and Brønsted sites, respectively) and OH, PO_4^{3-}, and Ca^{2+} vacancies (basic sites).[81,82] Moreover, even carbonates (incorporated in the HAP lattice due to exposure to air) could play a role in terms of surface acidity-basicity.

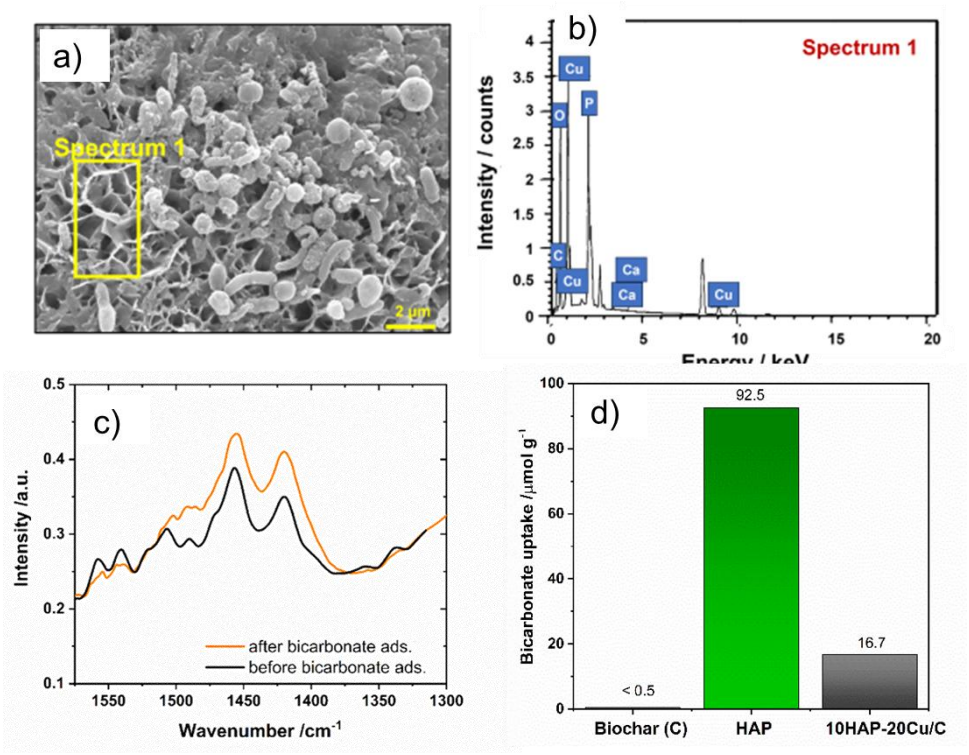

Figure 3-5 a) SEM-SE image of the colonized composite (20Cu/10HAP-MS900) surface and b) corresponding EDX spectrum of a selected area; c) Magnification of 1300-1600 cm^{-1} region of the FT-IR spectra of HAP before and after bicarbonate adsorption; d) Bicarbonate uptake by MS900 (biochar), HAP,10HAP/20Cu-MS900 at 30 ± 1°C determined by retro-titrations d).

Finally, phosphates can also serve as a nutrient source for microbial metabolism. The multi-functionalized surface plays a crucial role in modulating the interaction between electroactive chemical species, electroactive microorganisms, and the environment. Another key role is pH stabilization, always due to the presence of different moieties on the surface of HAP. The presence of these moieties determines the pH at the electrode/solution interface.[83,84] When HAP encounters water media, these ions maintain the pH within the range of 6 to 8, providing a buffering effect and creating an optimal environment for microorganism metabolism, which results in a good bioelectromethanogenesis activity.[85]

The surface properties of HAP have not only biochemical advantages but also chemical benefits. The hydroxylated surface of HAP could also effectively interact with reagents and products of CO_2 reduction processes. Several studies have reported that the presence of groups able to provide hydrogen-bonding interactions is beneficial for electroreduction processes, since it facilitates easy

proton transfer and stabilizes key intermediates. HAP is known to adsorb CO_2 molecules, but in aqueous BES, CO_2 is dissolved, forming $CO_{2\,(aq)}$ and establishing an equilibrium with its bicarbonate ion form ($HCO_{3\,(aq)}^-$). Accumulation of bicarbonate ion at the electrode surface has a beneficial role in the electroreduction of CO_2 since it enhances the reaction rate, shifting the diffusion of reagents from the bulk of the solution to the electrode. The bicarbonate uptake capacity of bare biochar, bare HAP, and the 10HAP-20Cu-MS900 composite was evaluated through back-titration experiments, described in 2.2.3. While biochar exhibited no ability to retain bicarbonate anions, hydroxyapatite, characterized by the coexistence of acidic and basic surface functionalities, proved to be an effective adsorbent (92.5 mmol g^{-1} at 30 °C, **Figure** 3-5-d). Bicarbonate ions uptake was further confirmed by FT-IR, revealing the presence of a B-type carbonation: the intensity of carbonate signal (1419 cm^{-1} and 1456 cm^{-1}) increased after the contact of HAP with bicarbonate aqueous solution, as displayed in **Figure** 3-5-c. The bicarbonate adsorption capacity of HAP was retained by the composite material, which was able to adsorb up to 17 mmol g^{-1} of bicarbonate anions at 30 °C (**Figure** 3-5-d). The enhanced bicarbonate uptake associated with the presence of HAP in the composite may account for the improved CO_2 reduction performance observed during the experiments.[82]

Overall, these findings suggest that investigating the role of the active HAP-based interface in CO_2 bio-electroreduction could guide the design of composite biomaterials with improved performance.

3.2. CO_2 Electrochemical reduction

Electrochemical reduction of carbon dioxide is one of the most promising alternatives accessible as CCU technologies, along with other innovative CO_2 remediation solutions. CO_2ER is a sustainable path for several reasons: i) it does not require high temperatures or high pressures to meet external energy requirements; ii) it can be combined with either renewable or non-renewable energy sources; iii) it is recognized as a versatile process with a high atom economy when its selectivity is controlled; and iv) its economics can be highly competitive for specific markets, like those for CO and formic acid. However, CO_2ER has several drawbacks pertaining to the kinetics and thermodynamics of this reaction.[86] First, CO_2 activation is the limiting step, as CO_2 is a very stable molecule (in fact, overpotential is needed), and also the control of discrete electron transfers can be kinetically limiting. CO_2ER suffers from the presence of parasitic hydrogen evolution reaction, which is more favorable in the electrocatalytic conditions. From the catalytic perspectives, metal electrocatalysts are often expensive, deactivated or not stable in long-term reaction conditions. According to these considerations, many efforts have been put into developing efficient catalysts to overcome these obstacles.

In the next paragraph, the development of a novel electrocatalyst based on carbon nitride, hydroxyapatite, and copper active centres is reported in its synthesis, characterization, and testing in the electrochemical reduction of CO_2 into methane and formic acid.

The study of carbon-HAP materials derived from previous studies[87], where N-doped graphene sheets functionalized with HAP and Cu nanoparticles, demonstrated high selectivity towards formate species. The idea of a composite material aimed to exploit the single properties of each component: copper nanoparticles demonstrated enhanced selectivity towards high added-value compounds, carbon scaffold brought high surface area, controlled porosity, and overall high conductivity; finally, a proper dispersion of HAP onto the surface of the catalysts will introduce numerous amphoteric moieties, complementary to the carbon acidic sites.

In the previous studies, despite promising results, N-doped carbon materials have exhibited non-homogeneous phase distribution of the components and poor interfacial contact among carbon, hydroxyapatite, and copper nanoparticles, ultimately limiting their electrocatalytic performance. In this chapter, a one-pot synthetic strategy was implemented to produce a carbon nitride-based (@CN) electrocatalyst functionalized with copper nanoaggregates and synthetic hydroxyapatite (HAP_Cu@CN).

3.2.1. Synthesis and physico-chemical characterization of CN-based materials.

The one-pot synthetic approach was inspired by the work of Gao et al.,[88] who developed a one-pot synthesis of Ru-doped carbon nitride via pyrolysis of covalent organic frameworks (COFs), achieving outstanding performance in electrocatalytic water splitting, Oxygen Evolution Reaction (OER) and Hydrogen Evolution Reaction (HER). Building upon these advances and the one-pot synthetic strategy proposed above, in this paragraph, the one-pot synthesis was adapted for the formation of a carbon nitride scaffold, co-functionalized with copper as the active phase and HAP as an inorganic modifier, using COF itself as precursor. CIN-1 type COFs are a specific family of covalent organic frameworks, which involve the formation of an immine bond (C=N) in a 2D macrostructure with a sp^2 hybridization, resulting in a porous structure with high surface area, chemical, and thermal stability. The presence of different electronegative atoms, like N, O, or S could coordinate metallic species and then delocalize the charge on the 2D structure. Metal-doped COFs are gaining interest in different fields such as adsorption processes and catalytic reactions.

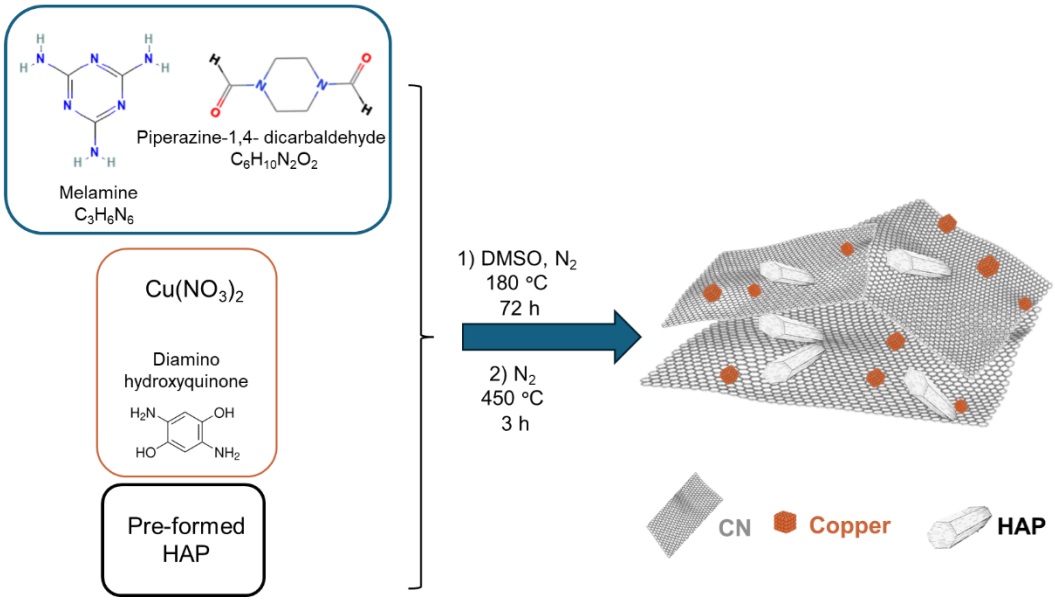

Scheme 3-1 Schematic diagram of one-pot synthesis of ternary composite material HAP_Cu@CN.

Following the procedure explained in paragraph 2.1.3.2, two organic precursors (melamine and piperazine-di-carbaldehyde) were condensed to form an iminium-type covalent organic framework. Copper was co-introduced in the form of a complex, formed by copper ions and 2,5-diaminohydroquinone, as the ligand. copper complexes should be directly bonded to the covalent organic framework to ensure a stable anchoring of metal species in the final materials.[88,89] For HAP_Cu@CN, pre-synthetized hydroxyapatite was also added during the formation of the covalent organic framework, as depicted in **Scheme** 3-1.

Two CIN-1 based materials were obtained, labelled as Cu@CIN-1 and HAP_Cu@CIN-1. Composite materials were characterized in their main properties to assess the formation of CIN-1 covalent organic framework. It is important to highlight that some of the analyses of characterizations were carried out exclusively on the ternary precursor, for different reasons: i) the role of HAP was explored as catalyst for condensation reaction and, ii) this ternary material represents an innovative material that comprise HAP as inorganic modifier and iii) the binary composite has already been studied in its characteristics in previous works.[90,91] The formation of COF is important because the chemical

structure with consecutive C=N bonds can be used as a molecular precursor of carbon nitride. From the compositional perspective, the composition values are reported in **Table** 3-2. Cu@CIN-1 contained a relative composition of 35.6 wt% carbon, 27.6 wt% nitrogen, and 3.8 wt% hydrogen, and a copper content of 26.9 wt%. In comparison, HAP_Cu@CIN-1 exhibited lower elemental composition of C, N, H, and Cu (24.4 wt%, 16.5 wt%, 2.9 wt%, and 12.6 wt%, respectively) because of the dilution by the introduction of the inorganic HAP phase. A small amount of S is present (5.8 wt% and 9.8 wt% for binary and ternary composite, respectively) for both materials because of the use of DMSO as the solvent for the condensation reaction. Additionally, the absence of oxygen quantification (due to experimental setup) and the presence of a copper ligand in the synthetic mixture, which makes the reaction pathways more elaborate with higher formation of C=N bonds, prevented the evaluation of the molar ratio between the species.

Table 3-3 Material composition as obtained from XRF-HCNS analyses.

Materials	Composition (%wt) [a]						
	H	C	N	Cu	S [b]	Ca	P
Cu@CIN-1	3.8	35.6	27.6	26.9	5.8	/	/
Cu@CN	1.7	45.7	28.8	21.9	1.3	/	/
HAP_Cu@CIN-1	2.9	24.4	16.5	12.6	9.8	23.5	10.3
HAP_Cu@CN	1.3	31.3	19.9	10.9	0.6	27.1	12.4

a. Oxygen content was not evaluated due to experimental set-up for HCNS analyses. The percentage error is below 10% and it is calculated from reproducibility analyses on the sample.

The accurate determination of the atomic composition of COFs is challenging due to the multistep nature and complexity of their synthetic procedures. Therefore, the focus is centered on morphological and spectroscopic analyses, which allow the identification of expected functional groups or chemical bonds, also confirming the molecular structure. XRPD pattern (**Figure** 3-6-a) of HAP_Cu@CIN-1 clearly shows the typical reflections of crystalline hydroxyapatite, consistent with

JCPDS 00-064-0738, with the most intense reflection peaks at 25.90° (002), at 31.86° (211), and at 32.90° (300). Furthermore, reflections at around 22.9° and 25.3° can be ascribed to unconverted melamine molecules. CIN-1 is known to exhibit a broad low intensity peak in the 2θ in the 10-27° range, particularly the (001) interplanar stacking peak and (100) in-planar stacking of Schiff base (C=N bonds)[92] which are masked by the diffraction pattern of more crystalline phases of melamine and hydroxyapatite. From a spectroscopic analysis with Raman displayed in **Figure** 3-6-b, iminium covalent organic framework formation is assessed by the co-presence of CH_2 in-phase (1360 cm^{-1}) scissoring and imine (C = N) stretching vibrations (1562 cm^{-1}) for both Cu@CIN-1 and HAP_Cu@CIN-1.[9]

TEM images of HAP_Cu@CIN-1 composite (**Figure** 3-6-c) show granular morphology of iminium-based COF (CIN-1) that surrounds hydroxyapatite nanorods completely. High-resolution images (**Figure** 3-6-d) coupled with EDX analysis (**Figure** 3-6-e) confirm the wrapping of CIN-1 around the surface of HAP nanostructures. Due to the presence of a multifunctional surface with acidic and basic moieties, hydroxyapatite can adsorb and can catalyze the condensation of the two organic precursors (melamine and piperazine di-carbaldehyde), stabilizing the organic framework during synthesis and pyrolysis.[93] In fact, it has been reported that HAP is an excellent catalyst for condensation reactions involving aldehydes and amines (in a Michael-type reaction), and it has been successfully used to promote the oxidative coupling of amines to imines to produce N-doped carbon. Chu et al. [94] pointed out that HAP not only served as a template during the synthetic process of N-doped carbon materials, but also acted as a catalyst to promote the decomposition of the precursor phenyl compounds. Furthermore, they accompanied experimental approaches with DFT calculations confirming the catalytic mechanism, in which carbonyl groups adsorbed on the HAP surface synergistically activated benzylamine and initiated the oxidative coupling reaction.

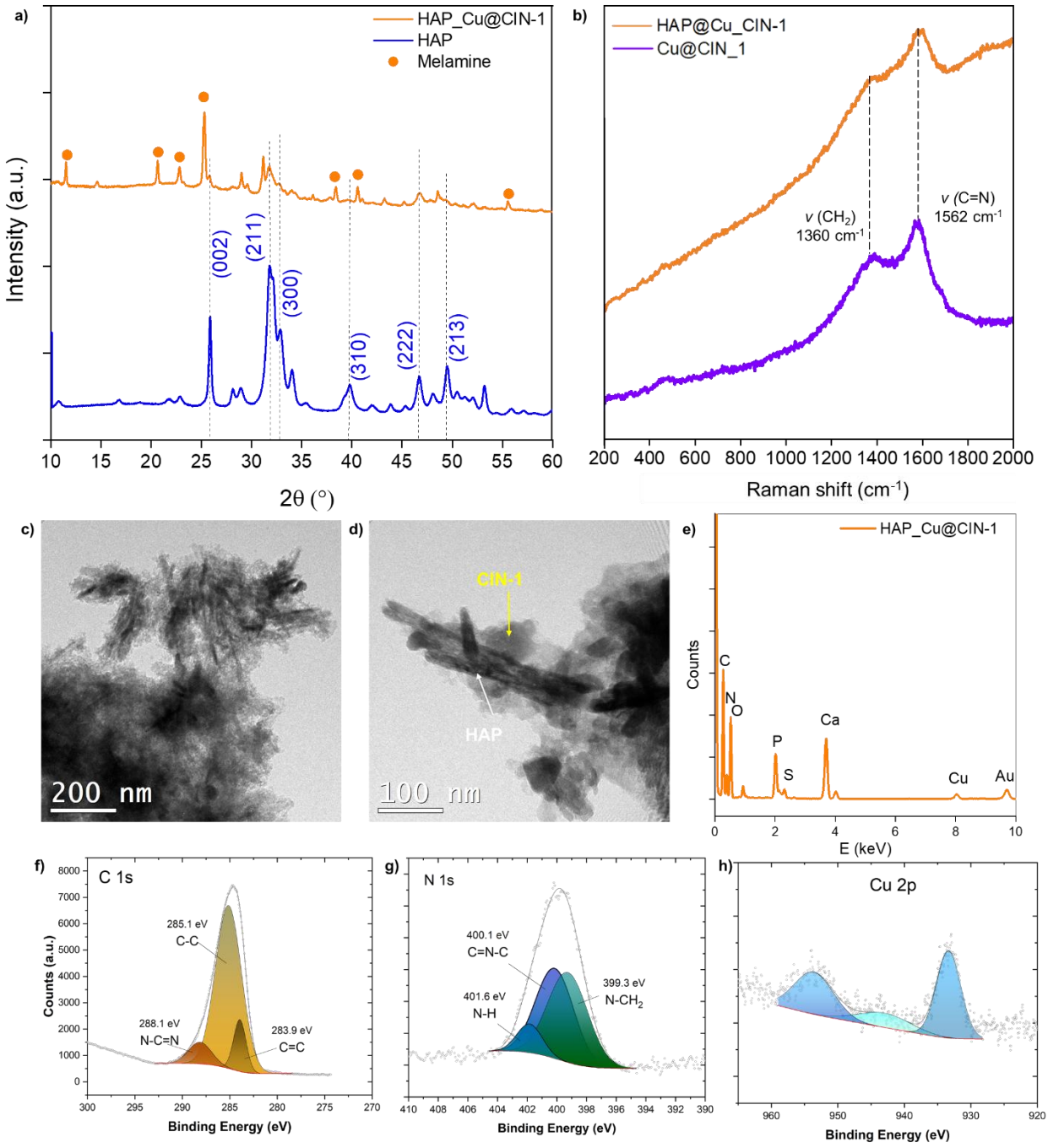

Figure 3-6 a) XRPD patterns of Cu@CIN-1 and HAP. Melamine reflection peaks are highlighted as orange circle; b) Raman spectra of Cu@CIN-1 and HAP_Cu@CIN-1. c, d, e) Representative TEM and HRTEM and EDX spectrum of HAP_Cu@CIN-1; High-resolution XP spectra for f) C 1s, g) N 1s and h) Cu 2p of HAP_Cu@CIN-1 composite.

X-ray photoelectron spectroscopy (XPS) was employed to investigate the surface composition and the chemical states of the elements present in the HAP_Cu@CIN-1 composite. The survey spectrum (**Figure** S-6-7) revealed the presence of bands assigned to C 1s, N 1s, O 1s, S 2p, P 2p, Ca, 2p, and Cu 2p signals. Specifically, C 1s and N 1s peaks derived from the COF scaffold, while Ca 2p, P

2p, and O 1s are associated with the hydroxyapatite phase. S 2p is associated with the sulphur impurities derived from the use of DMSO in the synthetic procedure.

The C 1s photopeak is very complex: its deconvolution into three components centered at 283.9, 285.1, and 288.1 eV was performed (**Figure** 3-6-f). The peak at 283.9 eV is attributed to C=C bonds in aromatic or graphitic carbon environments, the signal at 285.1 eV corresponds to sp^3-hybridized C–C/C–H bonds, and the peak at 288.1 eV is assigned to C=N or N=C–N groups, characteristic of imine or amide functionalities.[95] Similarly, the N 1s spectrum was resolved into three components located at 399.3, 400.1, and 401.6 eV (**Figure** 3-6-g). The peak at 399.3 eV is associated with imine-type nitrogen (C=N), 400.1 eV is typically assigned to amine or pyrrolic nitrogen, and the higher binding energy component at 401.6 eV corresponds to protonated or quaternary nitrogen species. These assignments are consistent with the expected chemical environment in the CIN-1 framework.[96]

The XP spectrum of copper (**Figure** 3-6-h) further confirmed the presence of Cu^{2+} species, in line with the oxidation state of the copper precursor. The Cu $2p_{3/2}$ signal appeared at approximately 933.4 eV, and the Cu $2p_{½}$ component was observed at 953.8 eV, resulting in a spin-orbit splitting of around 20 eV, as reported in copper-coordinating systems.[96] The Cu 2p peak was accompanied by the characteristic shake-up satellite feature in the 938-945 eV range.

Altogether, the morphological and the spectroscopic analyses demonstrate the successful formation of the CIN-1 framework in both Cu@CIN-1 and HAP_Cu@CIN-1. Then, the as-prepared materials were subjected to annealing at 450 °C under an inert atmosphere, promoting the conversion of the CIN-1 framework into a carbon nitride-like scaffold rich in graphitic domains, labelled as Cu@CN and HAP_Cu@CN.

From the composition perspective (**Table** 3-2), both materials suffered from a decrease in hydrogen (1.7 wt.% and 1.3 wt.% for Cu@CN and HAP_Cu@CN, respectively) and nitrogen content and an increasing contribution in carbon (45.7 wt.% and 31.3 wt.% for Cu@CN and HAP_Cu@CN), as a result of partial deamination of the materials. The copper content (12.6 wt.% for Cu@CN and 10.9 wt.% for HAP_Cu@CN) is in good agreement with the target design composition of 10 wt.%. In both

composites, preformed HAP was incorporated to achieve a final HAP content of 10 wt.%, calculated based on the COF synthetized and its corresponding yield (approximately 45%). This composition was chosen based on the previous results with carbon-HAP-Cu composites used in other electrochemical systems, where the 10 wt.% for Cu and 20 wt% for HAP was a good compromise between stability and catalytic activity.

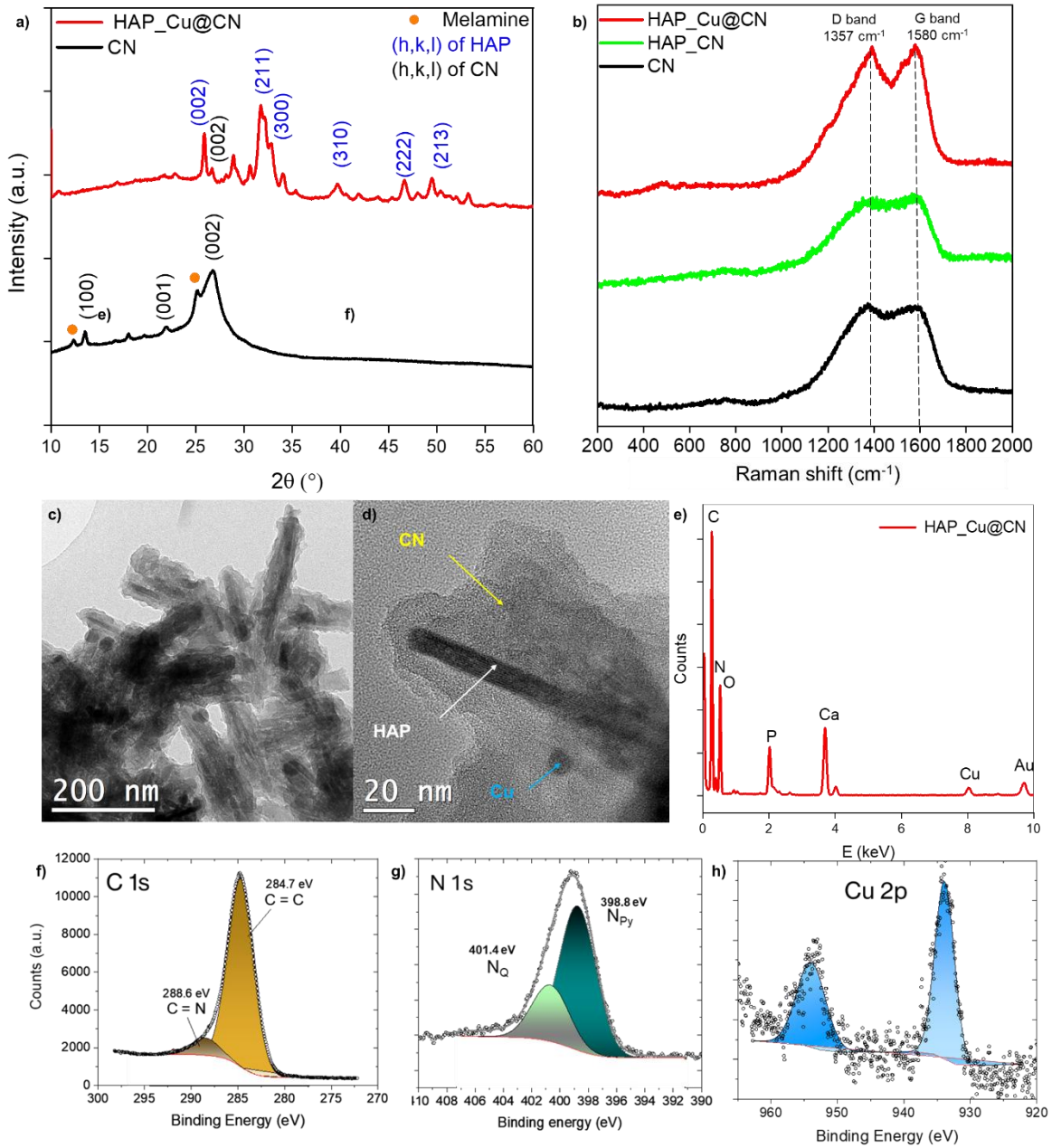

Figure 3-7 a) XRPD patterns of the HAP_Cu@CN and CN; b) Raman spectra of CN, HAP_Cu@CN, Cu@CN. c, d, e) Representative TEM, HRTEM and EDX spectrum of HAP_Cu@CN. High-resolution XP spectra for f) C 1s, g) N 1s and h) Cu 2p of HAP_Cu@CN composite.

XRPD analysis, shown in **Figure** 3-7-a refers to HAP_Cu@CN obtained from thermal annealing of HAP_Cu@CIN-1 and compared with that of the pristine carbon nitride (CN) prepared under identical conditions but in the absence of hydroxyapatite and copper. As for HAP_Cu@CIN-1, HAP_Cu@CN displays the characteristic reflections of HAP in a broader background (than HAP_Cu@CIN-1), indicating an amorphous nature of carbon support. In addition, two diffraction peaks located at approximately 13.1° and 27.5° are observed, which can be attributed to the (100) and (002) planes of graphitic carbon nitride (g-C_3N_4), respectively. The (002) reflection peak is associated with interlayer stacking of conjugated aromatic systems and represents the most intense feature in the CN diffractogram.[97] The absence of melamine-related peaks in the ternary pattern clearly indicates the complete conversion of the organic molecular precursor; on the other hand, residual melamine signals are still visible in the CN diffractogram, suggesting once more that the presence of HAP and Cu in the composite significantly enhances the condensation and the polymerization reaction. This observation implies that HAP acts as a structural promoter and facilitates the formation of stacking molecular planes of the carbon nitride matrix.

To further confirm the formation of carbon nitride (even catalyzed by HAP nanorods) Raman spectra were collected. After thermal annealing, the Raman spectra (**Figure** 3-7-b) of CN-based composites (Cu@CN and HAP_Cu@CN) clearly present the characteristic D- and G-bands at around 1357 and 1580 cm^{-1}, which stand for *disorder* and *graphitic* bands, respectively. D-bands are usually related to the defectivity deriving from N-doping in the carbon matrix and are referred to the sp^3 bonds of the carbon, while G-bands are connected to the presence of highly graphitic domains given by the presence of sp^2 bonds of carbon. [98] Interestingly, when HAP is admixed to the composite, the D- and G-bands are more pronounced and resolved, meaning that hydroxyapatite has an effective role in promoting the formation of graphitic domains in the material.[99]

TEM-EDX analysis (**Figure** 3-7-c) of HAP_Cu@CN composite reveals a homogenous distribution of copper nanoaggregates and hydroxyapatite nanorods across the carbon matrix, indicating intimate interfacial contact among the three components and the absence of segregated, isolated single phases. High-resolution images coupled with EDX mapping (**Figure** 3-7-c,d,e, and **Figure** S-6-8) confirm the presence of spherical copper nanostructures, preferentially deposited on the carbon

nitride surface. Such behavior can be rationalized considering that copper was covalently coordinated to the hydroxyquinone molecular ligand during the synthesis.[100] The copper complex ensures its anchoring onto the carbonaceous phase during synthesis and pyrolysis, minimizing interaction with the inorganic components. Regarding HAP, the inorganic nanorods are completely enveloped in the carbon nitride scaffold, as it can be seen initially in the COF precursor: these findings are consistent with previous work[101] that reported the successful integration of hydroxyapatite nanorods with mesoporous graphitic carbon nitride via a hydrothermal approach. In their study, the carbon nitride sheets were shown to wrap around the HAP structures, facilitating strong interfacial interactions. A similar morphology was also observed by some authors,[102] who demonstrated via TEM analysis that HAP nanoparticles can be uniformly embedded within lamellar g-C_3N_4 architectures, forming well-integrated agglomerates.

Looking specifically at the surface properties of the materials, the XPS survey (**Figure** S-6-7) spectrum confirms the presence of all the expected elements in the HAP_Cu@CN composite, including C, N, O, Ca, P, and Cu. The high-resolution spectrum in the C 1s region (**Figure** 3-7-f) displays an intense, asymmetric envelope that can be deconvoluted into two primary components centered at 284.7 eV and 288.6 eV. The peak at 284.7 eV corresponds to graphitic or aromatic carbon (C=C/C–C), typical of sp^2-hybridized carbon atoms in conjugated systems. The component at 288.6 eV is attributed to carbon atoms bonded to nitrogen in imine (C=N) or carbonyl-like environments, commonly observed in g-C_3N_4 and other nitrogen-rich carbonaceous frameworks.[103] In the N 1s region, the spectrum exhibits a broad feature that can be resolved into two distinct peaks (**Figure** 3-7-g). The component at 398.8 eV is assigned to sp^2-hybridized nitrogen involved in C=N bonds, while the higher binding energy peak at 401.3 eV corresponds to protonated nitrogen species ($N–H^+$) or quaternary nitrogen atoms, indicating structural defects, terminal amino groups, or positively charged nitrogen sites.[104,105] In the Cu 2p region, two main peaks, with the respective deconvoluted sub-bands, are observed at 931.3-935.2 eV and 951.2–955.7 eV (**Figure** 3-7), corresponding to the Cu $2p_{3/2}$ and Cu $2p_{1/2}$ contributions. The absence of strong satellite peaks and the binding energies of the two peaks confirm the presence of reduced species of copper, as Cu^0 and/or Cu(I), which could be reduced by N-doped carbon.[106] Reduced copper is significantly

important for CO_2ER as a reduction centre, and the continuous electron flow in CA experiments can limit the passivation and the oxidation of copper into Cu(II), which will become completely inactive for electrochemical CO_2 conversion.

3.2.2. Electrochemical characterization

After assessing the chemical and structural properties of binary and ternary materials, an overview of electrochemical properties is necessary before testing the composites in the CO_2ER. Two main techniques are used for the electrochemical properties: linear sweep voltammery (LSV) and cyclic voltammetry (CV). LSV and CV are the most widely used voltametric techniques because they are unmatched in their ability to provide information on the steps involved in electrochemical processes: applying a potential, the electrode can be used as a tool for producing reactive species in a small solution layer surrounding its surface, and, at the same time, to monitor chemical reactions involving these products.[107] Focusing on LSV, the analyses were carried out following the procedure in paragraph 2.2.4 in two different enriched electrolytic solutions: saturation with N_2 or CO_2. Measurements in N_2-saturated solution provide information about side electrochemical reactions, such as the hydrogen evolution reaction (HER), as the only reducible species is H^+ ion (which can reduce to H_2 following the semi-redox reaction displayed Eq. 3-1). On the other hand, in CO_2-enriched solution, the currents slope could changes evidently showing the presence of CO_2ER. Direct comparison of the two current-potential profiles allows the identification of CO_2ER or HER in our catalytic system, giving information about the onset potential of the reaction.

$$2H^+ + 2e^- \rightarrow H_2 \text{ (1 atm. 25°C, } E^0 = 0 \text{ V } \textit{vs} \text{ RHE)} \qquad \text{Eq. 3-1}$$

Particularly from a qualitative comparison, the higher the onset potential, the higher the energy requirement for activating the CO_2 reaction. The electrocatalytic performance of the reference materials (CN and HAP), as-synthesized key component, binary (Cu@HAP and HAP@CN), and ternary (HAP_Cu@CN) materials were initially evaluated using linear sweep voltammetry (LSV) under a N_2 or CO_2 atmosphere.

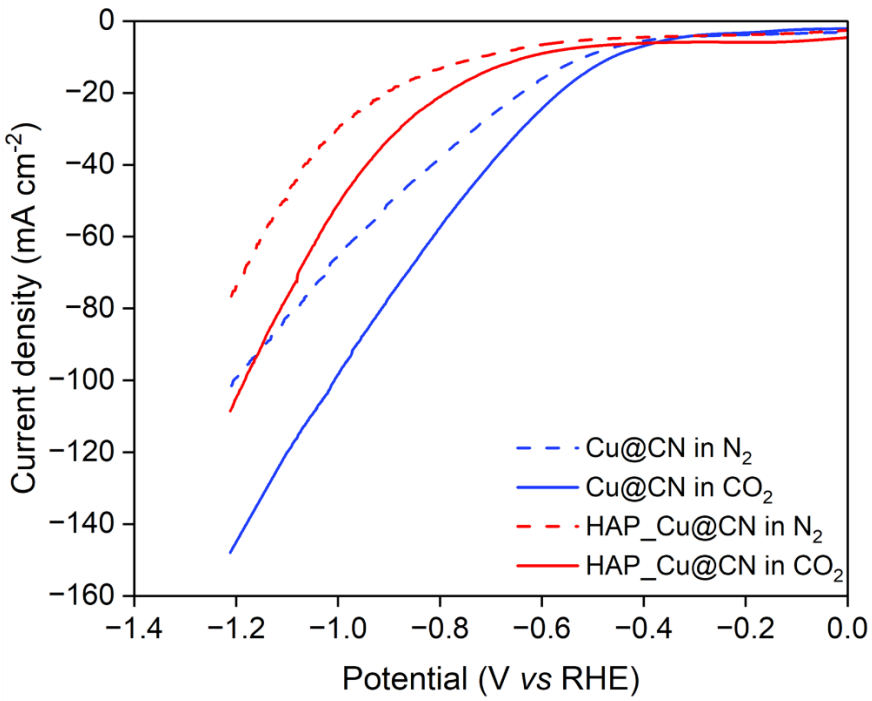

Figure 3-8 . Linear Sweep Voltammetry (LSV) results for Cu@CN (light blue) and HAP_Cu@CN (red) under N_2-saturated (dashed line) and CO_2 -saturated (solid line) 0.1 M $KHCO_3$ aqueous solution at 20 mV s^{-1} scan rate.

Figure S-6-9 represents all LSV of reference materials. As expected, bare HAP is characterized by very low current density (-10 mA cm^{-2}) due to the insulating properties of this ceramic material. On the contrary, LSV results reveal that for the CN component, the overall current density reached -120 mA cm^{-2} under N_2 flow due to high conductivity properties of the material. The current delivered in the CO_2 aqueous solution is almost halved to be around -60 mA cm^{-2}, starting with an onset potential of -0.7 V (*vs* Reference Hydrogen Electrode, RHE). The different CN behavior observed in the two environments can be attributed to the absence of catalytic active centres (e.g., metal sites) required for the CO_2 electroreduction. Although bare carbon nitrides are currently used as photocatalysts for CO2 photoreduction, their use as electrocatalysts in CO2ER is less common.[108,109] In electrocatalysis, carbon nitrides are considered highly conductive support materials that can be properly doped and functionalized to promote CO_2 reduction with high current densities.[110]

Accordingly, in our case when Cu is deposited on CN (Cu@CN), CO_2ER activity is observed. In **Figure** 3-8, Cu@CN exhibited high overall current density in CO_2-saturated electrolyte, reaching -

110 mA cm^{-2} at -1.0 V (RHE), along with a relatively low onset potential of -0.6 V (*vs* RHE), indicating clear electrochemical activity towards CO_2 reduction. On the other hand, the addition of Cu on HAP did not yield the same effect: in the reference CN-free Cu@HAP binary materials no significant improvement was observed in the performance compared to bare HAP. The combination of HAP and CN, in the reference Cu-free binary material (HAP@CN), resulted in a higher current density (-40 mA cm^{-2}) than HAP and Cu@HAP, in both gaseous flows at the same onset potential (-0.9 V *vs* RHE). However, the increase in delivered current due to the presence of conductive scaffold is beneficial only to HER reaction, as the onset potential for CO_2 electroreduction is quite higher than the potential for H_2, which means that the Cu-free reference material is not a good catalyst for CO_2ER.

The results discussed so far for the binary reference materials clearly indicate that CN is an essential component to ensure electrical conductivity and thus enable efficient electron transport, whereas the presence of Cu is indispensable for directing these electrons toward CO_2 reduction. In the absence of Cu, CO_2ER is disfavoured in favour of the hydrogen evolution reaction (HER). By contrast, HAP, due to its insulating properties, does not appear to play a key role in the binary materials. However, a different and intriguing behaviour emerges from the analysis of the LSV results obtained for the ternary HAP_Cu@CN composite.

HAP_Cu@CN shows behaviour consistent with the trends identified in the binary reference Cu@CN composite. In CO_2-saturated electrolytes, the ternary HAP_Cu@CN material achieved significantly higher current densities compared to N_2-saturated conditions, displaying an onset potential of −0.8 V (vs RHE) and a progressive increase in current up to −55 mA·cm^{-2} at −1.0 V (*vs* RHE). Notably the presence of HAP plays a non-negligible role in modulating the CO_2 reduction pathways, as evidenced by the shift of the onset potential towards less cathodic values. Such an effect could lead to modified reaction kinetics or to the stabilization of intermediate species, ultimately facilitating the onset of CO_2 conversion at lower overpotentials and enhancing the overall catalytic efficiency of the composite system.

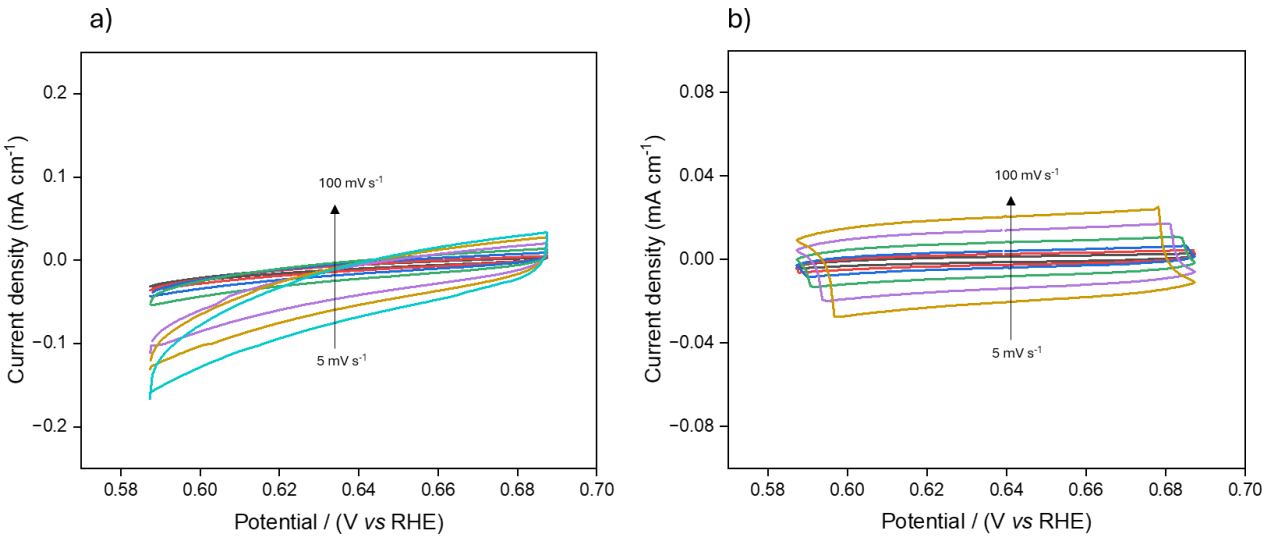

Figure 3-9 Cyclic voltammetry (CV) at different scan rates (from 5 to 100 mV s^{-1}) evaluated in non-Faradic region (-0.58 to -0.70 V vs RHE) for a) Cu@CN b) HAP_Cu@CN.

Cyclic voltammetry curves, displayed in **Figure** 3-9, were recorded in a non-Faradic region to evaluate the extent of double layer capacitance (C_{dl}) and electrochemical surface area (ECSA). These parameters are directly related to the electrochemically accessible surface and the kinetics of interfacial electron transfer, and thus provide insight into the overall electrochemical performance and effective conductivity of the material. By the slope of the scan rate *vs* the capacitive current (i_c) curve, the C_{dl} (**Figure** S-6-10) was obtained, and ECSA was calculated from the ratio C_{dl}/C_s, where C_s is the specific capacitance of the material. As carbon matrix is the main component of the composite (binary and ternary), a plausible value of 7.5 µF cm^{-2} as C_s was selected, based on studies on other carbon-based materials.[111] ECSA comparison among composites can be evaluated due to the acknowledgment that the ECSA is proportional to its C_{dl} value for electrocatalysts with a similar composition. Distinct electrochemical behavior can be observed for binary and ternary composites. Cu@CN exhibits higher charge storage capability, with a double layer capacitance (C_{dl}) of 0.3 mF, compared to the ternary one which shows a C_{dl} of 0.2 mF. The ECSA, estimated from the C_{dl} values, follows a similar trend: Cu@CN has higher area (0.04 cm^2) than HAP_Cu@CN that reaches 0.03 cm^2. These results indicate that the binary composite possesses a larger population of electrochemically active sites, which is consistent with its higher current densities and lower onset

potential observed in the LSV curves. The slightly reduced ECSA value is directly related to the insulator properties coming from the HAP which inhibit the passage of electrons limiting the overall electric double layer.

3.2.3. CO_2 Electroreduction test

From the electrochemical characterization, only Cu@CN and HAP_Cu@CN showed CO_2 reduction activity, as a matter of fact chronoamperometric tests (1h) were carried out on only these two composites. Starting with Cu@CN, it behaves as electrocatalyst[112], as evidenced by the results shown in **Figure** 3-10-a. Despite the inevitable contribution of the parasitic HER at low cathodic potentials (-0.5 V and -0.6 V vs RHE), Cu@CN exhibited clear electrocatalytic activity toward CO_2 reduction. The Faradic efficiency (FE) values for HER and CO_2ER are consistent with LSV results because beyond -0.6 V, the H_2 FE decreased below 50%, concomitant with the appearance of CH_4 as the main product. The selectivity reached approximately 60%, indicating that the material favors further reduction pathways, since CH_4 formation involves an 8-electron transfer process.[113] Cu@CN possesses strong reduction capability due to the high dispersion of copper species that enhances electron transfer properties, as it owns a large number of electroactive sites[114,115], in agreement with both LSV and CV analyses. HAP_Cu@CN showed modest current density (-55 mA cm^{-2} at -1.0 V *vs* RHE), due to the higher catalytic, Consistently with LSV measurements, after onset potential (-0.8 V vs RHE), CO_2ER occurred. As **Figure** 3-10-b shows, starting with low cathodic potential (-0.5 V and -0.6 V), H_2 is the principal product, as expected. After -0.7 V, two main products appeared during CO_2ER, methane and formic acid, particularly $HCOO^-$ was the main product at higher cathodic potential (60% at -1.0 V), limiting also HER. Though high cathodic potential, meaning high energetic supply for the catalytic system, CH_4 is quite limited (< 10%) at -1 V and formate is the main product.

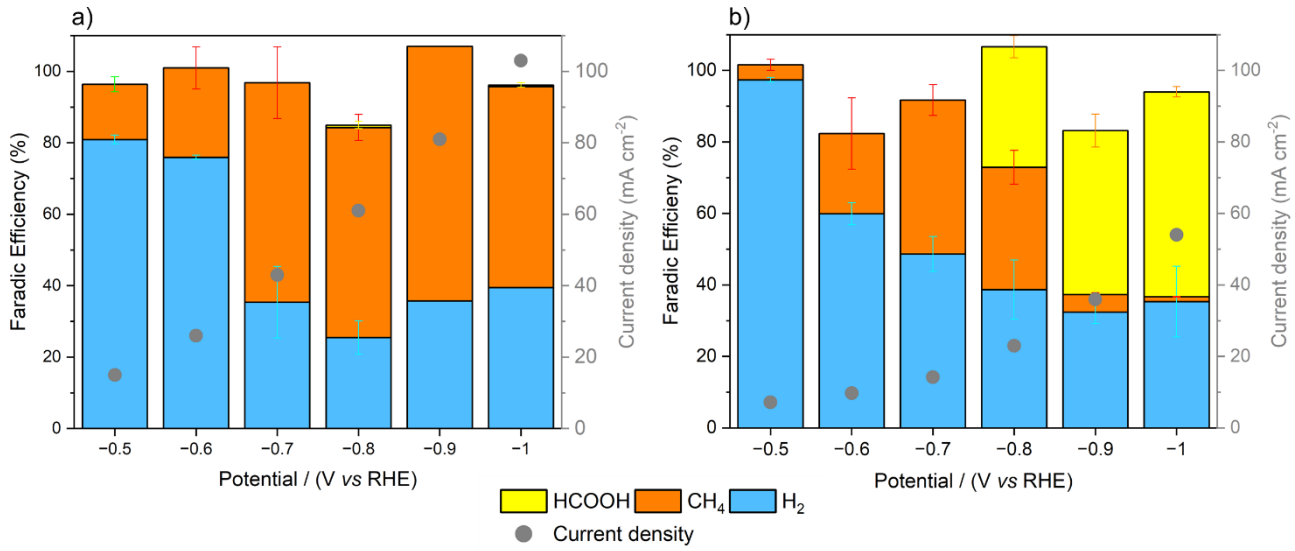

Figure 3-10 Faradic efficiencies and current densities on a) Cu@CN, b) HAP_Cu@CN evaluated in CO_2ER in $KHCO_3$ aqueous solution (0.1 mol L^{-1}), 1 h, RT.

In some cases for HAP_Cu@CN, noticeable fluctuations in FE can be observed. At -0.6, -0.7 and -0.9 V (vs RHE), FE does not reach 100%. Since the collected liquid showed no evidence of leakage, these deviations are likely attributable to limitations in gas collection. Specifically, the adhesion of gas bubbles to the surface of the inked carbon paper, potentially facilitated by the composites' porosity, may have hindered efficient gas recovery. As a result, the measured amount of CH_4 and H_2 were underestimated, leading to a lower apparent Faradaic efficiency. While experimental variability could be considered a contributing factor, reproducibility tests indicated a low relative error of 10-15% (**Figure** 3-10), effectively ruling out this possibility.

Also, kinetic studies of the two electroactive materials (Cu@CN and HAP_Cu@CN) were carried out. Tafel plots of the two composites were studied (**Figure** 3-11-a) and compared with each other. The admixing of hydroxyapatite in the composite did not limit the electron transfer ability towards CO_{2ads} species on the surface of the catalyst, as the values of the slopes of the Tafel lines (**Figure** 3-11-a) differed only of ca. 100 mV dec^{-1}. HAP-containing composite showed a Tafel line with a slope of 527 mV dec^{-1}, while a value of 664 mV dec^{-1} was observed for Cu@CN. The results are consistent with the CA tests: a lower Tafel slope value is an indication of a more active catalyst, as a smaller

overpotential is required to reach a higher current density.[116] In this case: particularly, HAP_Cu@CN favoured the formation of formate, enhancing the overall kinetics of the system. Catalytic results and kinetics evaluation observed with the ternary composites show that HAP plays a main role in the interfacial process between electrode and electrolyte.

Based on chronoamperometry (CA) tests and the evaluation of kinetic limitations through Tafel analysis, both Cu@CN and HAP_Cu@CN can be considered effective electrocatalysts for CO_2 reduction, exhibiting high selectivity toward methane and formic acid, respectively, without significant kinetic limitations. Before discussing the reaction mechanisms in detail, it is important to assess the energy efficiency (EE%) of these systems, as this parameter provides key insights into their economic viability and potential for scale-up beyond laboratory conditions. According to the literature, energy efficiency (EE%) is defined as the ratio between the energy effectively used to produce a given product and the total energetic input, taking into account both overpotential and ohmic losses.[117] The overpotential is evaluated with respect to the standard reduction potentials for methane and formic acid (0.2 V and -0.2 V *vs* RHE, respectively). Ohmic losses, associated with the internal resistance of the cell, are related to the geometric configuration of the system and were estimated from the high-frequency intercept of the Nyquist plot, yielding a value of approximately 20 Ω, in agreement with literature data for H-type cells used in CO_2ER.[118] The calculated energy efficiency for both composites ranges between 20 and 25% at -1.0 V (*vs* RHE), indicating that, at present, these systems are not yet economically competitive. This relatively low efficiency is mainly attributed to the cell configuration, as H-type cells with aqueous electrolytes are known to suffer from significant ohmic drops due to the distance between electrodes. Nevertheless, considering the promising catalytic performance, further improvements could be achieved by optimizing the electrochemical setup. In particular, the use of alternative configurations such as single cell setups, the use of solid electrolytes, or gas diffusion electrodes (GDEs) could significantly reduce ohmic resistance and enhance overall energy efficiency.

Prior to addressing the role of HAP in the catalyst, it is important to focus on some important steps of the HCOOH formation from CO_2, as these insights are crucial for understanding intermediate

stabilization and the resulting reaction selectivity. The conversion to HCOOH is strictly related to the initial binding of activated CO_2 ($*CO_2$) and stabilization of the intermediate on the catalyst. One of the most accepted hypotheses for the formation of oxygenated reduced product (such as formate itself) is the presence of a double proton-coupled electron transfer (PCET). Activated $*CO_2$ reacts through an electron and proton transfer (1st PCET) to form the activated intermediate formyl ∗OCHO. Furthermore, ∗OCHO undergoes another electron and proton transfer (2nd PCET) to form the intermediate ∗HCOOH, thus forming the HCOOH product. The stabilization of both the intermediates, which is a key aspect of CO_2ER pathways, is the result of an *interfacial effect* where ions of the electrolyte co-participate with functional groups of the catalyst to engage in non-covalent interactions (hydrogen bonding, for example) with the adsorbed species that help in stabilizing such intermediates/adsorbed species. These interfacial effects are localized in a so-called *microenvironment*, which is a region that arises in the proximity of the active site through localized solvation, hydrogen-bond networks, and confined ionic arrangements[119]. Thus, the active site emerges not as a static center, but as a dynamic micro-system defined by multiple and interdependent forces. As a matter of fact, various studies demonstrated that hydrogen bonds in this *microenvironment* between the key intermediates (e.g. *COOH) and the inorganic modifiers could stabilize the intermediate itself [120,121], leading to oxygenated reduced products.[122] The participants in the so-called microenvironment are necessarily, the catalytic surface and the CO_2 molecules, alongside the electrolytic layer in the proximity of the electrocatalyst: the electrolyte is the carrier for ion migration and reactants transformation, which should maintain as a proton donor with certain proton activity but cannot be too active to induce HER. Furthermore, catalytic surface can induce modification, not only at the CO_2 adsorbed, but also at the electrolytic interface in different ways such as suitable dissolution and interface enrichment capability for non-polar CO_2, ionic strength, local pH, electrochemical double layer (EDL) structure, interaction of electrolyte-catalyst and ion adsorption effects, etc.[123]

In this case, HAP plays a crucial role in directing selectivity toward formic acid, as its hydroxylated surface can interact with both dissolved CO_2 in an aqueous solution and with reaction intermediates,

forming an extensive network of hydrogen bonds at the interface, working directly at the electrode-electrolyte interface. Various studies demonstrated that hydrogen bonds between the key intermediate, *COOH, and the inorganic modifier could stabilize the *COOH intermediate, leading to oxygenated reduced products.[122] This suggests that the presence of HAP affects the local environment at the interface of the electrode and modulates the reaction pathways through stabilization of intermediates, which is the radical anion $CO_2^{\bullet-}$ upon CO_2 activation. The $CO_2^{\bullet-}$ radical anions could be stabilized through coordination of their oxygen atoms with the acid sites on the surface of HAP: indeed, Ca^{2+} and/or hydroxyl vacancies can establish electrostatic interactions with the partially negative O atoms, thus leading to coordination and stabilization. Furthermore, proton transfer might be facilitated due to both the stabilization and proximity of metal active sites. DFT studies analysed the correlation of presence hydrogen bonding which is greatly beneficial for proton migration.[124]

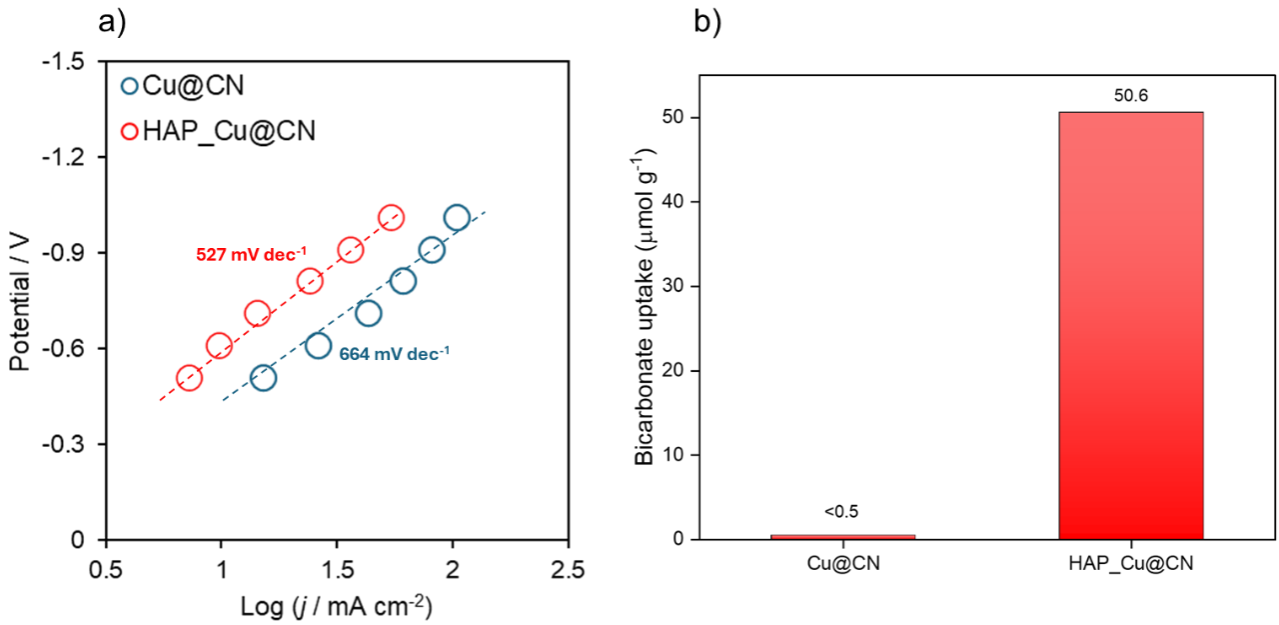

Figure 3-11 **.** Tafel plots of copper-based composite materials from cathodic polarization of LSV plots a) and bicarbonate uptake by Cu@CN and HAP_Cu@CN at 30 °C determined by retro-titrations b)

Furthermore, it is important to rationalize and study the interaction between CO_2 and the surface catalyst as it is strongly influenced by the local availability of dissolved carbon species. CO_2 cannot

serve as the direct carbon source for the reduction occurring at the cathode surface, since it first dissolves forming $CO_{2\ (aq)}$. The $CO_{2(aq)}$ species are the ones adsorbed onto the catalyst and then activated for the reduction reaction. But it is important to emphasize that when gaseous CO_2 is bubbled into an aqueous electrolyte, it enters a dynamic chemical equilibrium involving $CO_{2(g)}$, $CO_{2(aq)}$, and HCO_3^- species. Consequently, any variation in the concentration or consumption of one of these species, such as depletion of $CO_{2(aq)}$ due to reduction, inevitably perturbs the equilibrium, inducing shifts in the relative distribution of the others (HCO_3^- and then $CO_{2(aq)}$). This interconnected speciation is therefore central to understanding CO_2 adsorption, activation, and reaction pathways at the electrode-electrolyte interphase. Furthermore, the equilibria between CO_2 and bicarbonate are relatively fast which buffer the pH in the bulk electrolyte. Although the buffering bicarbonate electrolyte minimizes the increase in pH, H^+ in the interfacial region can be rapidly depleted leading to the promoted local pH after applying high potential. When the pH above 9.9, the concentration of the dissolved CO_2 decreases rapidly and thus the concentration ratio of $[CO_2]/[H^+]$ which favours the competing HER side reaction.[125] Spectroscopic studies combining fast Attenuated Total Reflectance (ATR-SEIRAS) and isotopic labeling, have provided important insights into CO_2ER mechanisms, revealing the key role of interfacial equilibria in governing surface-reactive species.[126]To evaluate the ability of the materials to interact with these dissolved species, bicarbonate uptake tests were performed as explained in the paragraph 2.2.3. The results, depicted in **Figure** 3-11-b revealed that Cu@CN exhibited negligible bicarbonate uptake, whereas the presence of hydroxyapatite significantly enhanced the adsorption capacity, with the HAP_Cu@CN composite reaching 50.6 μmol g^{-1} at 30 °C. The enrichment of bicarbonate species at the solid-liquid interface increases the local concentration of $CO_{2(aq)}$ near the electrode surface, thereby facilitating its subsequent activation and reduction, as demonstrated by Berben et al.[127] The presence of HAP can participate in different actions, even simultaneously enhancing the selectivity towards formate: stabilization of intermediate, pH buffering, coordination with HCO_3^- ions.

While the role of HAP in the ternary composite has been thoroughly discussed in relation to its ability to promote formation, the high FE towards CH_4 for the binary composite, Cu@CN, deserves further

attention, as it also helps to consolidate the key aspects of using HAP as modifier. Since formate (HCOO*/HCOO-) is an intermediate to methane formation, it is reasonable to assume that formate is also generated using Cu@CN as catalyst, but it is continuously reduced. The reduction of formate to methane requires further electron and proton transfers steps, and the results obtained with HAP_Cu@CN suggest that these steps are partially inhibited in the presence of hydroxyapatite. As for the electron transfer step, HAP is an insulating material which slightly decreases electron transfer. This behaviour is confirmed by the lower current density in LSV analyses for HAP_Cu@CN compared to Cu@CN; as a consequence of the reduced electron transfer, formate becomes the main product for the ternary composite. Conversely, the highly conductive and catalytically active Cu@CN composite enables efficient charge transfer, promoting further reduction of the formate intermediate and ultimately leading to methane formation. Proton transfer also plays a critical role, as methane formation requires a high availability of protons and a suitable local pH at the electrode-electrolyte interface. In the case of HAP_Cu@CN, this condition is not fully satisfied. HAP acts as buffer material stabilizing the local pH and preventing the formation of acidic microenvironment. While this buffering behaviour is beneficial for stabilizing intermediate and for shifting the equilibrium towards bicarbonate ions, it simultaneously limits the proton availability for the subsequent reduction steps. In contrast, with Cu@CN composite, no buffering effect occurs, allowing the pH to shift more favourably for the reduction pathways involving multiple proton transfers. As a matter of fact, Varela work[128] found that CO_2 reduction to CH_4 is dependent of pH, consistent with CO* protonation as the rate-limiting step. Despite the high proton concentration, hydrogen evolution is not dominant in this case, likely due to the high activity of copper sites, which favours CH_4 formation.

Taken all the effects, the presence of H-bond donors, moieties able to stabilize $CO_2^{\bullet-}$, intrinsic insulating nature, pH buffering effects in HAP collectively inhibit proton and electron transfer for the deeply reduced product such as CH_4. Consequently, in the presence of HAP, the reaction pathway is steered toward formate, which is preferred thanks to the presence of H-bond donors and moieties able to stabilize $CO_2^{\bullet-}$, whereas in Cu@CN system, the absence of buffering and insulating effects enable further proton-electron transfer, allowing methane formation.[123]

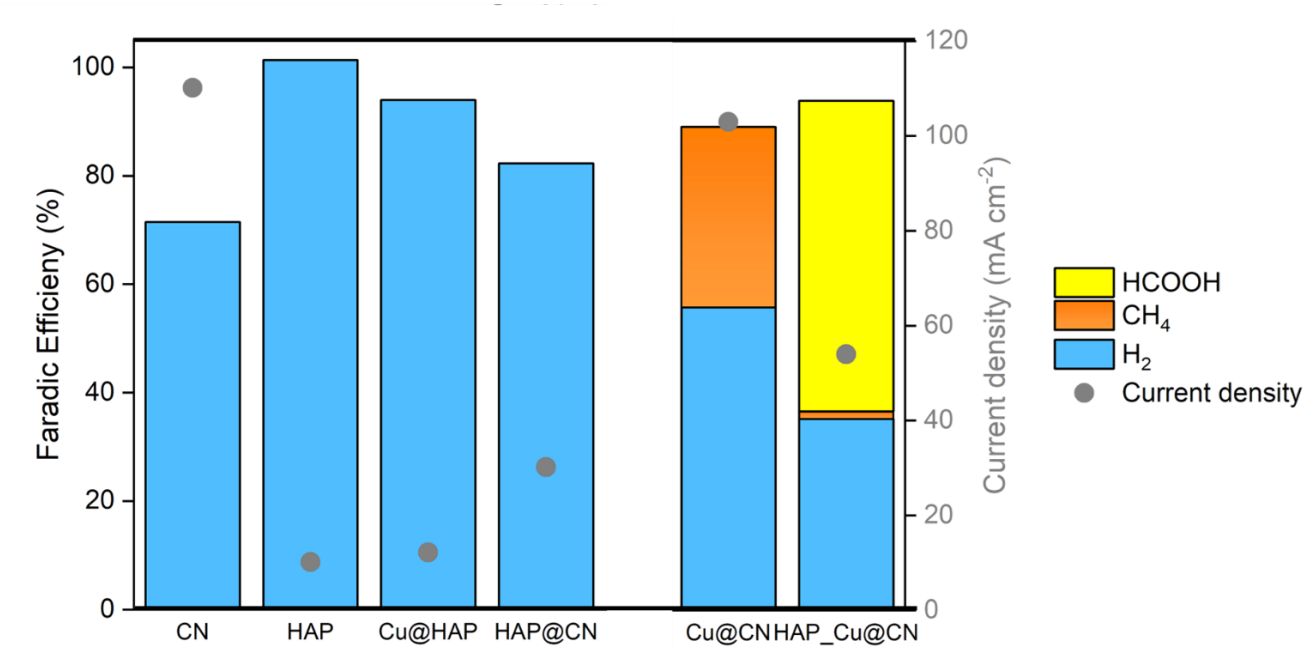

Figure 3-12 Faradic efficiency on different materials evaluated in CO_2ER in $KHCO_3$ aqueous solution (0.1 mol L^{-1}), 1 h, RT at fixed potential of -1 V (vs RHE).

To further emphasize the added value of the binary and ternary composites, CA tests were performed on a set of reference materials. Even though LSV profiles already suggested the absence of any significant CO_2 reduction activity, chronoamperometric tests were performed by applying different cathodic potentials to evaluate their electrocatalytic behaviour under CO_2 reduction conditions. The FEs in all applied potential range are depicted in **Figure** S-6-11. A further focus was placed on the potential of –1.0 V (vs RHE), as it represents the most cathodic condition applied in this study and is theoretically associated with the highest CO_2 conversion rate. The results of CO_2ER catalytic tests at applied potential of -1.0 V (vs RHE) are shown in **Figure** 3-12.

When CN was used as the electrocatalyst, only H_2 was detected due to the absence of metallic active sites. Particularly, FE to H_2 was not 100%, but reached about 70%, probably due to the accumulation of H_2 bubbles on the inked coated carbon paper, which hindered efficient gas release and consequently collection and detection. The quantities of H_2 gas were underestimated, leading to a lower apparent FE. For two HAP-containing reference materials (HAP and HAP@CN), H_2 was again the only detected product but with a much lower current density of -10 mA cm^{-2} (meaning lower

conversion), reflecting their intrinsic insulating properties. The same behaviour is observed for the last HAP-based reference composite, Cu@HAP , as no CO_2 reduction activity occurred. The electron transfer to copper sites appeared to be strongly hindered by the insulating features of HAP, as further confirmed by the shape of CV curves. As a result of this limited charge transport and the low current densities**,** the hydrogen evolution reaction (HER) remained the only active process**,** favoured by its lower energy requirement compared to CO_2 reduction.

Finally, on ternary composite material (HAP_Cu@CN), long-term stability test (**Figure** S-6-11) was performed up to 8 h at a cathodic potential of -1.0 V. The composite showed a high initial current density with a very noisy background indicating an activation phase, which stabilized after a short period. Then, gradually, the current stabilized around -60 mA cm^{-2} over 7 hours, with a very slight decrease over the entire monitoring period. Although copper-based catalysts are known to be prone to passivation, which can reduce the electrochemical activity over time,[129] the long-term stability test showed only a slight decrease in current (approximately 10% of the initial value), indicating that the studied composite can be considered stable over the tested period.

Additional tests were also carried out on a physical mixture of Cu@HAP and CN to assess the influence of interfacial contact between the components. In this case, no chemical or structural integration occurred among the phases, unlike in the one-pot synthesized composite. The deposition of the mixture onto the carbon paper electrode was less homogeneous and more difficult to control. Consequently, the LSV curves (**Figure** S-6-12-a) showed no significant differences between N_2 and CO_2-saturated electrolytes, anticipating in some ways the absence of CO_2 reduction activity as confirmed by CA tests, displayed in **Figure** S-6-12-b. In the absence of such contact, as in the case of the physically mixed CN-Cu@HAP, the electron transfer between the catalytic sites and the conductive carbon matrix is strongly hindered. In one-pot synthetized material, the enveloping of carbon scaffold around HAP nanorods and Cu nanoparticles likely acts as a junction, enabling a continuous flow of both electrons and adsorbed reagents across the electrocatalyst surface. In the composite (HAP_Cu@CN), the HAP-CN framework gives rise to confined interfacial domains that enable efficient charge and mass transport, establishing a well-integrated composite, confirmed by TEM analyses, seems to be crucial to ensure effective interaction between the catalyst and the

reagent. These interfacial regions support electron transfer through the CN network, while protons (H^+) interact with CO_2 molecules adsorbed and stabilized on the phosphate groups of HAP. Such a synergistic interplay between the components effectively enhances the CO_2 electroreduction reaction (CO_2ER). On the other hand, in the mechanical mixture, such interfacial coupling is absent, and the synergistic mechanism cannot be established. While electron transfer remains thanks to the CN framework, CO_2 molecules could not be in the proximity of these regions, making H^+ ions, which also are the most abundant species in the electrolytic interface, the only reducible species and thus leading to the production of H_2, as confirmed by CA tests.

Another important factor that needs to be evaluated is the amount of HAP present in the composite, which requires the same attention as the presence of intimate contact, discussed above. Since HAP is intrinsically an insulating material, the content is expected to influence the reaction pathways through limiting the current in the electrocatalytic setup or steering the reaction selectivity. Even though previous works[55,56,87] reported that 10-20 wt% HAP in the final composites showed optimal results in terms of conductivity, activity, and selectivity, three samples with different amounts of HAP (5, 25, 50 wt%) were synthesized and tested in CO_2ER to confirm the influence of hydroxyapatite in our electrocatalytic systems. The CO_2 electroreduction activity of these composites was first evaluated through LSV analyses. The LSV curves for 5HAP_Cu@CN, 25HAP_Cu@CN, and 50HAP_Cu@CN are shown (**Figure** S-6-13). In all cases, higher current densities were observed in N_2-saturated solutions compared to CO_2, indicating that the HER prevails under these conditions. The insulating nature of hydroxyapatite (HAP) was reflected in the trend of current density: as the HAP content decreased, the current increased, with 5HAP_Cu@CN reaching 50 mA cm^{-2} at -1.2 V (vs RHE), as highest value among the three composites. Notably, the values remained lower than the one of binary Cu@CN and ternary HAP_Cu@CN, likely due to incomplete homogenization of the three components. Consequently, the material behaves more like a quasi-mechanical mixture, where phase segregation limits interfacial contact and impairs efficient electron transport. Analysis of the onset potentials revealed a shift toward more negative values of potential for all samples. Notably, only 5HAP_Cu@CN displayed a slightly more favourable onset compared to Cu@CN and

HAP_Cu@CN, suggesting limited CO_2ER activity. 25HAP_Cu@CN and 50HAP_Cu@CN showed highest value of onset potential around -0.9 V and -1.0 V meaning high energy requirements for CO2ER which are not comparable to the ones of Cu@CN and HAP_Cu@CN (-0.6 and -0.8 V vs RHE). Chronoamperometry (CA) tests were performed to validate the LSV observations, with Faradaic efficiencies reported in **Figure** S-6-14. Hydrogen remained the primary product across all potentials for the three composites, consistent with LSV trends. A comparison among the samples highlight the critical role of HAP loading in steering the product selectivity (**Figure** 3-13). Composites with HAP below 10 wt% behaved similarly to Cu@CN, achieving approximately 30% selectivity for CH_4 and HCOOH. At 10 wt% HAP, as in HAP_Cu@CN, formate became the dominant product, attributable to an optimal balance of HAP properties, including intermediate stabilization, pH buffering, optimal conductivity. At higher HAP contents, however, the insulating effect overcame the modifier role, suppressing CO_2ER and favouring HER. Overall, these results demonstrate that HAP loading is a decisive parameter, as non-optimal amounts adversely affect charge transfer and catalytic performance.

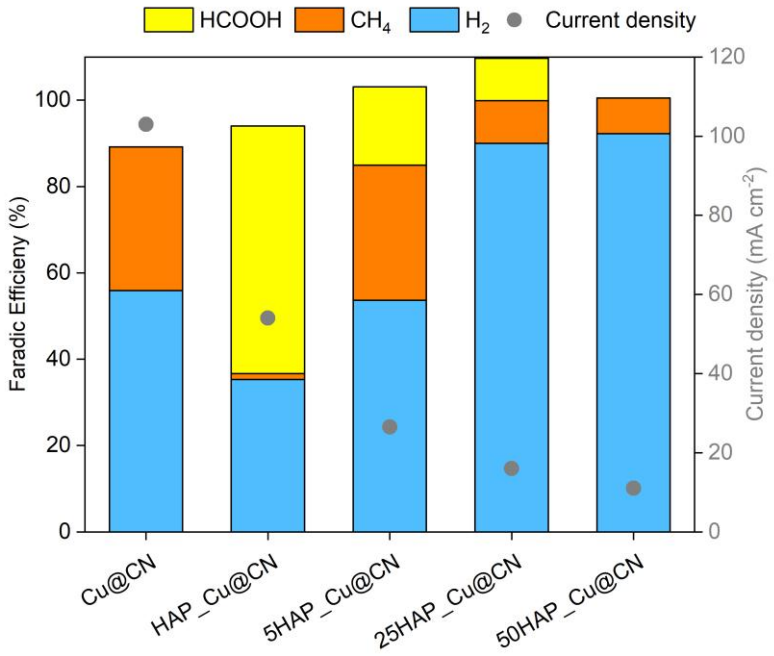

Figure 3-13 Faradic efficiency results for composites with different HAP content evaluated in CO_2ER in $KHCO_3$ aqueous solution (0.1 mol L^{-1}), 1 h, RT at fixed potential of -1 V (vs RHE).

Finally, after assessing the key role of HAP and the benefits associated with the proper incorporation of an apatite-based material, it is useful to consider how HAP_Cu@CN and Cu@CN position themselves within the broader landscape of CO_2ER electrocatalysts. Overall, the composites presented in this work show electrocatalytic activity and selectivity comparable to other copper-supported catalysts reported in the literature, as summarized in **Table** 3-4. In particular, Cu@CN and HAP_Cu@CN displayed relatively low onset potential and achieve high faradaic efficiency for methane and formate (>50%) at -1.0 V (vs RHE). However, when examining formate production in other composites that do not include HAP, several differences emerge. First, the carbon supports commonly reported in the literature are typically commercial materials characterized by well-defined porosity, ordered structures and a high degree of graphitization. These structural features are known to influence CO_2ER activity and selectivity. In contrast, the carbon matrix used in this study was obtained though the pyrolysis of a covalent organic framework, leading to the formation of graphitic domain embedded within an overall amorphous structure with the aim to form a homogenous and highly linked composite.

Second, in many literature examples, copper is deposited onto carbon supports though controlled techniques such as electrodeposition methods (e.g., square-wave electrochemical redox cycling) or by immobilizing commercial nanoparticles with well-defined particle sizes, surface morphologies, and exposed crystal facets. These parameters are well known to directly affect catalytic selectivity toward carbon reduced products. [90,130,131]In the present dissertation, copper wad incorporated though a one-pot synthetic procedure, without the same level of control over particle size of surface characteristics. Finally, it should also be considered that experimental operating conditions can strongly affect product selectivity. For instance, in high pressure electrolyzer, FE for formate exceeding 80% have been reported under elevated CO_2 pressures (30-60 atm), enhancing CO_2 dissolution levels in the electrolytic solution. In comparison, HAP_Cu@CN demonstrates promising CO_2ER performance under atmospheric pressure conditions. Moreover, the synthetic approach adopted here enables a highly integrated composite structure, promoting intimate contact between the different components, which may contribute to the observed catalytic behaviour.

Table 3-4 Comparative view of some promising electrocatalytic materials in the CO_2ER containing copper.

Electrocatalyst	Support	Electrolyte [a] / *mol L^{-1}*	Current density / *mA cm^{-2}*	Faradic Efficiency / *%*	Ref.
Cu	Carbon nanotubes (CNT)	0.5 mol L^{-1}	10 (-1.5 V_{AgAgCl})	28 $_{HCOOH}$	132
Cu NP	CNT	0.5 mol L^{-1}	15 (-1.2 V_{RHE})	40 $_{HCOOH}$	133
Cu NP+HAP	Graphene nanosheet	0.5 mol L^{-1}	20 (-1.2 V_{RHE})	50 $_{HCOOH}$	87
Cu NP	N-doped carbon	0.1 mol L^{-1}	2 (-1.0 V_{RHE})	40 $_{HCOOH}$	134
Cu	PANI	0.1 mol L^{-1}	30 (-1.0 V_{RHE})	72 $_{C2}$	135
Cu_2O (SW)	Cu	0.1 mol L^{-1}	1	27$_{HCOOH}$ (Under 1 atm of CO_2)	136
Cu_2O (SW)	Cu	0.1 mol L^{-1}	0.1	98 $_{HCOOH}$ (Under 60 atm of CO_2)	136
Cu@CN	Carbon nitride	0.1 mol L^{-1}	120 (-1.0 V_{RHE})	60 $_{CH4}$	This work
HAP_Cu@CN	Carbon nitride	0.1 mol L^{-1}	110 (-1.0 V_{RHE})	60 $_{HCOOH}$	This work

a. $KHCO_3$ as the electrolyte solution

3.3. Concluding remarks

Across this Chapter, CO_2ER has been addressed as an important strategy for CO_2 remediation. In particular, CO_2ER can be viewed as a strategy for combining process innovation and material engineering. On one hand, bioelectrochemical systems offer a biologically assisted route for CO_2 conversion to methane, where microorganisms and tailored cathodic materials enable power-to-gas concepts. On the other hand, purely electrochemical approaches focused on rationally designed composite materials to achieve deeper control over interfacial mechanisms, charge transport leading to governed product selectivity.

Firstly, innovative biochar-based composite cathodes incorporating copper and hydroxyapatite were presented in this Chapter. The materials were fully characterized and tested in BES cells. The marked differences in methane production observed among the various biocathodes (single, binary, and ternary materials) highlight the pivotal roles of Cu nanoparticles and hydroxyapatite dispersed on the biochar surface in catalysing CO_2 reduction. Beyond catalytic effects, hydroxyapatite also contributed to interfacial stability and functionality, highlighting the potential of multicomponent architectures as a platform for next-generation biocathodes, where surface chemistry, porosity, and component distribution are jointly optimized to maximize microbial activity, reaction rates, and selectivity. Finally, despite competitive catalytic activity, these materials showed some agglomeration of phases, which hindered the overall capacities. For example, it is noteworthy that the observed performance was determined primarily by the external surface area of the cathode, while the internal porous structure of the biochar remained largely unfunctionalized. Therefore, further efforts to have a more homogeneous dispersion of components in the composite can lead to higher catalytic activities.

To overcome these main limitations, an innovative synthetic route for having a homogeneously dispersed components on the composite was presented. Particularly, a one pot strategy, starting fro COF precursor, was applied to produce binary (Cu@CN) and ternary (HAP_Cu@CN) functional composite materials comprising copper nanoaggregates and hydroxyapatite nanorods. Through structural, morphological, and spectroscopic analyses, the composites showed firstly COF features

and after pyrolysis, carbon nitride characteristics. In particular, the analyses revealed the coexistence of carbon-nitrogen functionalities and copper. Additionally, the ternary material (HAP_Cu@CN) exhibited the characteristic features of HAP, confirming its thermal and chemical stability. Notably, HAP was identified as promoter for carbon nitride formation, due to its anchoring properties that facilitate condensation and interlayer stacking of molecular precursor. For all these reasons, it results that the composite had features of carbon nitride totally wrapped around HAP nanorods, where copper is also distributed as nanospheres, indicating an intimate contact among the three phases. The final materials presented also high conductivity due to the presence of graphitic patterns and copper sites: the high dispersion of copper and the conductive nature of the carbon support collectively favoured efficient charge transport within the composite. Cu@CN and HAP_Cu@CN were then tested in CO_2ER, demonstrating interesting catalytic properties: the first displayed high current densities and low onset potential, indicating strong catalytic activity and efficient electron transfer, converting CO_2 towards CH_4. On the other hand, HAP_Cu@CN exhibited a slightly higher onset potential but showed selectivity towards formate. The main difference was associated once again with the presence of amphoteric HAP: the typical exposure of HAP surface enhanced adsorption capacity towards CO_2, it stabilized intermediates of reaction, and it steered the selectivity towards formate, through hydrogen bonding, ionic interactions, and pH buffering effects. Overall, the combination of copper, carbon nitride, and hydroxyapatite creates a synergistic system in which structural design and interfacial chemistry jointly determine catalytic efficiency and product distribution in CO_2 electroreduction.

The purpose of the multicomposite material in a one-pot technique was to improve the composites made using a multi-step process that suffered from copper phase or HAP phase segregation. The one-pot strategy assured a very close contact among the three phases. A more synergistic effect on the CO_2ER resulted from the intimate contact: i) from a design standpoint, the charge transfer could flow easily through the conductive components, decreasing the overall overpotential; ii) once the CO_2 was activated and stabilized, the proximity of copper active sites led the reduction process in favoured way. Furthermore, the optimal integration of components improved the structural stability, sustaining high activity over time throughout the reaction. Moreover, this synthetic strategy enables

the modular integration of key components into binary or ternary materials, allowing the catalytic selectivity to be tailored toward different target products and, consequently, toward distinct application domains, such as energy conversion or chemical manufacturing.

Surely, as future perspective, the long-term durability and stability of the catalysts should be systematically investigated. Long time electrochemical tests are necessary to evaluate possible degradation phenomena, including structural changes, copper leaching, or modifications of the carbon nitride framework. Alongside these tests, post-reaction characterization would provide valuable insights into structural and chemical changes occurring during operation. These studies could also support the design of more robust composite catalysts able to maintain activity and selectivity during prolonged operation.

On the other side, to further integrate sustainability principles into CCU technologies and based on the results discussed in this Chapter, two possible directions emerge for the development of composite materials for CO_2 remediation. On one hand, further work may continue along a multiprotocol approach (the one introduced in 3.1), focusing on improving the morphological and porous properties of biochar to achieve a more homogeneous dispersion of the active phases, an aspect addressed in the following Chapter. On the other hand, an alternative strategy would be further developing the one-pot approach, exploring different molecular precursor for CN scaffold using greener and cost-effective reagents and solvents to enhance the overall sustainability of the process; this last direction was not investigated in the present dissertation.

Focusing on the first route, namely the multistep protocol, an additional opportunity to improve sustainability lies in the reconsideration of both the carbon and hydroxyapatite sources. In this Chapter, the carbon scaffold was derived from a pyrolysis of maize stalk or from the annealing of covalent organic framework (CIN-1). Additionally, the latter came from a long synthetic route that used different chemical reagents with significant environmental impact and cost, resulting in a material that cannot be considered fully sustainable. Similarly, the hydroxyapatite phase used was synthetized using commercial saline precursors in a co-precipitation method. In the following chapter, a different biochar was studied from sugarcane (biomass with larger environmental

availability), and it is not obtained from a synthetic route; for inorganic phase, hydroxyapatites were obtained from ashes of waste-to-energy plant with different protocols. All the materials were first studied separately to identify their optimal physicochemical characteristics and later considered as potential components of a composite catalyst for CO_2 electroreduction.

4. Waste-to-Resource strategies for improved and sustainable materials

4.1. Carbon materials from natural sources

As described in the previous paragraphs, two different carbon scaffolds for CO_2ER and bioelectromethanogenesis were made and utilized. The composite electrocatalyst used in the bioelectromethanogenesis tests included a biochar produced by pyrolysis of maize stalk. Two key limitations of this material were poor surface area and predominance of microporosity, which arise from the high fibrous texture of the pristine biomass. On the other hand, the carbonaceous support (CN) utilized in CO_2ER, while highly conductive, was prepared using costly bulk chemicals and several solvents in contrast with the fundamentals of sustainability.

Looking for new biochar that are both highly functional, conductive, and sustainable is one of the challenges of scientific communities. Among biomasses, sugarcane is one of the most widely cultivated crops to produce alimentary goods (sugar) and energetic sources (bioethanol). After processing, sugarcane waste was often burnt, enhancing greenhouse gases emission (e.g. CO_2). To decrease the environmental impact, the interest on valorisation of residues is nowadays increasing. For this purpose, one of the most used processes to transform sugarcane waste into added value materials is its controlled pyrolysis.

In collaboration with Ricerca sui Sistemi Energetici-RSE S.p.A., an experimental procedure for the pyrolysis of sugarcane waste was optimized to obtain biochar. Two different pyrolysis temperatures (600 and 900°C) were studied to evaluate the morphological and structural features of the obtained biochars (labelled as ECCO_600 and ECCO_900).

4.1.1. Structural and morphological features of ECCO biochar

Two biochar were obtained from the pyrolytic treatment of sugarcane waste. This biomass residue consists of bagasse and field waste, which are fibrous residue and leaves, respectively. Usually, the first residue has been used as a source for carbonaceous supports because it is a lignocellulosic biomass rich in cellulose and hemicellulose with a low amount of lignin (20 wt %) and a high moisture content. Generally, the co-presence of high content of water and cellulose structure provides a porous structure with high surface area, even after pyrolytic treatment at high temperatures (> 600°C). Two different treatments were carried out on the sugarcane bagasse to evaluate the main differences induced by pyrolysis temperature (600 and 900°C).

ECCO_600 and ECCO_900 were characterized through different techniques to evaluate their morphological features. From SEM images in **Figure** 4-1, both ECCO_600 and ECCO_900 exhibit a highly lamellar structure, derived from the collapse of vegetal cell walls. Pyrolysis at high temperatures leads to the presence of a different pore distribution, comprising macropores and mesopores. Moreover, fractures are visible in some agglomerates of biochar, likely due to the pyrolysis temperature, which led to initial breaking of the lignocellulosic structure and might enhance the exposed area.

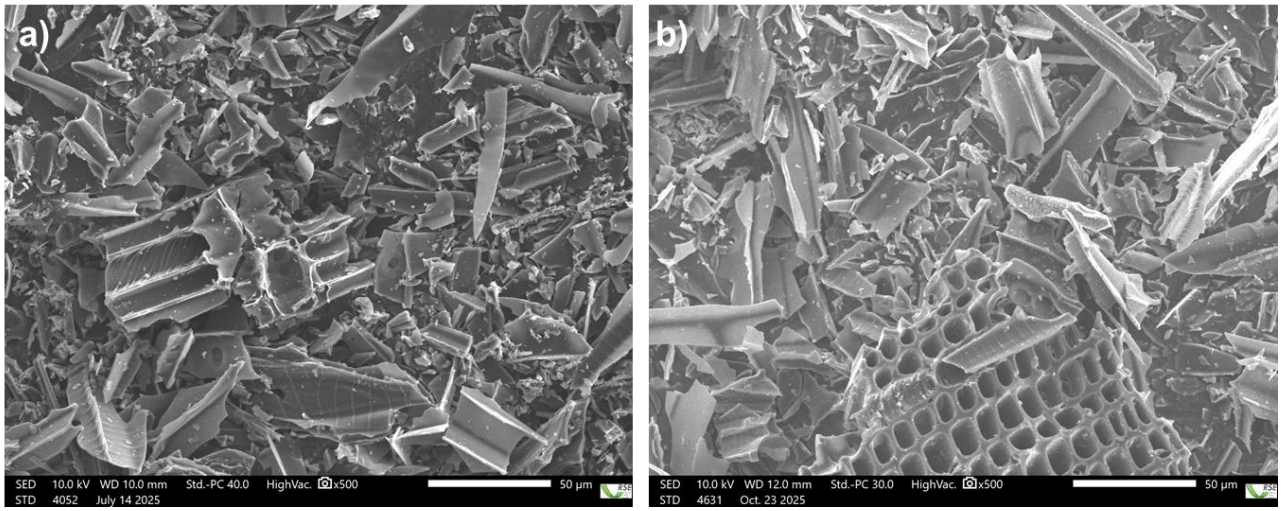

Figure 4-1. SEM images at 500x magnification (50 µm as scale) of a) ECCO_600 and b) ECCO_900.

EDX analyses (**Figure** 4-2), coupled with SEM imaging, revealed the presence of only C and O elements, assessing the absence of impurities in the sugarcane waste. Interestingly, the decomposition of cellular components during pyrolytic treatment resulted in an enrichment in carbon compared to the pristine biomass (the O/C molar ratio of sugarcane bagasse is typically 0.9-1).[137]

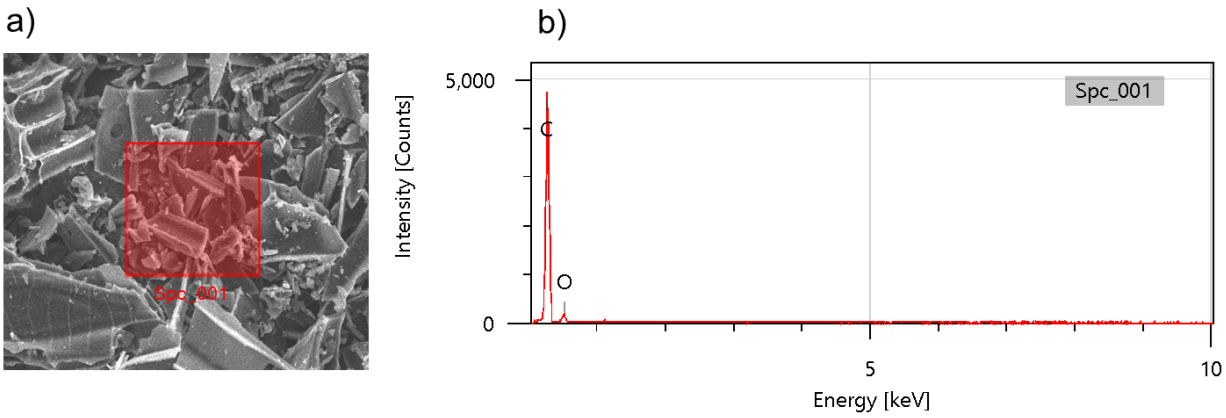

Figure 4-2 Representative SEM image of ECCO_600 a) with relative EDX spectrum (b). The red square identifies the zone where EDX spectrum was recorded.

The surface morphology was studied by N_2 adsorption-desorption isotherms. The results are reported in **Table** 4-1. The ECCO_600 and ECCO_900 materials presented specific surface areas (SSAs) of 223 and 125 $m^2\ g^{-1}$, respectively. As expected, increasing the pyrolysis temperature led to a decrease in SSA, due to pore collapse and agglomeration phenomena induced by high-temperature processing. For comparison, the previously obtained maize stalk-derived biochar (prepared by pyrolysis at 900°C) had a relatively low SSA (9 $m^2\ g^{-1}$), increasing by a factor of 10 when the biomass source was changed. This improvement can be attributed to the intrinsic structure of lignocellulosic sugarcane, which promotes a more ordered porous network and exposes a greater surface area.

Table 4-1 Specific surface area of biochar determined by N_2 adsorption-desorption isotherms.

Sample	Specific Surface Area[a] $m^2\ g^{-1}$
Maize Stalk Biochar	9.0±0.1
ECCO_600	223±15
ECCO_900	125±1

a. Evaluated by BET 2-parameter. The standard deviation was obtained from error propagation on Eq. 2-2, starting from the experimental value of V_m (and its relative standard deviation).

To further investigate the structural features, XRPD analyses were performed on the materials. The **Figure** 4-3-a displayed the experimental XRD patterns. Upon pyrolysis, both ECCO materials displayed a broad background due to the presence of amorphous region in the materials. However, the two characteristic reflections of graphitic carbon can be detected: the first at around 2θ of 25° and the second at around 45°, corresponding to the (002) and (100) reflections of graphitic domains, respectively. ECCO_900 exhibited slightly sharper peaks compared to ECCO_600, confirming that higher pyrolysis temperatures promote the formation of larger graphitic domains within the carbon structure. Raman spectroscopy was employed to evaluate the degree of graphitization of the biochar materials, with the intensity ratio of the D and G bands (I_D/I_G) serving as an indicator of structural order (the lower the I_D/I_G ratio, the higher the structural order and the graphitic character).(**Figure** 4-3-b). The spectra of ECCO_600 and ECCO_900 displayed the characterist

ic D-band and G-band at approximately 1350 cm^{-1} and 1580 cm^{-1}, respectively. The D-band is associated with structural disorder, while the G-band corresponds to ordered graphitic domains. ECCO_900 exhibited a lower I_D/I_G ratio (0.9) compared to ECCO_600 (I_D/I_G = 1.4), confirming a higher degree of graphitization directly related to the higher pyrolysis temperature. These Raman results are consistent with the XRPD patterns and EDS results, indicating that the pyrolysis of sugarcane bagasse at 900 °C provides a biochar material possessing a low oxygen content and a well-ordered graphitic structure, which generally corresponds to enhanced electrical conductivity.

These structural and electronic properties indicate that the ECCO_900 material may hold significant potential for electrocatalytic processes and bioelectromethanogenesis applications.

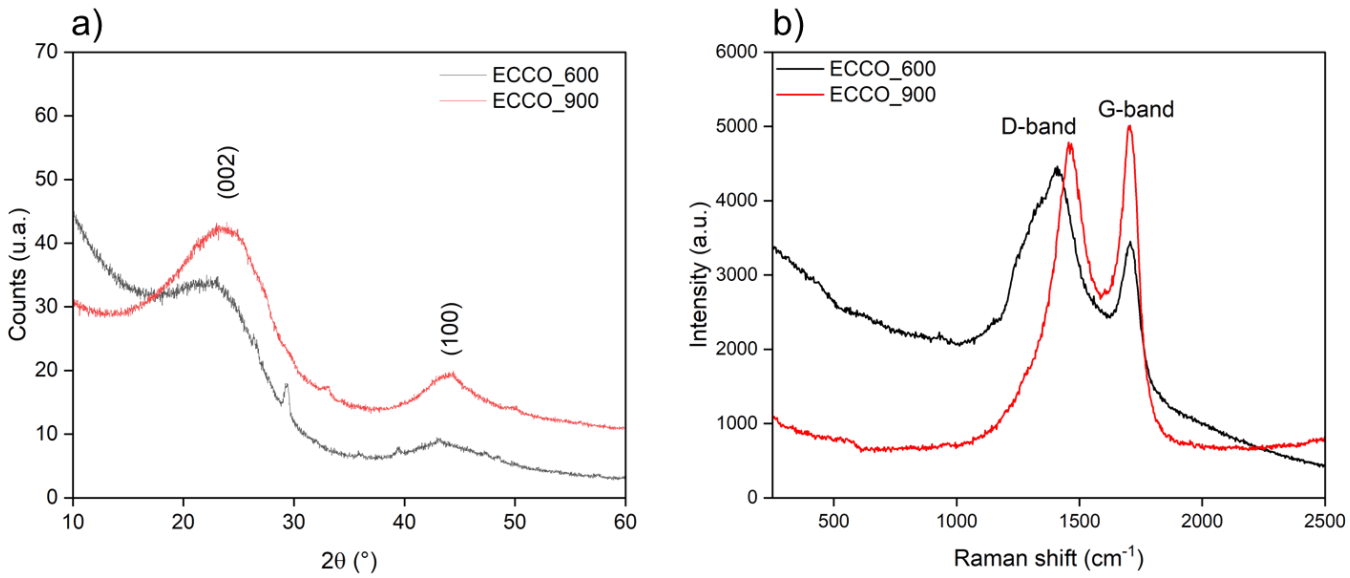

Figure 4-3 XRPD (a) and Raman spectra (b) of ECCO_600 and ECCO_900

4.2. Hydroxyapatite from ashes

The application of sustainability principles in material preparation and material engineering has become central and a growing topic of attention for society and scientific community. Particularly, the recovery of materials from waste is increasingly discussed in the context of sustainable production. One of the most abundant wastes is biomass derived from agricultural residues, food waste, and municipal sewage. Incineration plants for biomass and biomass wastes have been a proper way to deal with large amounts of discards. As for the organic part of wastes is transformed into gases and thermal energy, inorganic residues have been collected as ashes, usually released in the environment. The inorganic ashes represent a different source for inorganic materials, such as calcium phosphate solids.[138] Starting from the already known extraction process of hydroxyapatite (HAP) from eggshell and bones, incineration ashes, can be exploited as a valuable feedstock for HAP recovery. In collaboration with Centrale Termoelettrica Enomondo Herambiente/Caviro Extra and Istituto di Scienza, Tecnologia e Sostenibilitá per lo Sviluppo dei Materiali Ceramici, CNR-ISSMC from Faenza, four different hydroxyapatites have been extracted from ashes (with four different methods), fully characterized, and tested as catalysts. Furthermore, correlations between extraction parameters and morphology/surface characteristics have been assumed. Regarding the surface characteristics of hydroxyapatite, as it possesses a multifunctional surface and crystal lattice flexibility, HAP is suitable for both catalytic applications and environmental remediation processes.[139,140] Finally, to understand the additional value of sustainable hydroxyapatite, a comparison between the ashes-based HAPs and synthetic HAP has been made.

4.2.1. Extraction procedure, compositional and morphological characterization

The inorganic ashes of the thermovalorization plant based in Faenza, containing silica (SiO_2), calcium oxide (CaO), phosphate oxide (PO_x), and metal residue (Al, Fe, Mg and so on), have been treated to obtain hydroxyapatite. The extraction procedures, depicted in **Figure** 4-4, were implemented at CNR-ISSMC in Faenza, Italy. Generally, the extraction technique involved a

dissolution step in an acidic medium (HCl), which then contained Ca and P precursors, and a reprecipitation in a basic medium (NaOH). For the four samples, two main parameters were changed: temperature and contact time of leachate solution with basic aqueous solution. In particular, HAP_1 and HAP_2 were formed after dropping leachate into NaOH solutions with long maturation time at 40°C, while HAP_3 and HAP_4 were obtained after "one-pot" mixing of the two solutions with lower contact time (5 to 60 minutes) at a lower temperature (25°C). One important parameter kept constant in all four procedures was the basic pH, considering that hydroxyapatite is the thermodynamically stable calcium phosphate phase under strongly basic conditions. In fact, several studies confirmed that the formation of HAP under basic conditions goes through different transient phases: particularly amorphous calcium phosphate (ACP) to octacalcium phosphate (OCP), finally to HAP.[141,142]

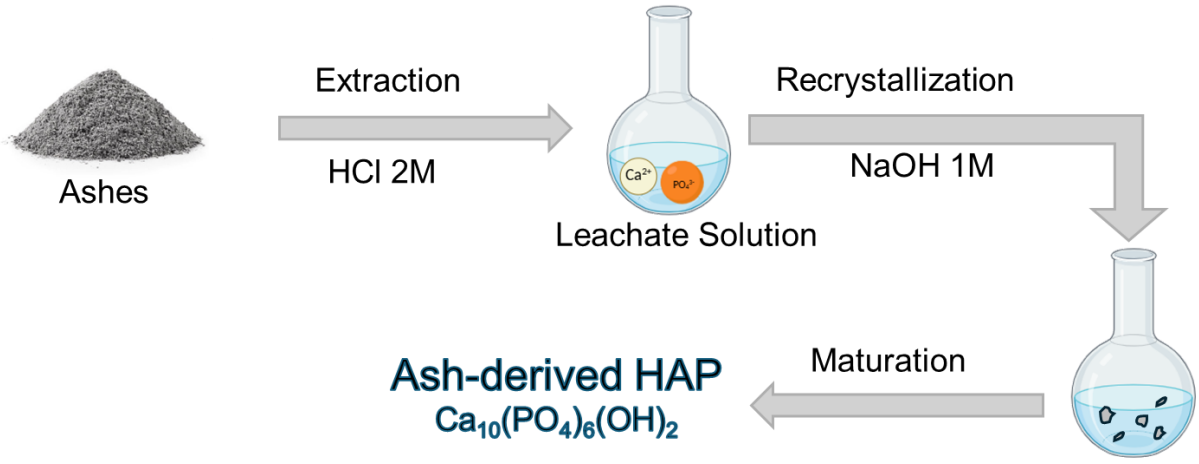

Figure 4-4 Flow diagram representation of the ash-derived HAP samples preparation steps.

The composition of the four hydroxyapatites was determined by ICP-OES and reported in **Figure** 4-5 and **Table** S-6-1, alongside the Ca/P molar ratio, which is a key parameter to identify specific calcium orthophosphate phases. The Ca/P ratio values of HAP_1 (1.82) and HAP_2 (1.79) were close to that of stoichiometric HAP (1.67). On the other hand, HAP_3 and HAP_4 have a Ca/P ratio slightly higher than HAP_1, HAP_2 with values of 2.06 and 2.03. Comparing the value of Ca and P content, all the four hydroxyapatites have a similar content of calcium, corresponding to

approximately 30%, while for P content, HAP_3 and HAP_4 exhibit a low amount of phosphorus in the chemical composition, resulting in a Ca/P ratio higher than HAP_1 and HAP_2. Given the heterogeneity of the elemental composition, comprising different oxides such as alumina or silica, of the ashes, a detailed compositional analysis is required to identify which elements are incorporated into the calcium phosphate (CaP) solid and to quantify their respective amounts. Generally, HAP_1 and HAP_2 contained lower amounts of Al (4 mol% ca.), Mg (8 mol% ca.), and Si (7-8 mol% ca.) in respect to HAP_3 and HAP_4, which comprised 7 mol% ca of aluminium, 13 mol% ca. for magnesium and 14 mol% of silicon. HAP_1 and HAP_2 which had higher contact time and maturation time showed lower presence of external elements and it reflected to Ca/P ratio which are near to the stoichiometric hydroxyapatite value (1.67). The higher maturation time allowed to the formation of apatitic framework *expelling* the oxides and ions which are not comprised in the hydroxyapatite structure.[143] On the other hand, the high content of Mg, Al and Si elements has been detected for the other two samples (HAP_3 and HAP_4) where a rapid contact time and low maturation time were maintained. For HAP_3 and HAP_4 the formation of CaP structure likely encapsulated also Al_2O_3, MgO and SiO_2 while forming hydroxyapatite structure resulting in higher elemental content and consequently lower content of phosphorus, in terms of phosphate ion. The substitution of the oxides with phosphate had an impact on Ca/P molar ratio of sample 3 and 4 which are different from stoichiometric hydroxyapatite, HAP_1 and HAP_2. Among the other trace elements, Fe and Na are the most abundant, although their molar percentages remain below 3% (**Table** S-6-1).

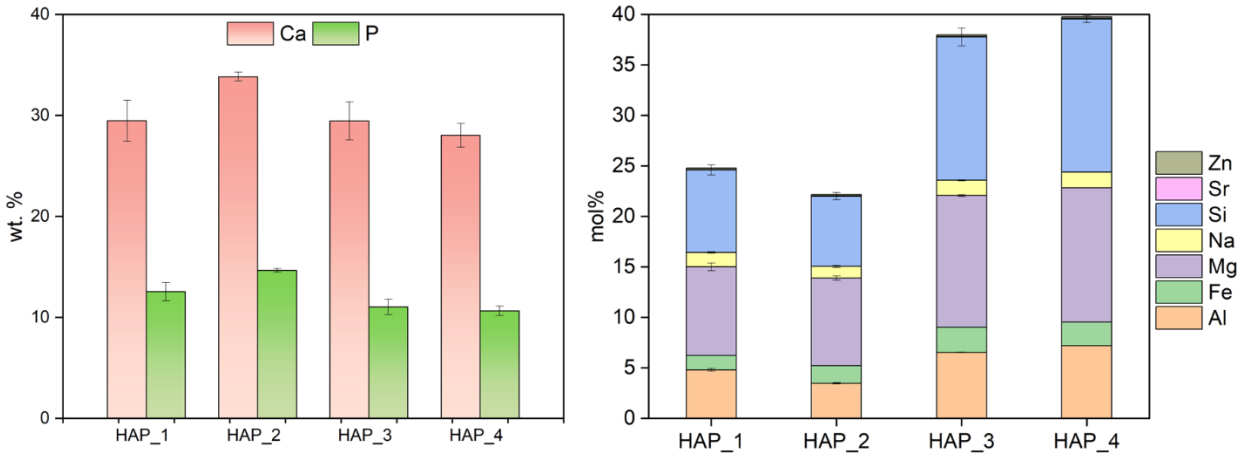

Figure 4-5 Graphic representation of ICP results: weight percentage (wt %) of Ca and P (left), molar percentage (mol %) of hetero atoms mol % (right)

To obtain an initial comparison between bulk and surface features, EDX analyses were performed to provide a preliminary assessment of the surface composition of the HAP samples and to compare these results with the overall chemical composition determined by ICP-OES. The EDX results revealed the absence of *hetero* elements in the HAP structure, such as Fe, Al, and Si, suggesting that these elements are mainly incorporated in the bulk phase. Mg and Na were the only external elements detected by EDX (**Figure** S-6-14). In addition, the Ca/P ratios calculated from EDX were notably different from those obtained by ICP-OES measurements: 1.31 for HAP_1, 1.47 for HAP_2, 1.92 for HAP_3, and 1.24 for HAP_4. Importantly, all these values deviate significantly from the stoichiometric Ca/P ratio of HAP (1.67). Considering the HAP samples affected by Ca deficiency (HAP_1, HAP_2 and HAP_4), this can be explained by accounting for the inclusion of other elements (e.g. Mg and Na) in the crystalline lattice. Considering the external elements, the ratio (Ca+Mg+Na/P) shifts towards stoichiometric value: for example, 1.76 for HAP_1 and 1.74 for HAP_2. These findings indicate a discrepancy between bulk and surface compositions, even though EDX analyses does not give a full comprehensive view of apatite surface.[144]

Even though ashes from thermovalorisation processes have mainly inorganic characteristics (as confirmed by ICP-OES and EDX analyses), organic residues cannot be totally excluded and during extraction processes of hydroxyapatite, organic materials from biomass can be incorporated into the structure. To detect the presence of organic compounds, thermogravimetric analyses (TGA) were employed. For all samples, the thermograms (**Figure** 4-6) display a sudden drop in TGA curve at *ca.* 70°C, corresponding to a weight loss of ca. 10%. This weight loss could be ascribed to water desorption. Particularly, the mass drop phenomenon began almost at room temperature, more precisely at ca. 30°C and it ended at ca. 150°C, as deduced from the dTg curve, from which the maximum rate of water desorption was computed in the range from 65 °C to 80°C. The second mass drop, which slope is gentler, happened in temperature range of 275-315 °C and it is assigned to the loss of CO_2 from the structure. To further confirm both water loss and decarbonilation of hydroxyapatite structures, infrared spectroscopy was coupled with TGA analyses: The IR analysis, depicted in **Figure** S-6-13, clearly showed how only water (3700 cm^{-1} and 1500 cm^{-1} regions) and CO_2 (2400 cm^{-1} bands) left the sample over the course of the analysis. Finally, as no other mass drops phenomena occurred, no organic compounds were incorporated into ashes derived HAP samples during the extraction processes and furthermore thermal stability can be assessed as no phase transformation occurred during the whole TGA analyses.

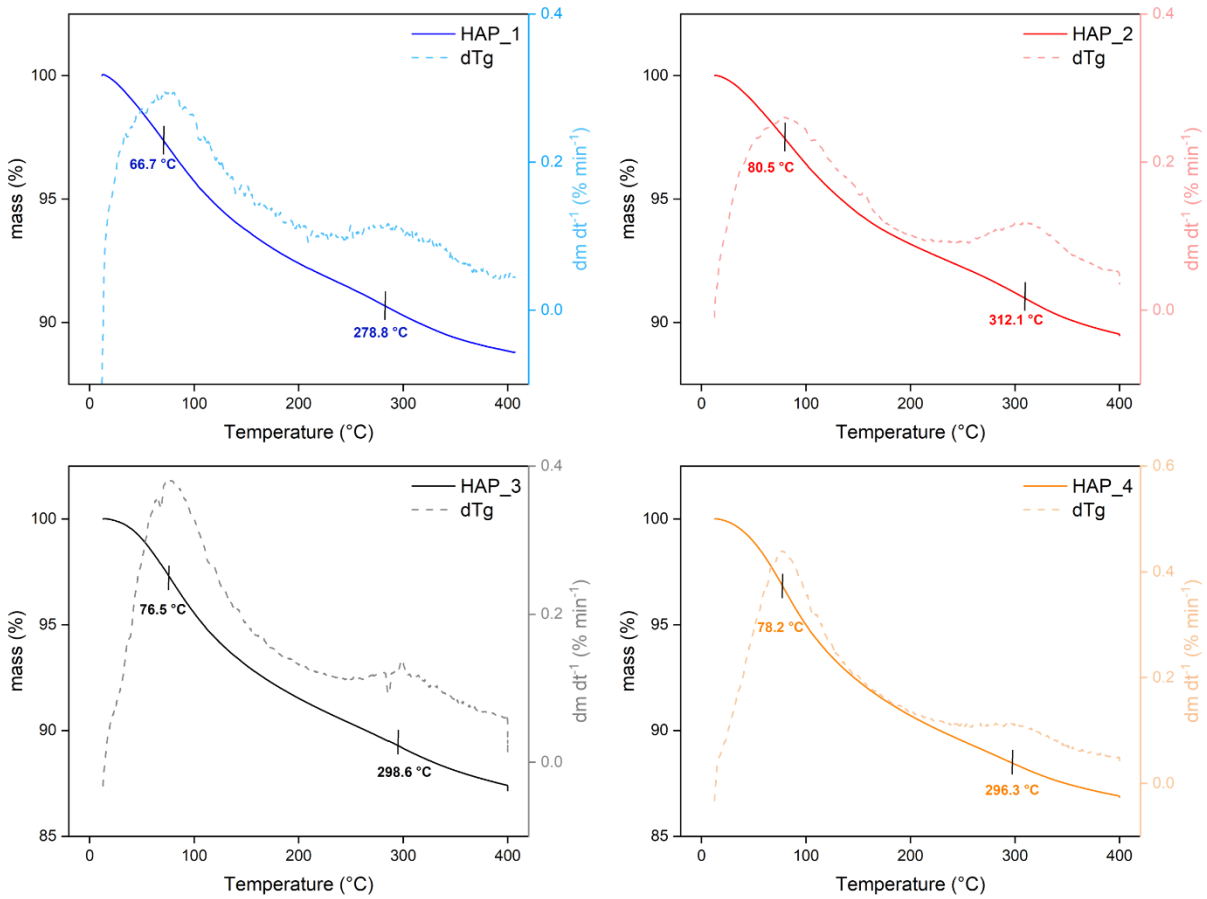

Figure 4-6 TGA/DTGA profiles of the ashes derived HAP samples: HAP_1 (blue line), HAP_2 (red line), HAP_3 (black line), HAP_4 (orange line). Thermogravimetric profiles obtained under nitrogen flow (10 mL·min^{-1}) following three steps program: i) heating from 35°C to 400°C, at controlled heating rate (β = 10°C·min-1); ii) isothermal step at 400°C for 2 h; iii) cooling from 400°C to 50°C.

After assessing the compositional characteristics of the ashes-derived samples and excluded the presence of organic compounds, morphology has been studied through transmission electron microscopy (TEM), electron diffraction (SAED) and X-ray diffraction analysis. In **Figure** 4-7, TEM images at low and high magnification are reported for the four ashes-derived sample. For HAP_1, TEM images (a, b) a longitudinal macrostructure composed by multiple overlapping layers which resembles the typical needle-shaped HAP structure. By studying the sample at higher magnification, as shown in images c) and d), nanocrystals in the size range of 5 to 10 nm are displayed where; the rows of atoms are visible as well, in a parallel and regularly spaced pattern., starting to confirm the presence of a crystalline HAP sample. Regarding HAP_2, the longitudinal arrangement of multiple

layers is even more sharp and defined than HAP_1 (e, f). Going further with magnification (g, h), the nanocrystals exhibit greater growth reaching up to 30 nm of length and width above 5 nm. TEM images of HAP_3 (i, j) showed agglomerates of crystallites in typical nanorods shape of hydroxyapatite, like the HAP_1 and HAP_2. With the images at high resolution (k, l), only some regions present an ordered structure, and the crystals boundaries are difficult to distinguish from the amorphous phase that seems to characterize most of this sample, indicating a lower degree of crystallinity in respect to the first two samples. A similar behaviour was observed for HAP_4. Low-magnification TEM images (m, n) revealed a longitudinal long-range order, along with agglomeration comparable to that of the previous HAP samples; however, at higher magnification (o, p) no ordered structure was detected: a continuous amorphous phase is present, composing all the observed regions where the atoms rows, which were recognizable in the previous samples, are also impossible to be identified To further confirm the differences between the first two HAP (more crystalline and with long range order) and the last two HAP, electron diffraction was employed (**Figure** S-6-15). For HAP_1 and HAP_2, electron diffraction investigation provided information on the structural order of the samples: the obtained pattern is rather defined, with cones that do not tend to shade into one another, with a slightly more defined pattern for HAP_2, as expected after analyzing TEM analyses. On the other hand, electron diffraction measurements on HAP_3 and HAP_4 showed uniform rings and the reflections are not distinguishable.

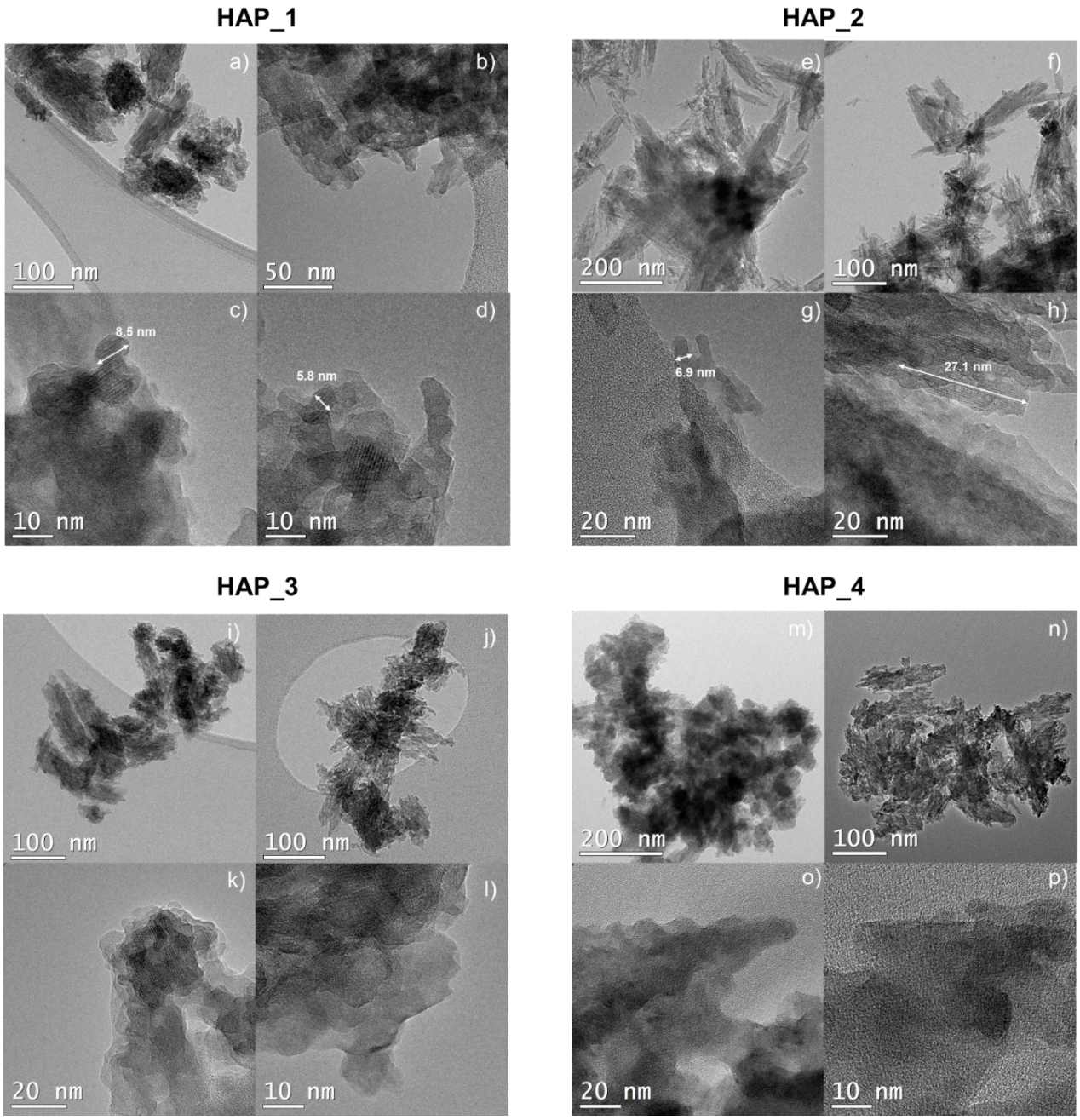

Figure 4-7 Morphological and structural characterization of the ashes derived hydroxyapatite samples: representative TEM images of HAP_1, HAP_2 HAP_3, HAP_4 (a, b, e , f, l, j, m , n). high resolution TEM images with magnification (20 and 10 nm) for HAP_1, HAP_2, HAP_3, HAP_4 (c, d, g, h, k, l, o, p). For HAP_1 and HAP_2 the average sizes of crystallites are displayed.

Alongside with TEM analyses, X-Ray Powder Diffraction (XRPD) was carried out to examine the structure and phase purity of the ash-derived HAP samples. For all the four patterns (**Figure** 4-8), almost all the diffraction peaks were identified and correlated to the hexagonal structure of stoichiometric HAP (JCPDS 00-009-0432). Two different patterns can be highlighted: for HAP_1 and

HAP_2 all the peaks result sharp and intense due high crystallinity of the samples, while for HAP_3 and HAP_4 the patterns present noticeably more amorphous patterns where broad peaks merge with the broad background. The XRPD data are consistent with TEM investigation and electron diffraction analyses where atom rows crystalline planes are well visible for the first two hydroxyapatite samples, while long-order lacks for HAP_3 and HAP_4. Furthermore, no secondary apatite phases or metal oxide reflections were observed, thereby confirming that all four extraction procedures are effective for producing phase-pure HAP and that the minor presence of foreign elements does not significantly modify the crystalline structure. Additionally, as confirmed by literature, low contact time and maturation time resulted in a more disordered HAP sample (HAP_3 and HAP_4 in this case).[145]

To conclude the morphology analyses of ashes-derived HAP samples, N_2 adsorption/desorption isotherms were performed to study the specific surface area (SSA) and the porosity of the samples. In **Figure** 4-9, the isotherms, reported for all the HAP samples, present a type IV profile with an H2-type hysteresis loop, which are typically associated with mesoporous materials. From the isotherms, SSA was calculated through 2-paramters BET equation and the results are reported in **Table** 4-2. The SSA values fall between 80 and 120 m^2 g^{-1}, consistent with surface area reported in other works.[146] Particularly HAP_2, which is the most crystalline sample, presented the lowest SSA (83 m^2 g^{-1}) while HAP_3 displayed the highest surface area, 119 m^2 g^{-1}, associated with higher amount of defects due to the amorphous features of the sample. Pore size and pore volume were then calculated on the desorption branch of isotherm, applying B.J. H. model in the 0.3 to 0.9 range of p/p^0. The mean pore radius is higher than 2 nm for all the four samples, confirming their mesoporous nature. Even the pore volume is similar for all the hydroxyapatite samples, with a value around 0.20 cm^3 g^{-1}, which is in good agreement with the values reported in literature. The compositional and structural information derived from ICP-OES, TEM, XRPD and BET analyses, confirmed that the extraction process of hydroxyapatite from ashes is a feasible way to obtain valorise residues of thermovalorisation process. In the next paragraph, structural functionalities were investigated to study the chemical properties and the surface features of the ashes-derived HAP samples.

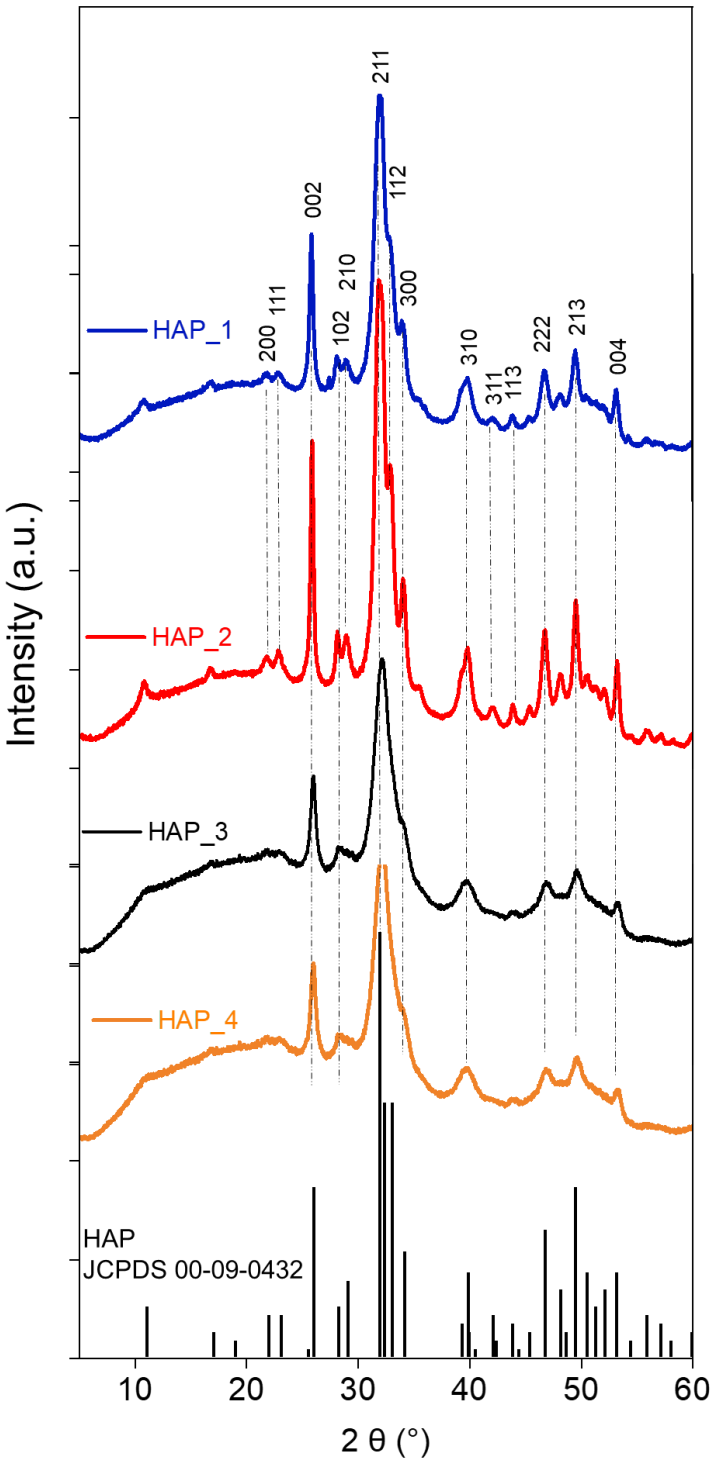

Figure 4-8 XRPD pattern of the ashes derived hydroxyapatite samples, with the reference crystallographic pattern of hydroxyapatite (HAP) indexed at the bottom. Reflection indexes are indicated according to reference pattern (JCPDS 00-009-0432)

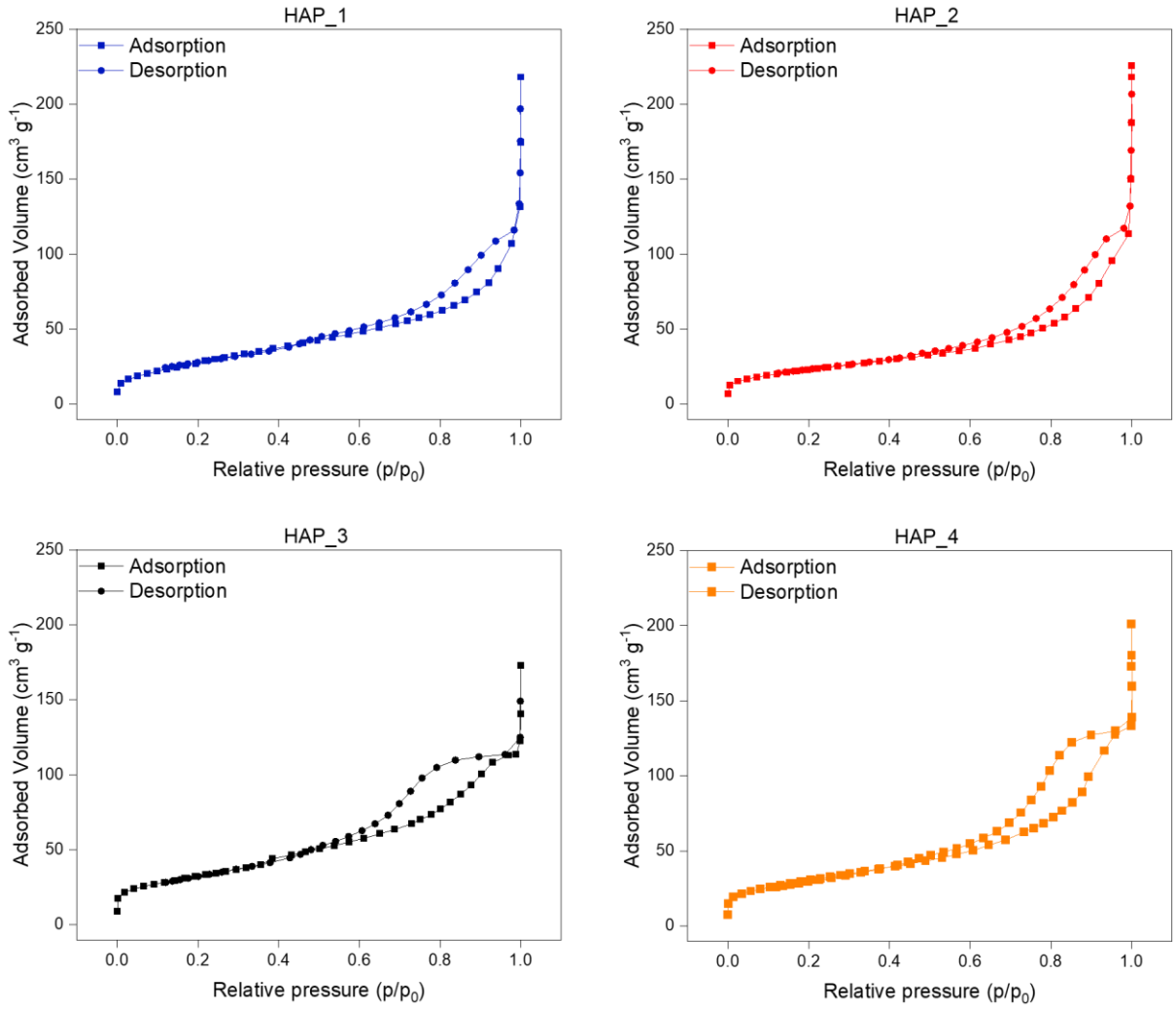

Figure 4-9 N_2 adsorption/desorption isotherm at -196 °C for HAP_1 (blue), HAP_2 (red), HAP_3 (black), HAP_4 (orange).

Table 4-2 Morphological properties of the ashes-derived HAP samples obtained from N_2 adsorption/desorption isotherms analyses.

	Vm[a] $cm^3 g^{-1}$	SSA[b, c] $m^2 g^{-1}$	Mean pore radius[d] nm	Pore volume[d] $cm^3 g^{-1}$
HAP_1	23.76 ± 0.45	103 ± 2	6.1	0.21
HAP_2	18.98 ± 0.09	83 ± 1	5.9	0.21
HAP_3	26.71 ± 0.19	119 ± 1	3.4	0.19
HAP_4	25.12 ± 0.52	110 ± 2	4.3	0.22

a. Monolayer volume obtained by 2-parameter BET model with proper standard deviation, calculated from propagation error of the slope of BET linear fitting (V_m is the inverse of the slope).
b. The dried sample was outgassed under vacuum conditions (10^{-2} torr) for 16 hours at 150 °C before analysis.
c. Evaluated from V_m (according to 2-parameters BET model) The standard deviation was obtained from error propagation on Eq. 2-2 starting from the experimental value of V_m (and its relative standard deviation).
d. Evaluated according to B.J.H. model.

4.2.2. Structural and spectroscopic characterization

The structural functionalities of the ash-derived HAP samples were further investigated using spectroscopy, providing insights into the presence of characteristic vibrational modes of the moieties of the HAP samples such as phosphate groups, hydroxyl environments, and possible lattice distortions induced by foreign elements. FT-IR spectroscopy performed on the ashes-derived HAP samples revealed distinct absorption bands associated with the vibrational modes of characteristic HAP functional groups (**Figure** 4-10). The spectra confirmed the presence of phosphate groups (v_3 as asymmetric stretching mode at 1100-1040 cm^{-1} and v_4 for the bending mode at 600-570 cm^{-1}) and hydroxyl groups related both to water adsorbed by HAP samples (as confirmed by TGA analyses) and OH structural functional group at 3450-3300 cm^{-1}, respectively, and the signal at 1640 cm^{-1} for OH^- bending mode. As expected, the spectra also exhibited carbonate-related bands at 1480-1420 cm^{-1} and around 870 cm^{-1}. The bands are assigned to stretching and bending, respectively. These features are consistent with either B-type substitution, where CO_3^{2-} ions replace PO_4^{3-} groups within the HAP lattice, or with carbonate species adsorbed at the surface. The last hypothesis could be related to the absorption of atmospheric CO_2 during the extraction process, which could be enhanced

by the co-presence with Mg^{2+}, which is known to promote the apatite carbonation and it is present in the lattice of HAPs (as confirmed by compositional analyses).[147] In contrast, characteristic signals of A-type substitution (CO_3^{2-} replacing OH^- groups in the lattice) were not detected in the FTIR analyses.

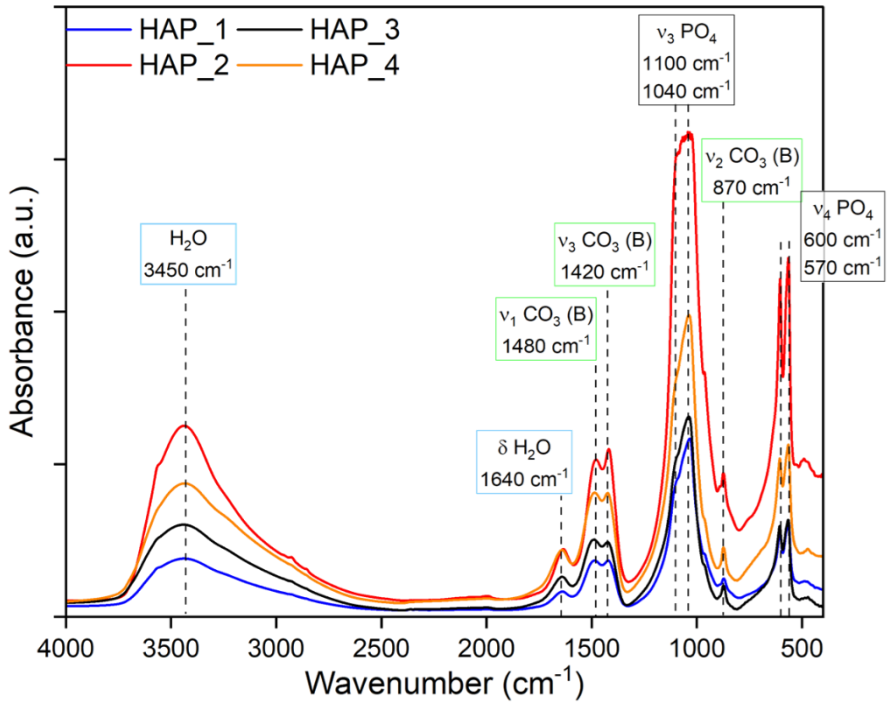

Figure 4-10 FT-IR spectra in the 4000-400 cm^{-1} range of the ashes-derived HAP samples. Principal vibrational modes of bond are highlighted: ν as stretching mode δ as bending mode, respectively.

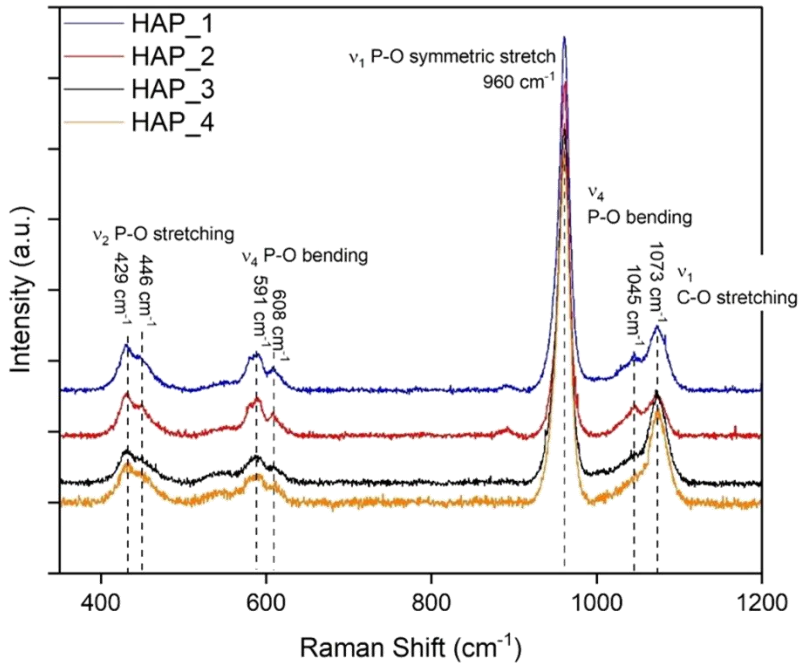

Figure 4-11 Raman spectra in the 350-1200 cm^{-1} range for all the ashes derived HAP samples. Phosphate and carbonates vibrational modes are highlighted.

Alongiside with infrared spectroscopy, Raman spectroscopy provided complementary insights into the presence of phosphate groups and B-type carbonates in the HAP samples. The typical bands of symmetric stretching and bending (429, 446, 960 and 1045 cm^{1}) of phosphate groups are displayed in **Figure** 4-11. As for carbonate signal, only C-O stretching mode is observed at 1073 cm^{-1}, which is assigned to typical B-type carbonate band (≈1070 cm^{-1}), confirming their incorporation into the structure of the ash-derived HAP samples.[148] No A-type carbonation signals are visible in Raman spectra, ruling out the presence of carbonation in OH^- groups in the lattice. Raman spectroscopy is consistent with FT-IR analyses and furthermore, some peaks in HAP_3 and HAP_4 are broader and not-well detectable due to the higher degree of structural disorder in these samples (as confirmed by TEM and XRPD analyses).

As phosphate groups are one of the most important moieties present in the HAP structure, ^{31}P solid state nuclear magnetic resonance was exploited to investigate phosphorus' chemical surrounding. The spectra (**Figure** S-6-16) of the four samples show no significant difference, indicating that P has similar chemical surroundings among the different HAP samples, as confirmed by FT-IR and Raman spectroscopies. To fully understand P states, deconvolution of P peak was carried out (**Figure** S-

6-16). Two protonation states were found and assigned to PO_4^{3-} and HPO_4^{2-} could be indicative, respectively, of the presence of a typical structural function and a non-apatitic environment as a surface layer.

4.2.3. Surface characterization

HAP exhibits multifunctional surface features such as acid-base character that can be tailored during synthesis or processing, thus making it a flexible material in different application such as adsorption and heterogeneous catalytic processes.[149] The study of the surface properties, in terms trough different techniques is important to comprehend the surface reactivity and the possible application in sustainable process. The surface properties of the ash-derived HAP samples were thoroughly investigated by means of XPS, liquid-solid titration and adsorption microcalorimetry.

Table 4-3 XPS results: surface composition of the ashes derived hydroxyapatite samples.

Element	Atomic percentage[a] *(%)* *(Binding Energy from XP spectra / eV)*			
	HAP_1	HAP_2	HAP_3	HAP_4
P 2p	8.57 *(132.72)*	8.15 *(132.57)*	8.73 *(132.84)*	8.95 *(132.83)*
Ca 1s	3.31 *(284.60)*	3.83 *(284.60)*	3.7 *(284.60)*	3.89 *(284.60)*
Ca 2p	16.57 *(346.95)*	16.18 *(346.69)*	16.49 *(346.84)*	16.64 *(346.82)*
O 1s	66.01 *(531.19)*	65.74 *(530.84)*	65.63 *(530.89)*	65.30 *(530.85)*
Mg 1s	5.24 *(1304.05)*	5.79 *(1303.26)*	5.12 *(1303.50)*	4.84 *(1303.50)*
Ca/P ratio	1.93	1.99	1.89	1.86

a. The percentages are corrected by ruling out the contribution of the adventitious carbon (C-C at 284.60 eV).

The surface chemical composition of the ash-derived HAP samples was verified using XPS. The survey spectra (**Figure** S-6-17) identifies as elements present in the surface: Mg (1304 eV), O (532 eV), Ca (348 eV), C (286 eV) and P (133 eV). From survey, only Mg is detected as external elements on the surface in an atomic percentage between 4% and 5% while Al, Si, Na and Fe are not present in the survey spectra. The XPS differs from EDX and ICP analyses (where different hetero atoms were present), assessing the incorporation of external elements in the bulk of the hydroxyapatite structure, avoiding surface segregation during extraction processes. The absence of these elements would not influence surface properties, changing the overall surface reactivity of HAP samples. The quantification of surface composition is reported in **Table** 4-3, and, also, the Ca/P ratio (one of the most important features for hydroxyapatitic materials) differs from ICP and EDX analyses. From XPS analyses, the surface Ca/P ratio is higher than stoichiometric HAP for all the four samples. According to the literature, such high values (Ca/P > 1.85) would suggest firstly, a Ca-enrichment on the surface and secondly an amphoteric character shifted towards basicity.[150] Regarding the C content, two different main peaks are visible in C 1s HR spectra (**Figure** 4-12, a-c-e-g), that after deconvolution are subdivide in the peaks concerning the adventitious carbon (C-C peak at ≈285.0 eV and C-O peak at 286.0 eV) and the carbonate species present on the surface at approximately 290 eV.[151] The C atomic percentage is approximately below 4 % for all the four ashes derived HAP samples with the lowest amount being HAP_1 with 3.31%, as a matter of fact looking at deconvolution spectra of HAP_1 displayed in **Figure** 4-13-a, three main components of adventitious carbon can be subdivided and centred at 285.11 eV, 286.00 eV and 288.46 eV related to C-C, C-O and C=O bond, respectively. For HAP_2, HAP_3 and HAP_4 (**Figure** 4-13, c-e-g) the adventitious carbon peak was divided into two main peaks related to C-C and C-O peak. For the three samples the binding energy were approximately at 285 and 286 eV (respectively), without significant energetic shifts, confirming the *quasi*-pure HAP surface. Looking at O 1s HR spectra, for the four samples two main peak are visible after the deconvolution of the main peak (**Figure** 4-13): the main component of O 1s HR spectra is related to the contribution of O belonging to the lattice of HAP samples with relative energies at 531 eV; the second component, less intense, is related to the coupling of O vacancies present on the surface and the oxygen of carbonates.[152,153] For Ca, P and Mg, representative HR

spectra and relative deconvolution are showed in **Figure** S-6-18 and **Table** S-6-2. For Ca 2p spectra, two main peaks centred at 347.64 and 351.22 eV are identified and associated with Ca $2p_{3/2}$ and Ca $2p_{1/2}$ components proper assigned to the Ca-O bond. No Ca-CO_3 signal was identified from the deconvolution of the HR spectra. For P 2p component, no proper deconvolution was carried out due to the highly symmetricity of the sample. As reported in literature, the absence of phosphate vacancies on the surface structure can lead to sharp and symmetric P peaks. Notably, looking at Mg 1s HR spectra, two main components were identified and centred at 1304.51 and 1305.02 eV. The first peak was attributed to Mg-O bond, the latter, interestingly, was assigned to Mg-CO_3 bond, during extraction process the formation of $MgCO_3$ could occur on the surface of HAP, as also reported in literature for Mg-substituted HAP The XPS analyses confirm the presence of only Mg as external atoms present on the surface and also confirm the carbonation of ashes-derived samples: the presence of carbonate (alongside the absence of phosphate vacancies), particularly at the surface, is a further confirmation of the spectroscopic analyses carried out with FT-IR and Raman, where B-type carbonation were identified for all the four samples.

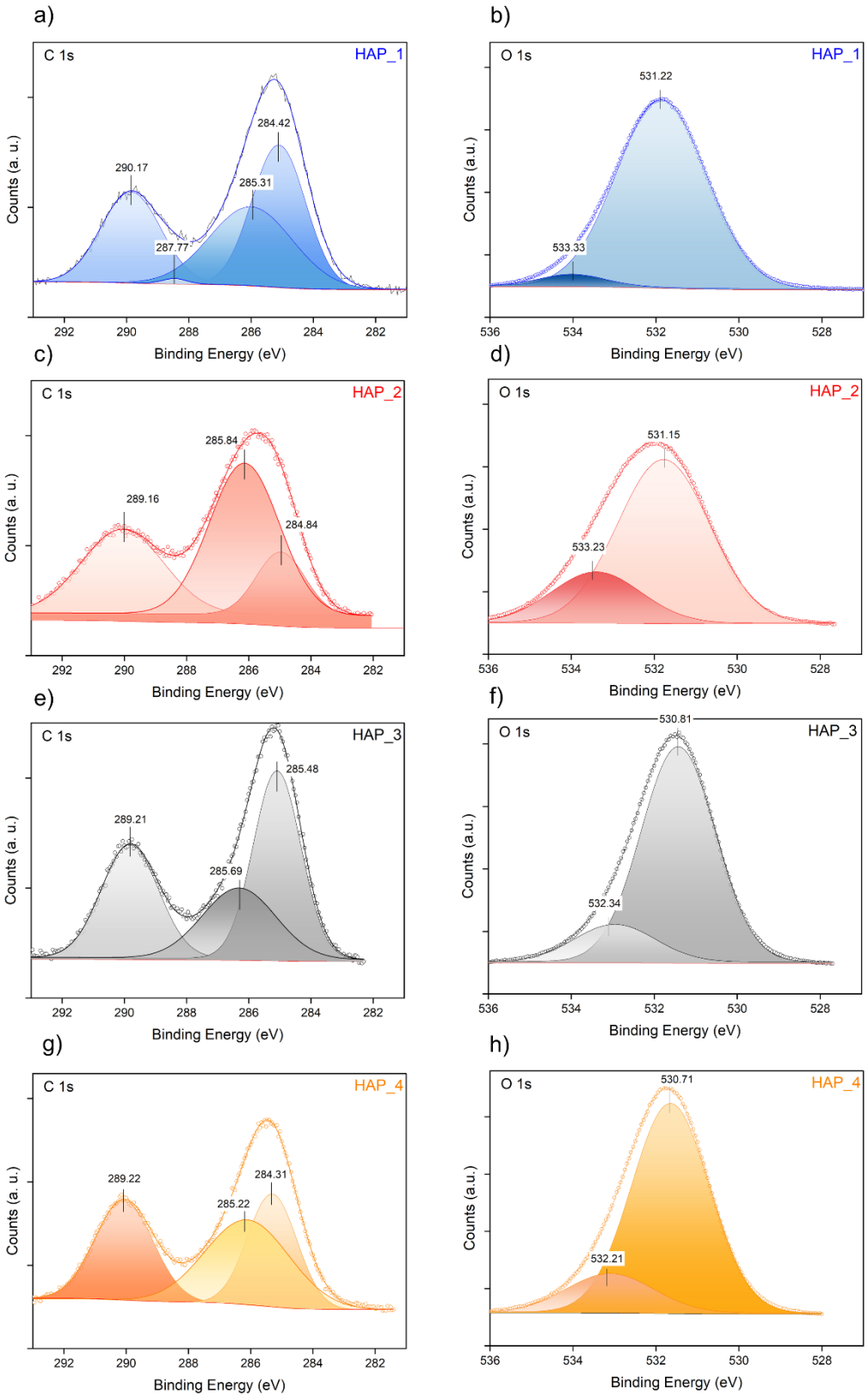

Figure 4-12 High Resolution (HR) XP spectra of C 1s (left) and O 1s (right) of the ashes-derived HAP samples: HAP_1 (a,b), HAP_2 (c,d), HAP_3 (e, f) and HAP_4 (g h), respectively. The principal deconvoluted peaks are indicated (all the collected data were processed with the peaks shifted by ruling out the contribution of adventitious carbon C-C at 284.6 eV).

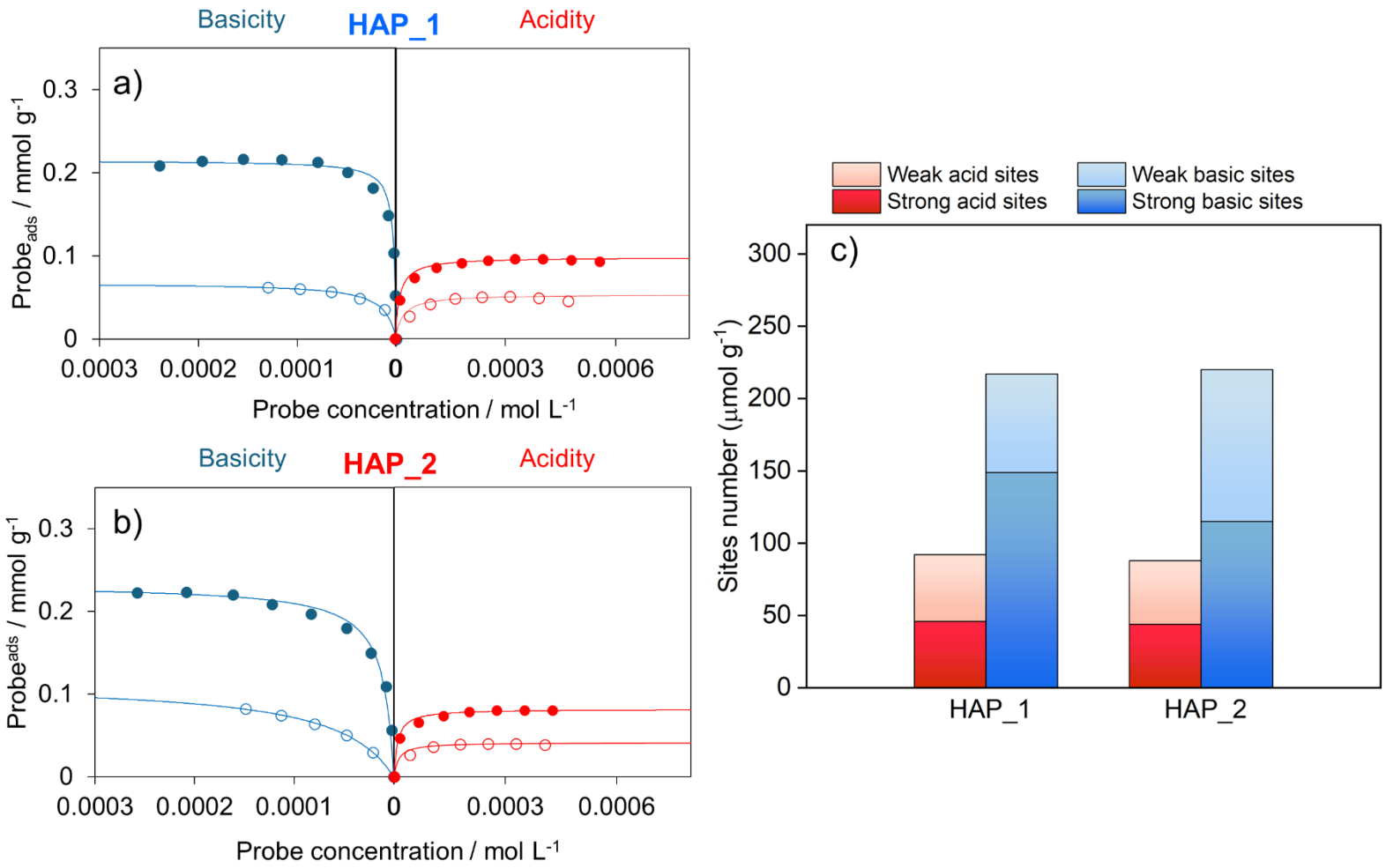

Figure 4-13 Adsorption isotherms of PEA (for acidity, right) and BA (for basicity, left) probes collected in cyclohexane at 30 C on HAP_1 (a) and HAP_2 (b) samples, collected in solid-liquid phase titration recirculation system. Full and empty markers represent I° run adsorption and II run adsorption on the surfaces. Blue lines and red lines represent the calculated Langmuir curves of PEA and BA adsorption on total and weak sites. The histogram (c) displays the distribution of the total number of sites into strong and weak sites (for details, see 1.2.3).

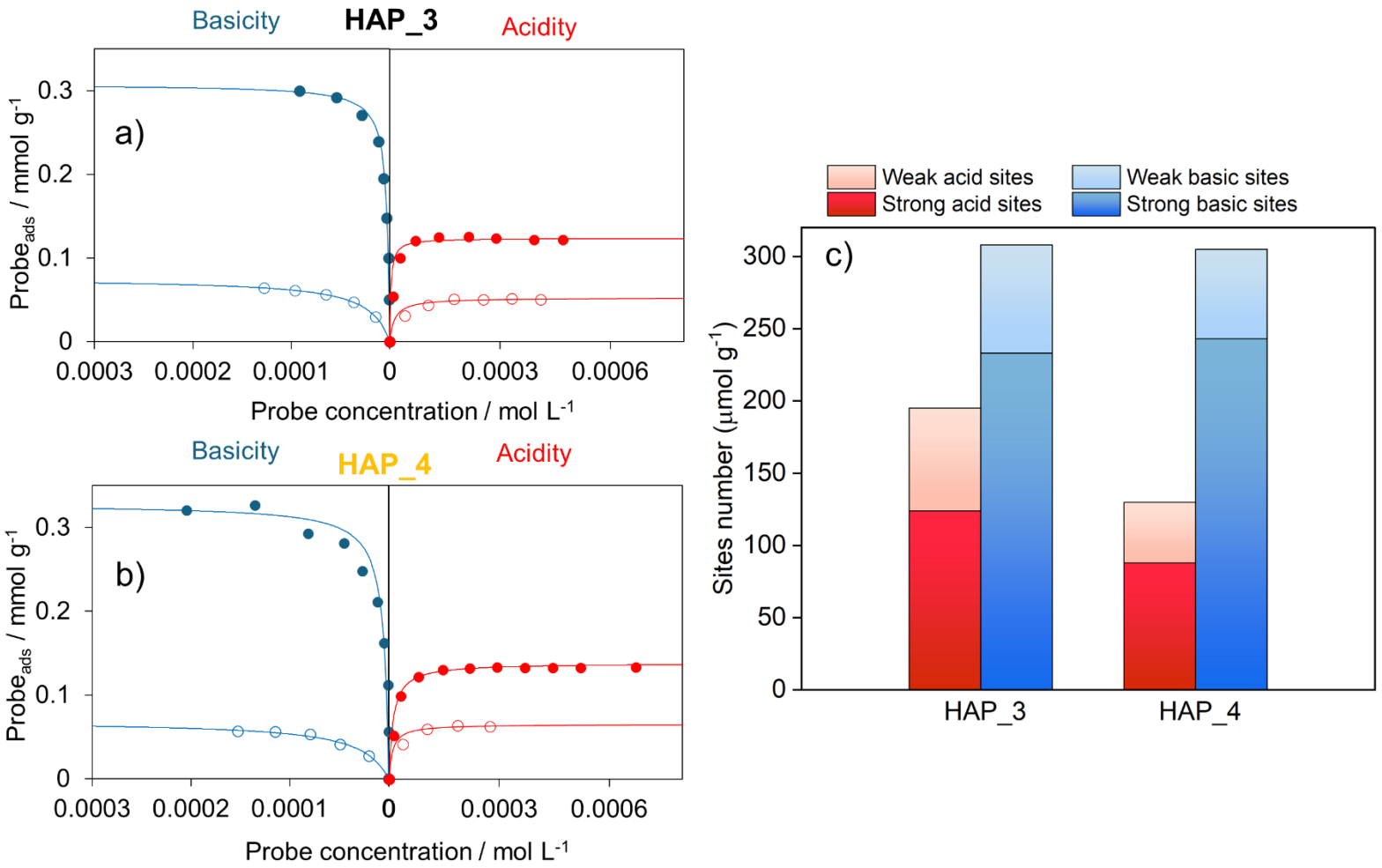

Figure 4-14 Adsorption isotherms of PEA (for acidity, right) and BA (for basicity, left) probes collected in cyclohexane at 30 °C on HAP_3 (a) and HAP_4 (b) samples, collected in solid-liquid phase titration recirculation system. Full and empty markers represent I° run adsorption and II run adsorption on the surfaces. Blue lines and red lines represent the calculated Langmuir curves of PEA and BA adsorption on total and weak sites. The histogram (c) displays the distribution of total number of sites into strong and weak sites (for details, see 1.2.3).

After assessing the chemical composition of the multifunctional surface of HAP samples, the study of the amphotericity undergoes through the study of nature, the number, the density, and the strength of acid and basic sites. The first step is to understand what type of sites are present on the surface: whether they act like Brønsted acids that donate protons, Lewis acids that accept electron pairs, or basic centres linked to oxygen atoms or hydroxyl groups. Then, it becomes important to study how many sites each surface possesses and the density of the sites, directly related to the availability and so the reactivity of the surface. Finally, the strength must also be considered, because weak and strong sites often lead the system down very different chemical pathways. Unfortunately, studying the exact nature of the sites is technically challenging: for example, using CO_2 adsorption with infrared spectroscopy gave back little information, as the sample carbonation hinder clear identification of basic sites (in the case of CO_2). As confirmed by structural and morphological analyses, the ashes-derived samples fell in the family of hydroxyapatite and therefore, hypothetically typical acid-base moieties could be found on the surface of the material, such as phosphate (Bronsted acid), hydroxyl vacancies (Lewis acid), Ca^{2+} sites (Lewis base), calcium vacancies and oxygen vacancies (Bronsted base).[149,154–156]

Concerning the acid-base functionalities of the ashes-derived HAP samples surfaces, the number of acidic and basic sites was determined by liquid–solid titrations in cyclohexane at 30 C using phenylethylamine (PEA) and benzoic acid (BA) as probe molecules through the recirculation chromatographic method by liquid-solid phase titrations. The titrations were carried out in a non-polar and aprotic solvent like cyclohexane to determine the intrinsic acidity/basicity. In **Figure** 4-13 and **Figure** 4-14, the adsorption isotherms are reported adsorption for HAP_1, HAP_2, HAP_3 and HAP__4. From the analysis of adsorption isotherms using the Langmuir model, the number of acid and basic sites was calculated and is reported in **Table** 4-4. All the Langmuir parameters (n_{ads}, b_{ads} and R^2) are reported in **Table** S-6-3 for the fresh ashes derived HAP samples.

For all samples, the number of basic sites exceeds that of acid sites, confirming the overall basic character of the ash-derived HAP samples, as expected from initial evaluation from Ca/P ratio. HAP_1 and HAP_2 exhibited a very low amount of acid sites (98 and 82 µeq g^{-1}, respectively),

roughly half of the corresponding basic sites (215 and 232 μeq g^{-1}). For HAP_3 and HAP_4, basic sites (308 and 328 μeq g^{-1}) were about three times more abundant than acid sites (124 and 130 μeq g^{-1}).

For a further comparison of the number of acid/base sites in the four samples, the surface densities of acid/base sites (expressed as μeq m^{-2}), obtained by normalizing the number of acid-base sites to the surface area of each sample, should be considered. Since HAP_3 and HAP_4 have a slightly higher SSA than HAP_1 and HAP_2, when comparing acid site density values, the differences between the four samples become negligible, reaching a value around 1 μeq m^{-2} for all the four samples. In contrast, for basic site density, the distinction between crystalline and amorphous samples is preserved: HAP_1 and HAP_2 show values of about 2 and 2.5 μeq m^{-2}, respectively, whereas the amorphous HAP_3 and HAP_4 display higher densities, reaching approximately 3 μeq m^{-2}, confirming the enhanced basicity of the latter two and more amorphous samples.

It is important to notice that higher amount of number acid site is typically associated with foreign elements incorporated in the HAP structure. In this case, Mg influenced the acidity of the samples as the amount is higher in HAP_3 and HAP:4 than HAP_1 and HAP:2, resulting in a slightly enhanced acidity. As expected from both morphology and the Ca/P ratio, the most amorphous sample displayed the highest intrinsic basicity due to exposed defects. A higher prevalence of basic over acidic sites was particularly evident when focusing on strong sites. Strong sites were quantified from the numerical interpretation of the isotherm curves obtained in the first and second adsorption runs (described in Paragraph 6.3). For acid strong sites, for all the four samples, the 50% of the titrated samples are attributed to strong sites. On the other hand, basic strong sites constituted the majority of the sites, approximately 60 to 80%: for HAP_1 and HAP_2, the results showed 149 and 115 μeq g^{-1}, respectively. Particularly, HAP_3 and HAP_4 showed not only higher total basic sites but almost doubled number of strong basic sites than HAP_1 and HAP_2. From the elaboration of adsorption isotherms, HAP_3 possesses 233 μeq g^{-1} while HAP_4 shows 243 μeq g^{-1}. Analysing the index of amphotericity, expressed as acid-to-base ratio (A/B), it decreases from the more crystalline samples to the more amorphous ones: HAP_1 and HAP_2 showed a ratio around 0.30-

0.38 and HAP_3 and HAP_4 exhibited the highest overall basicity, with A/B ratios of 0.30 and 0.27. Even if the amphotericity index is similar for HAP_1 and HAP_3, the absolute number of acid sites and basic sites are quite different: notably HAP_3 showed higher number of sites. The higher number of sites for the third sample than HAP_1 is related to a particular morphology enriched with different defects in the amorphous part of the structure, as discussed from TEM and XRD analyses. Additionally, HAP_3 exposes higher number of sites due to highest specific surface area (SSA) among the four samples. Furthermore, for HAP_3, a shift towards basicity with high number of basic sites (total and strong ones) was also expected from the highest Ca/P ratio (2.08 *ca.*), compared to the other samples.

With liquid-solid titration, the evaluation of strength is quite qualitative: the only parameter that evaluates the strength of the sites is the Langmuir parameter (b_{ads}), reported for all the samples in **Table** S-6-3. Overall, the Langmuir constants are quite consistent with the total, weak and strong sites of the HAP samples: in particular, the higher b_{ads} is related to the strong sites and consequentially the b_{ads} of weak sites corresponds to the weak sites. The strength of acidic and basic sites, along with the distribution of site strength on the ashes derived HAP samples was studied in greater detail through microcalorimetric-volumetric measurements[157] of base (NH_3) and acid (SO_2) probe molecule adsorption at 80°C, with the work of Dr. Luca Previtali in collaboration with Institute for Research on Catalysis and the Environment (IRCELyon, Lyon, FR).

The volumetric isotherms of adsorption for the ash-derived HAP samples are reported in **Figure** 4-15 (a), and **Figure** 4-16 (a) for both NH_3 and SO_2 analyses. The results of volumetric isotherms are reported in **Table** 4-4. As for acidity, from the volumetric isotherms of NH_3 adsorption, HAP_3 emerges as the samples with the greatest amounts of acid surface sites (409 µeq g^{-1}). Moreover, the more amorphous samples (HAP_3 and HAP_4) overall present a higher number of sites when compared to the more crystalline HAP_1 and HAP_2, that possess 315 and 301 µeq g^{-1}, respectively. The results are consistent with solid-liquid adsorption with PEA. Simultaneously with the volumetric measurements, the enthalpies of adsorption of the probe molecules were recorded as a function of equilibrium pressure. The resulting calorimetric isotherms, shown in **Figure** 4-15 (b),

illustrate that the heat evolved initially rises sharply, reflecting the interaction of the probe with the strongest acidic sites first. As the strongest sites are filled, the curve flattens, reflecting adsorption on progressively weaker acidic sites. Throughout the entire series, HAP_3 and HAP_4 show consistently higher heats of adsorption (38.0 and 33.4 J g^{-1}) than HAP_1 and HAP_2, indicating greater strength of acidic sites. Observing the differential heats, all samples appear to have a considerably heterogeneous acidic surface. In **Figure** 4-15 (c), the curves show steep changes in slope, indicating at least a bimodal distribution of acidic sites. A plateau can be observed for all the samples around 60-80 kJ mol^{-1}, which corresponds to the filling the medium-strength acidic sites. After the common plateau, the more crystalline HAP_1 and HAP_2 exhibit a sharper decrease in heat evolution, corresponding to the weakest sites. This suggests that the preparation method influenced the distribution of acidic site strengths, likely through differences in crystal structure that affect the types of acidic functionalities exposed at the surface. Furthermore, to better understand surface heterogeneity, the evolved heats were divided into discrete, consecutive intervals, and the probe molecule uptake was quantified for each interval to define distinct populations of acidic sites (**Figure** 4-15, d). This division allows the visualization of the most significant site populations. For NH_3 measurements, many surface sites fall within a medium-strength range (50-100 $kJ \cdot mol^{-1}$). A small population of weaker sites are observed for HAP_1 and HAP_2. On the other hand, HAP_3 is the only samples exhibiting a small population of sites with heats above 150 $kJ \cdot mol^{-1}$, confirming that the more amorphous samples possess the strongest acidic sites among the ash-derived samples studied, as a further confirmation of solid-liquid titration analysis.

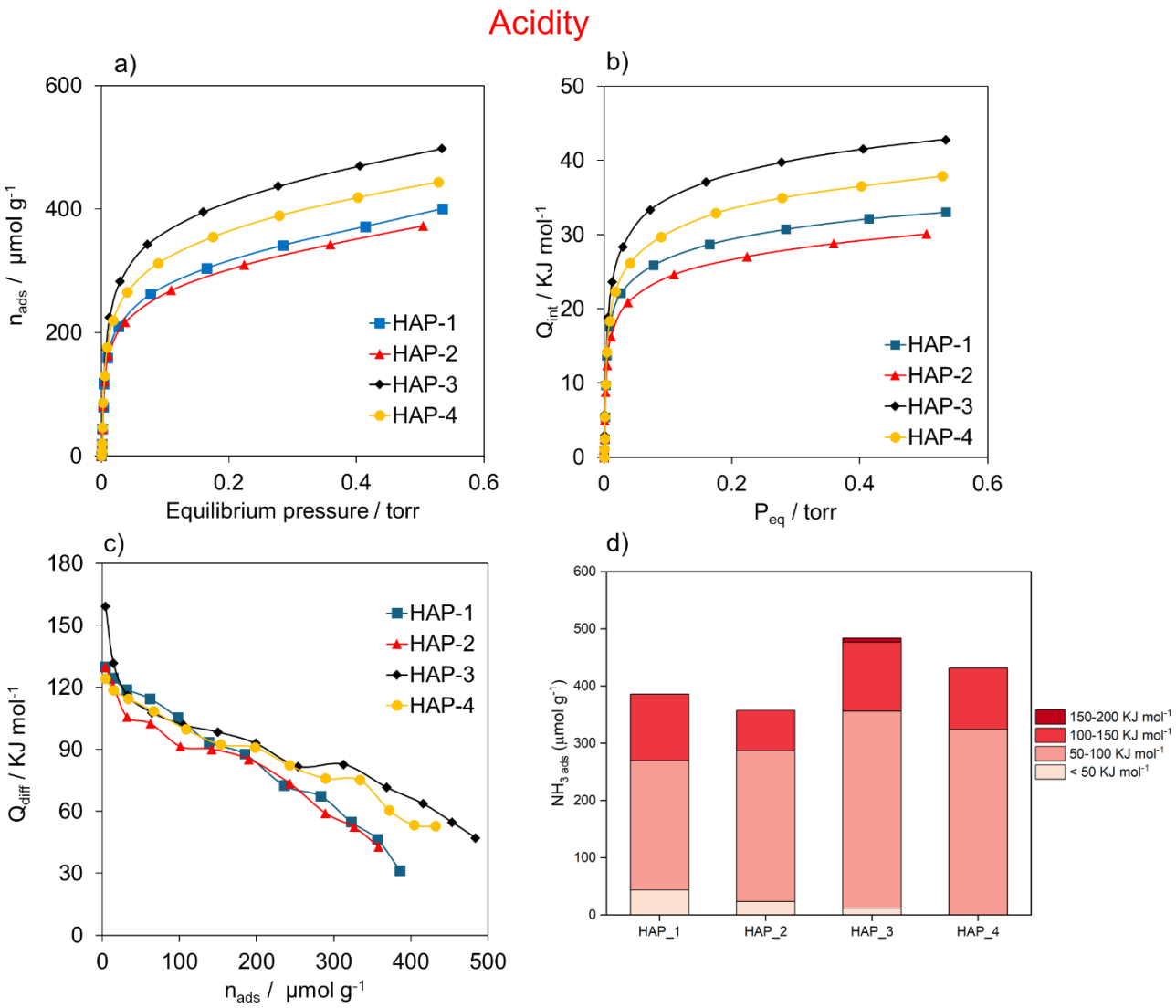

Figure 4-15 NH_3 Adsorption microcalorimetric results. Volumetric isotherm (a), calorimetric isotherm (b), differential heat of adsorption of NH_3 (c) collected at 80°C on the four ashes derived hydroxyapatite samples. Distribution of acid sites as a function of acidity strength (d).

Regarding basicity, SO_2 volumetric microcalorimetry adsorption were carried out. The volumetric isotherms (**Figure** 4-16, a) showed higher number of basic sites on the surface of the four HAP samples, than acid sites, confirming once more the shift towards basicity of the amphotericity of HAP. Even in this case, HAP_3 and HAP_4 display higher amount of total basic sites and strong sites: 500 µeq g^{-1} and 463 µeq g^{-1} for total basic sites, respectively. Considering HAP_1 and HAP_2, the more crystalline samples, both exhibit 352 and 388 µeq g^{-1} as total basic sites, respectively. Furthermore, 90% of the titrated sites are strong basic sites, as occurred in the case of BA solid-

liquid titration for all the four samples (**Table** 4-4). Simultaneously with the volumetric measurements, the enthalpies of adsorption of the basic probe molecules were recorded as a function of equilibrium pressure to better characterize the surface basicity. The resulting calorimetric isotherms display a consistent trend: at low equilibrium pressures, a sharp increase in the amount adsorbed and in the evolved heat indicates interaction with the strongest basic sites, which are occupied first. As the adsorption progresses, the four curves gradually flatten, reflecting the filling of weaker basic sites. Even in this case, two cases can be identified: HAP_1 and HAP_2 feature lower enthalpies around 53-57 J g^{-1} while the more amorphous samples reach approximately 70 J g^{-1} as evolved heat, meaning stronger interactions on basic sites. Finally, to assess the presence of different populations of basic sites with prevalence of strong sites, a plateau is observed at heat values of 150 kJ mol^{-1} in the differential heat curves for all the four samples. Then, in the medium strength range, HAP_3 and HAP_4 show once more the higher amounts of basic sites (**Figure** 4-16 c): particularly, HAP_3 showed the overall number of basic sites but also the stronger sites as it can be seen from the discrete interval of differential heats (**Figure** 4-16, d).

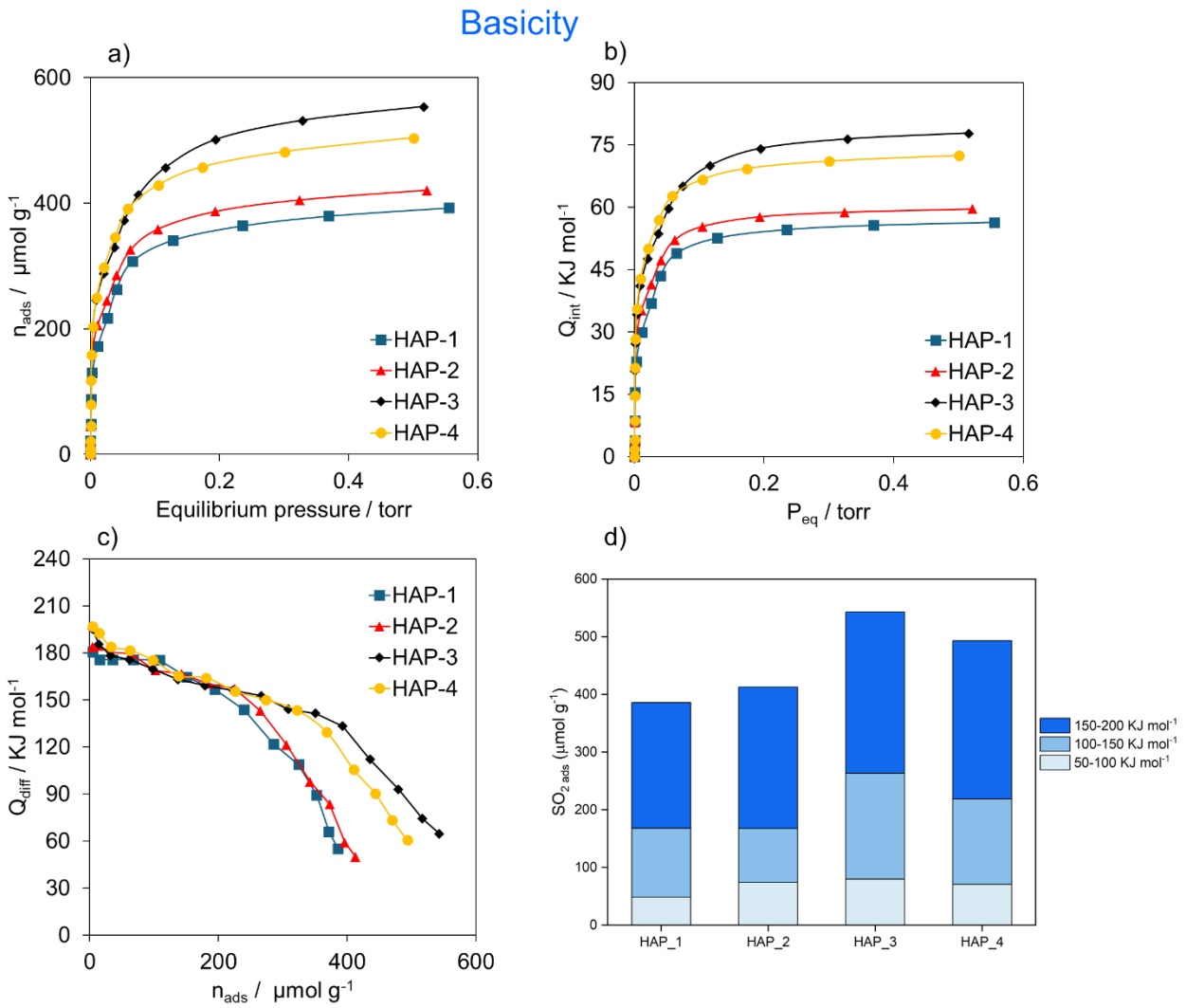

Figure 4-16 SO2 Adsorption microcalorimetric results. Volumetric isotherm (a), calorimetric isotherm (b), differential heat of adsorption of SO2 (c) collected at 80°C on the four ashes derived hydroxyapatite samples. Distribution of basic site as a function of basic strength (d).

From the physico-chemical characterization and surface analyses performed, it is important to highlight the possibility of modulating the morphological and surface properties, with particular attention to the acid-base feature. Generally, the amphoteric behaviour (A/B ratio) of all the ash-derived HAPs was shifted toward basicity, in agreement with the compositional and surface Ca/P ratios. In particular, the more amorphous HAP_3 and HAP_4 samples exhibited a higher number of both acidic and basic sites compared to HAP_1 and HAP_2. This suggests that the preparation pathway may influence the strength of the surface sites, possibly due to differences in crystallinity

and the presence of defects that affect the nature of the functional groups exposed on the surface. Modulating and tailoring such properties pave the way for promising applications in key fields such as environmental remediation and catalysis.[158,159]

Table 4-4 Summary of the surface acidity properties of the ashes-derived hydroxyapatite samples: surface acid and base sites measured by solid-liquid phase titration at 30°C ± 0.1 in cyclohexane and adsorption microcalorimetry at 80°C ± 0.1.

	Solid-liquid titration					Adsorption microcalorimetry				
	Total acid sites[a]	Strong acid sites[b]	Total basic sites[a]	Strong basic sites[b]	A/B[c]	Acid sites from I adsorption run[d]	Acid chemisorption sites[e]	Basic sites from I adsorption run[d]	Basic chemisorption sites[e]	A/B[c]
	µeq g^{-1}					µeq g^{-1}				
HAP_1	98	**46**	215	**149**	0.31	315	**116**	352±0.21	**302±6**	0.38
HAP_2	82	**44**	232	**115**	0.38	301	**115**	388	**330**	0.35
HAP_3	119±6	**61±15**	309±1	**233±1**	0.30	409	**158**	503	**439**	0.36
HAP_4	125±11	**60±18**	328	**243**	0.27	363	**120**	463	**401**	0.30

a. Total sites obtained from I run of solid-liquid phase titration with PEA (for acidity) and BA (for basicity). The analyses are reproduced three times for some samples to verify the reproducibility of the analyses. After the reproducibility the error percentage is 3% < Ɛ < 10%.
b. Strong sites obtained from the difference between sites obtained from I run and II run of solid-liquid phase titration. The analyses are reproduced three times for some samples to verify the reproducibility of the analyses. After the reproducibility the error percentage is 3% < Ɛ < 10%.
c. The A/B ratio (amphotericity index) was calculated on strong acid and strong basic sites ratio of the solid-liquid adsorption (6^{th} column) and volumetric microcalorimetry (11^{th} column). Particularly, for adsorption microcalorimetry, only the chemisorbed amount was considered for the A/B.
d. Moles of probe molecule adsorbed on the bare sample during the first adsorption run. They were calculated by interpolating the experimental amounts adsorbed at the fixed equilibrium pressure P_{eq}= 0.2 torr. *To confirm reproducibility, the analysis was repeated only on HAP_1, giving an error percentage Ɛ < 1%.*
e. Moles of probe molecule chemisorbed calculated by the difference of the total amount of probe molecule adsorbed in the first run ([c]) and the total amount re-adsorbed. *To confirm reproducibility, the analysis was repeated only on HAP_1, giving an error percentage Ɛ = 2%.*

4.2.4. Influence of the aqueous system on the structural properties and surface features of the ashes-derived hydroxyapatite.

Among the various media involved in these processes, water represents one of the most important and widely used solvent. Therefore, after investigating the intrinsic properties of the ash-derived samples, the following section focuses on studying the effect of water on the structural and surface characteristics of the HAP samples. Then, the HAP samples are examined directly in aqueous media (effective properties), with a specific application in the catalytic reaction of glucose isomerization. One of the most important properties of hydroxyapatite is its limited solubility under neutral conditions, which makes it an excellent support for catalytic reactions in aqueous media. Even tough HAP shows low solubility, the hydroxyapatite surface in contact with an aqueous environment undergoes a dynamic equilibrium where a continuous exchange of ions occurs. This process is found at the interface promoting the formation of a hydrated layer of hydroxyapatite which consists of flexible bonds of calcium, phosphate, hydroxyl ions and water molecules adsorbed on the surface of HAP. Due to the properties of the hydrated layer to be dynamic, it can continuously modify the overall properties of HAP, so the modification of the HAP due to water as solvent are herein studied both for the structure and the typical surface characteristics.[160]

For the study of stability of ashes-derived HAP samples, each material was kept in contact with milliQ water at 90°C for 8 hours, to mimic catalytic conditions with relatively high temperatures. The suspension was then filtered and the solid was recovered and dried to undergo structural and surface characterization analyses.

4.2.4.1. *Morphological and structural characterization*

To study the morphological changes after water treatment, XRPD analyses were carried out and compared with the patterns of *fresh* samples, showed in **Figure** 4-17. No significant differences are detected between the fresh and water treated samples. The main peak reflections (002), (210), (211), (222), (213) and (004) at respectively 2θ of 26°, 28°, 33°, 47°, 49° and 53° are well sharped and visible, thus confirming the stability of hydroxyapatite phase after harsh water treatment. A slight

difference can be observed in HAP_3 and HAP:4 samples, where some less intense peak in the region of between 2θ of 15° to 25° disappeared due to the broad background. In the most amorphous sample, the interaction with water slightly changes the short-range regularity enhancing marginally the apatite amorphous phase.

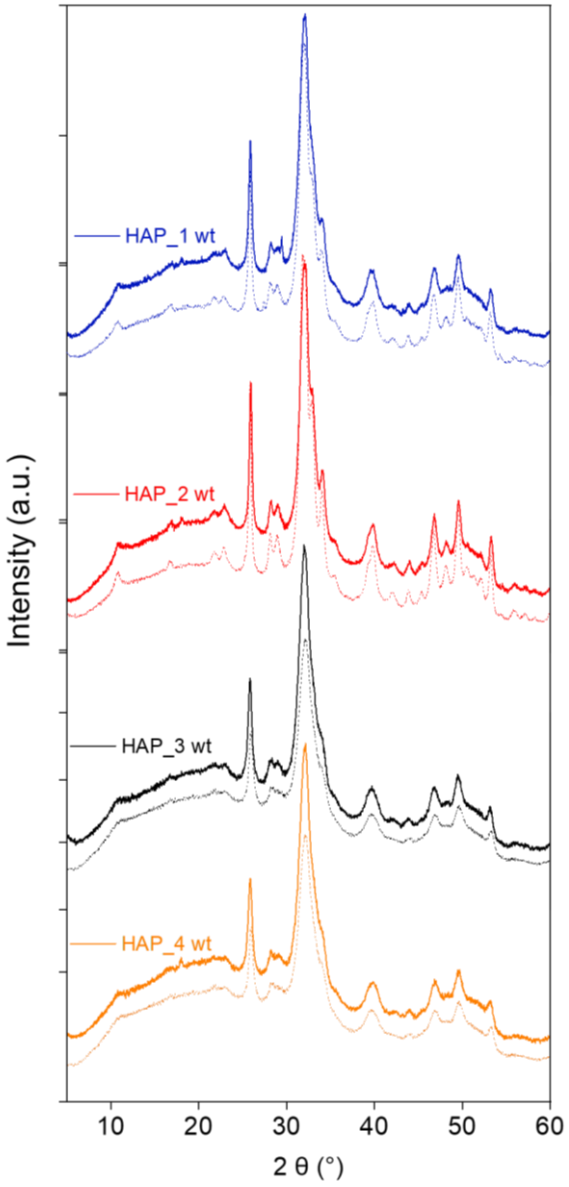

Figure 4-17 Comparison of XRPD pattern of the ashes derived hydroxyapatite samples after water treatment (continuous line) in comparison with the fresh sample (dotted line, *see* **Figure** 4-8).

To conclude the morphology analyses of ashes-derived HAP samples, N_2 adsorption/desorption isotherms were carried out to study the specific surface area (SSA) and the porosity of the samples, after water treatment. In **Figure** 4-18, the adsorption isotherms are reported and for all the four

samples, the loss of mesoporosity is visible from the type of isotherms displayed. HAP_1 and HAP_2 does not show the typical type IV isotherms, which they possess before water treatment. In HAP_3 and HAP_4, a very small mesoporosity is detected at relative pressure (p/p0) above 0.7. Even though the porosity of the samples is different, the specific surface area decreased generally of 10-15%. HAP_3 was the only sample affected the most by the water treatment as its SSA decreased from 119 m^2 g^{-1} to 75 m^2 g^{-1}. Even looking at the pore volume of samples (**Table** 4-5) after water treatment, the decreasing of pore volumes for each sample is further evidence of a minimal change in morphology. Due to the water treatment, the overall structure of the samples remains stable, as confirmed by XRPD patterns, but the morphology of crystallite is slightly changed. The water molecules could modify the structure forming lamellar and more open agglomerates, due to the dissolution-reprecipitation phenomena, which HAP is known to undergo.[161,162] For more amorphous samples, where a high number of defects, that can interact with water, is higher, the phenomenon is enhanced, explaining why HAP_3 is the most affected sample, in terms of specific surface area. Another possibility is the partial leaching of structural ions of HAP samples, that affected the overall changes in porous shape and surface area exposed.

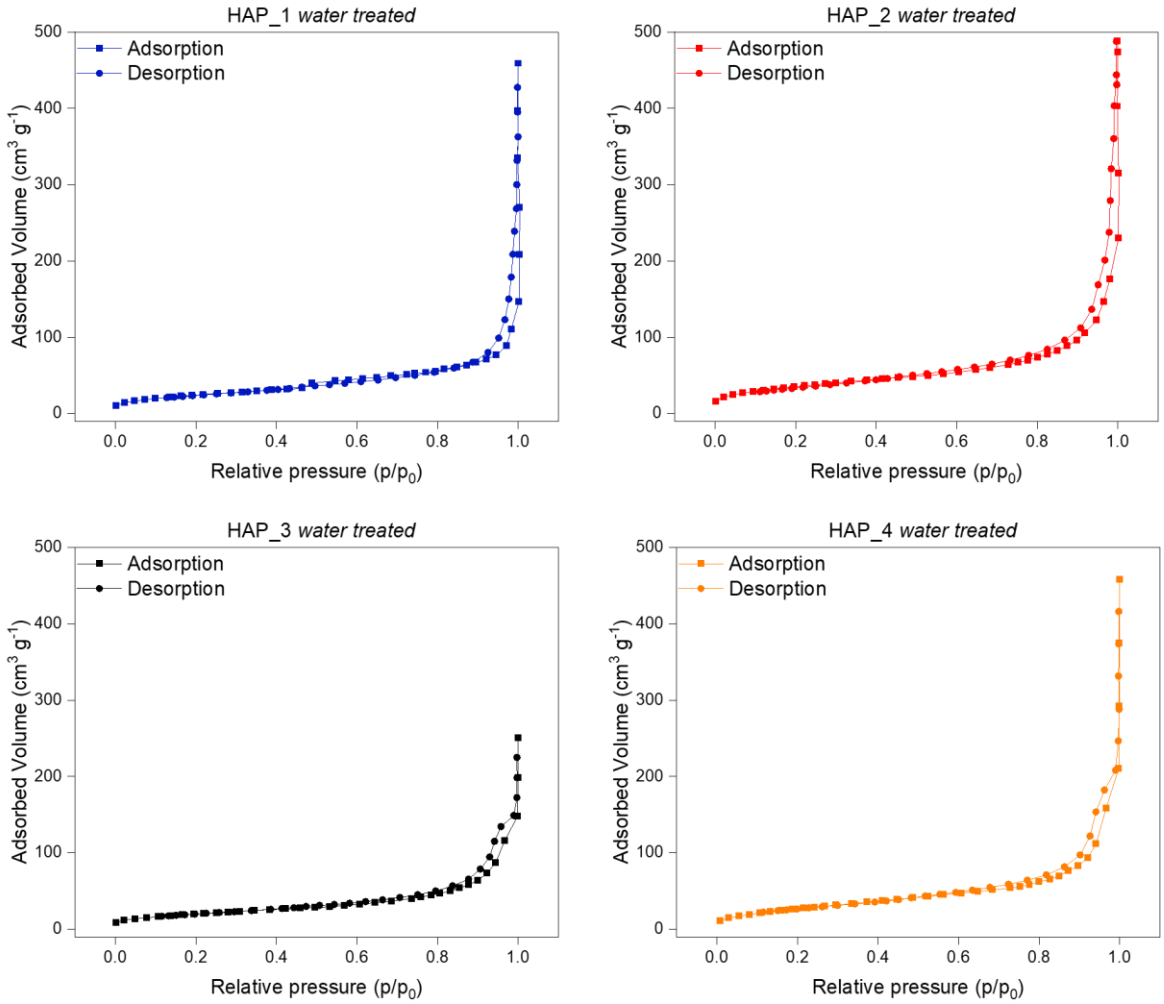

Figure 4-18 N_2 adsorption/desorption isotherm at -196 °C of ashes derived HAP samples after water treatment. (For fresh ashes derived HAP samples *see* **Figure** 4-10).

Table 4-5 Comparison of morphological properties of *fresh* HAPs and *water treated* ashes derived HAP samples.

	Water treated samples		
Sample	V_m[a] *$cm^3\ g^{-1}$*	SSA[b, c] *$m^2\ g^{-1}$*	Pore volume[d] *$cm^3\ g^{-1}$*
HAP_1	21.11± 0.45	92± 2	0.12
HAP_2	18.05± 0.19	78± 1	0.13
HAP_3	17.13 ± 0.23	75± 1	0.09
HAP_4	24.39 ± 0.35	106±2	0.11

a. Monolayer volume obtained by 2-parameter BET model with proper standard deviation, calculated from propagation error of the slope of BET linear fitting (V_m is the inverse of the slope).
b. The dried sample was outgassed under vacuum conditions (10^{-2} torr) for 16 hours at 150 °C before analysis.
c. Evaluated from V_m (according to 2-parameters BET model) The standard deviation was obtained from error propagation on Eq. 1-2.
d. Evaluated according to B.J.H. model.

4.2.4.2. *Acid-base surface characterization*

After water treatment the bulk structure of hydroxyapatite remain stable as confirmed by XRPD analyses and the morphology with relative surface area demonstrates to have only minor differences. Once assessed the principal structural properties, it is important to focus on the possible change of surface functionalities of the HAP samples. The ashes derived hydroxyapatite samples were then analysed in solid-liquid titration with basic (PEA) and acid (BA) probe in cyclohexane to monitor and analyse the number of sites after water treatment. In doing so, the study aims to comprehend if the surface of hydroxyapatite is as stable as the bulk of the materials, even in water the surface undergoes in a non-apatitic dynamic layer. The adsorption isotherms with PEA and BA are showed in **Figure** S-6-19 and the total sites calculated applying Langmuir model (which parameters are indicated in **Table** S-6-4) are reported in **Figure** 4-19 and **Table** 4-6. In the table, the total sites of the *fresh* samples are also reported to have a quantitative comparison.

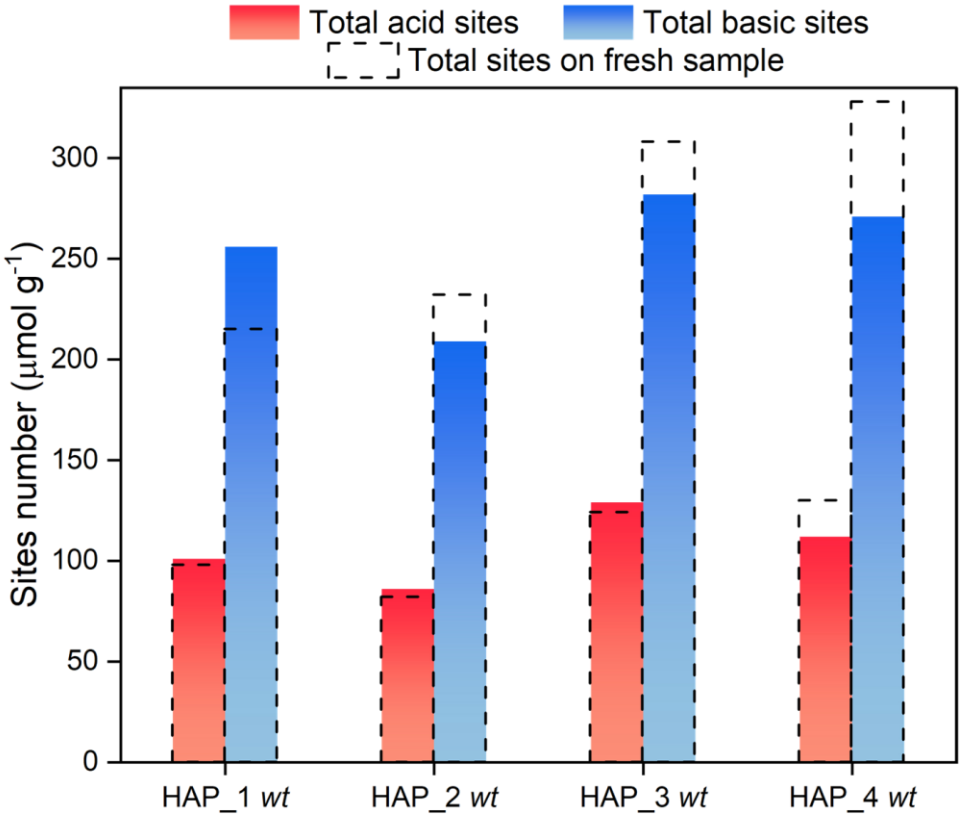

Figure 4-19 Representation of total acid (red) and basic (blue) sites, determined by solid-liquid titration in cyclohexane at 30°C of HAP water treated samples. In dotted line, total acid and basic sites of fresh HAP samples are displayed. The collected isotherms are represented in **Figure** S-6-19 For information of quantification of the strong and weak sites see **Table** S-6-4.

Based on the adsorption isotherms preliminary evaluation, the basicity features of ashes derived HAP samples is still confirmed even after water treatment. For all the four samples, there is still predominance of total basic sites over total acid sites. Looking more specifically at the total acid sites, the water treated samples possess the same number of acid sites of fresh HAPs (also considering the error tolerance of 8-10% of technique of solid-liquid titration). HAP_1, HAP_2 and HAP_3 possess approximately ≈100 µeq g^{-1} which was consistent with the fresh total sites. For HAP_4, since the total acid sites dropped from 130 µeq g^{-1} to 112 µeq g^{-1}, which is 13% fewer than the total sites of fresh samples, it appears that only HAP_4 was the sample that appeared to be impacted slightly more by water treatment. As for strong and weak sites, no remarked differences are observed as expected from the calculated total sites. Notably, HAP_2 and HAP_4 water treated

(WT) possess lower number of strong sites (0.029 μeq g^{-1} and 0.0.0436 μeq g^{-1}, respectively), which value is halved the value of fresh sample. On the other hand, the weak acid sites increased for both the samples resulting in an overall acidity as similar as the fresh sample. The formation and dissociation of hydrated layer changed partially the exposed sites for HAP_2 and HAP_4, maintaining a ratio between strong and weak sites very comparable to the fresh samples.

Considering the basicity of the water treated HAP samples, the total number of sites decreased approximately by 10% to 20%. The more affected samples are HAP_1 and HAP_4 which sites passed from 215 to 256 μeq g^{-1} and 328 to 271 μeq g^{-1}, respectively. Focusing on strong basic sites (**Table** S-6-4), for all the four samples the number of sites is marginally decreased confirming once more that the hydrated layer modified the exposure of sites. Notably, HAP_4 was the sample that seemed to suffer more the water treatment. Looking at amphotericity index, even after water treatment, the basic features are still confirmed for all the four samples. Notably the acidity-basicity ratio (A/B) is as similar as for the fresh samples considering HAP_1 and HAP_4. A more pronounced difference is observed for HAP_2 and HAP_4: the surface *restructuration* by water molecules enhanced more the strong basicity features of HAP_2 (from 0.38 to 0.25) and for HAP_4 (from 0.27 to 0.22).

Concluding the assessment of properties after water treatment a different behaviour of crystalline samples from amorphous ones is observed. After water treatment, HAP_1 and HAP_2 are typically very stable, with minimal changes in surface amphotericity. Referring to the two amorphous samples, HAP_3 and HAP_4, the greater number of surface and structural flaws can interact with water, and this water-surface interaction can cause some surface rearrangement of the sites. While the alterations for HAP_3 are appropriately tied to the material's morphology, the rearrangement for HAP_4 involves the surface acido-basicity of the materials. This confirms further the relationship between amorphous features (with relative defects) and water interactions.[163] It is important to focus that all the modification induced by water treatment are not in large extent that modify entirely the morphological structure and surface features. The hydrodynamic layer formed on the surface of HAP, upon drying, tends to revert toward the pristine configuration. The removal of adsorbed water seems to promote local reorganization in form of recrystallization of HAP surfaces. The water

exposure and the subsequent drying is a process largely reversible: such transitions between *dried* and *hydrated* layer highlight once more the dynamic nature of HAP: particularly the structural and chemical stability of ashes-derived samples.

Table 4-6 Summary of surface acid and base sites measured with solid-liquid phase titration at 30 °C ± 0.1 in cyclohexane for ashes derived fresh HAPs sample and water treated HAPs.

	Water treated samples				
	Acid sites[a]	Variation of acid sites[a]	Basic sites[a]	Variation of basic sites[a]	
	µeq g^{-1}	%	*µeq g^{-1}*	*%*	*A/B*[b]
HAP_1 WT	101	*3*	256	*16*	0.29
HAP_2 WT	86	*4*	209	*10*	0.25
HAP_3 WT	129	*4*	282	*8*	0.36
HAP_4 WT	112	*13*	271	*14*	0.22

a. Total sites obtained from I run of solid-liquid phase titration with PEA (for acidity) and BA (for basicity). Each value is coupled with variation of number of total sites in respect to fresh sample.
b. The amphotericity index was calculated on strong acid and strong basic sites ratio of the solid-liquid adsorption (6th column).

Once confirmed the reversibility of the process of formation-disappearance of hydration layer formation on HAP surfaces upon water exposure and drying, the amphotericity of ashes-derived samples was quantified directly in water. The solid-liquid titrations were carried out to calculate the effective acido-basicity ratio (E.A/E.B.). The exemplificative collected adsorption isotherms of PEA and BA in water are displayed in **Figure** 4-20 and the quantified total acid and basic sites are reported in **Table** 4-7. From a preliminary analysis, the total basicity prevails on the acidity of the sample: the basic sites are three times higher than acid sites: specifically, the basic sites exposed in water are 50 µeq g^{-1} and the total acid sites are much lower (12 µeq g^{-1}). At this very low amount of acid and basic sites, the detection of weak sites (by II run of liquid-solid titration) became very

difficult, preventing the subdivision of strong and weak sites. From the adsorption isotherms in water, it seems that total acido-basicity resemble strong acido-basicity.

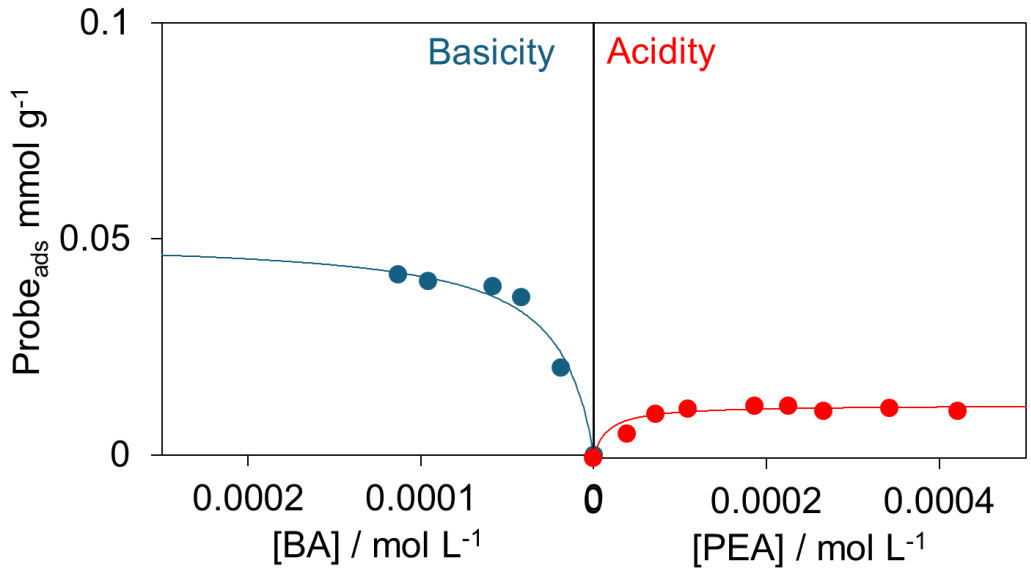

Figure 4-20 Adsorption isotherms of BA (left) and PEA (right) in water at 30°C on HAP_2 as an example of ashes derived HAP sample. Full markers represent I° run adsorption and blue and red lines represent Langmuir curves of BA and PEA adsorption, respectively. II run was not operated due to the low number of adsorption sites.

Furthermore, to highlight the importance of the hydrated layer, discussed above, a comparison between total acido-basicity in cyclohexane and water has been made (**Table** 4-7). The acid sites in water drastically reduced by 1/10 (from 82 to 12 μeq g^{-1}) while the basic sites were depleted by the 75 %. The formation of hydrated layer, though it is a key feature of HAP and very useful for ions mobility, tends to cover quite completely the surface itself, hindering quite large probe molecules (PEA or BA, in this case) to interact with the acid or basic sites. Many studies reported that the adsorption properties for water on HAP surfaces depends firstly on the surface of crystalline plane exposed; secondly the interaction between water molecules and constituents was based not only on physisorption but on chemisorption with dissociation of H_2O and formation of Ca-OH and PO-H covalent bonds HAP surface.[162]

Table 4-7 Comparison of the total surface acid and base sites measured in cyclohexane at 30°C (intrinsic acidity/basicity) and in water (effective acidity/basicity) at 30°C for HAP_2, trough solid-liquid titration in a recirculation system.

	Cyclohexane		Water	
	Acid sites[a]	Basic sites[a]	Acid sites[a]	Basic sites[a]
	μeq g^{-1}		*μeq g*$^{-1}$	
HAP_2	82	232	12	50

a. Total sites obtained from I run of solid-liquid phase titration with PEA (for acidity) and BA (for basicity).

4.2.4.3. *Catalytic isomerization of glucose into fructose by ashes derived HAP samples.*

The chemical conversion of glucose to fructose (**Scheme** 4-1) has been known for the past 100 years and constitutes one of a group of reactions collectively known as the *Lobry de Bruyn-Alberdavan Ekenstein* transformation.[164]

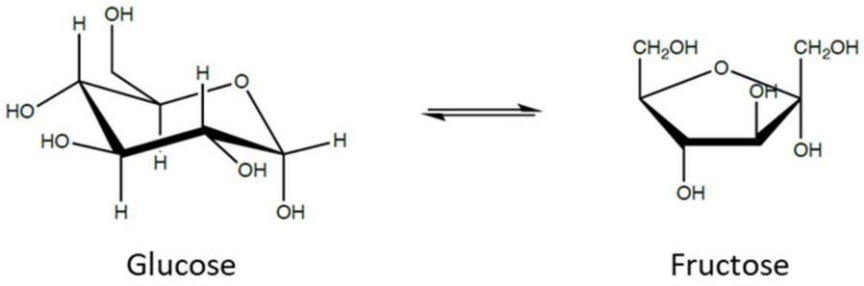

Scheme 4-1 Reaction scheme of glucose isomerisation into fructose.

The reaction is an equilibrium reaction, slightly endothermic (ΔH = 2.78 kJ·mol^{-1}) and with a free energy Gibbs positive, making it a reaction where the glucose species are predominant in respect to the fructose molecules. The study of catalytic system became so necessary to improve fructose production both for food industry and chemical manufacture. Since glucose is the building block of different biomass and also the main reagent for producing fructose reason, the isomerisation reaction is a key step in chemical processes.[165] One chemo-catalytic pathway, explored beyond the enzymatic route, is the homogenous catalytic conversion of glucose into fructose, which passes through basic catalysis. Through basic homogeneous catalyst, the mechanism of the reaction was futher confirmed, assessing the enediol mechanism involving the following steps: D-glucose ↔ trans-enediol ↔ D-fructose, as represented in **Scheme** 4-2. Particularly, the enediol anion intramolecular proton shift was the rate-determining step, based on kinetic data. Generally, strong inorganic bases (e.g., sodium hydroxide, calcium hydroxide, alluminate complexes) have been shown to be favourable for converting glucose to retro-aldolization byproducts via cation-ketose complexes, thus giving a poor fructose selectivity but very high conversion.[166].

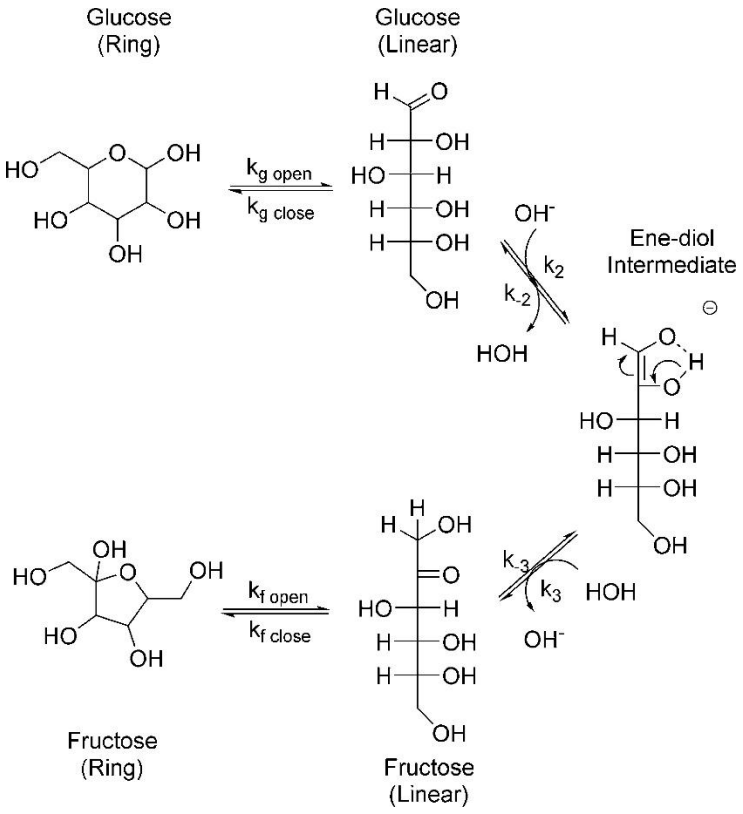

Scheme 4-2 Reaction mechanism for the homogeneous phase base-catalysed isomerization of glucose to fructose.

Since base-catalysed isomerisation is one of the possible mechanism, solid base catalysts can be used for glucose isomerization such as basic resins, metal oxides and hydrotalcites. [167] Furthermore, thanks to easy product identification and manageable experimental setup, glucose isomerisation has been chosen as model reaction to evaluate the different surface properties of ashes-derived HAPs.

Alongside these established materials**,** hydroxyapatites (HAP) derived from waste incinerator ashes are emerging as a sustainable inorganic base catalyst, as in the previous paragraph marked basicity and stability after water treatment have been assessed. Through this first evaluation by this specific reaction model, waste derived HAP samples could open the possibility to behave as catalytic materials for biomass valorisation. The choice of selecting the isomerisation of glucose as catalytic reaction for HAP samples is related to the consideration of this reaction as a model one. In heterogenous catalysis, model reactions are well-defined transformations, characterized by a known and widely accepted reaction mechanism. The concrete information about one specific reaction

make it suitable for extracting fundamental structure-activity relationships. By relying on these "known" systems, model reactions allow the identification of the key physico-chemical features that a catalyst must possess such as specific surface area, porosity, nature and strength of active sites, their accessibility and so on. A model reaction can be viewed as a diagnostic tool to reevaluate rationally the material optimization.[168] The glucose isomerisation to fructose represents a prototype of base-catalysed enediol mechanism reaction. Owing to this well-established pathway, it enables a rational evaluation of the correlation between catalytic activity (conversion and selectivity) and the morphological and surface properties of the ash-derived HAP samples. In particular, relationship can be drawn with porosity, number of acidic-basic sites, the influence of amphoteric character, and catalyst stability under aqueous conditions, which is critical for reactions involving biomass-derived substrates.[169] More broadly, the use of model reactions also provides valuable information on experimental design, helping to identify suitable reaction conditions and analytical protocols, as well as practical limitations such as mass transfer effects, catalyst deactivation, and reproducibility issues.

Following the procedure explained in the Experimental section (2.4), independent tests were carried out on the four ashes-derived HAP samples at fixed temperature (120°C). In **Figure** 4-21, the main catalytic results are displayed: for each HAP, the moles of glucose converted, and the moles of fructose produced are depicted as a function of time. The glucose isomerisation as already mentioned is an equilibrium reaction and for all the four curves the same trend can be observed: after a drop of glucose moles in the first 30 minutes, a plateau is reached. In the meantime, the fructose curve also reaches a steady state after an initial increasing in moles.

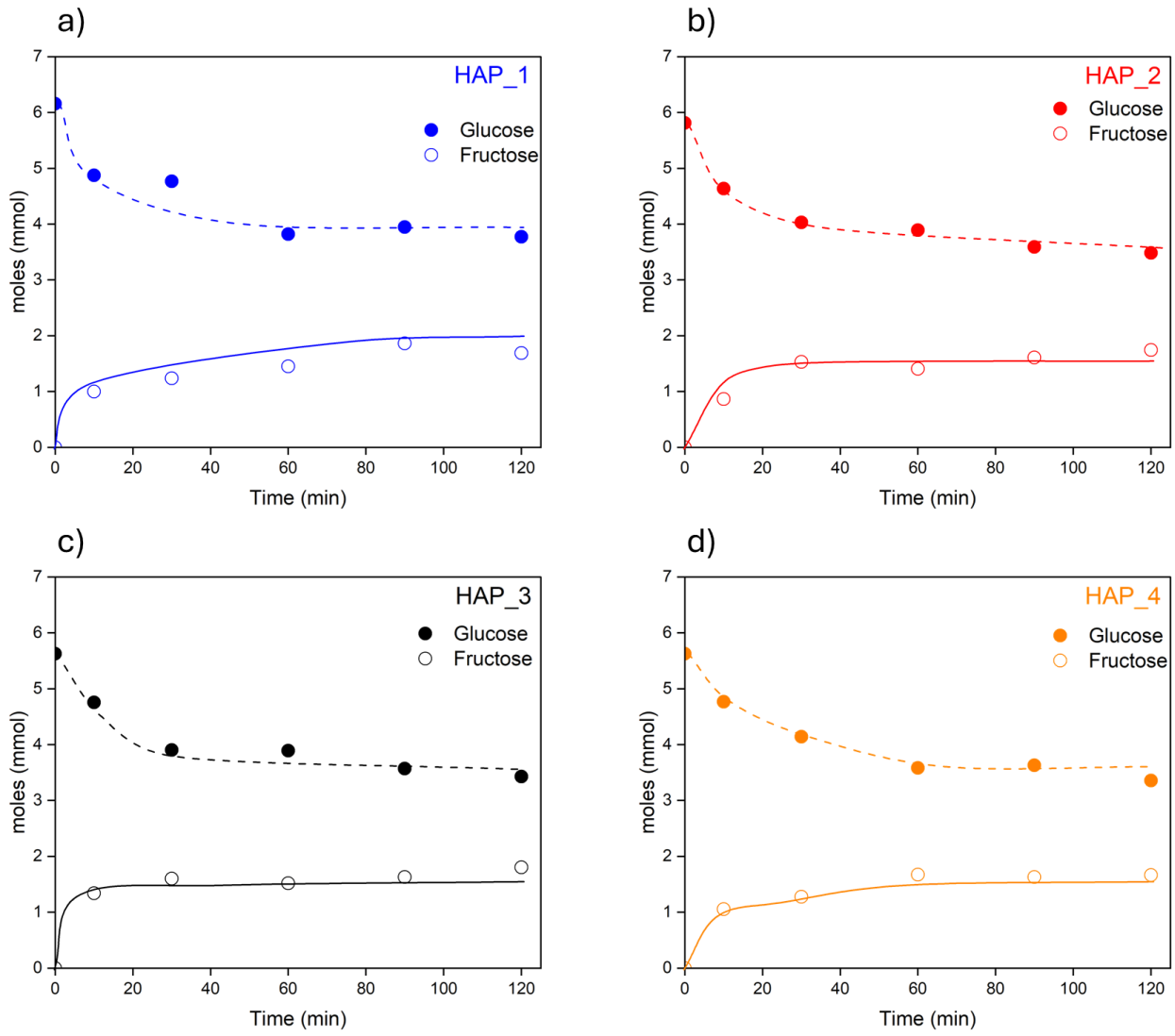

Figure 4-21 Results of the batch catalytic reaction of glucose isomerisation to fructose in water carried out at 120°C on a) HAP_1, b) HAP_2, c) HAP_3 and d) HAP_4 samples as function of time, expressed as residual glucose moles (full markers) and fructose moles detected (empty markers). Each experimental point is the result of independent catalytic test.

As the behaviour of the curves is almost complementary in a mirror-image way, the equilibrium reaction behaviour is further confirmed. Furthermore, as no other significant concentrated products are detected and the fructose curve is quite steady, the catalytic isomerisation could be assessed as high selective towards fructose as main product. In **Table** 4-8, the main results of conversion, selectivity and carbon balance are reported for all the four HAP samples. Two different behaviour can be distinguished, HAP_1 and HAP_2 showed conversion around 40% but selectivity around

70%; on the other hand, HAP_3 and HAP_4 showed lower conversion (34% and 26%, respectively) but quite higher selectivity (≈ 90%). The selectivity trend is then confirmed by carbon balance calculation, where HAP_1 and HAP_2 showed lower carbon balance. In fact, the samples (HAP_1 and HAP_2) after the reaction appears more brownish, as a result of higher carbon deposition on the surface in the forms of humins, that are the main byproduct in the biomass valorisation reactions. The conversion as a function time, displayed in **Figure** 4-22-a, further confirms the different behaviour of the first two samples in respect to the HAP_3 and HAP_4. The curves increased more rapidly for HAP_1 and HAP_2 rather than the other two HAPs, meaning higher activity for glucose isomerisation; on the other hand, this higher activity led for both samples, deactivation leading to lower selectivity and lower carbon balance, as mentioned before. Finally, the evaluation of initial velocity could be a further proof of different catalytic trends.

Table 4-8 Main catalytic results of Glucose isomerisation to fructose on ashes-derived HAP samples-

Sample	Conversion[a]	Normalized conversion[b]	Selectivity[a]	Carbon balance[a]	Initial velocity
	%	%	%	%	mmol g^{-1} min^{-1}
HAP_1	39	64	68	87	0.62
HAP_2	40	66	72	89	0.58
HAP_3	34	56	96	99	0.43
HAP_4	36	59	86	95	0.42

a. The values reported are calculated after 120 min, carrying out glucose isomerisation reaction at 120°C.
b. The normalization is carried out using equilibrium conversion (61 %) calculated from equilibrium constant (K_{eq} = 1.56) and free Gibbs energy at 120°C, using Tewari et al. extrapolation[49].

The results are reported in **Table** 4-8 and **Figure** 4-22-b. all the results were normalized for the mass of catalyst used in the catalytic reaction, keeping the catalyst-substrate ration constant (1:5). Even for kinetic evaluation, the first two HAP sample showed higher initial velocity: 0.62 mmol t^{-1} g^{-1} for HAP_1 being the “fastest” catalyst and 0.58 mmol t^{-1} g^{-1} for HAP_2. The initial velocity for HAP_3 and HAP_4 was quite lower than first and second HAP samples, with very similar value around 40 mmol t^{-1} g^{-1}.

It is important to underline that, glucose isomerisation has a thermodynamic value of equilibrium which corresponds to the maximum conversion at fixed temperature. Due to the correlation between, temperature, free Gibbs energy and equilibrium constant, an equilibrium conversion can be calculated, as explained in the Supplementary Information (6.3). Through the comparison with equilibrium conversion (61 %), all the four HAP samples reaches glucose conversion above 50%, shifting the reaction towards the fructose product. As expected, HAP_1 and HAP_2 remain the most active sample with a normalized conversion of 64% and 66%, respectively, among all the four ashes-derived hydroxyapatite. HAP_3 and HAP_4 have conversion values slightly lower than the first two HAPs, with 56 and 59% respectively.

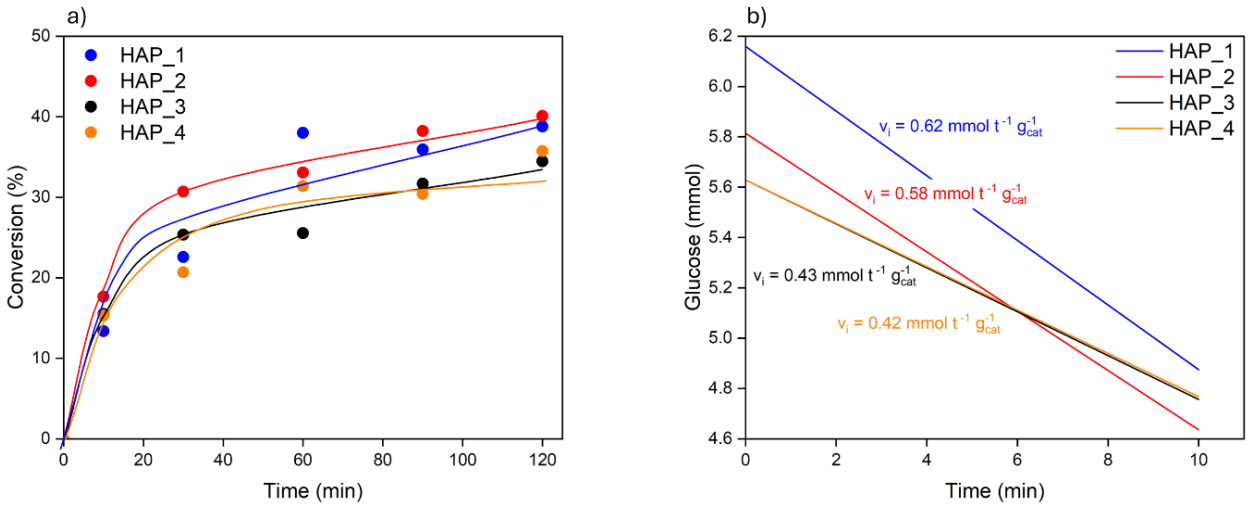

Figure 4-22 a) Conversion curves of ashes derived HAP samples in glucose isomerisation reaction to fructose carried out in water at 120°C, as a function of time; b) evaluation of initial rate of glucose isomerisation normalized by the mass catalyst.

To highlight the different properties of ashes-derived HAPs, a comparison with synthetic HAP was carried out. In **Figure** 4-23, the conversion results are reported both compared with equilibrium curve (a) and with all the tested HAPs at 120°C for 120 minutes. In all cases, HAPs from ashes demonstrate higher conversion than synthetic HAP. The main difference is related to lower amount of acid and basic sites, as reported in literature.[170] Furthermore, acido-basicity in water is completely changed in respect to the intrinsic amphotericity so it is lowered even more when synthetic HAP is

used as catalyst in water; on the other hand, even though ashes derived HAPs showed a lower amount of total sites in water, the effective sites are higher than stoichiometric HAP leading to higher conversion of glucose to fructose.

As briefly mentioned, higher conversion is directly related to the number of acidic-basic sites. Going further, two distinct situations can be identified: HAP_1 and HAP_2 showed higher conversion and lower selectivity leading to fast deactivation as carbon balance is far from 100%, while HAP_3 and HAP_4 have the opposite behaviour: lower conversion but higher selectivity towards fructose.

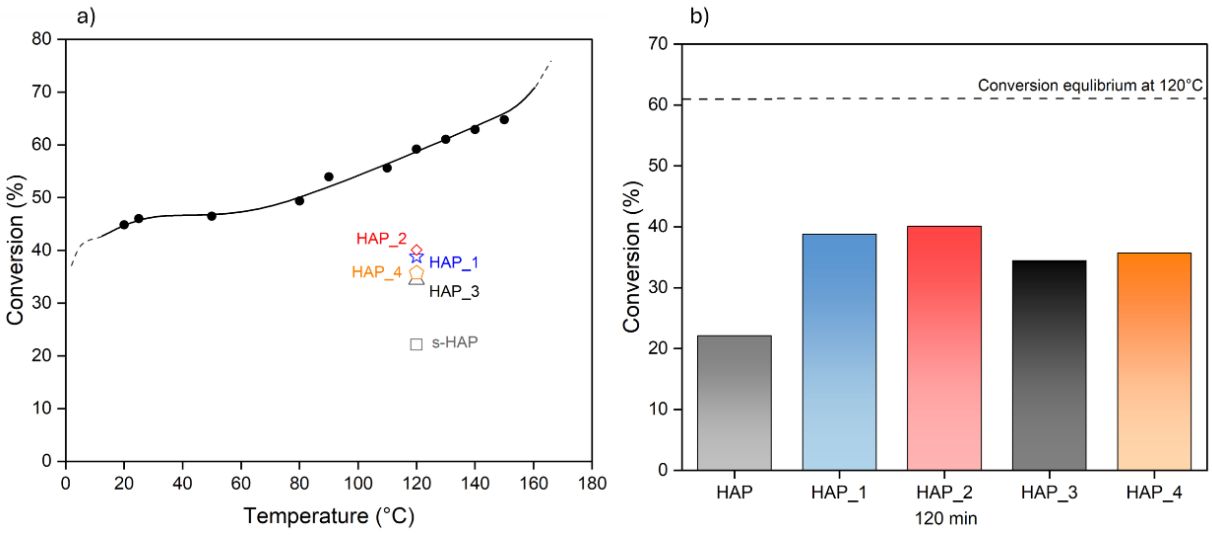

Figure 4-23 a) Equilibrium conversion curve (black markers and continuous line) calculated from elaboration of equilibrium constant at different temperatures (Paragraph 6.3) and glucose conversion of HAP samples (empty markers) at 120°C after 120 min; b) comparison of glucose conversion of different HAP samples (synthetic and ashes derived samples) at 120°C after 120 min.

Since conversion values are very similar (around 40%), it is important to focus on the relationship between selectivity and acido-basicity of HAP samples. As reported in **Figure** 4-24, the lower number of sites of HAP_1 and HAP_2 results in moderately higher glucose conversion (40% rather than 30% for HAP_3 and HAP_4) but limits fructose formation. In particular, the reduced availability of basic sites constrains the initial deprotonation step, which is crucial for initiating the isomerization pathway. In contrast, HAP_3 and HAP_4 exhibit a higher overall number of active sites, with a pronounced contribution from basic functionalities, which significantly affects reaction selectivity,

reaching values above 80%. The enhanced basicity correlates with increased fructose production, in agreement with mechanisms reported for homogeneous base-catalysed systems. According to literature, the deprotonation step is the rate-limiting and basic moieties can help in overcoming this kinetic barrier. As the reaction proceeds, enediol formation is followed by reprotonation of the acyclic intermediate, leading to fructose while suppressing condensation side reactions. This final step is found to be an intramolecular step which can be co-helped by external parameters (solvent or co-factor).[171,172] In this specific case, the re-protonation could be assisted by the acidic moieties of HAP_3 and HAP_4, which could both justify the higher selectivity towards fructose and limit the formation of humins.[172]

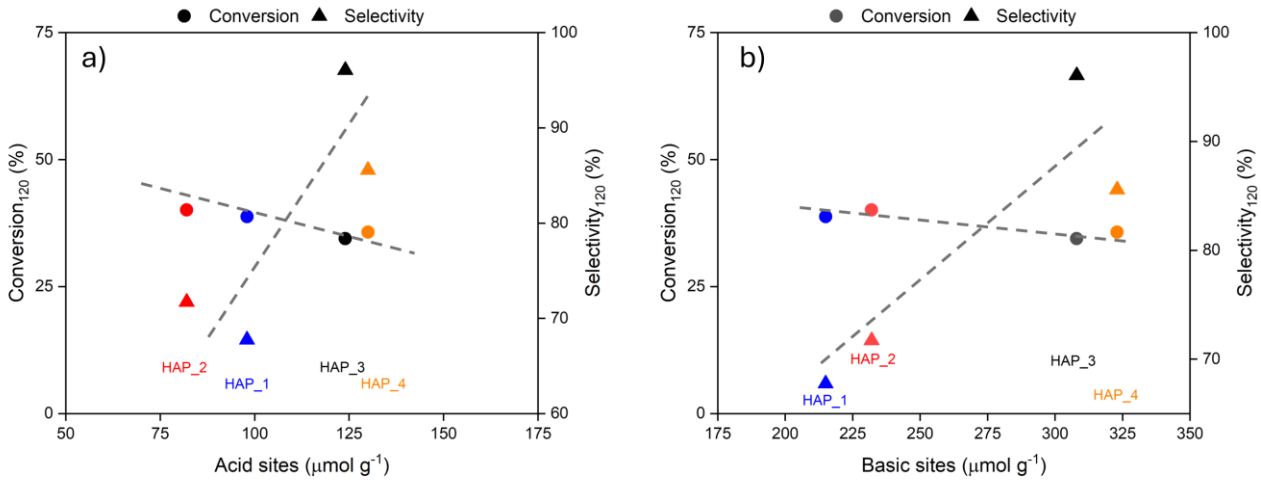

Figure 4-24 Correlation of glucose conversion and fructose selectivity at 120°C after 120 min with a) total acid sites of ashes derived HAP samples measured by solid-liquid phase titration at 30°C in cyclohexane (Paragraph 4.2.4.2); b) total basic sites of ashes derived HAP samples measured by solid-liquid phase titration at30°C in cyclohexane (Paragraph 4.2.4.2).

Finally, the catalytic results coupled with kinetic evaluation and possible proposed mechanism, confirmed once again the main differences between HAP_1-HAP_2 and HAP_3-HAP_4: While each pair shows high internal similarity in terms of structure, surface properties, and catalytic response, pronounced differences can be observed between the two groups. Once more, HAP_1 and HAP_2, that exhibit a higher degree of crystallinity, are characterized by fewer and slightly weaker acid-base sites, which translates into a lower selectivity. In contrast, HAP_3 and HAP_4, which display a more

amorphous character, result in higher number of stronger acid-base sites, leading to significantly enhanced activity in glucose isomerization.

4.2.5. Comparison with stoichiometric HAP

The ashes derived hydroxyapatite showed different properties mainly related to the process parameters of the extraction (dripping time, maturation time, mixing). Two distinguished class of ashes derived HAP were obtained: HAP_1 and HAP_2 more crystalline with oriented crystallites with needle-like morphology and HAP_3 and HAP_4 with more amorphous phase composed of disordered agglomerated crystallite. Even though morphological evidence shows two kinds of different hydroxyapatites, the surface properties are generally similar concerning amphotericity index or exposed acid-base sites. To highlight new features and properties of sustainable HAP derived from ashes, a comparison between these samples and synthetic HAP was carried out.

Synthetic HAP (s-HAP) was precipitated from calcium and phosphorus precursor solutions to obtain a stoichiometric HAP with Ca/P ratio of 1.67. As discussed in Paragraph 2.1.1.1, the experimental conditions during precipitation are critical for controlling the formation of specific calcium phosphate phases. To ensure the precipitation of pure s-HAP, high temperature (80 °C) and basic pH (10) were maintained throughout the synthesis. Ashes derived HAP samples and synthetic HAP are compared in terms of composition, morphology, and surface characterization.

From a preliminary comparison, it is important to highlight that synthetic HAP tends to crystallize in needle/rod-like shape, elongated along the c-axis. Since the conditions of synthesis are like the extraction parameters of the first two ashes derived hydroxyapatites, s-HAP, HAP_1 and HAP_2 possess high crystallinity with ordered crystallites in the range of 5 up to 30 nm. From a morphological view, N_2 adsorption/desorption isotherm display a type IV isotherm as the ashes-derived samples. From the elaboration through the BET equation, specific surface area (SSA) was calculated and compared with the ashes HAP samples.

The waste derived hydroxyapatites have similar SSA (from 80 to 100 m^2 g^{-1}) as showed in **Figure** 4-25, meaning that the formation of hydroxyapatites from inorganic salts or by controlled extractions, lead to the formation of highly mesoporous materials with similar surface area.[173] Notably s-HAP and HAP_2 have similar surface area, lower than the other sample, due to the high crystallinity of samples, as expected. The higher the crystallinity often corresponds to lower surface area due to the low defects on the surface and in the pores which does not allow molecules (such as N_2) to adsorb.

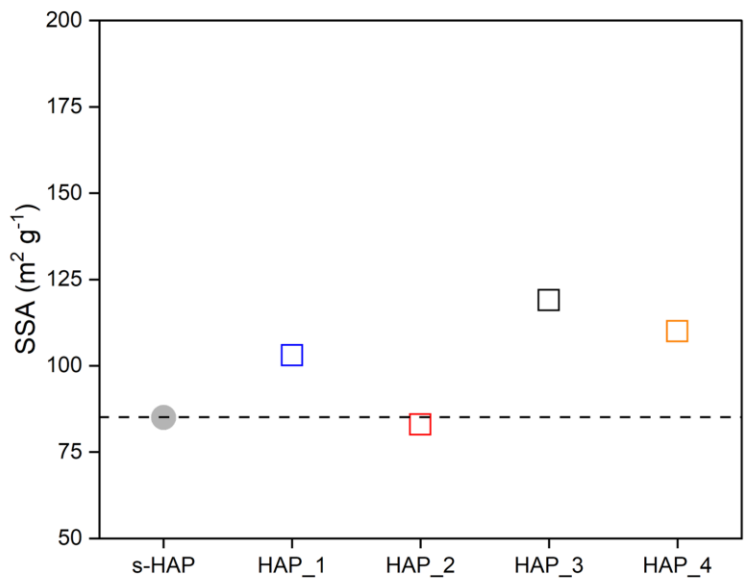

Figure 4-25 Comparison of the specific surface area values (SSA), calculated with BET equation from N_2 adsorption/desorption isotherms of synthetic HAP and ashes derived HAP samples.

As discussed in the previous paragraphs, the surface reactivity and the surface characteristics of ashes-derived HAP samples were discussed highlighting the overall basicity of the samples, leading to exploit the shifted amphotericity in base-catalysed reaction such as glucose isomerization. To further emphasize this specific features due to the different initial source (inorganic salts or ashes) and formation procedures (co-precipitation or extraction), a comparison between the amphoteric index was carried out, and reported in **Figure** 4-26. Furthermore, as reported in literature, the higher

the Ca/P ratio (Ca/P > 1.67), the higher the basicity: for this reason, Ca/P ratio (calculated from ICP-OES) was selected as independent variable.

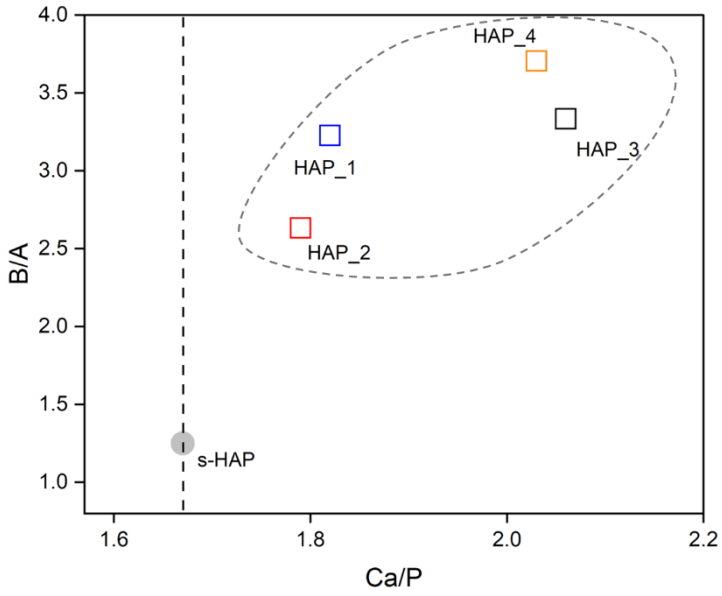

Figure 4-26 Amphotericity index A/B, calculated from the total sites derived from adsorption isotherms obtained via solid-liquid titration with PEA or BA in cyclohexane at 30°C, as a function of Ca/P ratio of each sample, for both synthetic HAP and ash-derived HAP.

B/A ratio was calculated from the adsorption isotherms of the solid-liquid titration with PEA and BA in cyclohexane at 30°C. As expected, synthetic HAP possess a more amphoteric surface (all the results of acido-basicity are reported in and **Table** S-6-6 and **Table** S-6-7), as B/A ratio is very close to 1 while the family of ashes derived HAP samples expose a more basic sites, particularly, with the more amorphous samples (HAP_3 and HAP_4) having higher total basic sites.

Furthermore, another important characteristic is the behaviour of HAP surfaces in water and how they interact with water molecules. The presence of different sites with different charges (Ca^{2+}, OH^- PO_4^{3-}, CO_3^{2-} and so on), can lead to different rearrangements of water molecules at the interface. For solid materials, an important characteristic is the point of zero charge (PZC), which determines the surface charge of the material. The PZC is defined as the pH value at which the surface exhibits no net charge, meaning electroneutrality on the surface. For example, when the pH is higher than

the PZC, deprotonated surface groups predominate, leading to negative surface charge that can theoretically attracts positive ions and accept protons, acting as Bronsted base. Even in this case, a comparison was carried out between synthetic HAP (which possess an amphoteric surface) and ashes derived samples.

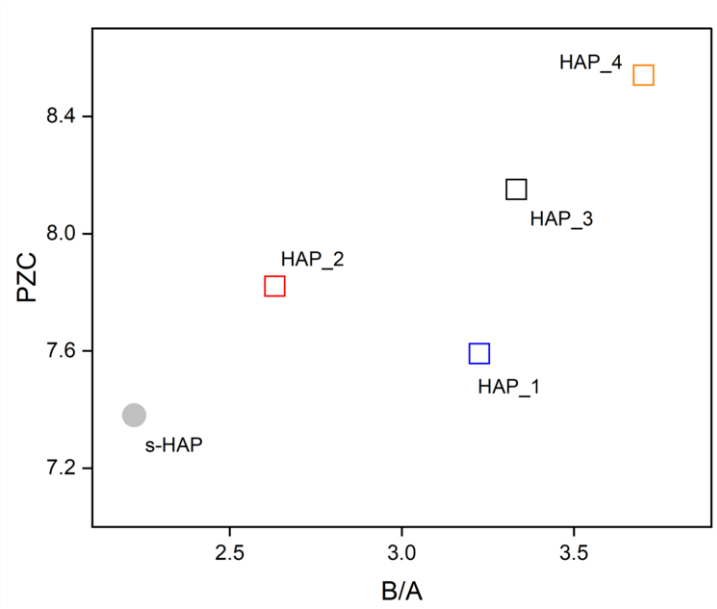

Figure 4-27 Point of zero charge as a function of basicity-acidity. ratio for synthetic HAP and ashes derived HAP samples.

In **Figure** 4-27, PZC is correlated with the amphotericity index of synthetic HAP and ashes-derived HAP samples. Even in this case, the more basic samples (HAP_3 and HAP_4) have the higher PZC (PZC > 8), leading to a negative charged surface. On the other hand, synthetic HAP impose a neutral pH to the aqueous layer with a PZC of 7.4, as expected from literature. In case of water exposure, the hydrated layer discussed in the previous paragraph will be arranged attracting the positive hydrogen ends of water molecules. Because of this new rearrangement, the attraction forces water molecules to align in a specific orientation relative to the surface, disrupting the natural hydrogen bonds network and creating a more ordered structure near the surface.

Ashes-derived HAP samples demonstrate a pronounced basicity. Different works explained that the primary factor governing the acid-base properties of HAP is the Ca/P molar ratio, typically adjusted

by varying precursor concentrations during synthesis or controlling extraction parameters. However, Ca/P ratio is not the only factors: the surface chemistry of HAP is far more complex. In fact, degree of carbonation, presence of hydroxyl groups and defects could play a decisive role in determining the amphotericity nature of the final HAP catalyst. [174–177]

4.3. Concluding remarks

The development of sustainable materials represents a key strategy toward circular and low-impact technologies, as exemplified by biochar from sugarcane waste and hydroxyapatite from ashes.

Vegetable biomasses have gained recognition as flexible and sustainable alternatives for carbon-based materials. Leveraging biomass as a feedstock for carbon production provides a renewable and environmentally friendly approach, aligning with the growing demand for cleaner energy technologies. In this chapter, a very preliminary study has been conducted on sugarcane biomasses with thermal treatment as main biochar conversion techniques. The main focus was the sugarcane feedstock, whose properties with a proper control of pyrolysis temperature, led to enhanced porosity, large surface area, and enhanced graphitization, which make them ideal for applications such as supercapacitors, batteries, fuel cell and good support for CO_2 electrocatalyst. Starting from these findings, different biomasses will be further investigated (such as cotton fibre and waste from paper industry) combining innovative raw materials with different pyrolytic techniques, that can enhance further the morphological and structural properties of the obtained biochar. Alongside the preliminary studies of sustainable carbon materials, deep studies on ashes derived HAP samples have been conducted. In conclusion, hydroxyapatite from ashes exhibit a complex and tuneable surface chemistry, different composition and diverse structural order, that are all strongly influenced by its extraction procedure. Regarding the importance of surface chemistry of HAP, the ash-derived samples show a clear amphoteric character, with a predominance of basic sites over acidic ones, particularly in the more amorphous (and Ca-richer) samples. Moreover, the presence of water clearly affects the surface reactivity, hindering both acidic and basic sites, but under drying, the surface (and the bulk properties) of HAPs return as the “fresh” sample, confirming that all the transformation on HAP samples, are largely reversible. These analyses underscore the dynamic nature of HAP surfaces: HAP confirmed to be a responsive system, which properties can be tailored. In this way, ashes-derived HAP samples become promising candidates for application where controlled surface reactivity is requires, such as biomass transformation reaction (i.e. glucose isomerisation over basic catalysis).

Building on these findings, biochar from sugarcane with good morphological properties and tuneable HAP from ashes can be combined for an optimal composite for CO_2ER. As main future perspective these composites could offer a synergistic platform for the reduction of carbon dioxide: carbon phase ensures electrical conductivity, metal sites drive selective CO_2 conversion, and HAP tunes the local chemical environment through acid-base interactions and water-mediated surface dynamics.

5. Concluding remarks and future perspectives.

This dissertation explored the sustainability concept as a common factor that correlates materials design, process innovation, environmental remediation, and circular economy principles. Particularly, environmental issues can be addressed through developing both sustainable processes and materials. In this work, innovative CO_2 remediation strategies and material engineering are presented and driven by sustainability principles.

From a process perspective, the thesis presents examples of CO_2 conversion routes, based on electrochemistry or bio-electrochemistry, where carbon dioxide is transformed into value-added chemicals or energy carriers. For the bioelectromethanogenesis process, a power-to-gas pathway was studied, besides contributing to CO_2 remediation, also advancing circular energy system technologies. Through the studies of biocompatible composite and highlighting the role of hydroxyapatite as a key inorganic component for biological systems, the dissertation advanced in understanding the reaction mechanism, interfacial phenomena, and catalytic selectivity. HAP-containing electrodes enhanced CH_4 production compared to HAP-free systems by increasing surface area, buffering local pH, adsorbing bicarbonate species, and promoting microbial adhesion. In this way, biological and electrochemical CO_2 conversion could be interconnected and can be exploited for environmental remediation, leading to energetic advantages.

On the electrochemical pathways, the focus was on the design of a composite that enhances the single features of single component and with a synergistic work could tailor the CO_2 reduction selectivity, overcoming the main disadvantage of the composite used in biochemical processes. In this work, a one-pot synthetic strategy led to binary or ternary composites, with a high intimate contact among the phases, that are also able to reduce CO_2 in a highly selective way, opening routes to other processes such as the application in bioelectromethanogenesis processes. With this synthetic pathway, the modulation and the combination of single components could modulate also the added-value products of carbon dioxide reduction. Structural analyses confirmed effective integration of CN, Cu, and HAP. When tested for CO_2 electroreduction (CO_2ER), HAP_Cu@CN

achieved 60% Faradaic efficiency toward formate at −1.0 V vs RHE, with H_2 as the only by-product, demonstrating that HAP steers selectivity by modifying the interfacial environment and stabilizing intermediates without significantly compromising charge transfer. On the other hand, Cu@CN showed higher selectivity towards methane, with preserving high conductivity of the material.

At the same time, strong emphasis was placed on the development of tailored materials both organic and inorganic, designed to meet specific requirements. Carbon-based materials derived from vegetable biomass were studied to optimize both graphitization and morphology, achieving high porous carbon scaffolds: Sugarcane-derived biochar, produced at two pyrolysis temperatures (600 and 900°C), exhibited significantly enhanced surface area (up to 200 $m^2\ g^{-1}$) and increased graphitic character compared to previously used biochar, indicating improved conductivity and suitability for electrochemical applications. In parallel, hydroxyapatites from ashes were extracted and deeply studied. Through the modulation of extraction parameters, different HAPs have been obtained with enhanced surface properties quite different from synthetic hydroxyapatite. As result, the four materials demonstrated tuneable crystallinity, Ca/P ratios, and acid-base surface properties. While bulk compositional differences were observed, all samples retained structural features comparable to synthetic HAP. Surface analyses revealed that more amorphous samples possessed higher densities of predominantly basic sites, advantageous for catalytic applications. Their morphology and surface reactivity, sensitive to synthesis conditions, make ash-derived HAPs a sustainable and tuneable platform for catalytic and electrochemical applications.

The study of sustainable materials, different designs of composite preparations, and the application of these composites in CO2 reduction processes are summarized in **Scheme** 5-1. Combining waste valorization through pyrolysis and chemical extraction to produce materials suitable for CO2 remediation demonstrates that chemistry and sustainability principles can work together to address environmental issues.

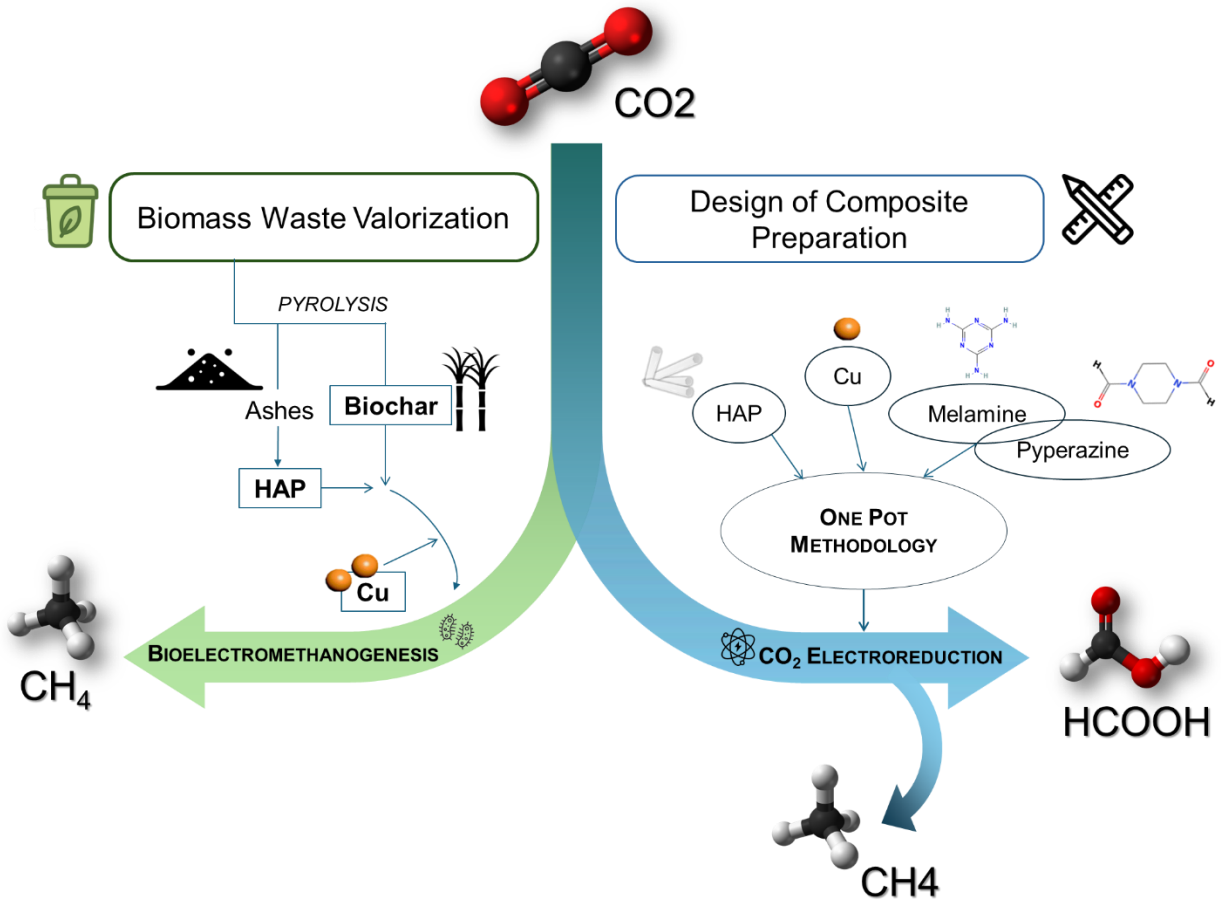

Scheme 5-1 Schematic representation of the two main aspects discussed in the thesis: the recovery of components from biomass waste and their utilization in composite materials for CO_2 remediation techniques (bioelectromethanogenesis and conventional CO_2 electroreduction (CO_2ER)).

After rationally tailored properties of organic and inorganic materials, the combination of both is the following step to produce the optimal composite materials for the application in remediation processes. Therefore, the rational coupling of optimized organic scaffolds with functional inorganic phases represents a key step toward designing composite materials with enhanced activity, selectivity, and stability. By leveraging the complementary properties of each component, these hybrid systems can be tailored to address the multifactorial requirements of CO_2ER and related remediation technologies, ultimately advancing the development of efficient and sustainable catalytic platforms.

Regarding bioelectromethanogenesis, future studies for should also investigate the interaction between these composites and microbial communities, evaluating possible effects on microbial adhesion, biofilm formation, and metabolic activity of the microorganisms. Once assessed the optimal components and the optimal biochemical features, the studies are essential to determine whether these materials could be effectively employed as cathodes in hybrid processes, such as bioelectromethanogenesis or other CO_2 conversion systems.

By integrating complementing properties including conductivity, catalytic activity, and surface functionality, composite materials provide significant benefits in both bioelectrochemical and CO_2 electroreduction systems. The composites used in bioelectromethanogenesis offer a more robust and biocompatible interface for microorganisms, which encourages microbial adhesion and improves long-term performance. Changing the methodology of design for CO_2ER composites lead to the optimization of the dispersion of each component which reflected to the local reaction environment and the effectiveness of charge transfer. These composites allow for customizable selectivity (CH_4 or $HCOO^-$). Furthermore, a greener-focused strategy has been implemented by investigating substitute sources for hydroxyapatite and biochar, such as biomass and materials obtained from waste, which helps to create catalytic systems that are more sustainable.

Overall, this work demonstrates that sustainable chemistry can be applied in different fields: looking for green materials, structural design and improving catalytic processes. By combining CO_2 remediation technique with material engineering, the thesis tries to offer a contribution both to environmental issues and to the sustainability of materials. The strategies explored in this work, tailoring organic and inorganic materials for sustainable application, may serve as a starting point for future investigations aimed at developing more efficient composites that can be exploited in environmental remediation processes, which can exploit chemical or chemo-biological pathways where catalysts can improve the overall efficiency.

6. References

(1) TECHNICAL SUMMARY CLIMATE CHANGE 2001: IMPACTS, ADAPTATION, AND VULNERABILITY A Report of Working Group II of the Intergovernmental Panel on Climate Change.

(2) Purvis, B.; Mao, Y.; Robinson, D. Three Pillars of Sustainability: In Search of Conceptual Origins. *Sustain. Sci.* **2019**, *14* (3), 681–695. https://doi.org/10.1007/S11625-018-0627-5/FIGURES/1.

(3) *Chemistry & the UN Sustainable Development Goals - American Chemical Society*. https://www.acs.org/green-chemistry-sustainability/education/chemistry-sustainable-development-goals.html (accessed 2025-10-26).

(4) *Home - United Nations Sustainable Development*. https://www.un.org/sustainabledevelopment/ (accessed 2026-01-03).

(5) *Materia rinnovabile - Circularity*. https://circularity.com/circularguide/materia-rinnovabile/ (accessed 2026-01-03).

(6) Slootweg, J. C. Sustainable Chemistry: Green, Circular, and Safe-by-Design. *One Earth* **2024**, *7* (5), 754–758. https://doi.org/10.1016/j.oneear.2024.04.006.

(7) Fu, D.; Davis, M. E. Carbon Dioxide Capture with Zeotype Materials. *Chem. Soc. Rev.* **2022**, *51* (22), 9340–9370. https://doi.org/10.1039/D2CS00508E.

(8) Bamisaye, M. E.; Ajayi, B. O.; Sereewatthanawut, I. Sustainable Waste Management of Construction Materials: Mathematical Modelling and Analysis. *Resources, Conservation & Recycling Advances* **2025**, *27*, 200274. https://doi.org/10.1016/J.RCRADV.2025.200274.

(9) *CO2 Emissions – Global Energy Review 2025 – Analysis - IEA*. https://www.iea.org/reports/global-energy-review-2025/co2-emissions (accessed 2025-10-26).

(10) Singh, G. J.; Singh, P. K.; Lal, P. Dynamic Approach to Study Relationship Among Carbon Dioxide Emissions, Urbanization, and Economic Growth in BRICS Countries. *Journal of the Knowledge Economy* **2024**, *16* (1), 3386–3403. https://doi.org/10.1007/S13132-024-01964-3/FIGURES/1.

(11) Barati, K.; Khojasteh-Salkuyeh, Y.; Ashrafi, O.; Navarri, P. Electrified Combined Reforming of Methane Process for More Effective CO2 Conversion to Methanol: Process Development and Environmental Impact Assessment. *Energy Convers. Manag.* **2023**, *287*, 117096. https://doi.org/10.1016/J.ENCONMAN.2023.117096.

(12) Hanson, E.; Nwakile, C.; Hammed, V. O. Carbon Capture, Utilization, and Storage (CCUS) Technologies: Evaluating the Effectiveness of Advanced CCUS Solutions for Reducing CO2 Emissions. *Results in Surfaces and Interfaces* **2025**, *18*, 100381. https://doi.org/10.1016/J.RSURFI.2024.100381.

(13) Yaashikaa, P. R.; Senthil Kumar, P.; Saravanan, A.; Karishma, S.; Rangasamy, G. A Biotechnological Roadmap for Decarbonization Systems Combined into Bioenergy Production: Prelude of Environmental Life-Cycle Assessment. *Chemosphere* **2023**, *329*, 138670. https://doi.org/10.1016/J.CHEMOSPHERE.2023.138670.

(14) Ketabchi, M. R.; Babamohammadi, S.; Davies, W. G.; Gorbounov, M.; Masoudi Soltani, S. Latest Advances and Challenges in Carbon Capture Using Bio-Based Sorbents: A State-of-the-Art Review. *Carbon Capture Science & Technology* **2023**, *6*, 100087. https://doi.org/10.1016/J.CCST.2022.100087.

(15) Soo, X. Y. D.; Lee, J. J. C.; Wu, W. Y.; Tao, L.; Wang, C.; Zhu, Q.; Bu, J. Advancements in CO2 Capture by Absorption and Adsorption: A Comprehensive Review. *Journal of CO2 Utilization* **2024**, *81*, 102727. https://doi.org/10.1016/J.JCOU.2024.102727.

(16) Chung, W.; Lim, H.; Lee, J. S.; Al-Hunaidy, A. S.; Imran, H.; Jamal, A.; Roh, K.; Lee, J. H. Computer-Aided Identification and Evaluation of Technologies for Sustainable Carbon Capture and Utilization Using a Superstructure Approach. *Journal of CO2 Utilization* **2022**, *61*, 102032. https://doi.org/10.1016/J.JCOU.2022.102032.

(17) Overview of Technological Pathways for CO2.

(18) Bakonyi, P.; Koók, L.; Rózsenberszki, T.; Kalauz-Simon, V.; Bélafi-Bakó, K.; Nemestóthy, N. CO2-Refinery through Microbial Electrosynthesis (MES): A Concise Review on Design, Operation, Biocatalysts and Perspectives. *Journal of CO2 Utilization* **2023**, *67*, 102348. https://doi.org/10.1016/J.JCOU.2022.102348.

(19) Enzmann, F.; Gronemeier, D.; Holtmann, D. Evaluation of Bioelectromethanogenesis Part I: Energy Calculations. *Chemie Ingenieur Technik* **2020**, *92* (1–2), 137–143. https://doi.org/10.1002/CITE.201900106.

(20) Goglio, A.; Carrara, A.; Elboghdady, H. G. E.; Cucina, M.; Clagnan, E.; Soggia, G.; De Nisi, P.; Adani, F. The Performance of Biochar Waste-Derived Electrodes in Different Bio-Electrochemical Applications. *J. Power Sources* **2025**, *625*, 235623. https://doi.org/10.1016/J.JPOWSOUR.2024.235623.

(21) Hori, Y.; Wakebe, H.; Tsukamoto, T.; Koga, O. Electrocatalytic Process of CO Selectivity in Electrochemical Reduction of CO2 at Metal Electrodes in Aqueous Media. *Electrochim. Acta* **1994**, *39* (11–12), 1833–1839. https://doi.org/10.1016/0013-4686(94)85172-7.

(22) Liu, K. Catalysts and Operating Conditions for Electrochemical Reduction of Carbon Dioxide. https://doi.org/10.4233/uuid:7e395294-c8da-4f71-8422-7d0f8a2be9c8.

(23) Saini, P.; Kumar, K.; Saini, S.; Sethi, M.; Meena, P.; Gurjar, A.; Weigand, W.; Parewa, V. Photocatalytic Single Electron Reduction of CO2 into Carbon Dioxide Radical Anion ($CO_2^{\cdot-}$): Generation, Detection and Chemical Utilization. *Journal of Energy Chemistry* **2025**, *105*, 525–559. https://doi.org/10.1016/J.JECHEM.2025.02.013.

(24) Huo, Z.; Song, Z.; Ren, D.; Liu, Y. Thermodynamics of Co2 Electroreduction. *Electrochemical Reduction of Carbon Dioxide: Fundamentals and Technologies* **2016**, 47–102. https://doi.org/10.1201/B20177-3.

(25) Electrochemical Reduction of Carbon Dioxide: Overcoming the Limitations of Photosynthesis. **2018**. https://doi.org/10.1039/9781782623809.

(26) Wang, J.; Cheng, T.; Fenwick, A. Q.; Baroud, T. N.; Rosas-Hernándezhernández, A.; Ko, H.; Gan, Q.; Iii, W. A. G.; Grubbs, R. H. Selective CO 2 Electrochemical Reduction Enabled by a Tricomponent Copolymer Modifier on a Copper Surface. *J. Am. Chem. Soc* **2021**, *143*. https://doi.org/10.1021/jacs.0c12478.

(27) Allwood, J. M. Sustainable Materials. *Nat. Rev. Mater.* **2016**, *1* (1), 1–2. https://doi.org/10.1038/NATREVMATS.2015.9;SUBJMETA.

(28) Chu, S.; Majumdar, A. Opportunities and Challenges for a Sustainable Energy Future. *Nature* **2012**, *488* (7411), 294–303. https://doi.org/10.1038/NATURE11475.

(29) Kumar Gupta, G.; De, S.; Franco, A.; Balu, A. M.; Luque, R. Sustainable Biomaterials: Current Trends, Challenges and Applications. *Molecules 2016, Vol. 21, Page 48* **2015**, *21* (1), 48. https://doi.org/10.3390/MOLECULES21010048.

(30) Pradhan, S.; Abdelaal, A. H.; Mroue, K.; Al-Ansari, T.; Mackey, H. R.; McKay, G. Biochar from Vegetable Wastes: Agro-Environmental Characterization. *Biochar* **2020**, *2* (4), 439–453. https://doi.org/10.1007/S42773-020-00069-9/FIGURES/7.

(31) Xie, Y.; Wang, L.; Li, H.; Westholm, L. J.; Carvalho, L.; Thorin, E.; Yu, Z.; Yu, X.; Skreiberg, Ø. A Critical Review on Production, Modification and Utilization of Biochar. *J. Anal. Appl. Pyrolysis* **2022**, *161*, 105405. https://doi.org/10.1016/J.JAAP.2021.105405.

(32) Lee, J.; Kim, J.; Hyeon, T. Recent Progress in the Synthesis of Porous Carbon Materials. *Advanced Materials* **2006**, *18* (16), 2073–2094. https://doi.org/10.1002/ADMA.200501576.

(33) Yu, S.; Wang, L.; Li, Q.; Zhang, Y.; Zhou, H. Sustainable Carbon Materials from the Pyrolysis of Lignocellulosic Biomass. *Materials Today Sustainability* **2022**, *19*, 100209. https://doi.org/10.1016/J.MTSUST.2022.100209.

(34) Mishra, R. K.; Mohanty, K. A Review of the Next-Generation Biochar Production from Waste Biomass for Material Applications. *Science of The Total Environment* **2023**, *904*, 167171. https://doi.org/10.1016/J.SCITOTENV.2023.167171.

(35) Seow, Y. X.; Tan, Y. H.; Mubarak, N. M.; Kansedo, J.; Khalid, M.; Ibrahim, M. L.; Ghasemi, M. A Review on Biochar Production from Different Biomass Wastes by Recent Carbonization Technologies and Its Sustainable Applications. *J. Environ. Chem. Eng.* **2022**, *10* (1), 107017. https://doi.org/10.1016/J.JECE.2021.107017.

(36) Zafeer, M. K.; Menezes, R. A.; Venkatachalam, H.; Bhat, K. S. Sugarcane Bagasse-Based Biochar and Its Potential Applications: A Review. *Emergent Materials 2023 7:1* **2023**, *7* (1), 133–161. https://doi.org/10.1007/S42247-023-00603-Y.

(37) Kokalj, F.; Alivojvodić, V.; Lešnik, L.; Petronijević, N.; Radovanović, D.; Samec, N. Enhancing Utilization of Municipal Solid Waste Bottom Ash by the Stabilization of Heavy Metals. *Sustainability 2025, Vol. 17, Page 1078* **2025**, *17* (3), 1078. https://doi.org/10.3390/SU17031078.

(38) Karlfeldt Fedje, K.; Sjöstedt, S.; Strömvall, A. M. Evaluating the Potential of Phytoextraction on Waste-to-Energy Bottom Ash—a Review. *Environmental Science and Pollution Research 2025 32:18* **2025**, *32* (18), 11423–11442. https://doi.org/10.1007/S11356-025-36399-Z.

(39) Blasenbauer, D.; Huber, F.; Lederer, J.; Quina, M. J.; Blanc-Biscarat, D.; Bogush, A.; Bontempi, E.; Blondeau, J.; Chimenos, J. M.; Dahlbo, H.; Fagerqvist, J.; Giro-Paloma, J.; Hjelmar, O.; Hyks, J.; Keaney, J.; Lupsea-Toader, M.; O'Caollai, C. J.; Orupõld, K.; Pająk, T.; Simon, F. G.; Svecova, L.; Šyc, M.; Ulvang, R.; Vaajasaari, K.; Van Caneghem, J.; van Zomeren, A.; Vasarevičius, S.; Wégner, K.; Fellner, J. Legal Situation and Current Practice of Waste Incineration Bottom Ash Utilisation in Europe. *Waste Management* **2020**, *102*, 868–883. https://doi.org/10.1016/J.WASMAN.2019.11.031.

(40) Silva, R. V.; de Brito, J.; Lynn, C. J.; Dhir, R. K. Environmental Impacts of the Use of Bottom Ashes from Municipal Solid Waste Incineration: A Review. *Resour. Conserv. Recycl.* **2019**, *140*, 23–35. https://doi.org/10.1016/J.RESCONREC.2018.09.011.

(41) Chuchro, M.; Jędrusiak, R.; Bielowicz, B. Statistical Analyses of Precious Metal Contents in Waste Incineration Bottom Ashes. *Scientific Reports 2025 15:1* **2025**, *15* (1), 8149-. https://doi.org/10.1038/s41598-025-91855-7.

(42) Liu, Z. S.; Li, W. K.; Huang, C. Y. Synthesis of Mesoporous Silica Materials from Municipal Solid Waste Incinerator Bottom Ash. *Waste Management* **2014**, *34* (5), 893–900. https://doi.org/10.1016/J.WASMAN.2014.02.016.

(43) Ibrahim, M.; Labaki, M.; Giraudon, J. M.; Lamonier, J. F. Hydroxyapatite, a Multifunctional Material for Air, Water and Soil Pollution Control: A Review. *J. Hazard. Mater.* **2020**, *383*, 121139. https://doi.org/10.1016/J.JHAZMAT.2019.121139.

(44) Yook, H.; Hwang, J.; Yeo, W.; Bang, J.; Kim, J.; Kim, T. Y.; Choi, J. S.; Han, J. W. Design Strategies for Hydroxyapatite-Based Materials to Enhance Their Catalytic Performance and Applicability. *Advanced Materials* **2023**, *35* (43), 2204938. https://doi.org/10.1002/ADMA.202204938;ISSUE:ISSUE:DOI.

(45) Yook, H.; Hwang, J.; Yeo, W.; Bang, J.; Kim, J.; Kim, T. Y.; Choi, J.-S.; Han, J. W. Design Strategies for Hydroxyapatite-Based Materials to Enhance Their Catalytic Performance and Applicability (Adv. Mater. 43/2023). *Advanced Materials* **2023**, *35* (43), 2370313. https://doi.org/10.1002/ADMA.202370313.

(46) Abbasi, M.; Rashnavadi, M.; Gholami, M.; Molaei, S. Antibacterial Property of Hydroxyapatite Extracted from Biological Sources and Doped with Cu2+ and Ag+ by Sol-Gels Method. *Scientific Reports 2025 15:1* **2025**, *15* (1), 12101-. https://doi.org/10.1038/s41598-025-89886-1.

(47) Wang, P.; Li, C.; Gong, H.; Jiang, X.; Wang, H.; Li, K. Effects of Synthesis Conditions on the Morphology of Hydroxyapatite Nanoparticles Produced by Wet Chemical Process. *Powder Technol.* **2010**, *203* (2), 315–321. https://doi.org/10.1016/J.POWTEC.2010.05.023.

(48) Viggi, C. C.; Simonetti, S.; Palma, E.; Pagliaccia, P.; Braguglia, C.; Fazi, S.; Baronti, S.; Navarra, M. A.; Pettiti, I.; Koch, C.; Harnisch, F.; Aulenta, F. Enhancing Methane Production from Food Waste Fermentate Using Biochar: The Added Value of Electrochemical Testing in Pre-Selecting the Most Effective Type of Biochar Biotechnology for Biofuels. *Biotechnol. Biofuels* **2017**, *10*, 303. https://doi.org/10.1186/s13068-017-0994-7.

(49) Tewari, Y. B.; Goldberg, T. *Thermodynamics of the Conversion of Aqueous Glucose to Fructose*; 1984; Vol. 1.

(50) Pant, D.; Van Bogaert, G.; Diels, L.; Vanbroekhoven, K. A Review of the Substrates Used in Microbial Fuel Cells (MFCs) for Sustainable Energy Production. *Bioresour. Technol.* **2010**, *101* (6), 1533–1543. https://doi.org/10.1016/j.biortech.2009.10.017.

(51) Clauwaert, P.; Tolêdo, R.; van der Ha, D.; Crab, R.; Verstraete, W.; Hu, H.; Udert, K. M.; Rabaey, K. Combining Biocatalyzed Electrolysis with Anaerobic Digestion. *Water Science and Technology* **2008**, *57* (4), 575–579. https://doi.org/10.2166/WST.2008.084.

(52) Yuan, H. Y.; Ding, L. J.; Zama, E. F.; Liu, P. P.; Hozzein, W. N.; Zhu, Y. G. Biochar Modulates Methanogenesis through Electron Syntrophy of Microorganisms with Ethanol as a Substrate. *Environ. Sci. Technol.* **2018**, *52* (21), 12198–12207. https://doi.org/10.1021/ACS.EST.8B04121.

(53) Molognoni, D.; Bosch-Jimenez, P.; Rodríguez-Alegre, R.; Marí-Espinosa, A.; Licon, E.; Gallego, J.; Lladó, S.; Borràs, E.; Della Pirriera, M. How Operational Parameters Affect Electromethanogenesis in a Bioelectrochemical Power-to-Gas Prototype. *Front. Energy Res.* **2020**, *8*. https://doi.org/10.3389/FENRG.2020.00174.

(54) Baturina, O. A.; Lu, Q.; Padilla, M. A.; Xin, L.; Li, W.; Serov, A.; Artyushkova, K.; Atanassov, P.; Xu, F.; Epshteyn, A.; Brintlinger, T.; Schuette, M.; Collins, G. E. CO2 Electroreduction to Hydrocarbons on Carbon-Supported Cu Nanoparticles. *ACS Catal.* **2014**, *4* (10), 3682–3695. https://doi.org/10.1021/CS500537Y/SUPPL_FILE/CS500537Y_SI_001.PDF.

(55) Ghiara, G.; Campisi, S.; Goglio, A.; Formicola, F.; Balordi, M.; Gervasini, A.; Trasatti, S. P. M.; Adani, F.; Franzetti, A.; Cristiani, P. Biochar Based Cathode Enriched with Hydroxyapatite and Cu Nanoparticles Boosting Electromethanogenesis. *Sustainable Energy Technologies and Assessments* **2023**, *57*, 103274. https://doi.org/10.1016/J.SETA.2023.103274.

(56) Ghiara, G.; Trasatti, S.; Goglio, A.; Cristiani, P. Testing Novel Multicomposite Materials for Electromethanogenesis. *E3S Web of Conferences* **2022**, *334*, 08012. https://doi.org/10.1051/E3SCONF/202233408012.

(57) Yaashikaa, P. R.; Kumar, P. S.; Varjani, S.; Saravanan, A. A Critical Review on the Biochar Production Techniques, Characterization, Stability and Applications for Circular Bioeconomy. *Biotechnology Reports* **2020**, *28*. https://doi.org/10.1016/j.btre.2020.e00570.

(58) Keiluweit, M.; Nico, P. S.; Johnson, M.; Kleber, M. Dynamic Molecular Structure of Plant Biomass-Derived Black Carbon (Biochar). *Environ. Sci. Technol.* **2010**, *44* (4), 1247–1253. https://doi.org/10.1021/ES9031419.

(59) Ferri, M.; Campisi, S.; Polito, L.; Shen, J.; Gervasini, A. Tuning the Sorption Ability of Hydroxyapatite/Carbon Composites for the Simultaneous Remediation of Wastewaters Containing Organic-Inorganic Pollutants. *J. Hazard. Mater.* **2021**, *420*. https://doi.org/10.1016/j.jhazmat.2021.126656.

(60) Kharissova, O. V.; Méndez, Y. P.; Kharisov, B. I.; González, L. T.; Dorozhkin, S. V. Hydroxyapatite-Based Materials as Catalysts: A Review. *Particuology* **2025**, *96*, 203–217. https://doi.org/10.1016/J.PARTIC.2024.11.007.

(61) Barbieri, O.; Hahn, M.; Herzog, A.; Kötz, R. Capacitance Limits of High Surface Area Activated Carbons for Double Layer Capacitors. *Carbon N. Y.* **2005**, *43* (6), 1303–1310. https://doi.org/10.1016/j.carbon.2005.01.001.

(62) Ju, H. K.; Badwal, S.; Giddey, S. A Comprehensive Review of Carbon and Hydrocarbon Assisted Water Electrolysis for Hydrogen Production. *Appl. Energy* **2018**, *231*, 502–533. https://doi.org/10.1016/j.apenergy.2018.09.125.

(63) Çelik, D.; Yıldız, M. Investigation of Hydrogen Production Methods in Accordance with Green Chemistry Principles. *Int. J. Hydrogen Energy* **2017**, *42* (36), 23395–23401. https://doi.org/10.1016/j.ijhydene.2017.03.104.

(64) Baek, G.; Shi, L.; Rossi, R.; Logan, B. E. Using Copper-Based Biocathodes to Improve Carbon Dioxide Conversion Efficiency into Methane in Microbial Methanogenesis Cells. *Chemical Engineering Journal* **2022**, *435*. https://doi.org/10.1016/j.cej.2022.135076.

(65) Gajaraj, S.; Huang, Y.; Zheng, P.; Hu, Z. Methane Production Improvement and Associated Methanogenic Assemblages in Bioelectrochemically Assisted Anaerobic Digestion. *Biochem. Eng. J.* **2017**, *117*, 105–112. https://doi.org/10.1016/J.BEJ.2016.11.003.

(66) Lim, E. Y.; Lee, J. T. E.; Zhang, L.; Tian, H.; Ong, K. C.; Tio, Z. K.; Zhang, J.; Tong, Y. W. Abrogating the Inhibitory Effects of Volatile Fatty Acids and Ammonia in Overloaded Food Waste Anaerobic Digesters via the Supplementation of Nano-Zero Valent Iron Modified Biochar. *Science of the Total Environment* **2022**, *817*. https://doi.org/10.1016/j.scitotenv.2022.152968.

(67) Poddar, A.; Lepcha, R. T.; Das, S. K. Taxonomic Study of the Genus Tepidiphilus: Transfer of Petrobacter Succinatimandens to the Genus Tepidiphilus as Tepidiphilus Succinatimandens Comb. Nov., Emended Description of the Genus Tepidiphilus and Description of Tepidiphilus Thermophilus Sp. Nov., Isolated from a Terrestrial Hot Spring. *Int. J. Syst. Evol. Microbiol.* **2014**, *64* (PART 1), 228–235. https://doi.org/10.1099/IJS.0.056424-0/CITE/REFWORKS.

(68) An, D.; Caffrey, S. M.; Soh, J.; Agrawal, A.; Brown, D.; Budwill, K.; Dong, X.; Dunfield, P. F.; Foght, J.; Gieg, L. M.; Hallam, S. J.; Hanson, N. W.; He, Z.; Jack, T. R.; Klassen, J.; Konwar, K. M.; Kuatsjah, E.; Li, C.; Larter, S.; Leopatra, V.; Nesbø, C. L.; Oldenburg, T.; Pagé, A. P.; Ramos-Padron, E.; Rochman, F. F.; Saidi-Mehrabad, A.; Sensen, C. W.; Sipahimalani, P.; Song, Y. C.; Wilson, S.; Wolbring, G.; Wong, M. L.; Voordouw, G. Metagenomics of Hydrocarbon Resource Environments Indicates Aerobic Taxa and Genes to Be Unexpectedly Common. *Environ. Sci. Technol.* **2013**, *47* (18), 10708–10717. https://doi.org/10.1021/ES4020184.

(69) Liu, Y. F.; Chen, J.; Liu, Z. L.; Hou, Z. W.; Liang, B.; Wang, L. Y.; Zhou, L.; Shou, L. Bin; Lin, D. D.; Yang, S. Z.; Liu, J. F.; Wu, X. L.; Gu, J. D.; Mu, B. Z. Long-Term Cultivation and Meta-Omics Reveal Methylotrophic Methanogenesis in Hydrocarbon-Impacted Habitats. *Engineering* **2023**, *24*, 264–275. https://doi.org/10.1016/J.ENG.2021.08.027.

(70) Mao, Z.; Cheng, S.; Sun, Y.; Lin, Z.; Li, L.; Yu, Z. Enhancing Stability and Resilience of Electromethanogenesis System by Acclimating Biocathode with Intermittent Step-up Voltage. *Bioresour. Technol.* **2021**, *337* (12), 125376. https://doi.org/10.1016/j.biortech.2021.125376.

(71) Spiess, S.; Sasiain Conde, A.; Kucera, J.; Novak, D.; Thallner, S.; Kieberger, N.; Guebitz, G. M.; Haberbauer, M. Bioelectrochemical Methanation by Utilization of Steel Mill Off-Gas in a Two-Chamber Microbial Electrolysis Cell. *Front. Bioeng. Biotechnol.* **2022**, *10*, 972653. https://doi.org/10.3389/fbioe.2022.972653.

(72) Baek, G.; Shi, L.; Rossi, R.; Logan, B. E. Using Copper-Based Biocathodes to Improve Carbon Dioxide Conversion Efficiency into Methane in Microbial Methanogenesis Cells. *Chemical Engineering Journal* **2022**, *435* (10), 135076. https://doi.org/10.1016/j.cej.2022.135076.

(73) Jiang, Y.; Su, M.; Zhang, Y.; Zhan, G.; Tao, Y.; Li, D. Bioelectrochemical Systems for Simultaneously Production of Methane and Acetate from Carbon Dioxide at Relatively High Rate. *Int. J. Hydrogen Energy* **2013**, *38* (8), 3497–3502. https://doi.org/10.1016/j.ijhydene.2012.12.107.

(74) Tian, Y.; Liang, D.; Li, D.; Liu, G.; Wu, J.; Xie, T.; Li, J.; Feng, Y. Re-Evaluating the Contribution of a Fe-Based Current Collector to Bioelectrochemical Methanogenesis: Role and Mechanisms. *Environ. Sci. Technol.* **2023**, *57* (51), 21757–21766. https://doi.org/10.1021/acs.est.3c07018.

(75) Gajaraj, S.; Huang, Y.; Zheng, P.; Hu, Z. Methane Production Improvement and Associated Methanogenic Assemblages in Bioelectrochemically Assisted Anaerobic Digestion. *Biochem. Eng. J.* **2017**, *117* (2), 105–112. https://doi.org/10.1016/j.bej.2016.11.003.

(76) Jiang, Y.; Su, M.; Zhang, Y.; Zhan, G.; Tao, Y.; Li, D. Bioelectrochemical Systems for Simultaneously Production of Methane and Acetate from Carbon Dioxide at Relatively High Rate. *Int. J. Hydrogen Energy* **2013**, *38* (8), 3497–3502. https://doi.org/10.1016/J.IJHYDENE.2012.12.107.

(77) Zeppilli, M.; Cristiani, L.; Dell'Armi, E.; Majone, M. Bioelectromethanogenesis Reaction in a Tubular Microbial Electrolysis Cell (MEC) for Biogas Upgrading. *Renew. Energy* **2020**, *158*, 23–31. https://doi.org/10.1016/J.RENENE.2020.05.122.

(78) Gomez Vidales, A.; Omanovic, S.; Li, H.; Hrapovic, S.; Tartakovsky, B. Evaluation of Biocathode Materials for Microbial Electrosynthesis of Methane and Acetate. *Bioelectrochemistry* **2022**, *148*, 108246. https://doi.org/10.1016/J.BIOELECHEM.2022.108246.

(79) Sharma, M.; Alvarez-Gallego, Y.; Achouak, W.; Pant, D.; Sarma, P. M.; Dominguez-Benetton, X. Electrode Material Properties for Designing Effective Microbial Electrosynthesis Systems. *J. Mater. Chem. A Mater.* **2019**, *7* (42), 24420–24436. https://doi.org/10.1039/C9TA04886C.

(80) Dong, H.; Huang, L.; Zhao, L.; Zeng, Q.; Liu, X.; Sheng, Y.; Shi, L.; Wu, G.; Jiang, H.; Li, F.; Zhang, L.; Guo, D.; Li, G.; Hou, W.; Chen, H. A Critical Review of Mineral–Microbe Interaction and Co-Evolution: Mechanisms and Applications. *Natl. Sci. Rev.* **2022**, *9* (10). https://doi.org/10.1093/NSR/NWAC128.

(81) Diallo-Garcia, S.; Osman, M. Ben; Krafft, J. M.; Casale, S.; Thomas, C.; Kubo, J.; Costentin, G. Identification of Surface Basic Sites and Acid–Base Pairs of Hydroxyapatite. *Journal of Physical Chemistry C* **2014**, *118* (24), 12744–12757. https://doi.org/10.1021/JP500469X.

(82) Silvester, L.; Lamonier, J. F.; Lamonier, C.; Capron, M.; Vannier, R. N.; Mamede, A. S.; Dumeignil, F. Guerbet Reaction over Strontium-Substituted Hydroxyapatite Catalysts Prepared at Various (Ca+Sr)/P Ratios. *ChemCatChem* **2017**, *9* (12), 2250–2261. https://doi.org/10.1002/CCTC.201601480.

(83) Santini, M.; Marzorati, S.; Fest-Santini, S.; Trasatti, S.; Cristiani, P. Carbonate Scale Deactivating the Biocathode in a Microbial Fuel Cell. *J. Power Sources* **2017**, *356*, 400–407. https://doi.org/10.1016/J.JPOWSOUR.2017.02.088.

(84) Attia, Y. A.; Fuerstenau, D. W. The Equilibrium Composition of Hydroxyapatite and Fluorapatite—Water Interfaces. *Colloids and Surfaces* **1988**, *34* (3), 271–285. https://doi.org/10.1016/0166-6622(88)80105-7.

(85) Bigica, M.; Ghiara, G.; Cristiani, P.; Campisi, S.; Gervasini, A. Interface Properties of Hydroxyapatite in Ternary Composites Cathodes for Electromethanogenesis. *New Journal of Chemistry* **2024**, *48* (22), 9909–9919. https://doi.org/10.1039/D4NJ01053A.

(86) Leonzio, G.; Hankin, A.; Shah, N. CO2 Electrochemical Reduction: A State-of-the-Art Review with Economic and Environmental Analyses. *Chemical Engineering Research and Design* **2024**, *208*, 934–955. https://doi.org/10.1016/J.CHERD.2024.07.014.

(87) Ferri, M.; Delafontaine, L.; Guo, S.; Asset, T.; Cristiani, P.; Campisi, S.; Gervasini, A.; Atanassov, P. Steering Cu-Based CO2RR Electrocatalysts' Selectivity: Effect of Hydroxyapatite Acid/Base Moieties in Promoting Formate Production. *ACS Energy Lett.* **2022**, *7* (7), 2304–2310. https://doi.org/10.1021/acsenergylett.2c01144.

(88) Gao, T.; Yan, Z.; Ordomsky, V.; Paul, S. Design of Two-Dimensional Heteropolyacid-Covalent Organic Frameworks Composite Materials for Acid Catalysis. *ChemCatChem* **2022**, *14* (15), e202101450. https://doi.org/10.1002/CCTC.202101450.

(89) Gao, T.; Kumar, K. S.; Yan, Z.; Marinova, M.; Trentesaux, M.; Amin, M. A.; Szunerits, S.; Zhou, Y.; Martin-Diaconescu, V.; Paul, S.; Boukherroub, R.; Ordomsky, V. Covalent Organic Framework Derived Synthesis of Ru Embedded in Carbon Nitride for Hydrogen and Oxygen Evolution Reactions. *J. Mater. Chem. A Mater.* **2023**, *11* (36), 19338–19348. https://doi.org/10.1039/D3TA01362F.

(90) Chen, Q.; Si, D. H.; Wu, Q. J.; Cao, R.; Huang, Y. B. Engineering Copper-Based Covalent Organic Framework Microenvironments to Enable Efficient CO2 Electroreduction with Tunable Ethylene/Methane Switch. *Adv. Funct. Mater.* **2024**, *34* (24), 2315368. https://doi.org/10.1002/ADFM.202315368.

(91) Han, Y.; Zhang, M.; Zhang, Y. Q.; Zhang, Z. H. Copper Immobilized at a Covalent Organic Framework: An Efficient and Recyclable Heterogeneous Catalyst for the Chan–Lam Coupling Reaction of Aryl Boronic Acids and Amines. *Green Chemistry* **2018**, *20* (21), 4891–4900. https://doi.org/10.1039/C8GC02611D.

(92) Schwab, M. G.; Fassbender, B.; Spiess, H. W.; Thomas, A.; Feng, X.; Müllen, K. Catalyst-Free Preparation of Melamine-Based Microporous Polymer Networks through Schiff Base Chemistry. *J. Am. Chem. Soc.* **2009**, *131* (21), 7216–7217. https://doi.org/10.1021/JA902116F/SUPPL_FILE/JA902116F_SI_001.PDF.

(93) Sumathi, S.; Buvaneswari, G. Synthesis of Apatite Structure Based BiNaCa3(PO4)3OH and Its Application for Condensation Reaction. *Ceram. Int.* **2012**, *38* (5), 3547–3552. https://doi.org/10.1016/J.CERAMINT.2011.12.070.

(94) Chu, M.; Zhai, Y.; Shang, N.; Zhang, X.; Wang, C.; Zhang, Y.; Wang, H.; Gao, Y. Functions of Hydroxyapatite in Fabricating N-Doped Carbon for Excellent Catalysts and Supercapacitors. *Catal. Sci. Technol.* **2019**, *9* (18), 4952–4960. https://doi.org/10.1039/C9CY00804G.

(95) Ge, M.; Li, X.; Zhang, M.; Liu, Z. Enhanced Photocatalytic Degradation Performance of Antibiotics Using Magadiite-Supported Carbon Nitride Under Visible Light Irradiation. *J. Inorg. Organomet. Polym. Mater.* **2022**, *32* (2), 678–686. https://doi.org/10.1007/S10904-021-02140-9/FIGURES/4.

(96) Bhunia, M. K.; Das, S. K.; Pachfule, P.; Banerjee, R.; Bhaumik, A. Nitrogen-Rich Porous Covalent Imine Network (CIN) Material as an Efficient Catalytic Support for C-C Coupling Reactions. *Dalton Transactions* **2012**, *41* (4), 1304–1311. https://doi.org/10.1039/C1DT11350J.

(97) Liu, J.; Zhang, Y.; Zhang, L.; Xie, F.; Vasileff, A.; Qiao, S.-Z.; Liu, J.; Zhang, L.; Xie, F.; Vasileff, A.; Qiao, S.-Z.; Zhang, Y.; Qiao, -Z S. Graphitic Carbon Nitride (g-C3N4)-Derived N-Rich Graphene with Tuneable Interlayer Distance as a High-Rate Anode for Sodium-Ion Batteries. *Advanced Materials* **2019**, *31* (24), 1901261. https://doi.org/10.1002/ADMA.201901261.

(98) Mao, Y.; Ning, C.; Zhang, N.; Sun, S.; Fan, E.; Xu, H.; Cao, W.; Shao, G.; Fan, B.; Wang, H.; Zhang, R. Enhancement of Photocatalytic Activity of G-C3 N4 by Hydrochloric Acid Treatment of Melamine. *Nanotechnology* **2019**, *30*, 315601. https://doi.org/10.1088/1361-6528/ab10fd.

(99) Sengupta, S.; Maiti, N.; Chadha, R.; Kapoor, S. Probing of Different Conformations of Piperazine Using Raman Spectroscopy. *Chem. Phys.* **2014**, *436–437*, 55–62. https://doi.org/10.1016/J.CHEMPHYS.2014.03.011.

(100) Yi, J. D.; Xie, R.; Xie, Z. L.; Chai, G. L.; Liu, T. F.; Chen, R. P.; Huang, Y. B.; Cao, R. Highly Selective CO2 Electroreduction to CH4 by In Situ Generated Cu2O Single-Type Sites on a Conductive MOF:

Stabilizing Key Intermediates with Hydrogen Bonding. *Angew. Chem. Int. Ed.* **2020**, *59* (52), 23641–23648. https://doi.org/10.1002/ANIE.202010601.

(101) Govindasamy, P.; Kandasamy, B.; Thangavelu, P.; Barathi, S.; Thandavarayan, M.; Shkir, M.; Lee, J. Biowaste Derived Hydroxyapatite Embedded on Two-Dimensional g-C3N4 Nanosheets for Degradation of Hazardous Dye and Pharmacological Drug via Z-Scheme Charge Transfer. *Scientific Reports 2022 12:1* **2022**, *12* (1), 1–16. https://doi.org/10.1038/s41598-022-15799-y.

(102) Mohammad, I.; Jeshurun, A.; Ponnusamy, P.; Reddy, B. M. Mesoporous Graphitic Carbon Nitride/Hydroxyapatite (g-C3N4/HAp) Nanocomposites for Highly Efficient Photocatalytic Degradation of Rhodamine B Dye. *Mater. Today Commun.* **2022**, *33*, 104788. https://doi.org/10.1016/J.MTCOMM.2022.104788.

(103) Wang, W.; Zhou, H.; Liu, Y.; Zhang, S.; Zhang, Y.; Wang, G.; Zhang, H.; Zhao, H. Formation of B□N□C Coordination to Stabilize the Exposed Active Nitrogen Atoms in G-C3N4 for Dramatically Enhanced Photocatalytic Ammonia Synthesis Performance. *Small* **2020**, *16* (13), 1906880. https://doi.org/10.1002/SMLL.201906880;PAGE:STRING:ARTICLE/CHAPTER.

(104) Li, G.; Pan, J.; Han, J.; Chen, C.; Lu, J.; Zhuang, L. Ultrathin Composite Membrane of Alkaline Polymer Electrolyte for Fuel Cell Applications. *J. Mater. Chem. A Mater.* **2013**, *1* (40), 12497–12502. https://doi.org/10.1039/C3TA12626A.

(105) Dai, H.; Gao, X.; Liu, E.; Yang, Y.; Hou, W.; Kang, L.; Fan, J.; Hu, X. Synthesis and Characterization of Graphitic Carbon Nitride Sub-Microspheres Using Microwave Method under Mild Condition. *Diam. Relat. Mater.* **2013**, *38*, 109–117. https://doi.org/10.1016/J.DIAMOND.2013.06.012.

(106) Galloni, M. G.; Campisi, S.; Gervasini, A.; Morandi, S.; Manzoli, M. How Hydroxyapatite Governs Surface Cu(II) and Fe(III) Structuring: Effects in the N2O Decomposition under Highly Oxidant Atmosphere. *Appl. Catal. A Gen.* **2023**, *655*, 119101. https://doi.org/10.1016/J.APCATA.2023.119101.

(107) Leslie, N.; Mauzeroll, J. Spatially Resolved Electrochemical Measurements. *Encyclopedia of Solid-Liquid Interfaces* **2024**, *1–3*, 461–478. https://doi.org/10.1016/B978-0-323-85669-0.00004-0.

(108) Liao, G.; Gong, Y.; Zhang, L.; Gao, H.; Yang, G.-J.; Fang, B. Semiconductor Polymeric Graphitic Carbon Nitride Photocatalysts: The "'holy Grail'" for the Photocatalytic Hydrogen Evolution Reaction under Visible Light. *2080* | *Energy Environ. Sci* **2019**, *12*, 2080. https://doi.org/10.1039/c9ee00717b.

(109) Chaulagain, N.; Alam, K. M.; Kadian, S.; Kumar, N.; Garcia, J.; Manik, G.; Shankar, K. Synergistic Enhancement of the Photoelectrochemical Performance of TiO2Nanorod Arrays through Embedded Plasmon and Surface Carbon Nitride Co-Sensitization. *ACS Appl. Mater. Interfaces* **2022**, *14* (21), 24309–24320. https://doi.org/10.1021/ACSAMI.2C02649/ASSET/IMAGES/LARGE/AM2C02649_0009.JPEG.

(110) Zhao, K.; Liu, Y.; Quan, X.; Chen, S.; Yu, H. CO2 Electroreduction at Low Overpotential on Oxide-Derived Cu/Carbons Fabricated from Metal Organic Framework. *ACS Appl. Mater. Interfaces* **2017**, *9* (6), 5302–5311. https://doi.org/10.1021/ACSAMI.6B15402/ASSET/IMAGES/LARGE/AM-2016-15402Q_0008.JPEG.

(111) Barbieri, O.; Hahn, M.; Herzog, A.; Kötz, R. Capacitance Limits of High Surface Area Activated Carbons for Double Layer Capacitors. *Carbon N. Y.* **2005**, *43* (6), 1303–1310. https://doi.org/10.1016/J.CARBON.2005.01.001.

(112) Ding, C.; Feng, C.; Mei, Y.; Liu, F.; Wang, H.; Dupuis, M.; Li, C. Carbon Nitride Embedded with Transition Metals for Selective Electrocatalytic CO2 Reduction. *Appl. Catal. B* **2020**, *268*, 118391. https://doi.org/10.1016/J.APCATB.2019.118391.

(113) Birhanu, M. K.; Tsai, M. C.; Kahsay, A. W.; Chen, C. T.; Zeleke, T. S.; Ibrahim, K. B.; Huang, C. J.; Su, W. N.; Hwang, B. J. Copper and Copper-Based Bimetallic Catalysts for Carbon Dioxide Electroreduction. *Advanced Materials Interfaces*. Wiley-VCH Verlag December 21, 2018. https://doi.org/10.1002/admi.201800919.

(114) Asset, T.; Garcia, S. T.; Herrera, S.; Andersen, N.; Chen, Y.; Peterson, E. J.; Matanovic, I.; Artyushkova, K.; Lee, J.; Minteer, S. D.; Dai, S.; Pan, X.; Chavan, K.; Calabrese Barton, S.; Atanassov, P. Investigating the Nature of the Active Sites for the CO2 Reduction Reaction on Carbon-Based Electrocatalysts. *ACS Catal.* **2019**, *9* (9), 7668–7678. https://doi.org/10.1021/acscatal.9b01513.

(115) Lum, Y.; Kwon, Y.; Lobaccaro, P.; Chen, L.; Clark, E. L.; Bell, A. T.; Ager, J. W. Trace Levels of Copper in Carbon Materials Show Significant Electrochemical CO $_2$ Reduction Activity. *ACS Catal.* **2016**, *6* (1), 202–209. https://doi.org/10.1021/acscatal.5b02399.

(116) van der Heijden, O.; Park, S.; Vos, R. E.; Eggebeen, J. J. J.; Koper, M. T. M. Tafel Slope Plot as a Tool to Analyze Electrocatalytic Reactions. *ACS Energy Lett.* **2024**, *9* (4), 1871–1879. https://doi.org/10.1021/ACSENERGYLETT.4C00266.

(117) Sajna, M. S.; Zavahir, S.; Popelka, A.; Kasak, P.; Al-Sharshani, A.; Onwusogh, U.; Wang, M.; Park, H.; Han, D. S. Electrochemical System Design for CO2 Conversion: A Comprehensive Review. *J. Environ. Chem. Eng.* **2023**, *11* (5), 110467. https://doi.org/10.1016/j.jece.2023.110467.

(118) Senthilkumar, P.; Mohapatra, M.; Basu, S. The Inchoate Horizon of Electrolyzer Designs, Membranes and Catalysts towards Highly Efficient Electrochemical Reduction of CO 2 to Formic Acid. *RSC Adv.* **2022**, *12* (3), 1287–1309. https://doi.org/10.1039/d1ra05062a.

(119) Juthathan, M.; Chantarojsiri, T.; Tuntulani, T.; Leeladee, P. Atomic- and Molecular-Level Modulation of Dispersed Active Sites for Electrocatalytic CO2 Reduction. *Chem. Asian J.* **2022**, *17* (12), e202200237. https://doi.org/10.1002/ASIA.202200237;PAGE:STRING:ARTICLE/CHAPTER.

(120) Tignor, S. E.; Shaw, T. W.; Bocarsly, A. B. Elucidating the Origins of Enhanced CO2 Reduction in Manganese Electrocatalysts Bearing Pendant Hydrogen-Bond Donors. *Dalton Transactions* **2019**, *48* (33), 12730–12737. https://doi.org/10.1039/C9DT02060H.

(121) Chapovetsky, A.; Welborn, M.; Luna, J. M.; Haiges, R.; Miller, T. F.; Marinescu, S. C. Pendant Hydrogen-Bond Donors in Cobalt Catalysts Independently Enhance CO2 Reduction. *ACS Cent. Sci.* **2018**, *4* (3), 397–404. https://doi.org/10.1021/ACSCENTSCI.7B00607/SUPPL_FILE/OC7B00607_SI_005.CIF.

(122) Wu, Q. J.; Si, D. H.; Wu, Q.; Dong, Y. L.; Cao, R.; Huang, Y. B. Boosting Electroreduction of CO2 over Cationic Covalent Organic Frameworks: Hydrogen Bonding Effects of Halogen Ions. *Angew. Chem. Int. Ed.* **2023**, *62* (7), e202215687. https://doi.org/10.1002/ANIE.202215687.

(123) Cazzulani, E.; Bigica, M.; Avola, T.; Campisi, S. The Hidden Strength of Weak Forces: The Role of Non-Covalent Interactions in Electrocatalytic CO2 Reduction. *Rendiconti Lincei. Scienze Fisiche e Naturali 2026* **2026**, 1–29. https://doi.org/10.1007/S12210-025-01400-X.

(124) Wang, Y. R.; Liu, M.; Gao, G. K.; Yang, Y. L.; Yang, R. X.; Ding, H. M.; Chen, Y.; Li, S. L.; Lan, Y. Q. Implanting Numerous Hydrogen-Bonding Networks in a Cu-Porphyrin-Based Nanosheet to Boost CH4 Selectivity in Neutral-Media CO2 Electroreduction. *Angew. Chem. Int. Ed.* **2021**, *60* (40), 21952–21958. https://doi.org/10.1002/ANIE.202108388;WGROUP:STRING:PUBLICATION.

(125) Raciti, D.; Mao, M.; Park, J. H.; Wang, C. Local PH Effect in the CO 2 Reduction Reaction on High-Surface-Area Copper Electrocatalysts . *J. Electrochem. Soc.* **2018**, *165* (10), F799–F804. https://doi.org/10.1149/2.0521810JES.

(126) Zhu, S.; Jiang, B.; Cai, W. Bin; Shao, M. Direct Observation on Reaction Intermediates and the Role of Bicarbonate Anions in CO2 Electrochemical Reduction Reaction on Cu Surfaces. *J. Am. Chem. Soc.* **2017**, *139* (44), 15664–15667. https://doi.org/10.1021/JACS.7B10462.

(127) Taheri, A.; Carr, C. R.; Berben, L. A. Electrochemical Methods for Assessing Kinetic Factors in the Reduction of CO2 to Formate: Implications for Improving Electrocatalyst Design. *ACS Catal.* **2018**, *8* (7), 5787–5793. https://doi.org/10.1021/ACSCATAL.8B01799.

(128) Varela, A. S. The Importance of PH in Controlling the Selectivity of the Electrochemical CO2 Reduction. *Curr. Opin. Green Sustain. Chem.* **2020**, *26*, 100371. https://doi.org/10.1016/J.COGSC.2020.100371.

(129) Chen, G.; Fu, J.; Liu, B.; Cai, C.; Li, H.; Zhang, Z.; Liu, K.; Lin, Z.; Liu, M. Passivation of Cu Nanosheet Dissolution with Cu 2+ -Containing Electrolytes for Selective Electroreduction of CO 2 to CH 4. *Environ. Sci. Nano* **2022**, *9* (9), 3312–3317. https://doi.org/10.1039/D2EN00561A.

(130) Wang, Y.; Liu, J.; Zheng, G.; Wang, Y.; Liu, J.; Zheng, G. Designing Copper-Based Catalysts for Efficient Carbon Dioxide Electroreduction. *Advanced Materials* **2021**, *33* (46), 2005798. https://doi.org/10.1002/ADMA.202005798.

(131) Loiudice, A.; Lobaccaro, P.; Kamali, E. A.; Thao, T.; Huang, B. H.; Ager, J. W.; Buonsanti, R. Tailoring Copper Nanocrystals towards C2 Products in Electrochemical CO2 Reduction. *Angew. Chem. Int. Ed.* **2016**, *55* (19), 5789–5792. https://doi.org/10.1002/ANIE.201601582.

(132) Jiang, K.; Sandberg, R. B.; Akey, A. J.; Liu, X.; Bell, D. C.; Nørskov, J. K.; Chan, K.; Wang, H. Metal Ion Cycling of Cu Foil for Selective C–C Coupling in Electrochemical CO2 Reduction. *Nature Catalysis 2017 1:2* **2018**, *1* (2), 111–119. https://doi.org/10.1038/s41929-017-0009-x.

(133) Song, Y.; Peng, R.; Hensley, D. K.; Bonnesen, P. V.; Liang, L.; Wu, Z.; Meyer, H. M.; Chi, M.; Ma, C.; Sumpter, B. G.; Rondinone, A. J. High-Selectivity Electrochemical Conversion of CO2 to Ethanol Using a Copper Nanoparticle/N-Doped Graphene Electrode. *ChemistrySelect* **2016**, *1* (19), 6055–6061. https://doi.org/10.1002/SLCT.201601169;WGROUP:STRING:PUBLICATION.

(134) Karapinar, D.; Huan, N. T.; Ranjbar Sahraie, N.; Li, J.; Wakerley, D.; Touati, N.; Zanna, S.; Taverna, D.; Galvão Tizei, L. H.; Zitolo, A.; Jaouen, F.; Mougel, V.; Fontecave, M. Electroreduction of CO2 on Single-Site Copper-Nitrogen-Doped Carbon Material: Selective Formation of Ethanol and Reversible Restructuration of the Metal Sites. *Angew. Chem. Int. Ed.* **2019**, *58* (42), 15098–15103. https://doi.org/10.1002/ANIE.201907994;PAGE:STRING:ARTICLE/CHAPTER.

(135) Xu, Y.; Zhao, Y.; Kochubei, A.; Lee, C. Y.; Wagner, P.; Chen, Z.; Jiang, Y.; Yan, W.; Wallace, G. G.; Wang, C. Copper/Polyaniline Interfaces Confined CO2 Electroreduction for Selective Hydrocarbon Production. *ChemSusChem* **2024**, *17* (19), e202400209. https://doi.org/10.1002/CSSC.202400209;WEBSITE:WEBSITE:CHEMISTRY-EUROPE;REQUESTEDJOURNAL:JOURNAL:1864564X;WGROUP:STRING:PUBLICATION.

(136) Li, J.; Kuang, Y.; Meng, Y.; Tian, X.; Hung, W. H.; Zhang, X.; Li, A.; Xu, M.; Zhou, W.; Ku, C. S.; Chiang, C. Y.; Zhu, G.; Guo, J.; Sun, X.; Dai, H. Electroreduction of CO2to Formate on a Copper-Based Electrocatalyst at High Pressures with High Energy Conversion Efficiency. *J. Am. Chem. Soc.* **2020**, *142* (16), 7276–7282. https://doi.org/10.1021/JACS.0C00122/ASSET/IMAGES/LARGE/JA0C00122_0004.JPEG.

(137) Jamilatun, S.; Amelia, S.; Pitoyo, J.; Ma'Arif, A.; Mufandi, I. Preparation and Characteristics of Effective Biochar Derived from Sugarcane Bagasse as Adsorbent. *International Journal of Renewable Energy Research (IJRER)* **2023**, *13* (2), 673–680. https://doi.org/10.20508/IJRER.V13I2.13719.G8737.

(138) Dorozhkin, S. V. Calcium Orthophosphates (CaPO4): Occurrence and Properties. *Morphologie* **2017**, *101* (334), 125–142. https://doi.org/10.1016/J.MORPHO.2017.03.007.

(139) Ibrahim, M.; Labaki, M.; Giraudon, J. M.; Lamonier, J. F. Hydroxyapatite, a Multifunctional Material for Air, Water and Soil Pollution Control: A Review. *J. Hazard. Mater.* **2020**, *383*, 121139. https://doi.org/10.1016/J.JHAZMAT.2019.121139.

(140) Campisi, S.; Castellano, C.; Gervasini, A. Tailoring the Structural and Morphological Properties of Hydroxyapatite Materials to Enhance the Capture Efficiency towards Copper(II) and Lead(II) Ions. *New Journal of Chemistry* **2018**, *42* (6), 4520–4530. https://doi.org/10.1039/C8NJ00468D.

(141) Elliot J. C. Structure and Chemistry of the Apatites and Other Calcium Orthophosphates - J.C. Elliott - Google Libros. **1994**, 63–230.

(142) Wang, L.; Nancollas, G. H. Calcium Orthophosphates: Crystallization and Dissolution. *Chem. Rev.* **2008**, *108* (11), 4628–4669. https://doi.org/10.1021/CR0782574.

(143) Abdelmoaty, A.; Mousa, S. Synthesis and Characterization of Hydroxyapatite Nanoparticles from Calcium Hydroxide Fouled with Gases Evolved from Smokestack of Glass Industry. *Sci. Rep.* **2024**, *14* (1), 1–8. https://doi.org/10.1038/S41598-024-60970-2;SUBJMETA.

(144) Cazalbou, S.; Eichert, D.; Ranz, X.; Drouet, C.; Combes, C.; Harmand, M. F.; Rey, C. Ion Exchanges in Apatites for Biomedical Application. *J. Mater. Sci. Mater. Med.* **2005**, *16* (5), 405–409. https://doi.org/10.1007/S10856-005-6979-2.

(145) Tourbin, M.; Brouillet, F.; Galey, B.; Rouquet, N.; Gras, P.; Abi Chebel, N.; Grossin, D.; Frances, C. Agglomeration of Stoichiometric Hydroxyapatite: Impact on Particle Size Distribution and Purity in the Precipitation and Maturation Steps. *Powder Technol.* **2020**, *360*, 977–988. https://doi.org/10.1016/J.POWTEC.2019.10.050.

(146) Silvester, L.; Jean-François Lamonier, ab; Rose-Nö elle Vannier, ab; Carole Lamonier, abc; Mickä el Capron, ab; Anne-Sophie Mamede, ab; FrédériqueFr, abc; Pourpoint, F.; Antonella Gervasini, abc; Dumeignil, F. Materials Chemistry A Materials for Energy and Sustainability Structural, Textural and Acid-Base Properties of Carbonate-Containing Hydroxyapatites †. *2*, 10977–11524. https://doi.org/10.1039/c4ta01628a.

(147) Paluszkiewicz, C.; Ślósarczyk, A.; Pijocha, D.; Sitarz, M.; Bućko, M.; Zima, A.; Chróścicka, A.; Lewandowska-Szumieł, M. Synthesis, Structural Properties and Thermal Stability of Mn-Doped Hydroxyapatite. *J. Mol. Struct.* **2010**, *976* (1–3), 301–309. https://doi.org/10.1016/J.MOLSTRUC.2010.04.001.

(148) Damayanti, H.; Noordiningsih, K.; Wahyudi, K.; Hernawan; Maryani, E.; Yuliati, A.; Rianti, D.; Asri, L. A. T. W.; Septawendar, R. Synthesis of Carbonate Hydroxyapatite Contained Magnesium Cations by Dry Mechano-Milling. *Mater. Lett.* **2023**, *338*, 133999. https://doi.org/10.1016/J.MATLET.2023.133999.

(149) Diallo-Garcia, S.; Osman, M. Ben; Krafft, J. M.; Casale, S.; Thomas, C.; Kubo, J.; Costentin, G. Identification of Surface Basic Sites and Acid–Base Pairs of Hydroxyapatite. *Journal of Physical Chemistry C* **2014**, *118* (24), 12744–12757. https://doi.org/10.1021/JP500469X.

(150) Lamonier, C.; Lamonier, J. F.; Aellach, B.; Ezzamarty, A.; Leglise, J. Specific Tuning of Acid/Base Sites in Apatite Materials to Enhance Their Methanol Thiolation Catalytic Performances. *Catal. Today* **2011**, *164* (1), 124–130. https://doi.org/10.1016/J.CATTOD.2010.10.035.

(151) Lovón-Quintana, J. J.; Rodriguez-Guerrero, J. K.; Valença, P. G. Carbonate Hydroxyapatite as a Catalyst for Ethanol Conversion to Hydrocarbon Fuels. *Appl. Catal. A Gen.* **2017**, *542*, 136–145. https://doi.org/10.1016/J.APCATA.2017.05.020.

(152) Lu, H. B.; Campbell, C. T.; Graham, D. J.; Ratner, B. D. Surface Characterization of Hydroxyapatite and Related Calcium Phosphates by XPS and TOF-SIMS. *Anal. Chem.* **2000**, *72* (13), 2886–2894. https://doi.org/10.1021/AC990812H.

(153) Raj, A. K. V.; H Banerjee, R.; Sanwal, J.; Pathak, N.; Chaudhary, N.; Arya, A.; Sengupta, P. Ordering of Oxygen Vacancies in Hydroxyapatite under Electron Irradiation. *Mater. Chem. Phys.* **2024**, *322*, 129609. https://doi.org/10.1016/J.MATCHEMPHYS.2024.129609.

(154) Fihri, A.; Len, C.; Varma, R. S.; Solhy, A. Hydroxyapatite: A Review of Syntheses, Structure and Applications in Heterogeneous Catalysis. *Coord. Chem. Rev.* **2017**, *347*, 48–76. https://doi.org/10.1016/j.ccr.2017.06.009.

(155) Bittencourt, A. F. B.; Mendes, P. C. D.; Valença, G. P.; Da Silva, J. L. F. Acid-Base Properties of Hydroxyapatite(0001) by the Adsorption of Probe Molecules: An *Ab Initio* Investigation. *Phys. Rev. Mater.* **2021**, *5* (7), 075003. https://doi.org/10.1103/PhysRevMaterials.5.075003.

(156) Campisi, S.; Tavoni, M.; Sprio, S.; Tampieri, A.; Folliard, V.; Auroux, A.; Gervasini, A. Unveiling the Effects of Ion Substitutions and Carbonation on Acid/Basic Surface Features of Hydroxyapatites. *Appl. Surf. Sci.* **2025**, *696*, 162980. https://doi.org/10.1016/J.APSUSC.2025.162980.

(157) Gervasini, A.; Auroux, A. Combined Use of Titration Calorimetry and Spectrofluorimetry for the Screening of the Acidity of Solid Catalysts in Different Liquids. *Thermochim. Acta* **2013**, *567*, 8–14. https://doi.org/10.1016/J.TCA.2013.03.028.

(158) Li, S.; Li, Y.; Shen, W.; Bai, Y.; Kong, L. Hydroxyapatite-Based Catalysis in Environmental Decontamination. *J. Clean. Prod.* **2022**, *380*, 134961. https://doi.org/10.1016/J.JCLEPRO.2022.134961.

(159) Yook, H.; Hwang, J.; Yeo, W.; Bang, J.; Kim, J.; Kim, T. Y.; Choi, J.-S.; Han, J. W. Design Strategies for Hydroxyapatite-Based Materials to Enhance Their Catalytic Performance and Applicability. *Advanced Materials* **2023**, 2204938. https://doi.org/10.1002/ADMA.202204938.

(160) Rootare, H. M.; Deitz, V. R.; Carpenter, F. G. Solubility Product Phenomena in Hydroxyapatite-Water Systems. *J. Colloid Sci.* **1962**, *17* (3), 179–206. https://doi.org/10.1016/0095-8522(62)90035-1.

(161) Astala, R.; Stott, M. J. First-Principles Study of Hydroxyapatite Surfaces and Water Adsorption. *Phys. Rev. B* **2008**, *78* (7), 075427. https://doi.org/10.1103/PhysRevB.78.075427.

(162) Pham, T. T.; Lemaire, T.; Capiez-Lernout, E.; Lewerenz, M.; To, Q. D.; Christie, J. K.; Di Tommaso, D.; de Leeuw, N. H.; Naili, S. Properties of Water Confined in Hydroxyapatite Nanopores as Derived from Molecular Dynamics Simulations. *Theor. Chem. Acc.* **2015**, *134* (5), 1–14. https://doi.org/10.1007/S00214-015-1653-3/TABLES/4.

(163) Chiatti, F.; Delle Piane, M.; Ugliengo, P.; Corno, M. Water at Hydroxyapatite Surfaces: The Effect of Coverage and Surface Termination as Investigated by All-Electron B3LYP-D* Simulations. *Theor. Chem. Acc.* **2016**, *135* (3), 1–15. https://doi.org/10.1007/S00214-016-1818-8/FIGURES/5.

(164) Bhosale, S. H.; Rao, M. B.; Deshpande, V. V. Molecular and Industrial Aspects of Glucose Isomerase. *Microbiol. Rev.* **1996**, *60* (2), 280–300. https://doi.org/10.1128/MR.60.2.280-300.1996.

(165) Li, H.; Yang, S.; Saravanamurugan, S.; Riisager, A. Glucose Isomerization by Enzymes and Chemo-Catalysts: Status and Current Advances. *ACS Catal.* **2017**, *7* (4), 3010–3029. https://doi.org/10.1021/ACSCATAL.6B03625.

(166) Fischer, M.; Drabo, P.; Delidovich, I. Study of Base-Catalyzed Isomerization of d-Glucose with a Focus on Reaction Kinetics. *Reaction Kinetics, Mechanisms and Catalysis 2022 135:5* **2022**, *135* (5), 2357–2377. https://doi.org/10.1007/S11144-022-02277-9.

(167) Delidovich, I. Recent Progress in Base-Catalyzed Isomerization of D-Glucose into D-Fructose. *Curr. Opin. Green Sustain. Chem.* **2021**, *27*, 100414. https://doi.org/10.1016/J.COGSC.2020.100414.

(168) Dong, Z.; Chen, W.; Xu, K.; Liu, Y.; Wu, J.; Zhang, F. Understanding the Structure–Activity Relationships in Catalytic Conversion of Polyolefin Plastics by Zeolite-Based Catalysts: A Critical Review. *ACS Catal.* **2022**, *12* (24), 14882–14901. https://doi.org/10.1021/ACSCATAL.2C04915.

(169) Delidovich, I. Toward Understanding Base-Catalyzed Isomerization of Saccharides. *ACS Catal.* **2023**, *13* (4), 2250–2267. https://doi.org/10.1021/ACSCATAL.2C04786.

(170) Kiani, D.; Baltrusaitis, J. Surface Chemistry of Hydroxyapatite for Sustainable N-Butanol Production from Bio-Ethanol. *Chem Catalysis* **2021**, *1* (4), 782–801. https://doi.org/10.1016/J.CHECAT.2021.06.005.

(171) Carraher, J. M.; Fleitman, C. N.; Tessonnier, J.-P. Kinetic and Mechanistic Study of Glucose Isomerization Using Homogeneous Organic Brønsted Base Catalysts in Water. **2015**. https://doi.org/10.1021/acscatal.5b00316.

(172) Liu, J.-J.; Zhang, G.-C.; Kwak, S.; Oh, E. J.; Yun, E. J.; Chomvong, K.; Cate, J. H. D.; Jin, Y.-S. Overcoming the Thermodynamic Equilibrium of an Isomerization Reaction through Oxidoreductive Reactions for Biotransformation. https://doi.org/10.1038/s41467-019-09288-6.

(173) Xin, Y.; Shirai, T. Noble-Metal-Free Hydroxyapatite Activated by Facile Mechanochemical Treatment towards Highly-Efficient Catalytic Oxidation of Volatile Organic Compound. *Sci. Rep.* **2021**, *11* (1), 1–13. https://doi.org/10.1038/S41598-021-86992-8;SUBJMETA.

(174) Rahavi, S. S.; Ghaderi, O.; Monshi, A.; Fathi, M. H. A Comparative Study on Physicochemical Properties of Hydroxyapatite Powders Derived from Natural and Synthetic Sources. *Russian Journal of Non-Ferrous Metals* **2017**, *58* (3), 276–286. https://doi.org/10.3103/S1067821217030178.

(175) Campisi, S.; Tavoni, M.; Sprio, S.; Tampieri, A.; Folliard, V.; Auroux, A.; Gervasini, A. Unveiling the Effects of Ion Substitutions and Carbonation on Acid/Basic Surface Features of Hydroxyapatites. *Appl. Surf. Sci.* **2025**, *696*, 162980. https://doi.org/10.1016/J.APSUSC.2025.162980.

(176) Miao, Y.; Tian, W.; Han, J.; Li, N.; Chen, D.; Xu, Q.; Lu, J. Oxygen Vacancy-Induced Hydroxyl Dipole Reorientation in Hydroxyapatite for Enhanced Piezocatalytic Activity. *Nano Energy* **2022**, *100*, 107473. https://doi.org/10.1016/J.NANOEN.2022.107473.

(177) Campisi, S.; Tavoni, M.; Sprio, S.; Tampieri, A.; Folliard, V.; Auroux, A.; Gervasini, A. Unveiling the Effects of Ion Substitutions and Carbonation on Acid/Basic Surface Features of Hydroxyapatites. *Appl. Surf. Sci.* **2025**, *696*, 162980. https://doi.org/10.1016/J.APSUSC.2025.162980.

Supplementary Information

6.1. Experimental Section

Acid-base liquid-solid titration in a recirculation HPLC line

The isotherms of PEA and BA adsorption on samples collected in I and II runs (**Figure** S-6-1) have been modeled according to Langmuir model equation. From the linearized equation (Eq. S-6-1)

$$\frac{C_e}{q_e} = \frac{1}{n_{max} b_{ads}} + \frac{C_e}{n_{max}} \qquad \text{Eq. S-6-1}$$

the relevant parameters n_{max}, and b_{ads} can be obtained: where, q_e is the adsorption capacity, C_e is the probe equilibrium concentration in solution (mol L^{-1}) detected by the HPLC line, n_{max} is the maximum amount of adsorbed probe (mol g^{-1}) and b_{ads} is the adsorption constant (L mol^{-1}). I run isotherm can be associated with probe adsorption on both strong and weak sites of the sample surface: so, its linear regression gives back the total number of surface acid/basic sites. On the other hand, II run isotherm accounts only for probe adsorption on weak acid/basic sites, since strongly interacting ones will not be freed by the mild desorption step occurred between the two titrations. As for strong adsorption sites, a proper elaboration occurred to avoid possible errors due to the mathematical subtraction between the experimental points of I run and II run because of the difference of C_e. In this elaboration, starting from the experimental points of C_e of the I run, n_{ads} of weak sites were calculated through the parameters (n_{max} and b_{ads}) of II run Langmuir elaboration. Then, a subtraction had been made between the experimental n_{ads} of I run and n_{ads} calculated in this way, corresponding to the number of strong adsorption sites attributed to the same C_e. Through C_e and the calculated number of strong sites (n_{ads}), Eq. S.1.1 can be applied to calculate n_{max} and b_{ads} for strong sites. Finally, by summing up the Langmuir isotherm modeled on II run experimental data and the one regarding to strong sites, a Langmuir isotherm (called Langmuir sum) was obtained, which could be superimposed to the I run experimental Langmuir curve.

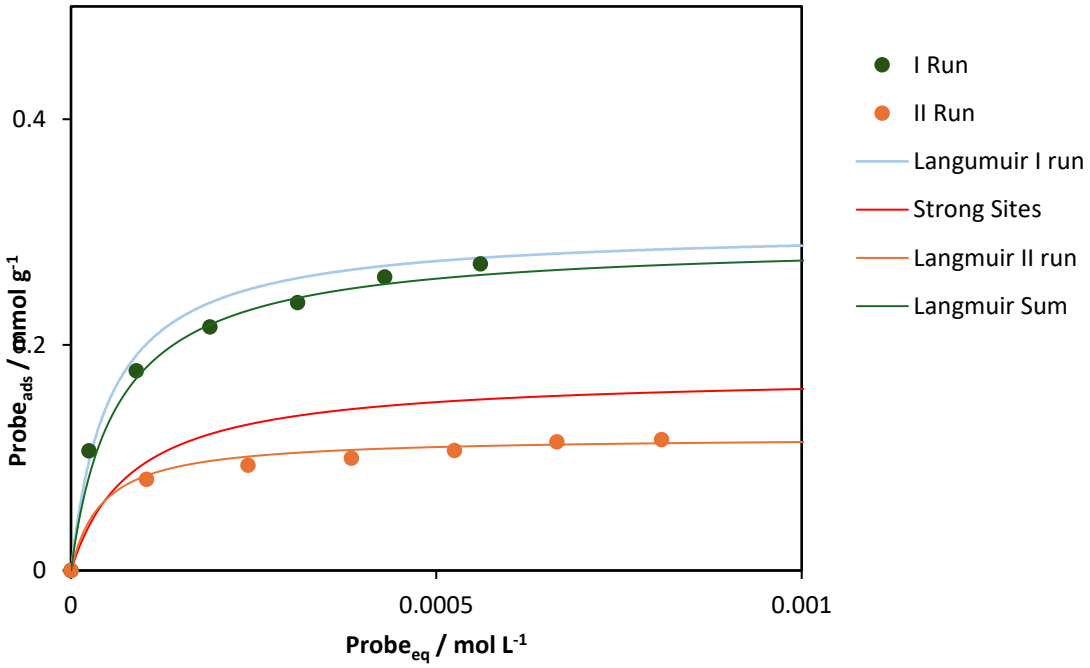

Figure S-6-1 Example of adsorption isotherms of probes at 30°C on powder sample. Green markers and orange markers represent experimental points of I and II adsorption runs, respectively. Green lines represent the calculated Langmuir curves of I run; orange lines represent the calculated Langmuir curves for II runs; red lines represent the calculated Langmuir curves on strong sites; light blue lines represent the adsorption trends of I runs, obtained as sum of red and black lines.

Adsorption microcalorimetry

Two experimental parameters are calculated from the adsorption microcalorimetry: the heat evolved was measured through the heat flux in the calorimeter, by thermocouples, and the equilibrium pressure related to each adsorbed amount was measured by means of a pressure transducer.

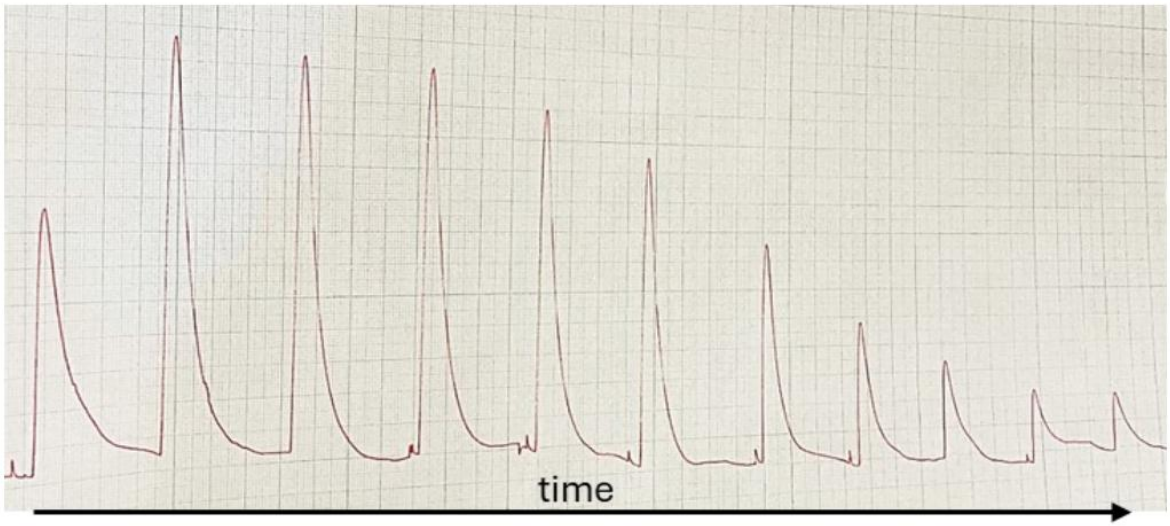

$$Q = K \int W \, dt$$

Figure S-6-2 Example of thermogram obtained by microcalorimetric technique and relative equation to calculate the evolved heat (area of peak). For the equation, Q is the evolved heat (µcal), K is the calorimetric constant (µcal mm^{-2}), W is the output of the detector (cal h^{-1}), dt (h) is the variable of integration.

The evolved heat was calculated measuring the area under the thermogram “peak” using the calibration factor obtained with the Joule effect calibration. Correlation between the evolved heat and the area below the thermogram “peak (**Figure** S-6-2) is provided by a calibration factor obtained with Joule effect calibration: a special crucible including a metallic wire of known electrical resistance (R) is posed inside the calorimeter cell; in the wire an accurately controlled current intensity (I) is circulated, which produces a known dissipated thermal power (P) equal to $P = R*I^2$.

As for the adsorbed amount the probe, from the difference of pressure before and after expansion, the adsorbed amounts were calculated using the ideal gas equation of state (which can be applied

given the extremely small amount (µmol) of gas expanded). The adsorption isotherms correlate the amount of probe molecule adsorbed with the corresponding equilibrium pressure. The first adsorption allowed us to measure the overall uptake of probe gas on catalyst. By subtracting the second isotherm from the first one, the irreversibly adsorbed amount (n_{chem}) of probe gas was obtained. An estimation of the number of strong acidic and basic sites can be derived from this amount (often associated with adsorption heats at least of the order of 100–150 kJ/mol).

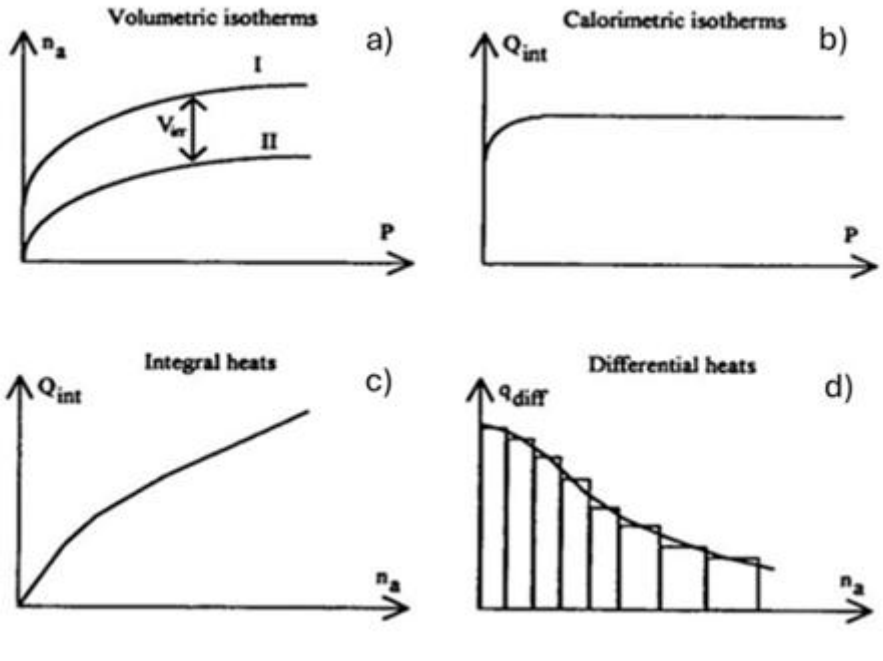

Figure S-6-3 Data obtained from volumetric microcalorimetry analyses.

The calorimetric and volumetric data obtained this way can be combined to obtain volumetric isotherms, calorimetric isotherms, integral heats, and differential heat (**Figure** S-6-3).

All the data combined gave: 1) the total number of sites, obtained from the adsorption experiment by interpolation of the experimental amounts adsorbed during the analysis (displayed in the volumetric isotherm, at the fixed equilibrium pressure of 0.2 torr, Fig. S-1 (a)). This pressure was selected as representative of the equilibrium point at which the monolayer is achieved; 2) the chemisorbed sites which are only the strong sites (n_{chem}), obtained by the difference of the total amount of probe molecules adsorbed (1) and the total amount re-adsorbed after sample evacuation,

calculated by interpolation of the experimental data at 0.2 torr; 3) energy distribution of surface active sites from the differential heat (q_{diff}), which is the molar heat of each dose of adsorbate, as a function of the amount of gas/vapor adsorbed (n_a). The curve of differential heat as a function of surface coverage is traditionally represented as histograms. For convention, the steps of histogram are often replaced by a continuous curve connecting the centers of steps. The variation of the differential heats of adsorption with coverage gives access to energy distribution of surface-active sites with respect to a given adsorbate and their varying reactivity on given adsorbents. The variation of the enthalpy of adsorption with successive adsorbed amounts (**Figure** 4-15, d) can also be better represented defining consecutive ranges of heat of adsorption and for each of them quantifying the related adsorbed amount (equal to the acid/basic sites). The information obtained can be represented by histograms, thus displaying the strength distribution of sites, grouped into populations.

6.2. Sustainable Electrochemical Processes

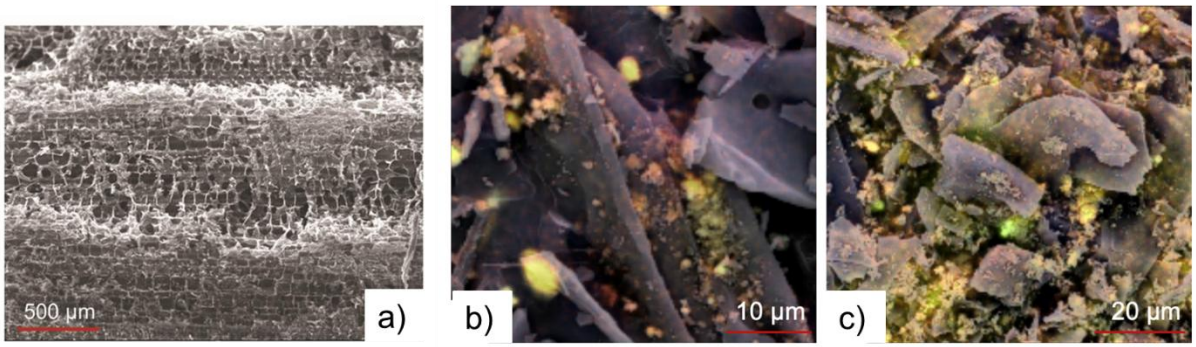

Figure S-6-4 SEM-SE observations of maize stalk sample (a); SEM elemental mapping of multi-composite powder: b) 5Cu/5HAP-MS900; c) 20Cu/10HAP-MS900. blue=C red=O; orange=P; yellow=Ca; green=Cu.

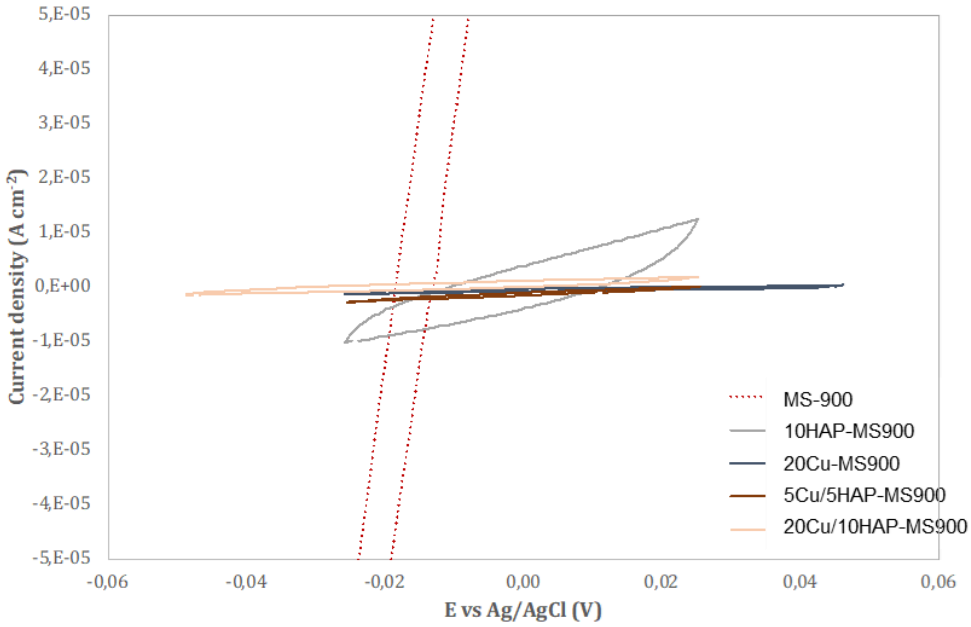

Figure S-6-5 Voltammograms from the CV analysis for the estimation of the ECSA.

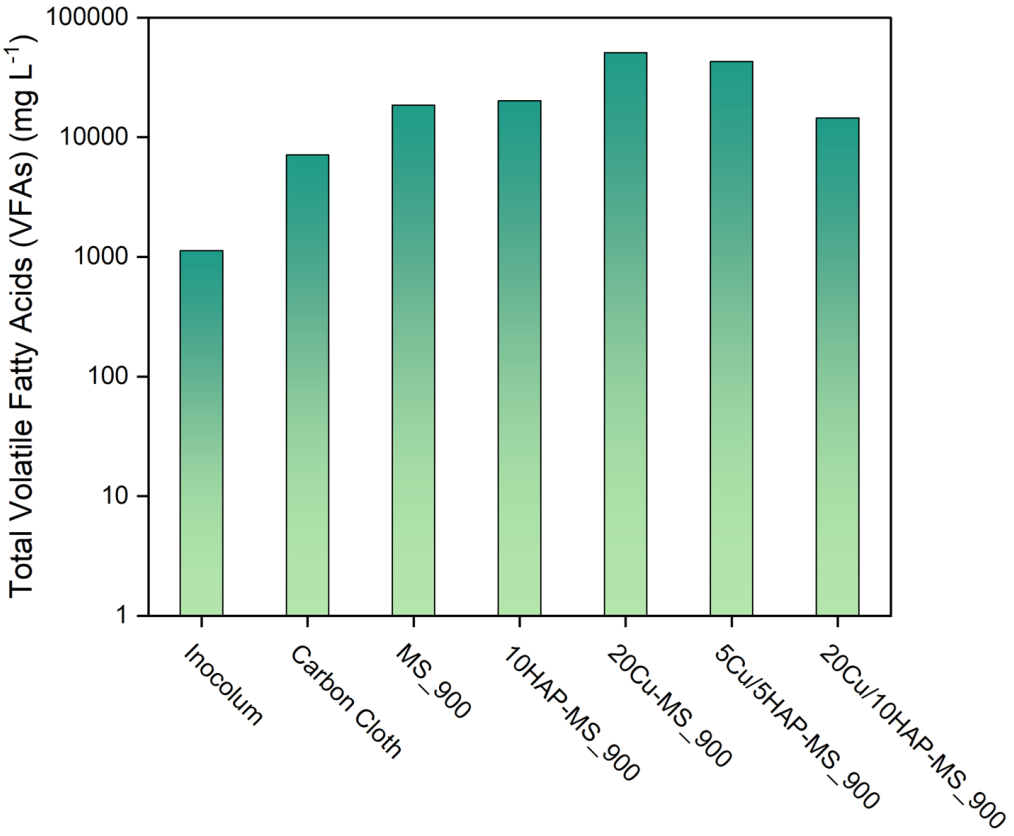

Figure S-6-6 Histograms of Total Volatile Fatty Acids measured in the cathodic compartment at the end of the test (8 days).

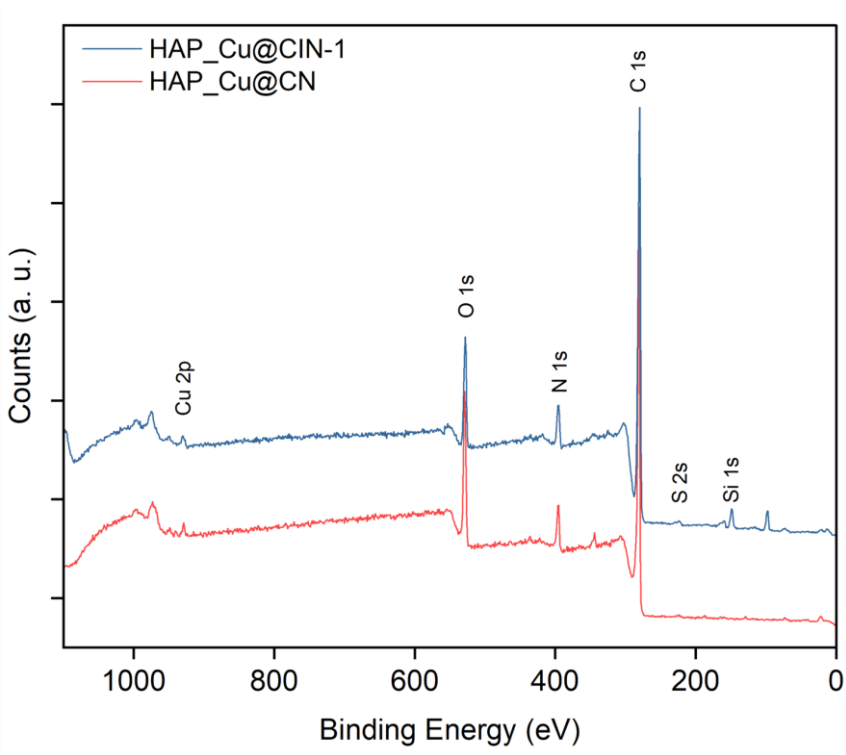

Figure S-6-7 XP survey spectrum of HAP_Cu@CIN-1 and HAP_Cu@CN. The principal elements detected on the surface are indicated in the image.

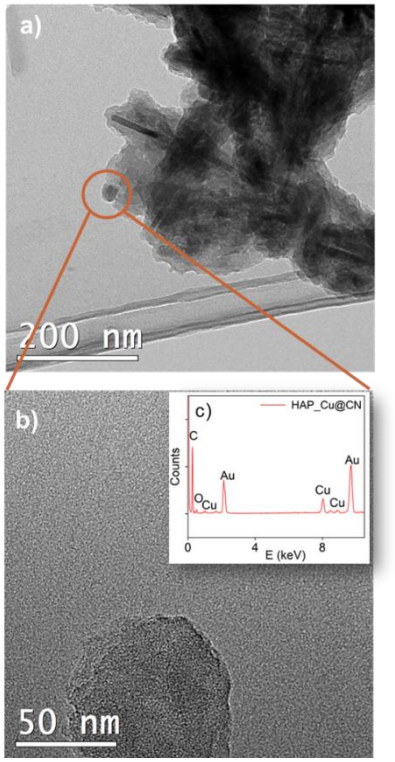

Figure S-6-8 Representative TEM of HAP_Cu@CN (a), HR-TEM and respective EDX spectra of spherical nanoaggregates containing Cu (b, c).

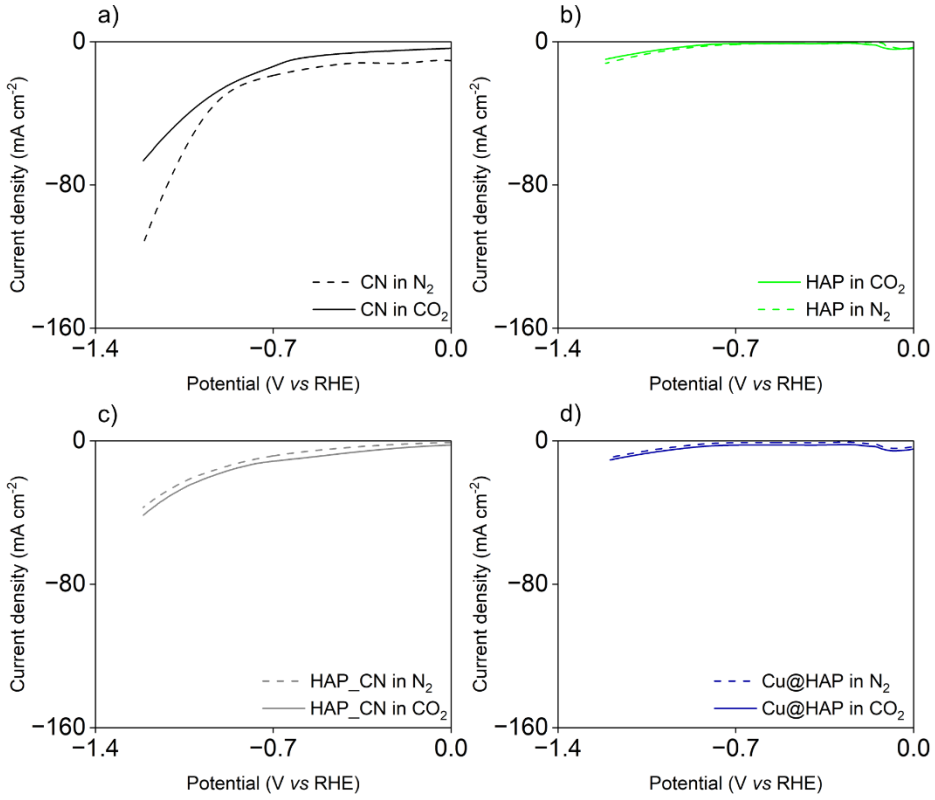

Figure S-6-9 . Linear Sweep Voltammetry (LSV) results for reference materials: CN (a, black), HAP (b, green), HAP_CN (c, grey), Cu@HAP (d, dark blue) under N_2-saturated (dashed line) and CO_2 -saturated (solid line) 0.1 M $KHCO_3$ aqueous solution at 20 mV s^{-1} scan rate.

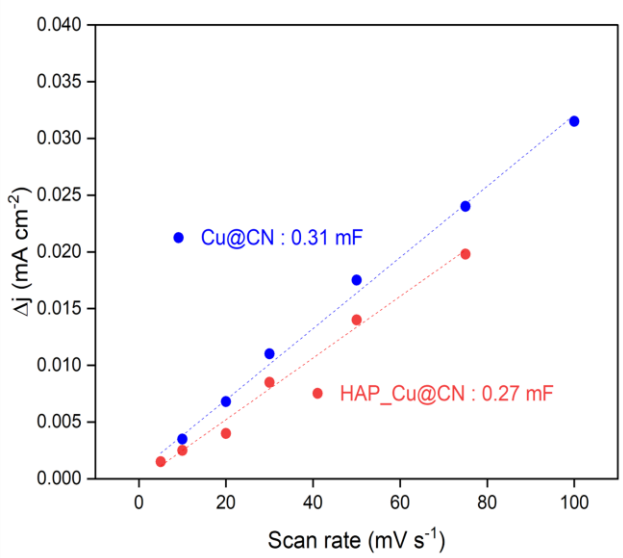

Figure S-6-10 C_{dl} curves of Cu@CN and HAP_Cu@CN, calculated from CV analyses. C_{dl} values are reported for Cu@CN and HAP_Cu@CN in mF.

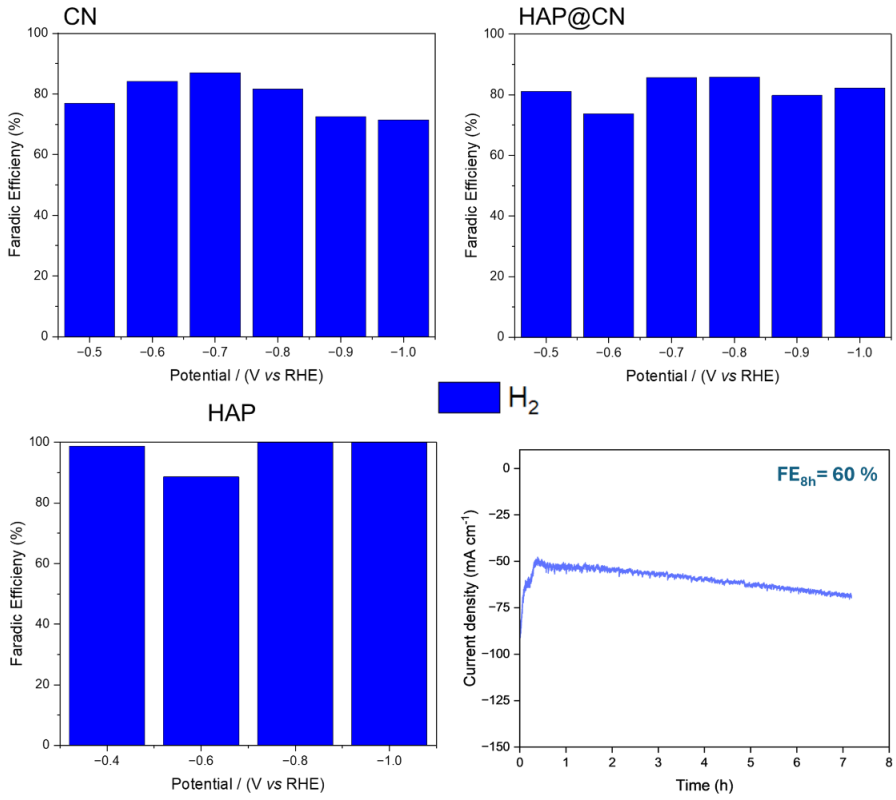

Figure S-6-11 Faradic efficiency of reference materials (CN, HAP@CN, HAP) for CO_2ER in $KHCO_3$ aqueous solution (0.1 mol L^{-1}), 1 h, RT at different potential (vs RHE). Long term stability test of HAP_Cu@CN at -1.0 V (vs RHE) for 8 h, RT, in $KHCO_3$ aqueous solution (0.1 mol L^{-1}).

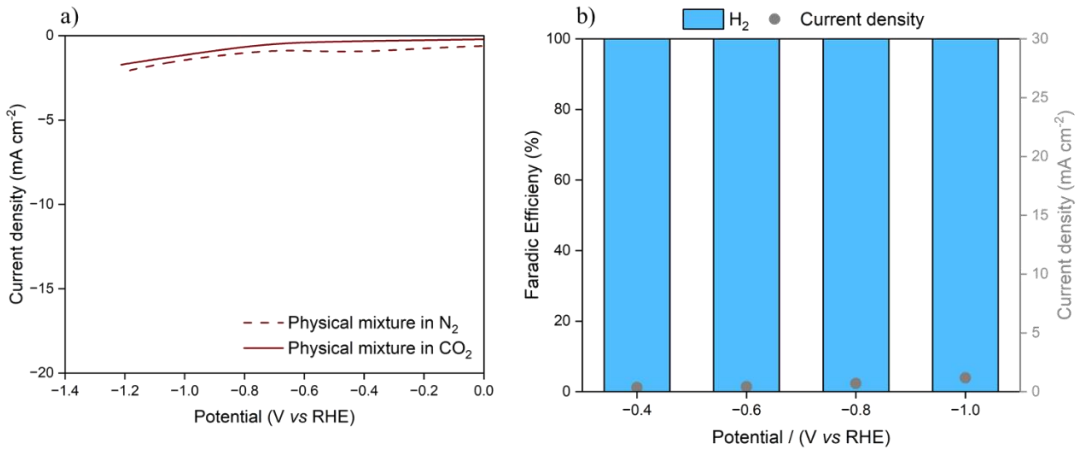

Figure S-6-12 (a) Linear Sweep Voltammetry (LSV) results for physical mixture of Cu@HAP (wt %) and CN N_2-saturated (dashed line) and CO_2-saturated (solid line) in 0.1 mol L^{-1}, $KHCO_3$ aqueous solution at 20 mV s^{-1} scan rate; (b) Faradic efficiency of physical mixture for CO_2ER in $KHCO_3$ aqueous solution (0.1 mol L^{-1}), for 30 min, RT at different potential (vs RHE).

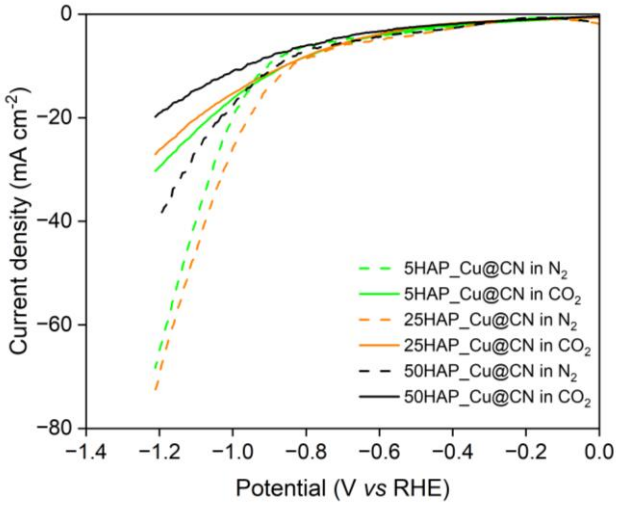

Figure S-6-13 Linear Sweep Voltammetry (LSV) results for composites with different HAP: 5HAP_Cu@CN (HAP 5 wt %), 25HAP_Cu@CN (HAP 25 wt %), 50HAP_Cu@CN (HAP 50 wt %) in N_2-saturated (dashed line) and CO_2-saturated (solid line) in 0.1 mol L^{-1}, $KHCO_3$ aqueous solution at 20 mV s^{-1} scan rate.

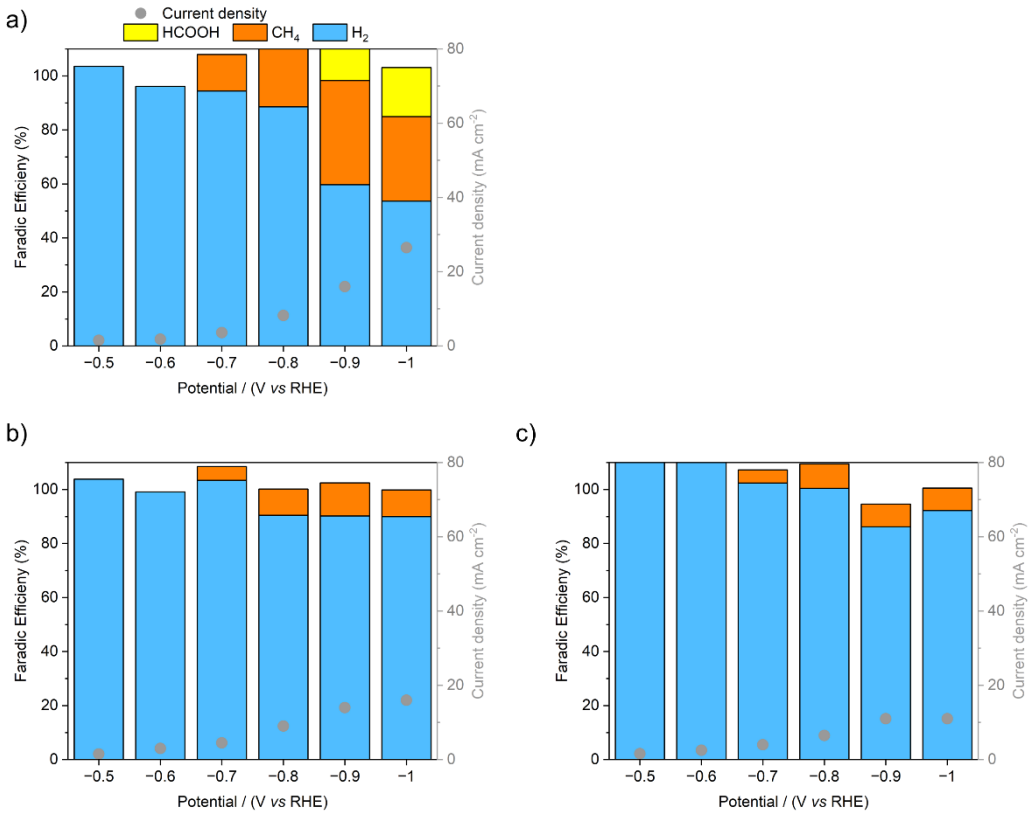

Figure S-6-14 Faradic efficiency of composites with different HAP weight percentage: a) 5HAP_Cu@CN (HAP 5 wt %), b) 25HAP_Cu@CN (HAP 25 wt %), c) 50HAP_Cu@CN (HAP 50 wt %) for CO_2ER in $KHCO_3$ aqueous solution (0.1 mol L^{-1}), 1 h, RT at different potential (vs RHE).

6.3. Sustainable Materials

Table S-6-1 Chemical composition of the hydroxyapatite samples determined by ICP-OES

Sample	Ca[a] (wt %)	P[a] (wt %)	Al (mol %)	Fe (mol %)	Mg (mol %)	Na (mol %)	Si (mol %)	Sr (mol %)	Zn (mol %)	Ca/P molar ratio
HAP_1	**29.48** ± 2.02	**12.54** ± 0.90	**4.80**± 0.13	**1.42** ± 0.02	**8.78** ± 0.37	**1.44** ± 0.07	**8.15** ± 0.50	**0.05** ± 0.01	**0.13** ± 0.01	**1.82** ± 0.01
HAP_2	**33.85** ± 0.44	**14.65** ± 0.19	**3.47**± 0.08	**1.74** ± 0.01	**8.68** ± 0.20	**1.16** ± 0.12	**6.95** ± 0.35	**0.05**± 0.01	**0.13** ± 0.01	**1.79** ± 0.01
HAP_3	**29.45** ± 1.88	**11.04** ± 0.77	**6.53** ± 0.04	**2.50** ± 0.02	**13.03** ± 0.09	**1.51**± 0.05	**14.19**± 0.88	**0.08** ± 0.01	**0.14** ± 0.01	**2.06** ± 0.02
HAP_4	**28.04** ± 1.18	**10.65** ± 0.46	**7.20**± 0.01	**2.33** ± 0.00	**13.31** ± 0.02	**1.55** ± 0.02	**15.14** ± 0.33	**0.08** ± 0.01	**0.14** ± 0.01	**2.03** ± 0.02

a. Ca and P percentage are expressed in weight percentage so the sum of molar percentage of remaining elements (3rd to 9th column) is not reaching to 100%.

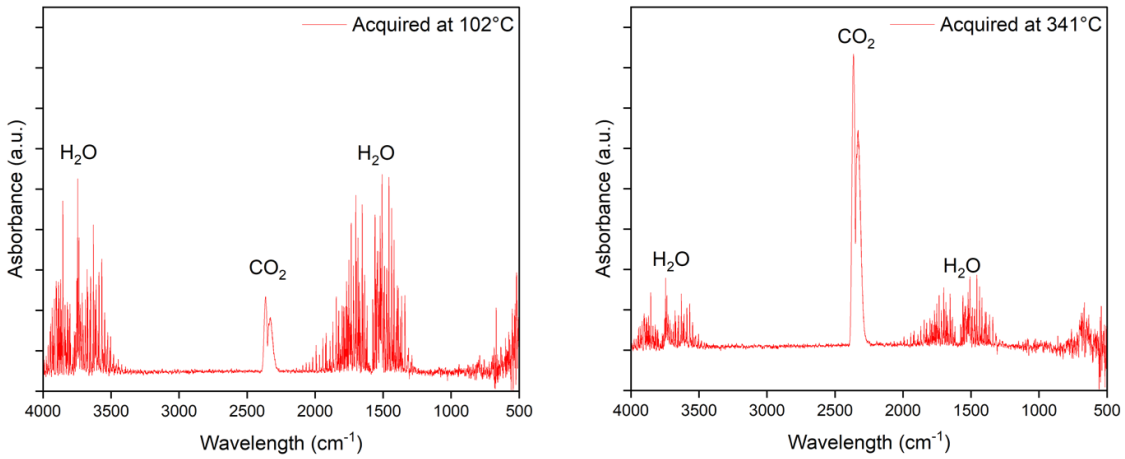

Figure S-6-15: FT-IR spectra of the gases leaving the furnace at a) 102 °C and b) 341 °C, during the TGA analysis of sample HAP_2. The spectra were acquired at the temperatures corresponding at the two mass losses highlighted by the DTG curve in **Figure** 4-7.

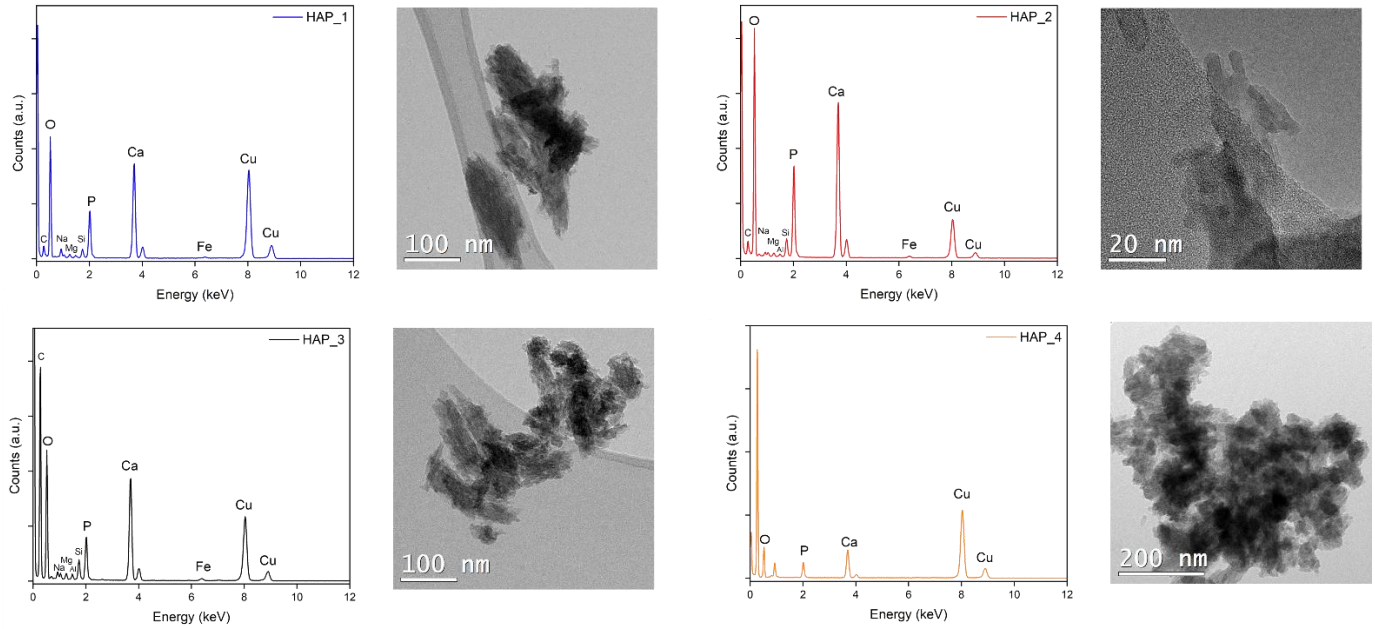

Figure S-6-16 EDX spectra and relative TEM images displaying the main element observed for HAP_1 (blue line), HAP_2 (red line), HAP_3 (black line), HAP_4 (orange line). The most intense signals are reported; Cu and C signals are not quantified as they are related to the TEM grid and of conductive coating, respectively.

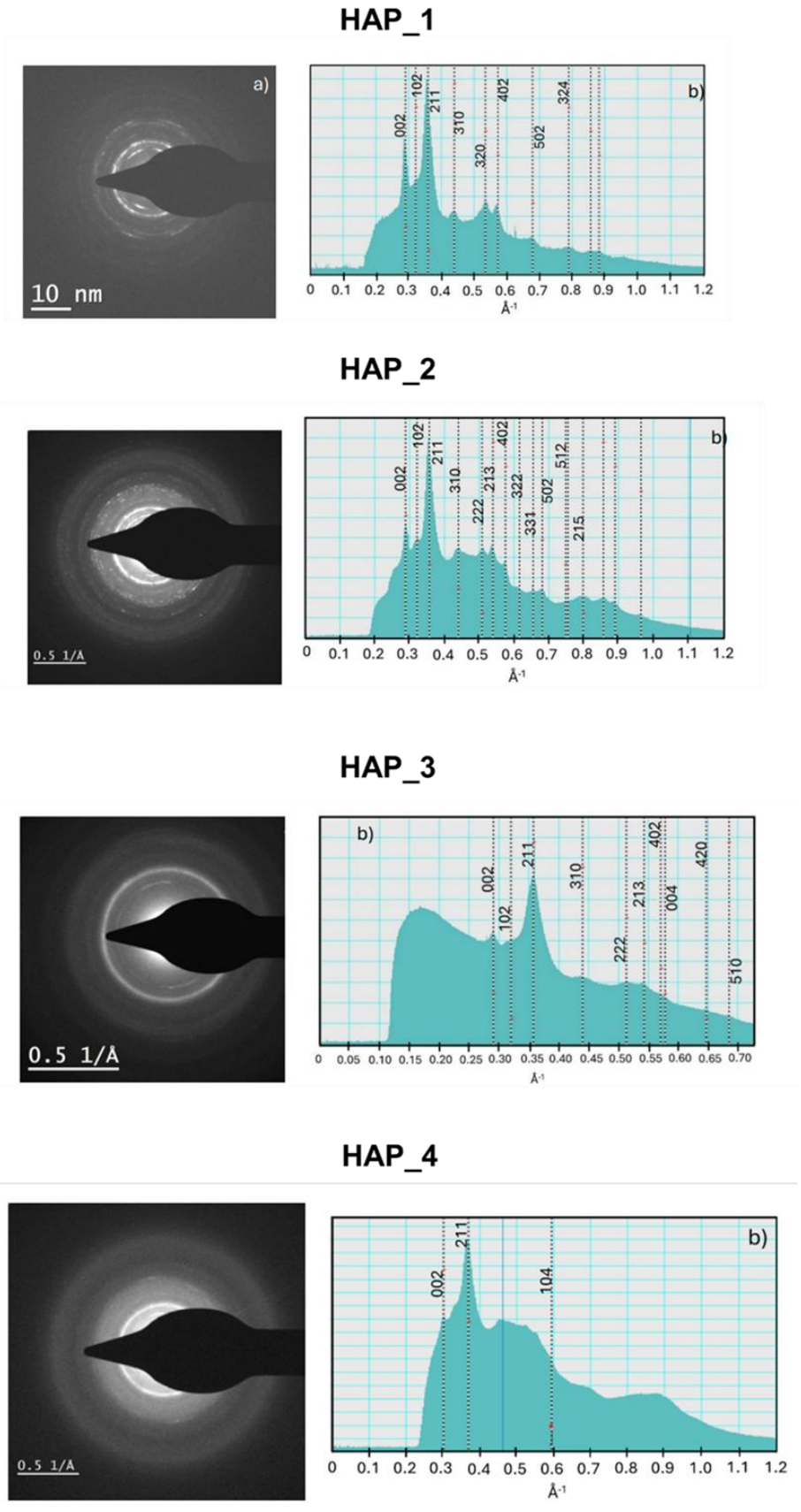

Figure S-6-17 Eectron diffraction patterns (left) and appropriate processing showing the reflections (right) for ashes derived hydroxyapatite samples with identification of the crystal planes.

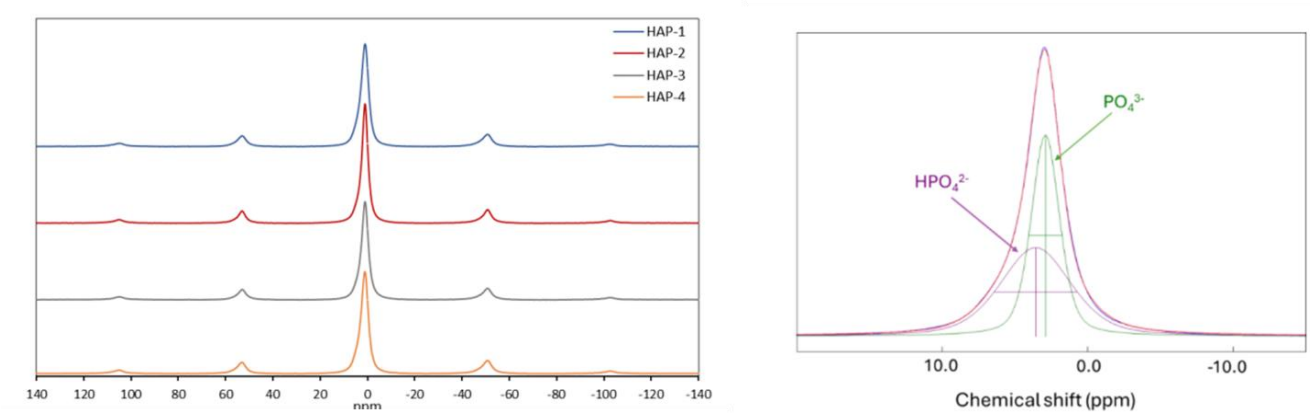

Figure S-6-18 ^{31}P ssNMR spectra of the ash-derived HAP samples, with four spinning side bands for each of them (left), NMR spectral decomposition for sample HAP_1 (illustrative), showing the two different contributions to the ^{31}P signal indicative of two protonation states coexisting inside the samples (right).

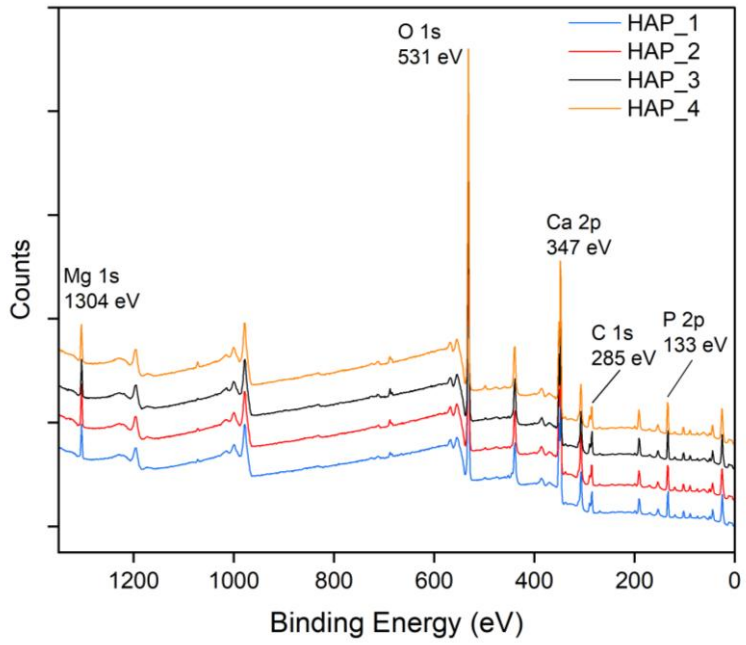

Figure S-6-19 : XP spectrum of ashes-derived HAP samples, reporting the main elements observed (Mg, O, Ca, C, P).

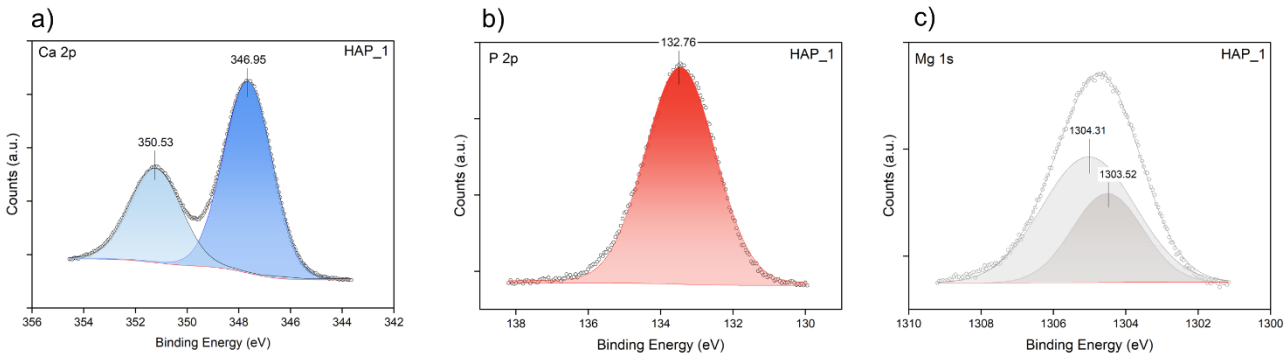

Figure S-6-20 Representative high resolution (HR) XP spectra of Ca 2p, P 2p and Mg 1s of HAP_1. The principal deconvoluted peak are indicated (all the data were processed by ruling out and shifting the peaks based on the contribution of adventitious carbon C-C at 284.6 eV).

Table S-6-2 XPS peak fittings of HR spectra of Ca, P, Mg of HAP_1 (**Figure** S-7-16): binding energies and their assignments according to NIST database (all the collected data were processed by ruling out the contribution of adventitious carbon C-C at 284.6 eV).

Peak fit	Binding Energy *eV*	Chemical bonds
Ca 2p	346.95 *Ca 2p$_{3/2}$*	Ca-O
	350.23 *Ca 2p$_{1/2}$*	
P 2p	132.76 *P 2p$_{1/2}$* and *2p$_{3/2}$*	P-O
Mg 1s	1303.52	Mg-O
	1304.31	Mg-(CO_3)

Table S-6-3 Regressed Langmuir parameters for PEA and BA adsorption isotherms collected at 30°C in cyclohexane on ashes derived HAP samples.

Sample		Acidity			Basicity		
		n_{max} *meq g^{-1}*	b_{ads} *L mol^{-1}*	R^2	n_{max} *meq g^{-1}*	b_{ads} *L mol^{-1}*	R^2
HAP_1	*I run*	0.098	86497	0.997	0.215	416248	0.999
	II run	0.054	51058	0.989	0.069	81912	0.999
	Strong sites	0.046	90737	0.998	0.149	537137	0.998
HAP_2	*I run*	0.082	100453	0.998	0.232	91955	0.998
	II run	0.041	95391	0.984	0.134	16441	0.998
	Strong sites	0.044	159206	0.998	0.115	521983	0.998
HAP_3	*I run*	0.124	319422	0.999	0.308	349853	0.999
	II run	0.053	75006	0.995	0.075	45462	0.999
	Strong sites	0.071	150405	0.968	0.233	567106	0.999
HAP_4	*I run*	0.130	110892	0.999	0.328	332406	0.998
	II run	0.073	97408	0.987	0.069	34712	0.993
	Strong sites	0.066	58061	0.989	0.243	751366	0.998

Influence of water system on ashes derived HAP samples.

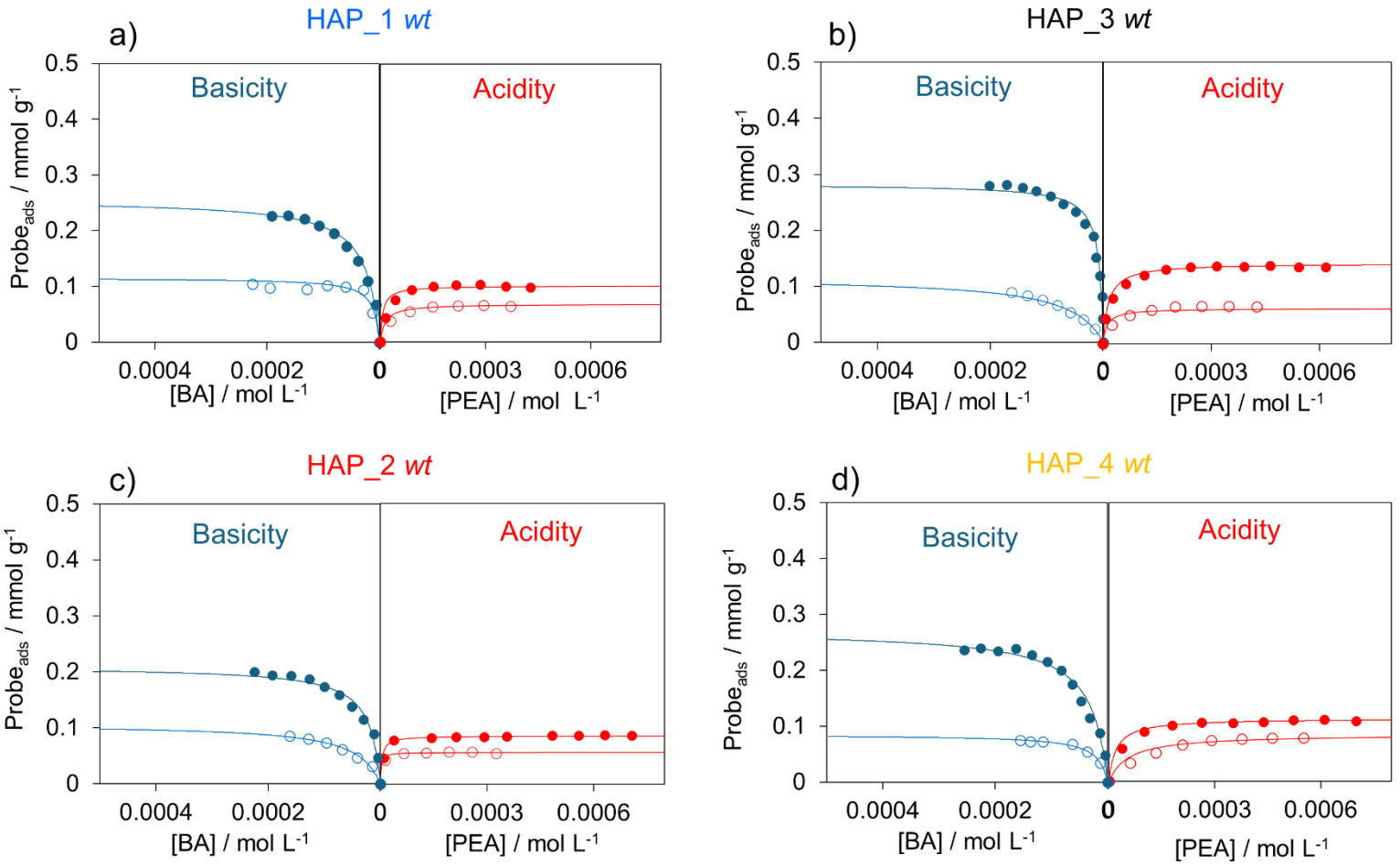

Figure S-6-21 Adsorption isotherms of PEA (for acidity) and BA (for basicity) probes collected in cyclohexane at 30 °C on *water treated* hydroxyapatite samples (a) HAP_1, b) HAP_2, c) HAP_3, d) HAP_4), collected in solid-liquid phase titration recirculation system. Full and empty markers represent I° run adsorption and II run adsorption on the surfaces. Blue lines and red lines represent the calculated Langmuir curves of PEA and BA adsorption. The detailed elaboration data is reported in paragraph 2.2.3. The adsorption isotherms on *fresh* samples are reported in **Figure** 4-20 and Figure 4-21

Table S-6-4 Regressed Langmuir parameters for PEA and BA adsorption isotherms collected at 30°C in cyclohexane on ashes derived HAP samples after treatment in water (80°C, 8 h).

Sample		Acidity *post* water treatment			Basicity *post* water treatment		
		n_{max} *meq g^{-1}*	b_{ads} *L mol^{-1}*	R^2	n_{max} *meq g^{-1}*	b_{ads} *L mol^{-1}*	R^2
HAP_1 WT	*I run*	0.101	95201	0.996	0.256	41896	0.990
	II run	0.068	72814	0.988	0.115	94972	0.991
	Strong sites	0.045	30871	0.937	0.157	18314	0.897
HAP_2 WT	*I run*	0.086	247306	0.996	0.209	49334	0.988
	II run	0.056	234114	0.996	0.107	22453	0.978
	Strong sites	0.029	273320	0.999	0.117	66655	0.993
HAP_3 WT	*I run*	0.129	74598	0.987	0.282	128089	0.996
	II run	0.071	54304	0.989	0.116	15973	0.974
	Strong sites	0.071	64266	0.999	0.198	247403	0.998
HAP_4 WT	*I run*	0.112	48585	0.997	0.271	32441	0.992
	II run	0.085	18143	0.943	0.085	52184	0.997
	Strong sites	0.036	133577	0.995	0.161	32109	0.818

Table S-6-5 Regressed Langmuir parameters for PEA and BA adsorption isotherms collected at 30°C in water (effective acidity/basicity) on HAP_2, as representative sample in water.

Sample		Effective acidity			Effective basicity		
		n_{max} *meq g^{-1}*	b_{ads} *L mol^{-1}*	R^2	n_{max} *meq g^{-1}*	b_{ads} *L mol^{-1}*	R^2
HAP_2	*I run*	0.012	62353	0.967	0.050	46364	0.982

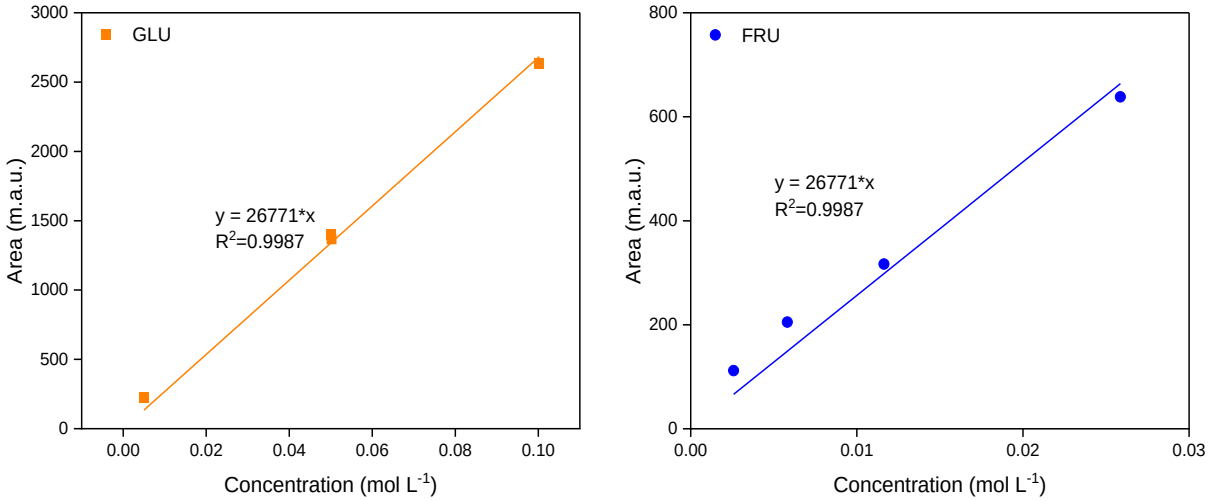

Figure S-6-22 Calibration lines of glucose (GLU) and fructose (FRU) for HPLC analytical setup, calculated from external standard solutions.

The conversion calculated from moles of glucose detected and quantified by HPLC analyses is compared to conversion equilibrium at 120 °C. From the work of Tewari and Goldberg, a proper correlation between free Gibbs Energy (ΔG^o), specific heat capacity (C_p) and temperature (T) was carried out and verified in different temperature ranges. The correlation is expressed following the equation (Eq. 6-2):

$$\Delta G_T^0 = \Delta H_{298.15}^0 + \int_{298.15}^{T} \Delta C_p^0 dT - T * \left[\Delta S_{298.15}^0 + \int_{298.15}^{T} \frac{\Delta C_p^0}{T} dT \right] \quad \text{Eq. 6-2}$$

where $\Delta G^o_{298.15}$ is 2780 J mol^{-1}, $\Delta C_p{}^o$ is 76 J mol^{-1} K^{-1}, $\Delta S^o_{298.15}$ is 8.15 J mol^{-1} K^{-1} and T is the working temperature different from 298.15 K. After integration, equilibrium constant (K_{eq}) was calculated from the equation Eq. 6-3:

$$K_{eq} = e^{\left(\frac{-\Delta G_T^0}{RT}\right)} \quad \text{Eq. 6-3}$$

Where R is the universal gas constant equal to 8.314 J mol^{-1} K^{-1}. The correlation is an exponential proportion between equilibrium constant and temperature, as it can be seen in **Figure** S-6-21

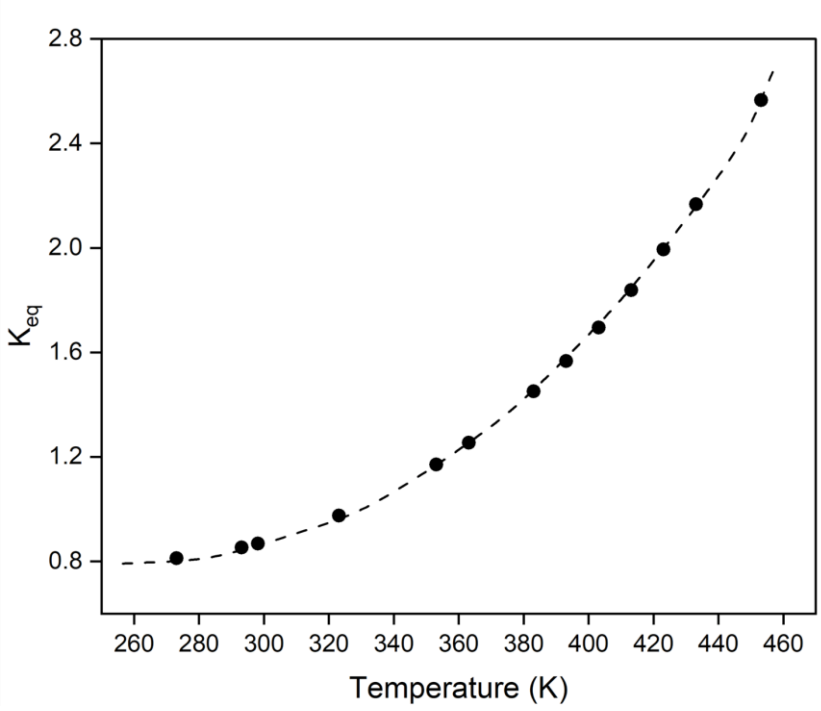

Figure S-6-23 Exponential correlation between equilibrium constant (K_{eq}) and T (K) for glucose isomerisation to fructose reaction in water.

Equilibrium constant can be expressed as a function of equilibrium concentration as reported in the following equation:

$$K_{eq} = \frac{[FRU]_{eq}}{[GLU]_{eq}} = \frac{x}{1-x} \qquad \text{Eq. 6-4}$$

Where $[FRU]_{eq}$ and $[GLU]_{eq}$ are the equilibrium concentration of fructose and glucose respectively, that can be expressed as a function of conversion *x*. In this way, a correlation between conversion and temperature was calculated and a comparison could be carried out.

Table S-6-6 Regressed Langmuir parameters for PEA and BA adsorption isotherms collected at 30°C in cyclohexane on synthetic HAP sample.

Sample		Acidity in Cyclohexane			Basicity in Cyclohexane		
		n_{max} *meq g^{-1}*	b_{ads} *L mol^{-1}*	R^2	n_{max} *meq g^{-1}*	b_{ads} *L mol^{-1}*	R^2
Synthetic HAP	*I run*	0.159	9554	0.988	0.196	137488	0.999
	II run	0.121	8345	0.983	0.115	133654	0.999
	Strong sites	0.0378	11860	0.906	0.0845	80342	0.974

Table S-6-7 Distribution of acid and basic sites as a function of heat developed after the introduction of dosed amount of probe (NH_3 and SO_2) for synthetic HAP sample.

	NH_3 Adsorption microcalorimetry				SO_2 Adsorption microcalorimetry			
	< 50	50-100	100-150	150-200	< 50	50-100	100-150	150-200
	kJ mol^{-1}				*kJ mol^{-1}*			
Synthetic HAP (n_{ads} / *µmol g^{-1}*)	52.7	268.0	35.5	n.d.	n.d.	25	158.5	86.2

Permissions

ELSEVIER LICENSE
TERMS AND CONDITIONS

Jan 05, 2026

This Agreement between Michele Bigica Università degli Studi di Milano ("You") and Elsevier ("Elsevier") consists of your license details and the terms and conditions provided by Elsevier and Copyright Clearance Center.

License Number	6182530851822
License date	Jan 05, 2026
Licensed Content Publisher	Elsevier
Licensed Content Publication	One Earth
Licensed Content Title	Sustainable chemistry: Green, circular, and safe-by-design
Licensed Content Author	J. Chris Slootweg
Licensed Content Date	May 17, 2024
Licensed Content Volume	7
Licensed Content Issue	5
Licensed Content Pages	5
Start Page	754
End Page	758
Type of Use	reuse in a thesis/dissertation
Portion	figures/tables/illustrations

Number of figures/tables/illustrations	2
Format	both print and electronic
Are you the author of this Elsevier article?	No
Will you be translating?	No
Title of new work	Towards Sustainable Materials for CO_2 Remediation: From Functional Carbon-Hydroxyapatite Composites to Waste-Derived Resources
Institution name	Università degli Studi di Milano
Expected presentation date	Feb 2026
Portions	Figure 1 Figure 2
The Requesting Person / Organization to Appear on the License	Michele Bigica Università degli Studi di Milano
Requestor Location	Via Petrarca, 42 Rivolta d'Adda, CR / Lombardia 26027 Italy
Publisher Tax ID	GB 494 6272 12
Total	0.00 EUR

Terms and Conditions

INTRODUCTION

1. The publisher for this copyrighted material is Elsevier. By clicking "accept" in connection with completing this licensing transaction, you agree that the following terms and conditions apply to this transaction (along with the Billing and Payment terms and conditions established by Copyright Clearance Center, Inc. ("CCC"), at the time that you opened your RightsLink account and that are available at any time at https://myaccount.copyright.com).

ELSEVIER LICENSE
TERMS AND CONDITIONS

Jan 05, 2026

This Agreement between Michele Bigica Università degli Studi di Milano ("You") and Elsevier ("Elsevier") consists of your license details and the terms and conditions provided by Elsevier and Copyright Clearance Center.

License Number	6182540155524
License date	Jan 05, 2026
Licensed Content Publisher	Elsevier
Licensed Content Publication	Sustainable Energy Technologies and Assessments
Licensed Content Title	Bioelectrochemical conversion of CO2 emissions as greenhouse gases capture and renewable electricity storage strategy: advancing power-to-methane technologies – a critical review
Licensed Content Author	Gabriele Soggia,Andrea Goglio,Pierangela Cristiani,Fabrizio Adani
Licensed Content Date	Aug 1, 2025
Licensed Content Volume	80
Licensed Content Issue	n/a
Licensed Content Pages	1
Start Page	104394
End Page	0
Type of Use	reuse in a thesis/dissertation

JOHN WILEY AND SONS LICENSE
TERMS AND CONDITIONS

Jan 05, 2026

This Agreement between Michele Bigica Università degli Studi di Milano ("You") and John Wiley and Sons ("John Wiley and Sons") consists of your license details and the terms and conditions provided by John Wiley and Sons and Copyright Clearance Center.

License Number	6182540403619
License date	Jan 05, 2026
Licensed Content Publisher	John Wiley and Sons
Licensed Content Publication	CHEMPLUSCHEM
Licensed Content Title	Copper-Based Catalysts for Electrochemical Reduction of Carbon Dioxide to Ethylene
Licensed Content Author	Xiao Chen, Yunxia Zhao, Jiayi Han, et al
Licensed Content Date	Jan 18, 2023
Licensed Content Volume	88
Licensed Content Issue	1
Licensed Content Pages	16
Type of use	Dissertation/Thesis
Requestor type	University/Academic
Format	Print and electronic
Portion	Figure/table

ELSEVIER LICENSE
TERMS AND CONDITIONS

Jan 05, 2026

This Agreement between Michele Bigica università degli Studi di Milano ("You") and Elsevier ("Elsevier") consists of your license details and the terms and conditions provided by Elsevier and Copyright Clearance Center.

License Number	6182540992506
License date	Jan 05, 2026
Licensed Content Publisher	Elsevier
Licensed Content Publication	Journal of Hazardous Materials
Licensed Content Title	Hydroxyapatite, a multifunctional material for air, water and soil pollution control: A review
Licensed Content Author	Maya Ibrahim,Madona Labaki,Jean-Marc Giraudon,Jean-François Lamonier
Licensed Content Date	Feb 5, 2020
Licensed Content Volume	383
Licensed Content Issue	n/a
Licensed Content Pages	1
Start Page	121139
End Page	0
Type of Use	reuse in a thesis/dissertation

ELSEVIER LICENSE
TERMS AND CONDITIONS

Jan 05, 2026

This Agreement between Michele BIgica Università degli Studi di Milano ("You") and Elsevier ("Elsevier") consists of your license details and the terms and conditions provided by Elsevier and Copyright Clearance Center.

License Number	6182541163309
License date	Jan 05, 2026
Licensed Content Publisher	Elsevier
Licensed Content Publication	Materials Today Sustainability
Licensed Content Title	Sustainable carbon materials from the pyrolysis of lignocellulosic biomass
Licensed Content Author	Shijie Yu,Longzhou Wang,Qinghai Li,Yanguo Zhang,Hui Zhou
Licensed Content Date	Nov 1, 2022
Licensed Content Volume	19
Licensed Content Issue	n/a
Licensed Content Pages	1
Start Page	100209
End Page	0
Type of Use	reuse in a thesis/dissertation

Publications

- Imparato, C.; Finocchio, E.; Campisi, S.; Bigica, M.; Gervasini, A.; Bifulco, A.; Avolio, R.; Clayden, N. J.; Errico, M. E.; Aronne, A. Insight into Titanium and Zirconium Phosphate-Based Materials for Reactive Surfaces. *Material Today Chemistry* (**2024**), *38*, 102126.

- Bigica, M.; Ghiara, G.; Cristiani, P.; Campisi, S.; Gervasini, A. Interface Properties of Hydroxyapatite in Ternary Composites Cathodes for Electromethanogenesis. *New Journal of Chemistry* (**2024**), *48* (22), 9909–9919.

- Cazzulani, E.; Bigica, M.; Avola, T.; Campisi, S. The Hidden Strength of Weak Forces: The Role of Non-Covalent Interactions in Electrocatalytic CO2 Reduction. *Rendiconti Lincei. Scienze Fisiche e Naturali 2026* (**2026)**, 1–29.

Attended School and Congresses

- XXIII National Catalysis Congress GIC 2023, (14^{th} -16^{th} June 2023 – Genova, Italy)

M. Bigica, G. Ghiara, P. Cristiani, S. Campisi, A. Gervasini *On the role of hydroxyapatite as a key component in cathode materials to drive the electroreduction of CO_2 to CH_4* XXIII National Catalysis Congress GIC 2023, Genova 14^{th} -16^{th} June 2023 **Poster communication.**

- National School of Physical Chemistry 2023 (19^{th} - 23^{rd} June 2023 – Verbania, Italy)

M. Bigica, G. Ghiara, P. Cristiani, S. Campisi, A. Gervasini *Dissecting the influence of hydroxyapatite surface features on the bioelectromethonegesis activity of ternary hydroxyapatite/copper/biochar composites*, National School of Physical Chemistry 2023, Verbania, 19^{th} -23^{rd} June 2023 **Poster communication.**

- C3-Day 2024 (4^{th} June, 2024 – Bologna, Italy).

3^{rd} edition of the Center of Chemical Catalysis C3-Day 2024 (4^{th} June, 2024 – Bologna, Italy).
M. Bigica, P. Cristiani, S.Campisi, A. Gervasini*, Exploring the role of hydroxyapatite as a*

pivotal component in composite cathodic materials to drive the electroreduction of CO_2 to CH_4, C3-day 2024, Bologna, 4 Giugno 2024, **Poster contribution**

- 9th EuChemS (7th -11th July 2024, Dublin – Ireland)

M. Bigica, A. Gervasini, S. Campisi, P. Cristiani, A. Khodakov, V. Ordomsky, *Functional and innovative carbon nitride/hydroxyapatite composite material for efficient carbon dioxide electrocatalytic reduction to formic acid*, 9th EuChemS, Dublin, 7th -11th July 2024, **Oral contribution**

- C1-Chem, Lille, (10th -12th July 2024, Lille – France)

M. Bigica, A. Gervasini, S. Campisi, A. Khodakov, V. Ordomsky, *Novel carbon nitride/hydroxyapatite composite material for effective CO_2 electroreduction into C1- based product*, C1-Chem, Lille, 10th -12th July 2024, **Oral contribution**

- International Conference on Environmental Catalysis ICEC 2025, (2nd-5th June 2025, Palermo – Italy)

M. Bigica, A. Gervasini, S. Campisi, P. Cristiani, A. Khodakov, V. Ordomsky *Innovative Metal Functionalized Hydroxyapatite/carbon Nitride Nanocomposite material To Enhance CO_2 Electroreduction To Formate* ICEC 2025, Palermo 2nd-5th June 2025, **Oral Contribution**

M. Bigica, S. Campisi, A. Gervasini, S. Sprio, M. Tavoni, G. Postole *Circular Economy-Driven Synthesis of Hydroxyapatites from Ash: A Comprehensive Analysis of Surface and Bulk Properties* ICEC 2025, Palermo 2nd-5th June 2025, **Poster Contribution**